Department of Pure and Applied Chemistry

New Materials for Electrochemical Synthesis of Ammonia

By

Ibrahim Ali Ahmed Amar

A thesis presented in fulfilment of the requirements for the degree of

Doctor of Philosophy

2014

Declaration of Authors Rights

List of publications

- Ibrahim A. Amar, Rong Lan, Christophe T.G. Petit, Shanwen Tao "Solid-state electrochemical synthesis of ammonia: a review" Journal Solid State Electrochemistry 15 (2011) 1845-1860
- Ibrahim A. Amar, Rong Lan, Christophe T.G. Petit, Valeria Arrighi, Shanwen Tao "Electrochemical synthesis of ammonia based on a carbonate-oxide composite electrolyte" Solid State Ionics 182 (2011) 133-138
- Ibrahim A. Amar, Christophe T.G. Petit, Lei Zhang, Rong Lan, Peter Skabara, Shanwen Tao "Electrochemical synthesis of ammonia based on doped-ceria-carbonate composite electrolyte and perovskite cathode" Solid State Ionics, 201 (2011) 94.

- Ibrahim A. Amar, Christophe T.G. Petit, Gregory Mann, Rong Lan, Peter Skabara and Shanwen Tao "Electrochemical synthesis of ammonia from N_2 and H_2O based on $(Li,Na,K)_2CO_3$−$Ce_{0.8}Gd_{0.18}Ca_{0.02}O_{2-\delta}$ composite electrolyte and $CoFeO_4$ cathode" International Journal of Hydrogen Energy, 39 (2014) 4322-4330.

- Rong Lan, Khaled Alkhazmi, Ibrahim A. Amar, Shanwen Tao " Synthesis of ammonia directly from wet air at intermediate temperature" Appiled Catalysis B: Environmental, 152-153 (2014) 212-217.

- Rong Lan, Khaled Alkhazmi, Ibrahim A. Amar, Shanwen Tao "Synthesis of ammonia directly from wet air using new perovskite oxide $La_{0.8}Cs_{0.2}Fe_{0.8}Ni_{0.2}O_{3-\delta}$ as catalyst" Electrochimica Acta, 123 (2014) 582-587.

Acknowledgements

All praise for Allah (God) for his greatest blessing that made all this happen. Where to start!? This thesis would never have been written without the enormous support and assistance of many people to whom I would like to express thanks.

First of all, I would like to express my sincere gratitude to my supervisor Professor Shanwen Tao for providing me a great opportunity to study as a PhD student at Heriot-Watt University and then at Strathclyde University. His continuous help, guidance and support made this work possible. I would like to show my gratitude to my supervisor Professor Peter J. Skabara. It is an honour for me to have a great opportunity to study under his supervision at Strathclyde University. He was always there when I needed direction, guidance, or just help. I would also like to thank Dr Valeria Arrighi, my second supervisor at Heriot Watt University, for her support and encouragement.

My thanks also go to all the members of the fuel cell group, especially Christophe Petit for his advice, sharing his knowledge, collecting the thermal analysis data and help in solving any technical issues. Special thanks to Dr Rong Lan who taught me how to set up the reactor and conditions for ammonia synthesis experiments. Thanks also to Lei Zhang for helping me to make the tri-layer single cell. Special thanks also go to Gregory Mann for collecting SEM data. Particular thanks to Peter Cowin for assistance, advice and fruitful discussion. I would like also to thank Mrs Marian Millar for the powder XRD and SEM data collection during my study at Heriot Watt University. I would also like to acknowledge the Libyan Cultural Affairs – London for their financial support.

Finally, I would particularly like to thank my mother, my wife and daughter and all members of my family for their prayers, support and encouragement.

Dedicated to

The Soul of my father Ali A. Amar and the soul of my friend Abu baker Almegbari (Hamza) who died while I was studying abroad, May Allah bless them

Table of Contents

List of Abbreviations

AC	Alternative Current
CE	Current Efficiency
CPE	Constant Phase Element
CSEs	Composite Solid Electrolytes
DC	Direct Current
DMFC	Direct Methanol Fuel Cell
DSC	Differential Scanning Calorimetry
EC	Equivalent Circuit
EIS	Electrochemical Impedance Spectroscopy
EM	Electron Microscopy
FCs	Fuel Cells
HER	Hydrogen Evolution Reaction
HTPCs	High Temperature Proton Conductors
ISE	Ion Selective Electrode
JCPDS	Joint Committee on Powder Diffraction Standards
MCFCs	Molten Carbonate Fuel Cells
MIECs	Mixed Ionic Electronic Conductors
PEMFs	Proton Exchange Membrane Fuel cells
TGA	Thermogravimeric Analysis
TEC	Thermal Expansion Coefficient
TEM	Transmission Electron Microscopy
TMNs	Transition metal nitrides
TPB	Triple Phase Boundary
SEM	Scanning Electron Microscopy
SOECs	Solid Oxide Electrolysis cells
SOFCs	Solid Oxide Fuel Cells

SSPCs	Solid State Proton Conductors
STA	Simultaneous Thermal Analysis
XRD	X Ray Diffraction

List of Figures

Abstract

This thesis has mainly focused on the electrochemical synthesis of ammonia at atmospheric pressure using three different catalyst types (nitride, spinel and perovskite). Attention also has been given to developing new electrolyte materials based on oxide-carbonate composites, with the aim of exploring their application in ammonia synthesis at low operating temperature (< 500 °C).

Ammonia was synthesised from H_2 and N_2 using an electrolyte supported cell based on $LiAlO_2$-$(Li/Na/K)_2CO_3$ as electrolyte, Ag-Pd as anode and either nitride (e.g. Co_3Mo_3N) or spinel ($CoFe_2O_4$) as cathode. The maximum rate of ammonia formation (3.27×10^{-10} mol s^{-1} cm^{-2} at 450 °C and 0.8 V) was obtained when Co_3Mo_3N was used as a cathode. Ammonia was also synthesised from H_2 and N_2 in an electrolytic cell based on Sm-doped ceria-carbonate composite (SDC-$(Li/Na/K)_2CO_3$) as an electrolyte, NiO-SDC as anode and perovskite oxide $La_{0.6}Sr_{0.4}Fe_{0.8}Cu_{0.2}O_{3-\delta}$ (LSFCu) catalyst as a cathode. The maximum rate was found to be 5.39×10^{-9} mol s^{-1} cm^{-2} at 450 °C and 0.8 V.

Ammonia was also synthesised successfully from water vapour (3% H_2O) and nitrogen, using a new electrolyte material based on Ca and Gd co-doped ceria-carbonate composite (CGDC-$(Li/Na/K)_2CO_3$). Perovskite oxide $Sm_{0.5}Sr_{0.5}CoO_{3-\delta}$ (SSCo) was used as an anode and either spinel or perovskite based catalysts were used as cathodes. The maximum rate of ammonia formation (4.0×10^{-10} mol s^{-1} cm^{-2} at 375 °C and 1.4 V) was attained with a $La_{0.75}Sr_{0.25}Cr_{0.5}Fe_{0.5}O_{3-\delta}$ (LSCrF) cathode. Ammonia was synthesised directly from air and water vapour (3% H_2O) in a symmetrical cell composed of LSCrF as electrodes (cathode and anode) and CGDC-$(Li/Na/K)_2CO_3$ composite as electrolyte. The maximum rate was found to be 1.94×10^{-11} mol s^{-1} cm^{-2} at 375 °C with an applied voltage of 1.2 V.

1 Introduction

1.1 General Introduction

The global demand for energy and food is expected to increase dramatically in the future as result of world population growth. It is anticipated that the global energy demand will be doubled and the world population will reach 9 billion by 2050, hence from 70-100 % more food will be required to feed them [1, 2]. The use of synthetic fertilisers is of crucial importance to supply such quantities. Ammonia-based fertilisers have and will be expected to continue to play an important role in satisfying this demand [1, 3, 4].

Currently, ammonia is mainly produced on large-scale via the Haber-Bosch process, which involves reaction of gaseous H_2 and N_2. In this process, the required hydrogen is entirely produced through the steam reforming of natural gases or coal, which consumes approximately 84 % of the energy required for the ammonia industry. In addition, 2.3 tons CO_2 are released per ton of NH_3 produced [5-7]. In order to reduce the current dependency on fossil fuels and to reduce the carbon emissions associated with their use, alternative energy sources are needed for ammonia production. Thus, finding clean, environmentally-friendly technologies for energy production are among the major challenges for developers, scientists and decision-makers throughout the world. Electrochemical synthesis processes are among the promising alternatives, particularly if the hydrogen required for ammonia synthesis is produced from non fossil fuel resources. Electrochemical synthesis of ammonia directly from water and nitrogen without the need for the hydrogen production step offers the possibility to reduce the environmental consequences associated with fossil fuel use in H_2 production [8-11]. Furthermore, it has been reported recently that ammonia can be synthesised directly from air and water at ambient conditions [11].

This chapter includes a brief overview on the history of ammonia synthesis, applications and also a comprehensive review of the previous research concerning solid state electrochemical synthesis of ammonia [12, 13].

1.1.1 Historical development of the ammonia synthesis process

The development of the process of ammonia synthesis has a long history. In 1754, Priestley obtained ammonia for the first time by heating ammonium chloride with lime (CaO). In 1784, Berthollet proved that ammonia consists of hydrogen and nitrogen and established their approximate ratios. In the 1800s, many experiments were done with the aim of direct synthesis of ammonia from its elements (N_2 and H_2). Unfortunately, because of limited knowledge of thermodynamics and the fact that chemical equilibrium was incompletely understood at that time, the early ammonia synthesis experiments were unsuccessful [5, 14].

In 1904, the German scientist Fritz Haber (1868-1934) began conducting research on producing ammonia at atmospheric pressure and a minimal concentration of ammonia (0.012 %) was obtained at 1000 °C on pure iron catalyst. In 1908, Haber filed his patent on the synthesis of ammonia and he was awarded the Nobel Prize in Chemistry for this invention in 1918. Meanwhile, ammonia was successfully synthesised using an iron-based catalyst discovered in 1910 by Alwin Mittasch (1869-1953). Carl Bosch (1874-1940) subsequently scaled up the ammonia synthesis process for which he was awarded a Nobel Prize in 1931. Hence, today's process is known as the Haber-Bosch process: a reaction of gaseous hydrogen and nitrogen on Fe-based catalyst at high temperature (~ 500 °C) and high pressure (150-300 bar) [14-17]. This is a reversible reaction and can be described according the following reaction (Equation 1.1);

$$N_{2(g)} + 3H_{2(g)} \rightleftharpoons 2NH_{3(g)} \qquad \Delta H_{298K} = -92.4 \text{ kJ/mol} \qquad \text{Equation 1.1}$$

The equilibrium constant (K_{eq}) for this reaction is given by;

$$K_{eq} = \frac{P^2_{NH_3}}{P^3_{H_2} \cdot P_{N_2}} \qquad \text{Equation 1.2}$$

It was realised from the early studies that the conversion of gaseous H_2 and N_2 into ammonia was limited by thermodynamics. According to Equation 1.1, there is decrease in total gas volume; therefore, very high pressure must be used to push the equilibrium towards the product side according to the Le Chatelier's principle. In

addition, the reaction is exothermic and therefore conversion increases with decreasing temperature. However, high temperature (~ 500 °C) and high pressure (150-300 bar) are required to achieve industrially acceptable conversion rates (10-15 %) [5].

1.1.2 Current and prospective applications of ammonia

Ammonia (NH_3) is a colourless alkaline gas at ambient temperature which is lighter than air and has a unique pungent, penetrating odour. Ammonia is one of the most widely produced chemicals worldwide and is not only a major end product but also an important intermediate in the manufacture of urea, nitric acid, ammonium nitrate, ammonium sulphate and ammonium phosphate among other products [15, 18, 19]. In 2011, the global production of ammonia was 136 million metric tons [20]. Additionally, ammonia finds widespread use in various industrial sectors including energy, refrigeration, transportation, fertilisers and other industries such as plastics, pharmaceuticals and explosives production. It is to be noted that the fertiliser industry is responsible for about 80 % of global ammonia consumption [21-24].

Ammonia and hydrogen are similar in that both can be utilised as a storage medium and clean energy carrier. However, due to the difficulty of H_2 storage, ammonia is preferable. In addition, ammonia contains 17.6 wt % hydrogen and carbon-free for the end user. As ammonia is easy to store and transport, there is an increasing interest in using ammonia as an indirect hydrogen storage material. The energy stored in ammonia can be recovered by direct ammonia fuel cells. Based on all these applications, ammonia has the potential to play an important role in the future world economy [25-32].

1.2 Literature review

In this section, the previous studies conducted on solid state ammonia synthesis will be reviewed. The key topics discussed include electrolytic cell components and requirements, plus solid state electrolytes (proton or oxide-ion conductors) with an emphasis on their applications in the field of ammonia synthesis. Finally, the factors that affect the ammonia formation rate are also discussed.

1.2.1 Solid state electrochemical synthesis of ammonia at atmospheric pressure

Electrochemical synthesis is the process of producing various chemicals, both inorganic and organic in a cell or electrochemical reactor when controlled potential or controlled current is applied [33, 34]. An electrochemical reactor is considered as the basis of any electrochemical technology and is defined as a device which can be used to prepare chemical products or materials using electrical energy [34, 35]. Unlike chemical reactors, in electrochemical reactors or electrolysis cells, there are interfaces at which electrochemical reaction take place (i.e. the electrode/electrolyte interfaces) and chemical changes are promoted using electrical energy as a driving force [34].

Electrochemical processes provide many advantages over traditional chemical processes including: mild operating conditions, as the experiments can be conducted at low temperature and pressure; a reduction in the number of synthesis steps, compared to non-electrochemical counterparts; cost effectiveness; clean and environmentally friendly production process, as aggressive and hazardous reagents can be avoided [33, 36, 37].

The increased global demand for ammonia has stimulated many research groups and developers to focus on finding new methods to synthesise ammonia, which have the potential to overcome the drawbacks of the Haber-Bosch process (i.e. high working pressure, high energy consumption and the low conversion). The electrochemical processes are regarded as one of the most promising alternatives. In these processes different electrolyte materials have been investigated including liquids, molten salts and solid state ionic conductors [12, 13].

In fact, the electrolytic reduction of dinitrogen to ammonia dates back to the end of the 1960s. In 1968, Van Tamelen and Akermark reported the cathodic electrolytic reduction of N_2 to NH_3 at ambient temperature and atmospheric pressure using non-aqueous based-electrolyte consisting of a solution of aluminum chloride and titanium tetraisopropoxide in 1,2-dimethoxyethane [38]. Since then several studies have been

conducted on electrochemical reduction of dinitrogen using either non aqueous-based [39, 40] or aqueous-based electrolytes [41, 42]. The hydrogen required for ammonia production using these liquid based electrolytes is provided by the electrochemical decomposition of water or an organic solvent (e.g. ethanol) at the anode. However, the electrolytic reduction of N_2 to NH_3 using liquid electrolytes is limited by slow kinetic reaction rates due to the low operating temperatures of these electrolytes [10].

Another approach to synthesising ammonia electrochemically is using an electrolyte based on a molten alkali-metal halide salt [9, 43-45]. Recently, Murakami et al. [43] demonstrated the synthesis of ammonia using an electrolyte consisting of an eutectic mixture of LiCl-KCl-CsCl to which Li_3N was added as nitride ion (N^{3-}) source. Porous Ni was used as hydrogen gas electrode (the anode) and as the nitrogen gas electrode (cathode). Ammonia was produced at the anode side and its formation rate was determined to be ~ 3.3×10^{-9} mol s^{-1} cm^{-2} at 400 °C with a Faradaic efficiency of 72 %. In another study, Murakami et al. [9] reported the synthesis of ammonia from water vapour and nitrogen using LiCl-KCl-CsCl mixture as electrolyte. Glassy carbon was used as the anode, while the cathode was porous Ni. Ammonia evolved at the anode side, with a maximum conversion of 23 %. However, instead of evolving oxygen, the glassy carbon anode was consumed to emit carbon dioxide. However, despite the encouraging Faradaic efficiency, one of the main limitations of this process is its requirements for operation under an inert atmosphere due to the air-sensitivity of the molten salts-based electrolyte which might be an issue for large-scale ammonia production, in practice [46].

Solid state electrolytes (SSE) or solid state ionic conductors are an important class of materials that exhibit high ionic conductivity but very low electronic conductivity [47]. A solid electrolyte is basically characterised according to the conducting ion. A large number of ionic conductors have been reported, among these H^+, O^{2-}, Li^+, Cu^+, Na^+, F^- and Ag^+ conductors [47, 48]. The utilisation of solid state electrolytes in heterogeneous catalysis was first proposed by Wagner in 1970 [49]. Currently, these materials have drawn considerable interest because of their potential applications in solid state batteries, fuel cells, gas sensors, gas separation

and electrosynthesis [8, 50-53]. Recently, Garagounis et al. [54] reviewed the recent applications of these materials in heterogeneous catalysis.

In terms of electrochemical synthesis of ammonia, Cook and Sammells, in 1988, successfully synthesised ammonia from its elements (H_2 and N_2) under ambient temperature and pressure over Ru catalyst in an electrolytic cell using solid polymer electrolyte (SPE) as proton conductor (H^+) [55]. In addition to polymer based electrolytes, oxide-based proton conductors have also been employed in the electrochemical synthesis of ammonia. In 1998, Marnellos and Stoukides [8] demonstrated electrocatalytic ammonia synthesis for the first time using a solid oxide proton conductor (SCYb) under atmospheric pressure and high temperature. Over a porous palladium (Pd) cathode, gaseous H_2 and N_2 were converted into ammonia with a conversion of greater than 78 % at 570 °C. This means that by using solid state electrolytic cells, conversions are higher than those predicted by thermodynamic equilibrium, eliminating the requirements for high pressures, whereas in the Haber-Bosch process, very high pressure (150-300 bar) are required to achieve industrially acceptable ammonia conversions of the order of 10-15 % [56].

1.2.1.1 The working principle

In 1996, Panagos et al. [57] proposed a model process using a solid state proton conductor to overcome the thermodynamic constraints of the traditional ammonia synthesis process. The principle is explained below in Figure 1.1. In the electrolytic cell, two metal porous electrodes are placed on either sides of the proton conductor. At the anode, gaseous H_2 will be converted to H^+ (Equation 1.3):

$$3H_2 \rightarrow 6H^+ + 6e^- \qquad \text{Equation 1.3}$$

At the cathode, the protons transported through the electrolyte will react with the adsorbed nitrogen, according to the following half-cell reaction:

$$N_2 + 6H^+ + 6e^- \rightarrow 2NH_3 \qquad \text{Equation 1.4}$$

Hence the overall reaction is

$$N_2 + 3H_2 \rightleftharpoons 2NH_3$$ Equation 1.5

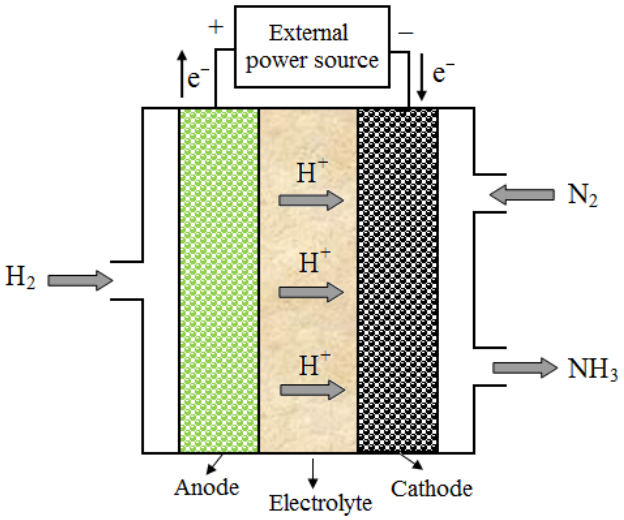

Figure 1.1 Schematic representation of the working principle of the electrochemical synthesis of ammonia

Thermodynamically, at temperature of 200 °C and above, the reaction (Equation 1.5) is non-spontaneous ($\Delta G > 0$). Thus, this reaction will occur when electrical energy is supplied via an external power source. The minimum voltage needed for the formation of the desired product also known as theoretical electrolysis voltage (E) can be calculated using Equation 1.6. For example, at 400 °C, the minimum required voltage for ammonia synthesis is 0.072 V [46].

$$E = -\frac{\Delta G}{nF}$$ Equation 1.6

Here ΔG is change in Gibbs free energy, n is the number of electrons consumed in the reaction of interest and F is Faraday's constant (96485 C/mol). For equation 1.5, n = 6.

1.2.1.2 Reaction rate and current efficiency

According to the Faraday's law, the amount of product (i.e. moles electrolysed, *N*) is correlated with the total charge passed through the electrolytic cell.

$$N(\text{mol electrolysed}) = \frac{Q}{nF} \quad \frac{(\text{coulombs})}{(\text{coulombs / mol})} \qquad \text{Equation 1.7}$$

Here *Q* is the total charge, *n* is the number of electrons consumed in the reaction of interest and *F* is Faraday's constant.

Basically, the change in the total charge with time during electrolysis is equal to the current and is given by

$$I(\text{amperes}) = \frac{dQ}{dt} \ (\text{coulombs/s}) \qquad \text{Equation 1.8}$$

Here *I* is the imposed current (in amperes, A) through the electrolytic cell.

As mentioned previously, the electrochemical reaction takes place at electrode-electrolyte interfaces. Thus, the rate of reaction occurring at that interface is directly related to the Faradaic current as expressed by Equation 1.9. This means that, by measuring the Faradaic current, the rate of electrochemical reaction (*r*) is also measured which is a unique feature of electrochemistry.

$$\text{Rate (mol/s)} = \frac{dN}{dt} = \frac{I}{nF} \qquad \text{Equation 1.9}$$

Since the electrochemical reactions are of heterogeneous nature, their rates are calculated as follows

$$\text{Rate (mol s}^{-1}\text{cm}^{-2}) = \frac{I}{nFA} = \frac{i}{nF} \qquad \text{Equation 1.10}$$

Here i is the current density (A/cm^2) and A is the electrode surface area (cm^2).

The current efficiency (CE) or Faradaic efficiency, can be classically defined as the ratio of the theoretical charge required for forming the product to the total charge consumed during the electrolysis time

$$\text{CE} = \frac{\text{charge consumed in forming product}}{\text{total charge consumed}} \qquad \text{Equation 1.11}$$

The current efficiency can be also expressed as the ratio of the actual (i.e. experimental) rate (r) to the theoretical rate of ammonia formation (I / nF)

$$CE = r / (I / nF) \qquad \text{Equation 1.12}$$

A value of one (or 100 %) for CE indicates there is only one electrochemical reaction occurring at the respective electrode. This means that the total charge passed through the electrolytic cell is consumed in the formation of the desired product. In other words, the protons pumped through the electrolyte by means of the imposed current are all used for ammonia production. On the other hand, a value below one (<100 %) implies that there is more than one process occurring at the respective electrode (i.e. additional electrochemical reactions such as the hydrogen evolution reaction, HER) [34, 58, 59].

1.2.1.3 Electrolytic cell components and requirements

The primary components of the solid state electrochemical device are two porous electrodes (anode and cathode) which are separated by a dense solid electrolyte, which allows ion transport of either protons or oxide ions and serves as a barrier to gas diffusion [60, 61]. Schematics of solid state electrochemical ammonia synthesis devices utilising proton conducting and oxide-ion conducting electrolytes are shown in Figures 1.2a and b, respectively.

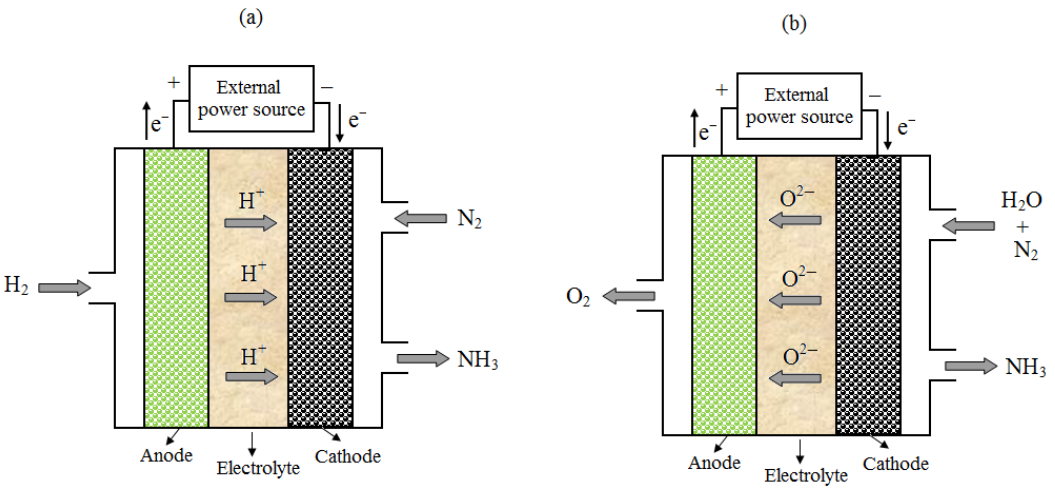

Figure 1.2 Schematic illustration of solid state electrochemical ammonia synthesis device; (a) proton conducting electrolyte, and (b) oxide-ion electrolyte

1.2.1.3.1 Cathode materials

As the cathode (electrocatalyst) represents the part of the cell at which the electrochemical reaction of interest takes place, the cathode materials should satisfy special requirements. The cathodes should possess high electronic conductivity, thermal stability at the operating temperature, sufficiently high catalytic activity to promote ammonia synthesis while inhibiting all competing reactions, particularly H_2 evolution, chemical inertia towards the electrolyte, suitable porosity and pore size to improve the catalyst surface area and to allow N_2 to reach the electrode/electrolyte interface (reaction sites). In addition to the electronic conductivity, a good electrocatalyst should also exhibit an ionic conductivity, to improve the triple phase boundary (TPB) of the electrode/electrolyte interface, where electrochemical reaction takes place [60-63].

The most commonly used electrocatalysts for ammonia synthesis are precious metals such as Pd and Ag-Pd alloy [8, 64]. Modified catalysts namely industrial Fe and Ru-MaO catalysts, have also been employed [55, 65]. However, due to their high costs, the noble metals are not preferred. Moreover, the metal catalysts conduct only electrons. Alternatively, oxides with mixed electronic and ionic conductivity have

been employed for electrocatalytic ammonia synthesis. These oxides include perovskites (e.g. $SmFe_{0.7}Cu_{0.1}Ni_{0.2}O_{3-\delta}$) [66] and double perovskite (e.g. $SmBaCuMO_{5+\delta}$ M = Co, Fe, Ni) based catalysts [67]. Another group of mixed ionic-electronic conductors (MIEC) that have been utilised for ammonia synthesis are the oxides with K_2NiF_4-type structure (e.g. $Sm_{1.5}Sr_{0.5}MO_4$ M = Co, Fe, Ni) [68].

1.2.1.3.2 Anode materials

The main role of the anode in electrochemical synthesis of ammonia is the oxidation of H_2. To be considered as an efficient anode material, there are certain requirements that need to be fulfilled, including high electronic conductivity, ionic conductivity, good chemical, redox and mechanical stabilities, porous structure and high catalytic activity for H_2 oxidation and thermal compatibility with the contacting electrolyte [60, 62, 63, 69]. The most commonly used anode materials are the precious metals such as Pt, Pd, Ag, and Ag-Pd [65, 70-73]. However, despite their good catalytic activity for hydrogen oxidation, the high costs of the precious metal catalysts (e.g. Pt, Pd) discourage their application − practically speaking − in cost-effective devices. On the other hand, Ni is less expensive and exhibits excellent catalytic activity for hydrogen oxidation [74]. Therefore, Ni-cermets (e.g. Ni-SDC) have been also used as anode materials for ammonia synthesis applications [66, 68, 75].

1.2.1.3.3 Electrolyte materials

The electrolyte is another important component of the electrolytic ammonia synthesis device. An electrolyte materials should satisfy the following criteria; high ionic conductivity ($\geq 10^{-2}$ S cm^{-1}) in order to minimise the ohmic losses, negligible electronic conductivity, chemical stability in both oxidising/reducing environments, good mechanical strength, thermal stability, high density in order to be gas tight to eliminate reactants crossover and have a thermal expansion coefficient (TEC) matched to that of both contacting electrodes [60, 62, 63]. In the literature, several materials have been utilised as solid electrolytes for ammonia synthesis including

proton conductors, such as oxide-types (perovskite, fluorites, and pyrochlores) [8, 76, 77], polymers (e.g. Nafion) [55] and composite-based electrolytes (GDC-phosphate salts) [78]. In addition, oxide ion conductors such as yttria-stabilised zirconia (YSZ) have also been employed as electrolytes in electrolytic ammonia synthesis [10]. The applications of these electrolytes in electrochemical synthesis of ammonia will be discussed in detail in the following sections.

In addition to the individual requirements of each component of the electrolytic cell, the cell component materials have to be easy to fabricate into the form required, depending on the reactor design, have matched thermal expansion coefficients (TEC) to give stable interfaces and prevent materials failure due to the thermal expansion mismatch and the cost of raw materials and fabrication should be as low as possible. Furthermore, long term stability and lifetime should be taken into consideration [60, 63, 69].

1.2.2 Electrochemical synthesis of ammonia based on proton conducting electrolytes

Solid state proton conductors (SSPC) represent a class of ionic solid electrolytes that have the ability to conduct hydrogen ions (H^+) [79]. Stotz and Wagner were the first to discuss the existence of protons in some oxides, including CuO, Cu_2O, NiO, and in some stabilised zirconias at elevated temperatures in the presence of water vapour [80]. In 1981, Iwahara et al. [81] found that some perovskites, such as strontium cerate ($SrCeO_3$) exhibited good protonic conductivity at high temperatures (600-1000 °C) in a hydrogen containing atmosphere. Since then, several investigations have focused on the protonic conductivity of these materials [82-85]. Kreuer [86, 87] reviewed the proton conduction phenomena and the potential applications of the proton conductors in electrochemical devices. The proton conductivities of some solid state electrolytes are listed in Table 1.1. These materials have found a wide range of applications as electrolytes in fuel cells [51, 88, 89], hydrogen pumps [90, 91], hydrogen gas sensors [52, 92], hydrogen separators [53, 93], steam electrolysis [94, 95] and in ammonia synthesis [8, 71, 96, 97] and

decomposition [98, 99]. Kreuer et al. [100] classified the solid-state proton conductors, into high-, intermediate and low-temperature proton conductors, according to their operating temperature. The proton conductors, rates of ammonia formation and synthesis temperatures are listed in Table 1.2.

Table 1.1 The protonic conductivity of some solid electrolyte materials

Material	**Proton conductivity ($S\ cm^{-1}$)**	**Temperature (ºC)**	**References**
Perovskite-type			
$SrCe_{0.95}Yb_{0.05}O_{3-\delta}$ (SCYb)	0.05×10^{-2}-1.8×10^{-2}	800-1000	[101]
$SrCe_{0.95}Y_{0.05}O_{3-\delta}$ (SCY)	4.27×10^{-3}	600	[102]
$SrZr_{0.95}Y_{0.05}O_{3-\delta}$ (SZY)	3.05×10^{-3}-2.1×10^{-2}	600-1000	[103]
$BaCe_{0.85}Y_{0.15}O_{3-\delta}$ (BCY)	1.04×10^{-2}	600	[104]
$BaCe_{0.85}Sm_{0.15}O_{3-\delta}$ (BCS)	4.75×10^{-2}-7.78×10^{-2}	800-900	[85]
$La_{0.9}Sr_{0.1}Ga_{0.8}Mg_{0.2}O_{3-\delta}$ (LSGM)	1.4×10^{-2}	520	[105]
$La_{0.9}Ca_{0.1}Ga_{0.8}Mg_{0.2}O_{3-\delta}$ (LCGM)	0.42×10^{-2}	520	[105]
$La_{0.9}Ba_{0.1}Ga_{0.8}Mg_{0.2}O_{3-\delta}$ (LBGM)	0.82×10^{-2}	520	[105]
$BaCe_{0.85}Gd_{0.15}O_{3-\delta}$ (BCGO)	1.4×10^{-2}	600	[73]
$Ba_3(Ca_{1.18}Nb_{1.82})O_{9-\delta}$ (BCN18)	1.3×10^{-2}	600	[106]
$BaCe_{0.9}Ca_{0.1}O_{3-\delta}$ (BCC)	7.64×10^{-4}	600	[107]
$BaCe_{0.85}Dy_{0.15}O_{3-\delta}$ (BCD)	0.93×10^{-2}	600	[108]
$BaCe_{0.65}Zr_{0.2}Er_{0.15}O_{3-\delta}$ (BCZE)	4.73×10^{-3}-1.37×10^{-2}	500-800	[109]
$BaCe_{0.7}Zr_{0.2}Sm_{0.1}O_{3-\delta}$ (BCZS)	2.56×10^{-3}-1.10×10^{-2}	500-800	[110]
$Ba_{0.98}Ce_{0.8}Y_{0.2}O_{3-\delta}$ + 0.04ZnO (BCYZ)	1.59×10^{-2}	600	[111]
Pyrochlore-type			
$La_{1.95}Ca_{0.05}Zr_2O_{7-\delta}$ (LCZ)	6.8×10^{-2}	600	[112]
Fluorite-type			
$Ce_{0.8}La_{0.2}O_{2-\delta}$ (LDC)	1.9×10^{-2}	650	[76]
$Ce_{0.8}Y_{0.2}O_{2-\delta}$ (YDC)	2.3×10^{-2}	650	[76]
$Ce_{0.8}Gd_{0.2}O_{2-\delta}$ (GDC)	2.6×10^{-2}	650	[76]
$Ce_{0.8}Sm_{0.2}O_{2-\delta}$ (SDC)	3.8×10^{-2}	650	[76]
$(Ce_{0.8}La_{0.2})_{0.975}Ca_{0.025}O_{2-\delta}$ (LCDC)	5.9×10^{-2}	800	[113]
Polymer-type			
Nafion	0.11	80	[114]

Table 1.2 Summary of the SSPC electrolytes and the rates of ammonia formation

Proton Conductor	Electrolytic Cell	T (ºC)	NH_3 Formation rate (mol s^{-1} cm^{-2})	Ref
Perovskite-type				
SCYb	H_2, Pd |SCYb| Pd, N_2, NH_3, He	570	4.5×10^{-9}	[8]
SCYb	H_2, Pd |SCYb| Pd, N_2, NH_3, He	570	1.6×10^{-9}	[71]
SCYb	Steam H_2O, Pd |SCYb| Ru, N_2, NH_3	650	3.75×10^{-13}	[10]
SCY	H_2, Ag-Pd |SCY| Ag-Pd, N_2, NH_3	480	2.84×10^{-9}	[102]
BCN18	H_2, Ag-Pd |BCN18| Ag-Pd, N_2, NH_3	620	1.42×10^{-9}	[64]
BCZN	H_2, Ag-Pd |BCZN| Ag-Pd, N_2, NH_3	620	1.82×10^{-9}	[64]
BCNN	H_2, Ag-Pd |BCNN| Ag-Pd, N_2, NH_3	620	2.16×10^{-9}	[64]
BCS	H_2, Ag-Pd |BCS| Ag-Pd, N_2, NH_3	620	5.23×10^{-9}	[115]
BCGS	H_2, Ag-Pd |BCGS| Ag-Pd, N_2, NH_3	620	5.82×10^{-9}	[115]
LSGM	H_2, Ag-Pd |LSGM| Ag-Pd, N_2, NH_3	550	3.37×10^{-9}	[96]
LCGM	H_2, Ag-Pd |LCGM| Ag-Pd, N_2, NH_3	520	$1.6\ 3\times10^{-9}$	[105]
LSGM	H_2, Ag-Pd |LSGM| Ag-Pd, N_2, NH_3	520	2.53×10^{-9}	[105]
LBGM	H_2, Ag-Pd |LBGM| Ag-Pd, N_2, NH_3	520	2.04×10^{-9}	[105]
LBGM	H_2, Ag-Pd |LBGM| Ag-Pd, N_2, NH_3	520	1.89×10^{-9}	[116]
BCGO	H_2, Ni-BCGO |BCGO| Ag-Pd, N_2, NH_3	480	4.63×10^{-9}	[73]
SZY	H_2, Ag |SZY| Fe catalyst, N_2, NH_3	450	6.2×10^{-12}	[65]
BCGO	H_2, Ag-Pd |BCGO| Ag-Pd, N_2, NH_3	480	3.09×10^{-9}	[72]
BCY	H_2, Ag-Pd |BCY| Ag-Pd, N_2, NH_3	500	2.1×10^{-9}	[104]
BCY	H_2, Ni-BCY |BCY| BSCF, N_2, NH_3	530	4.1×10^{-9}	[75]
BCD	H_2, Ag-Pd |BCD| Ag-Pd, N_2, NH_3	530	3.5×10^{-9}	[108]
BCC	H_2, Ag-Pd |BCC| Ag-Pd, N_2, NH_3	480	2.69×10^{-9}	[117]
BCZE	H_2, Ag-Pd |BCZE| Ag-Pd, N_2, NH_3	450	3.27×10^{-9}	[109]
BCZS	H_2, Ag-Pd |BCZS| Ag-Pd, N_2, NH_3	500	2.67×10^{-9}	[110]
BCYZ	H_2, Ag-Pd |BCYZ| Ag-Pd, N_2, NH_3	500	2.36×10^{-9}	[111]
Pyrochlore-type				
LCZ	H_2, Ag-Pd |LCZ| Ag-Pd, N_2, NH_3	520	2.0×10^{-9}	[101]
LCC	H_2, Ag-Pd |LCC| Ag-Pd, N_2, NH_3	520	1.3×10^{-9}	[77]
LCZO	H_2, Ag-Pd |LCZO| Ag-Pd, N_2, NH_3	520	2.0×10^{-9}	[77]
Fluorite-type				
LDC	H_2, Ag-Pd |LDC| Ag-Pd, N_2, NH_3	650	7.2×10^{-9}	[76]
YDC	H_2, Ag-Pd |YDC| Ag-Pd, N_2, NH_3	650	7.5×10^{-9}	[76]
GDC	H_2, Ag-Pd |GDC| Ag-Pd, N_2, NH_3	650	7.7×10^{-9}	[76]
SDC	H_2, Ag-Pd |SDC| Ag-Pd, N_2, NH_3	650	8.2×10^{-9}	[76]
LDC	H_2, Ag-Pd | LDC| Ag-Pd, N_2, N H_3	650	7.2×10^{-9}	[113]
LCDC	H_2, Ag-Pd |LCDC| Ag-Pd ,N_2, NH_3	650	7.5×10^{-9}	[113]
YDC	H_2, Ag-Pd |YDC| Ag-Pd, N_2, NH_3	650	6.5×10^{-9}	[78]
Composites				
YDC-Phosphates	H_2, Ag-Pd |YDC-Phosphates| Ag-Pd, N_2, NH_3	650	9.5×10^{-9}	[78]
YDC-Phosphates	Natural gas, Ag-Pd |YDC-Phosphates| Ag-Pd, N_2, NH_3	650	6.95×10^{-9}	[118]
Polymer-type				
Nafion	10%H_2-Ar, Pt |Nafion| Ru, N_2, NH_3	25	4.86×10^{-13}	[55]

Nafion	H_2O, Pt |Nafion| Ru, N_2, NH_3	90	2.12×10^{-11}	[70]
Nafion	H_2, Ni-SDC |Nafion| SFCN, N_2, NH_3	80	1.13×10^{-8}	[66]
SPSF	H_2, Ni-SDC |SPSF| SSCo, N_2, NH_3	80	6.5×10^{-9}	[119]
Nafion	H_2, Ni-SDC |Nafion| SSN, N_2, NH_3	80	1.05×10^{-8}	[68]
Nafion	H_2, Ni-SDC |Nafion| SSC, N_2, NH_3	80	0.98×10^{-8}	[68]
Nafion	H_2, Ni-SDC |Nafion| SSF, N_2, NH_3	80	0.92×10^{-8}	[68]
Nafion	H_2, Ni-SDC |Nafion| SSN, N_2, NH_3	80	1.05×10^{-8}	[120]
SPSF	H_2, Ni-SDC | SPSF | SSN, N_2, NH_3	80	1.03×10^{-8}	[120]
Nafion	H_2, Ni-SDC |Nafion| SBCF, N_2, NH_3	80	7.0×10^{-9}	[67]
Nafion	H_2, Ni-SDC |Nafion| SBCC, N_2, NH_3	80	7.5×10^{-9}	[67]
Nafion	H_2, Ni-SDC |Nafion| SBCN, N_2, NH_3	80	8.7×10^{-9}	[67]

SCYb = $SrCe_{0.95}Yb_{0.05}O_{3-\delta}$; SCY = $SrCe_{0.95}Y_{0.05}O_{3-\delta}$; LCZ = $La_{1.9}Ca_{0.1}Zr_2O_{6.95}$; BCN18 = $Ba_3(Ca_{1.18}Nb_{1.82})O_{9-\delta}$; BCZN = $Ba_3CaZr_{0.5}Nb_{1.5}O_{9-\delta}$; BCNN = $Ba_3Ca_{0.9}Nd_{0.28}Nb_{1.82}O_{9-\delta}$; LCC = $La_{1.95}Ca_{0.05}Ce_2O_{7-\delta}$; LCZO = $La_{1.95}Ca_{0.05}Zr_2O_{7-\delta}$; LDC = $Ce_{0.8}La_{0.2}O_{2-\delta}$; YDC = $Ce_{0.8}Y_{0.2}O_{2-\delta}$; GDC = $Ce_{0.8}Gd_{0.2}O_{2-\delta}$; SDC = $Ce_{0.8}Sm_{0.2}O_{2-\delta}$; BCS = $BaCe_{0.9}Sm_{0.1}O_{3-\delta}$; BCGS = $BaCe_{0.8}Gd_{0.1}Sm_{0.1}O_{3-\delta}$; LSGM = $La_{0.9}Sr_{0.1}Ga_{0.8}Mg_{0.2}O_{3-\delta}$; SFCN = $SmFe_{0.7}Cu_{0.1}Ni_{0.2}O_{3-\delta}$; BCGO = $BaCe_{0.85}Gd_{0.15}O_{3-\delta}$; SZY = $SrZr_{0.95}Y_{0.05}O_{3-\delta}$; BCY = $BaCe_{0.85}Y_{0.15}O_{3-\delta}$; BCD = $BaCe_{0.85}Dy_{0.15}O_{3-\delta}$; BCC = $BaCe_{0.9}Ca_{0.1}O_{3-\delta}$; LDC = $Ce_{0.8}La_{0.2}O_{2-\delta}$; LCDC = $(Ce_{0.8}La_{0.2})_{0.975}Ca_{0.025}O_{2-\delta}$; YDC = $Ce_{0.8}Y_{0.2}O_{1.9}$; SSCo = $Sm_{0.5}Sr_{0.5}CoO_{3-\delta}$; SSC = $Sm_{1.5}Sr_{0.5}CoO_4$ SSN = $Sm_{1.5}Sr_{0.5}NiO_4$; SSF = $Sm_{1.5}Sr_{0.5}FeO_4$; LCGM = $La_{0.9}Ca_{0.1}Ga_{0.8}Mg_{0.2}O_{3-\delta}$; LBGM = $La_{0.9}Ba_{0.1}Ga_{0.8}Mg_{0.2}O_{3-\delta}$; SPSF = Sulfonated Polysulfone; SBCF = $SmBaCuFeO_{5+\delta}$; SBCC = $SmBaCuCoO_{5+\delta}$; SBCN = $SmBaCuNiO_{5+\delta}$; BSCF = $Ba_{0.5}Sr_{0.5}Co_{0.8}Fe_{0.2}O_{3-\delta}$; BCZE = $BaCe_{0.65}Zr_{0.2}Er_{0.15}O_{3-\delta}$; BCYZ = $Ba_{0.98}Ce_{0.8}Y_{0.2}O_{3-\delta}$ + 0.04ZnO; BCZS = $BaCe_{0.7}Zr_{0.2}Sm_{0.1}O_{3-\delta}$

1.2.2.1 Perovskite-type oxides

The perovskite-type oxides have the typical formula ABO_3, in which the A-site is occupied by a large 12-coordinated cation, typically a rare earth and the B-site is occupied by a small six-coordinated cation (BO_6 octahedra) which is frequently a transition metal [121]. Figure 1.3 represents the typical perovskite structure of barium cerate-based oxides ($BaCeO_3$). Many zirconate and cerate perovskite oxides, namely calcium zirconate ($CaZrO_3$), strontium zirconate ($SrZrO_3$) or strontium cerate ($SrCeO_3$) show reasonable proton conductivity at elevated temperatures and under a hydrogen-containing atmosphere. Additionally, their formula could be written as $AB_{1-x}M_xO_{3-\delta}$ in which M is a trivalent cation such as Y^{3+}, Gd^{3+}, Yb^{3+}, Nd^{3+}, Sm^{3+} , or divalent cation, such as Ca^{2+} and δ the oxygen deficiency in the oxide lattice [103, 112, 122].

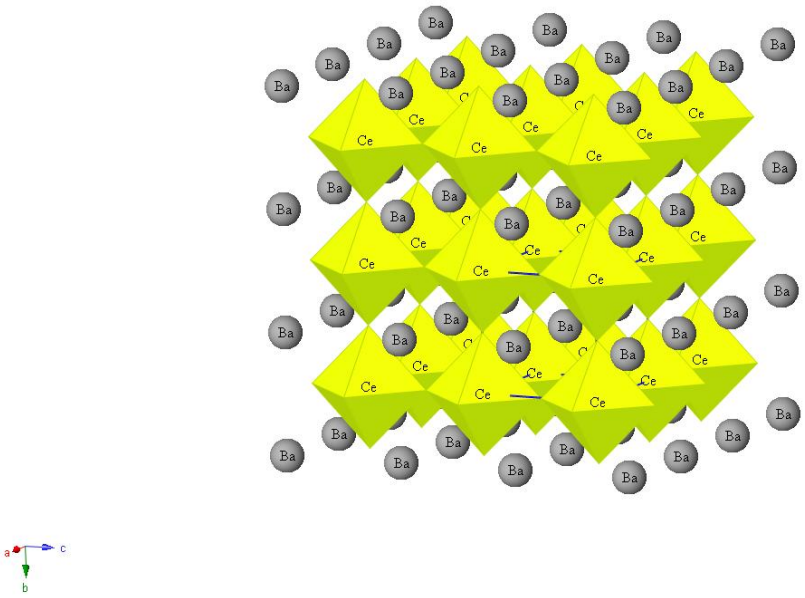

Figure 1.3 The perovskite ABO_3 structure

1.2.2.1.1 $SrCeO_3$-based electrolytes

As reported by Iwahara et al. [81], $SrCeO_3$-based oxides were the first class of perovskites to exhibit protonic conductivity under a hydrogen containing atmosphere and elevated temperatures. The basic formula of doped strontium cerates can be written as follows $SrCe_{1-x}M_xO_{3-\delta}$ in which M is an aliovalent cation such as Yb^{3+}, Sc^{3+}, Y^{3+}, etc.

Based on the model proposed by Panagos et al. [57] in 1998, Marnellos and Stoukides [8] confirmed the first experimental ammonia synthesis from its constituents (H_2 and N_2) at atmospheric pressure using the solid oxide proton conductor. In their study, Yb-doped $SrCeO_3$ in the form of $SrCe_{0.95}Yb_{0.05}O_{3-\delta}$ (SCYb) was used as an electrolyte and porous palladium (Pd) for the electrodes. In addition, more than 78 % of the electrochemically supplied protons were converted into ammonia. Two years later, Marnellos et al. [71, 123] used the aforementioned conditions to synthesise ammonia using two different reactors (double- and single-

chamber cells) and it was found that nearly 80 % of the electrochemically supplied hydrogen was converted into ammonia at 570-750 °C and atmospheric pressure.

In addition to Yb-doped $SrCeO_3$, ammonia could be synthesised electrochemically using Y-doped $SrCeO_3$ as electrolyte. Su et al. [102] demonstrated that ammonia was successfully synthesised from H_2 and N_2 using SCY in the form of $SrCe_{0.95}Y_{0.05}O_{3-\delta}$ as electrolyte and Ag-Pd alloy as electrodes (anode and cathode). With an applied potential of 0.6 V, ammonia was produced with a maximum rate of 2.84×10^{-9} mol s^{-1} cm^{-2} at 480 °C under atmospheric pressure.

As mentioned above, ammonia has been synthesised from pure H_2 and N_2. However, recently, Skodra and Stoukides [10] successfully synthesised ammonia for first time from nitrogen and steam (water) rather than molecular hydrogen, in an electrolytic cell based on a solid oxide protonic conductor (Figure 1.4). The ammonia was synthesised in the electrolytic cell at 450-700 °C using SCYb as solid electrolyte, Ru-MaO catalyst as cathode, and Pd as anode. No ammonia was detected at temperatures lower than 500 °C and the maximum rate of ammonia formation was approximately 4×10^{-13} mol s^{-1} cm^{-2} and a Faradaic efficiency of 0.0011 % at 650 °C with an applied voltage of 2 V. This low conversion of nitrogen and steam into ammonia was ascribed to the poor electronic conductivity of the working electrode and, consequently, it was difficult to impose high proton fluxes through the electrolytic cell. Moreover, the rate of ammonia decomposition should be taken into consideration, since the working temperatures were high (450-700 °C). The principle is as follows:

At the anode, steam is electrolysed to H^+ and O_2 according to the following reaction:

$$3H_2O \rightarrow 6H^+ + \tfrac{3}{2}O_2 + 6e^- \qquad \text{Equation 1.13}$$

at the cathode, the H^+ transported through the solid electrolyte will react with the adsorbed nitrogen to produce ammonia (Equation 1.4);
hence the overall cell reaction is:

$$3H_2O + N_2 \rightarrow 2NH_3 + \tfrac{3}{2}O_2$$ Equation 1.14

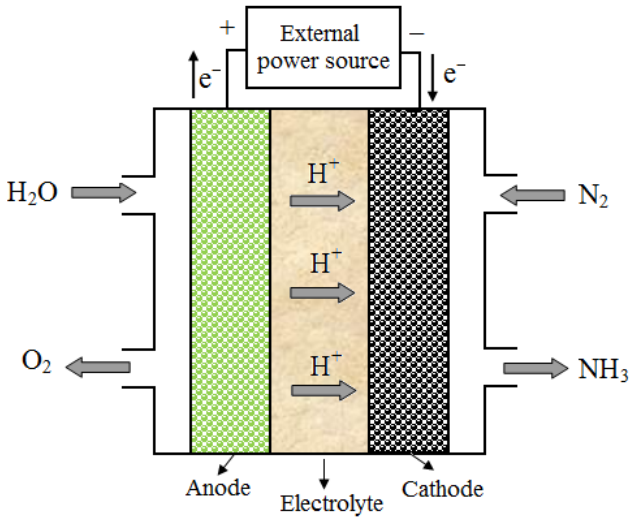

Figure 1.4 Schematic diagram of the ammonia synthesis device using steam (H_2O) and N_2

It is worth stressing that using water instead of hydrogen is advantageous in that the costs of both the production and further purification of hydrogen will be eliminated and only nitrogen needs to be purified. Furthermore, pure oxygen can be produced at minimal cost [10].

1.2.2.1.2 $BaCeO_3$-based electrolytes

$BaCeO_3$-based electrolytes are one of the most commonly investigated proton conductors. Doped barium cerates in the form of $BaCe_{1-x}M_xO_{3-\delta}$ (M = Y^{3+}, Gd^{3+}, Yb^{3+}, Nd^{3+}, Dy^{3+} or Sm^{3+}) are considered as promising candidates for use as electrolyte materials for solid oxide fuel cells (SOFC) [10, 85, 108]. In addition, the proton conductivities of these materials are higher than those of $SrCeO_3$ and $SrZrO_3$ based materials [87, 124]. However, despite their high conductivities, these materials are not stable in air below around 800 °C and they can react easily with carbon dioxide to form alkaline earth carbonates and consequently lose their protonic

conduction [125]. In addition, $BaCeO_3$ is also unstable in the presence of water-containing atmosphere. It can react with water forming $Ba(OH)_2$ and CeO_2 [126, 127].

Gd-doped $BaCeO_3$ (BCGO) in the form of $BaCe_{0.8}Gd_{0.2}O_{3-\delta}$ has been employed as an electrolyte in devices for solid state electrochemical synthesis of ammonia. Furthermore, Ag-Pd alloy was utilised as electrodes (cathode and anode) and ammonia was successfully synthesised from its elements (H_2, N_2) with a maximum rate of 3.09×10^{-9} mol s^{-1} cm^{-2} with an applied potential of 0.6 V at 480 °C under atmospheric pressure [72]. Chen et al. [73] reported that ammonia was synthesised in an electrolytic cell based on $BaCe_{0.85}Gd_{0.15}O_{3-\delta}$ (BCGO), Ag-Pd and Ni-BCGO as solid electrolyte, cathode and anode, respectively. When applying a constant current of 1.5 mA, ammonia was produced with current efficiency above 70 % which corresponds to a maximum rate of 4.63×10^{-9} mol s^{-1} cm^{-2} at 480 °C and atmospheric pressure. Li et al. [115] demonstrated the synthesis of ammonia using two different proton conductors based on single and double-doped $BaCeO_3$ oxides in the form of $BaCe_{0.9}Sm_{0.1}O_{3-\delta}$ (BCS) and $BaCe_{0.8}Gd_{0.1}Sm_{0.1}O_{3-\delta}$ (BCGS) respectively. Using BCS and BCGS as electrolytes and Ag-Pd as electrodes, Ammonia was synthesised at atmospheric pressure with maximum rates of 5.23×10^{-9} mol s^{-1} cm^{-2} and 5.82×10^{-9} mol s^{-1} cm^{-2} for BCS and BCGS, respectively, at 620 °C and with applied voltage of 0.6 V.

Y-doped $BaCeO_3$ (BCY), in the form of $BaCe_{0.85}Y_{0.15}O_{3-\delta}$ has been utilised as a solid electrolyte to synthesise ammonia at atmospheric pressure. Ag-Pd alloy was used as electrodes (cathode and anode). The ammonia formation rate reached a highest value of 2.1×10^{-9} mol s^{-1} cm^{-2}, which corresponds to a current efficiency of above 60 % at 500 °C with an applied current of 0.75 mA [104]. Recently, Wang et al. [75] successfully assembled a tri-layer membrane reactor in which the electrolyte thickness was approximately 30 μm. Ammonia was synthesised at atmospheric pressure using $BaCe_{0.85}Y_{0.15}O_{3-\delta}$ (BCY) as electrolyte, perovskite-type catalyst in the form $Ba_{0.5}Sr_{0.5}Co_{0.8}Fe_{0.2}O_{3-\delta}$ (BSCF) as cathode and Ni-BCY as and anode. By imposing a DC current of 1 mA, ammonia was successfully synthesised from H_2 and N_2 and the maximum rate of ammonia formation was found to be up to 4.1×10^{-9} mol s^{-1} cm^{-2}, which corresponding to current efficiency of ~ 60 % at 530 °C. The results

indicated that by reducing the electrolyte thickness, the rate improved and was higher than the reported value for $BaCe_{0.85}Y_{0.15}O_{3-\delta}$ (thickness ~ 0.8 mm) [104]. This could be due to the fact that, by reducing the thickness of the electrolyte, the ohmic losses across the electrolyte could be minimised [75].

Dy-doped $BaCeO_3$ in the form of $BaCe_{0.85}Dy_{0.15}O_{3-\delta}$ (BCD) was employed as an electrolyte for ammonia synthesis at intermediate temperature and atmospheric pressure. Ag-Pd was deposited on both sides of the dense electrolyte to work as cathode and anode and by applying a current of 1.2 mA, ammonia was synthesised from its elements (H_2, N_2) with a maximum rate of 3.5×10^{-9} mol s^{-1} cm^{-2}, corresponding to a Faradaic efficiency of about 50 % at 530 °C [108].

Unlike the rare earth metals oxide-doped $BaCeO_3$-based electrolytes, Ca-doped $BaCeO_3$ (BCC) exhibits low proton conductivities. However, due to the abundance and cheapness of calcium oxide, Ca-doped $BaCeO_3$ is still an interesting electrolyte for cost-effective devices [117]. In addition, it has been reported that this material exhibits both protonic and oxide conduction at 600-1000 °C [122]. Recently, Liu et al. [117] investigated the protonic conduction behaviour of BCC at intermediate temperature within the range of 300-600 °C and its application in ammonia synthesis. $BaCe_{1.9}Ca_{0.1}O_{3-\delta}$ (BCC) and Ag-Pd were used as solid electrolyte and electrodes, respectively, to synthesise ammonia from wet H_2 and dry N_2 under atmospheric pressure. The maximum rate of ammonia formation and the current efficiency were found to be 2.69×10^{-9} mol s^{-1} cm^{-2} and about 50%, respectively, with an applied current of 0.8 mA at 480 °C.

As mentioned above, $BaCeO_3$-based electrolytes exhibit high proton conductivity, in spite of their low chemical stability in the presence of CO_2 or H_2O-containing atmospheres. In contrast, $BaZrO_3$-based electrolytes exhibit high chemical stability. However, the total protonic conductivities of these materials are relatively low compared to $BaCeO_3$-based electrolytes. In recent years, attempts have been made to investigate electrolytes based on $BaCeO_3$-$BaZrO_3$ materials, with the aim of obtaining both high ionic conductivity and chemical stability [128, 129]. Recently, Wang et al. [110] investigated the ionic conductivity, chemical stability of

$BaCe_{0.7}Zr_{0.2}Sm_{0.1}O_{3-\delta}$ (BCZS) and its application as an electrolyte to synthesise ammonia under atmospheric pressure. In this study, Ag-Pd alloy was used as cathode and anode. Ammonia was successfully synthesised from H_2 and N_2 and with an imposed current of 0.80 mA at 500 °C, the maximum ammonia formation rate and the current efficiency were found to be 2.67×10^{-9} mol s^{-1} cm^{-2} and ~ 50 % respectively.

1.2.2.1.3 $SrZrO_3$-based electrolytes

In general, alkaline earth zirconate oxides of $AZrO_3$ (A= Ca, Sr, Ba) exhibit extremely high chemical stability in atmospheres containing CO_2 and H_2O, compared to alkaline earth cerate oxides [124, 125, 130-132]. In addition to its chemical stability, at high temperatures $SrZrO_3$ showed proton conduction when it was doped with trivalent cations such as In^{3+}, Sc^{3+}, Y^{3+}, etc [64].

Ouzounidou et al. [65] reported that ammonia was synthesised successfully using two different cell configurations (single or double chambers) based on $SrZrO_3$ oxides. In this study, the electrolytic cell composed of an industrial Fe-based catalyst as cathode, Y-doped $SrZrO_3$, in the form of $SrZr_{0.95}Y_{0.05}O_{3-\delta}$ as electroyte and Ag as anode. Moreover, ammonia was synthesised from its elements (H_2 and N_2) at atmospheric pressure, with maximum ammonia production rates of up to 6.2×10^{-12} mol s^{-1} cm^{-2} at 450 °C with an applied voltage of 2 V.

1.2.2.1.4 $LaGaO_3$-based electrolytes

In 1994, Ishihara et al. [133] reported that Sr and Mg co-doped $LaGaO_3$ ($La_{0.9}Sr_{0.1}Ga_{0.8}Mg_{0.2}O_{3-\delta}$, LSGM) displayed high oxide-ion conductivity at intermediate temperature (500-800 °C); therefore it was regarded as a promising electrolyte for SOFCs in this temperatures range. Its ionic conductivity (> 10^{-2} S cm^{-1} at 600 °C) is higher than that of yttria-stabilised zirconia (YSZ) and Scandia-stabilized zirconia (SSZ)-based oxides and comparable to that of gadolinia-doped ceria (GDC). Unfortunately, LSGM suffers from high chemical reactivity with the electrodes and catalysts (e.g. Ni, Pt), volatilisation of gallium oxide and a high cost,

because of using gallium [134, 135]. It is to be noted that the proton conduction in LSGM was first discovered by Ma et al. in 2006 [136].

The applications of lanthanum gallate ($LaGaO_3$)-based oxide as the electrolyte in the electrochemical synthesis of ammonia under atmospheric pressure have also been investigated. Zhang et al. [96] reported that ammonia was successfully synthesised from its elements (H_2 and N_2) using $La_{0.9}Sr_{0.1}Ga_{0.8}Mg_{0.2}O_{3-\delta}$ (LSGM) and Ag-Pd as electrolyte and electrodes respectively. In addition, when 1 mA was imposed through the cell, ammonia was produced with a maximum rate of 2.37×10^{-9} mol s^{-1} cm^{-2}, corresponding to a current efficiency above 70 % at 550 °C. In addition to LSGM, ammonia was synthesised electrochemically under atmospheric pressure using Ba and Mg doped-$LaGaO_3$ as electrolyte. Chen et al. [116] demonstrated that ammonia could be synthesised from H_2 and N_2 in an electrolytic cell using $La_{0.9}Ba_{0.1}Ga_{0.8}Mg_{0.2}O_{3-\delta}$ (LBGM) and Ag-Pd alloy as electrolyte and electrodes respectively. The rate of ammonia formation was found to be 1.89×10^{-9} mol s^{-1} cm^{-2} which corresponds to Faradaic efficiency above 60 % at 520 °C with an applied current of 1 mA. Recently, Cheng et al. [105] reported that ammonia was successfully synthesised using series of alkaline earth cations doped-$LaGaO_3$ based oxides in the form of $La_{0.9}M_{0.1}Ga_{0.8}Mg_{0.2}O_{3-\delta}$ (M = Ca, Sr, Ba) as solid electrolytes. Furthermore, Ag-Pd alloy was used as electrodes (cathode and anode). When a constant current density of 1 mA cm^{-2} was imposed through the cells at 520 °C, ammonia was produced with maximum rates of 1.63×10^{-9}, 2.53×10^{-9} and 2.04×10^{-9} mol s^{-1} cm^{-2}, corresponding to the Faradaic efficiencies of 47 %, 73 % and 60 % when M = Ca, Sr and Ba, respectively.

1.2.2.1.5 Complex perovskite-type oxides

Complex perovskites represent another group of solid oxide electrolytes which belong to the category of high temperature proton conductors (HTPC). They are considered as nonstoichiometric mixed perovskites of the form $A_3(B'B''_2)O_9$ type in which A is always a divalent cation (e.g. Ca^{2+}, Sr^{2+}, Ba^{2+}, etc.) while B' is either divalent or trivalent cation (e.g. Ca^{2+}, Nd^{3+}) and B'' is a pentavalent cation (e.g. Ta^{5+},

Nb^{5+}). Generally, the formula of these oxides is written as $A_3B'_{1+X}B''_{2-X}O_{9-\delta}$ [137-140].

The application of these oxides as electrolytes in solid state electrochemical synthesis of ammonia has been investigated. Li et al. [64] reported that ammonia was synthesised successfully from its elements (H_2 and N_2) using three electrolytes with different composition, namely: $B_3(Ca_{1.18}Nb_{1.82})O_{9-\delta}$ (BCN18), $Ba_3Ca_{0.9}Nd_{0.28}Nb_{1.82}O_{9-\delta}$ (BCNN), and $Ba_3CaZr_{0.5}Nb_{1.5}O_{9-\delta}$ (BCZN). In addition, Ag-Pd alloy was employed as electrodes (cathode and anode). When a voltage of 0.6 V was imposed through the electrolytic cells at 620 °C and atmospheric pressure, ammonia was produced with maximum rates of 1.42×10^{-9}, 1.82×10^{-9}, and 2.16×10^{-9} mol s^{-1} cm^{-2} for BCN18, BCZN, and BCNN, respectively.

1.2.2.2 Pyrochlore-type oxides

In addition to the perovskite-based electrolytes, nonperovskite oxides including; pyrochlores, fluorites, phosphates and sulphates also exhibit protonic conduction at elevated temperatures under hydrogen-containing atmosphere [141]. Generally, the pyrochlore-type oxides have $A_2B_2O_7$ formula in which A is a trivalent cation (e.g. La, Sm, Gd etc.) and B is a tetravalent cation (e.g. Zr, Ce etc.), as shown in Figure 1.5. It should be noted that, these oxides are known as fluorite-related materials. Moreover, these materials have attracted great attention as fast ionic conductors because of the presence of many non-occupied sites [142-144]. Shimura et al. [145] reported proton conduction in lanthanum zirconate-based oxides ($La_2Zr_2O_7$) at high temperature and under a hydrogen-containing atmosphere.

In recent years, the application of pyrochlore-based electrolytes in the electrochemical synthesis of ammonia under atmospheric pressure has been investigated. Xie et al. [101] demonstrated the synthesis of ammonia from its elements (H_2 and N_2) using Ca-doped $La_2Zr_2O_7$ in the form of $La_{1.9}Ca_{0.1}Zr_2O_{6.95}$ (LCZ) as an electrolyte and Ag-Pd alloy as electrodes (cathode and anode). In that study, the maximum rate of ammonia formation was up to 2.0×10^{-9} mol s^{-1} cm^{-2} which corresponds to Faradaic efficiency above 80 % at 520 °C with an applied voltage of 0.6 V. Wang et al. [77] reported that ammonia was synthesised using Ca-

doped $La_2Ce_2O_7$, in the form of $La_{1.95}Ca_{0.05}Ce_2O_{7-\delta}$ (LCC), and Ca-doped $La_2Zr_2O_7$, in the form of $La_{1.95}Ca_{0.05}Zr_2O_{7-\delta}$ (LCZ), as solid electrolytes and Ag-Pd alloy as cathode and anode. Upon imposing a voltage of 0.8 V at 520 °C, ammonia was produced with a maximum rate of 2.0×10^{-9} mol s^{-1} cm^{-2} for LCZ and 1.3×10^{-9} mol s^{-1} cm^{-2} for LCC.

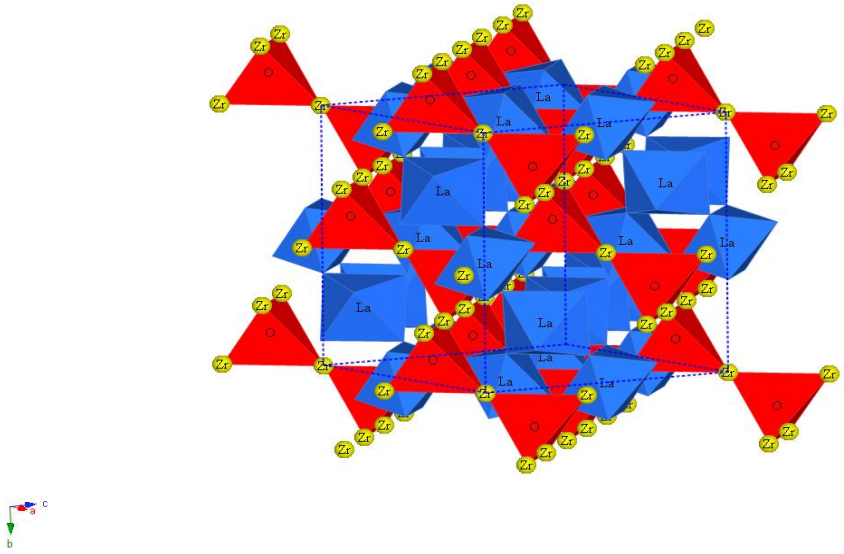

Figure 1.5 The pyrochlore, $La_2Zr_2O_7$ structure

1.2.2.3 Fluorite-type oxides

The fluorite-type oxides are considered as the traditional oxygen ion-conducting electrolytes. The fluorite oxide has the general formula AO_2, in which A is a large tetravalent cation, and is presented in Figure 1.6. Examples of materials that easily adopt the fluorite structure are ceria (CeO_2), uranium dioxide (UO_2) and thorium dioxide (ThO_2) [121]. It is well known that rare earth-doped ceria-based electrolytes (e.g. SDC, GDC) are oxygen ion conductors (O^{2-}) and have been widely used as electrolytes in intermediate temperature solid oxide fuels (IT-SOFCs) [146-148]. The possibility of proton conduction in these materials was first suggested by Nigara et al. [149] in 1998. Since then, several subsequent research studies have been conducted to confirm this possibility [149-151]. Unfortunately, these electrolyte materials exhibit mixed ionic-electronic conducting behaviour due to the partial

reduction of Ce^{4+} to Ce^{3+} in a reducing atmosphere and at high temperature [147, 152]. The presence of electronic conduction in electrolyte is not good for electrochemical synthesis.

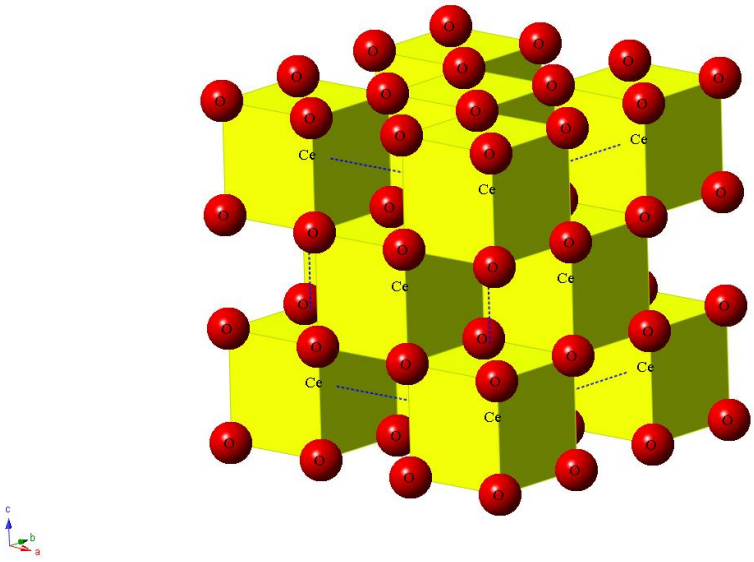

Figure 1.6 The fluorite, CeO_2 structure

Liu et al. [76] investigated the proton conduction and the application of rare earth-doped CeO_2 in ammonia synthesis under atmospheric pressure. In that study, Ag-Pd alloy was used as electrodes and the electrolyte was one of the following doped ceria oxides; $Ce_{0.8}La_{0.2}O_{2-\delta}$ (LDC), $Ce_{0.8}Y_{0.2}O_{2-\delta}$ (YDC), $Ce_{0.8}Gd_{0.2}O_{2-\delta}$ (GDC) and $Ce_{0.8}Sm_{0.2}O_{2-\delta}$ (SDC). Ammonia was produced from H_2 and N_2 at 650 °C with imposed voltage of 0.6 V and SDC had the highest formation rate (8.2×10^{-9} mol s^{-1} cm^{-2}) compared to that for LDC, YDC, GDC (7.2×10^{-9}, 7.5×10^{-9}, 7.7×10^{-9} mol s^{-1} cm^{-2} respectively). Liu et al. [113] reported that ammonia was synthesised using La-doped ceria ($Ce_{0.8}La_{0.2}O_{2-\delta}$, LDC) and La and Ca co-doped ceria ($(Ce_{0.8}La_{0.2})_{0.975}Ca_{0.025}O_{2-\delta}$, LCDC) as electrolytes and Ag-Pd alloy as electrodes (cathode and anode). The maximum rates of ammonia formation were 7.2×10^{-9} and 7.5×10^{-9} mol s^{-1} cm^{-2} at 650 °C for LDC and CLC, respectively. Consequently, one could conclude that the rates of ammonia formation of doped-CeO_2 exceeded that for pyrochlore-based and perovskite-type oxides.

1.2.2.4 Composite-type electrolytes

Composite electrolytes represent a mixture of two or more phases with different properties such as enhanced ionic or thermal conductivities and mechanical properties [153]. In recent years, ceria-salt composite materials have drawn considerable interest owing to their potential applications as electrolytes for intermediate temperature fuel cells and hydrogen sensors. These materials consist of two phases, ceria-based oxide as a host phase and a second salt phase such as carbonates, halides, sulphates or hydrates [154-160].

Wang et al. [78] prepared a new composite electrolyte based on fluorite oxide (Y-doped ceria) and binary phosphates ($Ca_3(PO_4)_2$-K_3PO_4) and investigated its application for ammonia synthesis at atmospheric pressure. Y-doped ceria in the form of $Ce_{0.8}Y_{0.2}O_{1.9}$ (YDC) was mixed with the binary phosphates, according to the different weight ratios. The YDC-phosphates composite and Ag-Pd alloy were used as solid electrolyte and electrodes. When a voltage of 0.6 V was imposed through the electrolytic cell at 650 °C, ammonia was formed with rates of 6.5×10^{-9}, 5.8×10^{-9}, 9.5×10^{-9} and 7.8×10^{-9} mol s^{-1} cm^{-2} for pure YDC, YDC-phosphates (70:30 wt %), and YDC-phosphates (80:20 wt %),YDC-phosphates (90:10 wt %), respectively.

It should be noted that pure H_2 and N_2 have been commonly used in the electrochemical synthesis of ammonia. However, there are some problems associated with using H_2. These include production, purification, storage and transportation [161, 162]. Wang et al. [118] therefore investigated the synthesis of ammonia from natural gases (methane or ethane) and N_2 under atmospheric pressure in an electrolytic cell based on composite electrolyte. In that study, when YDC-($Ca_3(PO_4)_2$-K_3PO_4) (80:20 wt%) was used as electrolyte and Ag-Pd alloy was used as electrodes, ammonia was produced at maximum rate of 6.95×10^{-9} mol s^{-1} cm^{-2} at 650 °C, with an applied voltage of 1 V. Accordingly, the principle of ammonia synthesis (Figure 1.7) using natural gases and nitrogen is as follows:

$$2CH_4 \rightarrow C_2H_6 + H_2 \qquad \text{Equation 1.15}$$

$$2CH_4 \rightarrow C_2H_4 + 2H_2 \qquad \text{Equation 1.16}$$

$$C_2H_6 \rightarrow C_2H_4 + H_2$$ Equation 1.17

As illustrated in Figure 1.7, at the anode, the natural gases (methane or ethane) will be converted to hydrogen which will be electrochemically transported in the form of protons through the electrolyte to the cathode at which will react with the adsorbed N_2 to produce ammonia according to Equation 1.3 and Equation 1.4. Although the need for reforming could be eliminated by direct operation with natural gases, carbon deposition resulted from fuel cracking at the anode should be taken into consideration [163].

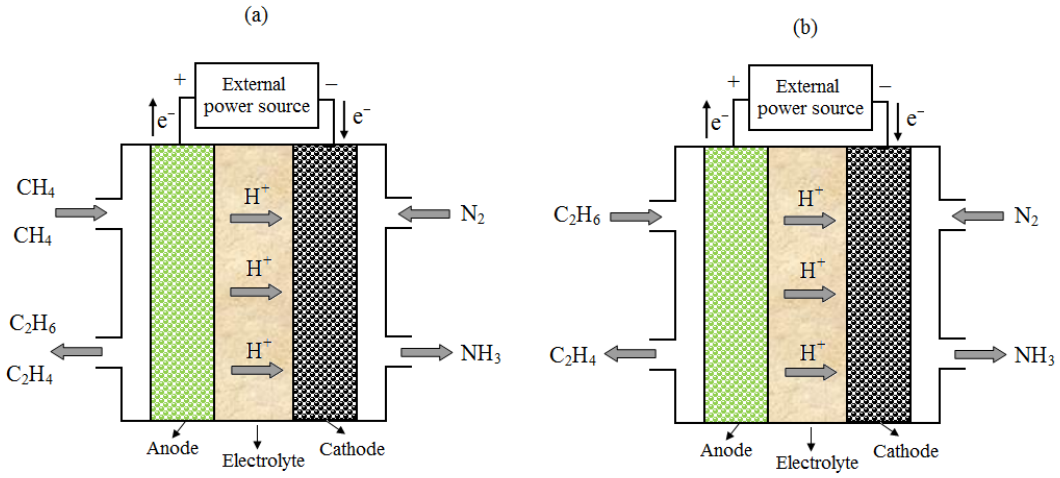

Figure 1.7 Ammonia synthesis principle using natural gases and nitrogen

Among the previously mentioned composite electrolytes, oxide-carbonate-based systems, in particular doped ceria-carbonate have drawn considerable attention in recent years owing to their increasing applications as electrolytes for intermediate/low temperature (300-600 °C) fuel cells (LT/IT-FCs) [155, 164-169]. These composite electrolytes consist of doped ceria (e.g. SDC or GDC) as a host phase and carbonate (e.g Na_2CO_3, $(Li/Na)_2CO_3$, $(Li/Na/K)_2CO_3$) as a second phase [166, 170-172]. These materials exhibit high ionic conductivity (> 0.1 S cm^{-1}) below 600 °C, which is higher that of pure doped ceria (10^{-2} S cm^{-1}) at 600 °C (Figure 1.8) [155, 166, 173]. In addition, it has been reported that doped ceria-carbonate composites are co-ionic (O^{2-}/H^+) conductors in the presence of oxygen and wet hydrogen-containing atmospheres [156, 165].

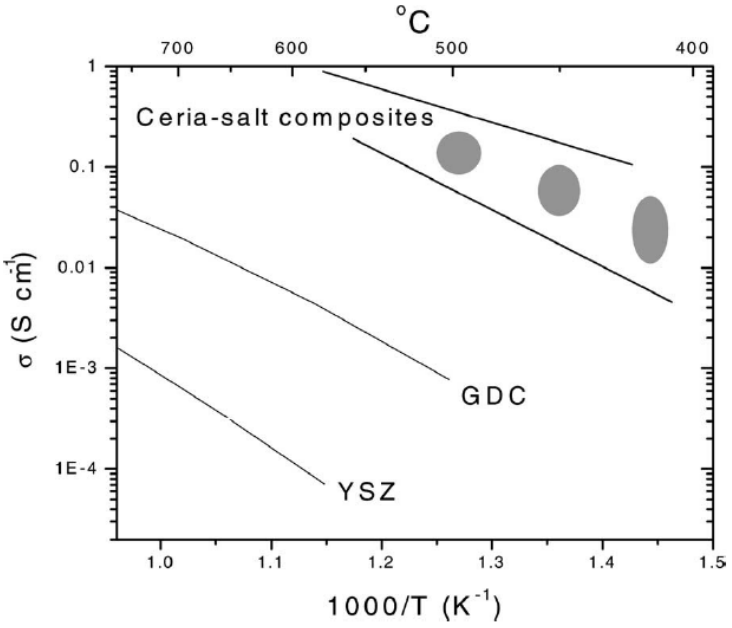

Figure 1.8 Electrical conductivity of ceria-salt composite compared to non-composite electrolytes [155]

According to Zhu et al. [155, 174-176], the enhancement in the ionic conductivity of ceria-composite electrolytes could be explained by the interfacial conduction mechanism. Unlike traditional single-phase electrolyte materials (e.g. YSZ, SDC), in the doped ceria-carbonate composites, the interfacial regions between the two phases provide a smooth pathway for ionic conduction. In the ceria-carbonate composite, the oxygen ion conduction (O^{2-}) occurs through the doped ceria phase and the interface between the two phases (Figure 1.9). In contrast, the proton conduction (H^{+}) occurs only at the interface between the doped ceria and the carbonate (Figure 1.9). Protons can be transported via an intermediate carrier (HCO_3^-), formed by coupling CO_3^{2-} with H^{+} [169, 177]. In recent years, the concept of ternary ionic conduction ($O^{2-}/H^{+}/CO_3^{2-}$) in ceria-carbonate composite electrolytes has been also proposed [172, 178]. Although many studies have been conducted to explain the conduction mechanism in doped ceria-composite electrolytes, the multi ionic ($O^{2-}/H^{+}/CO_3^{2-}$) transport mechanism in these materials is still not very clear.

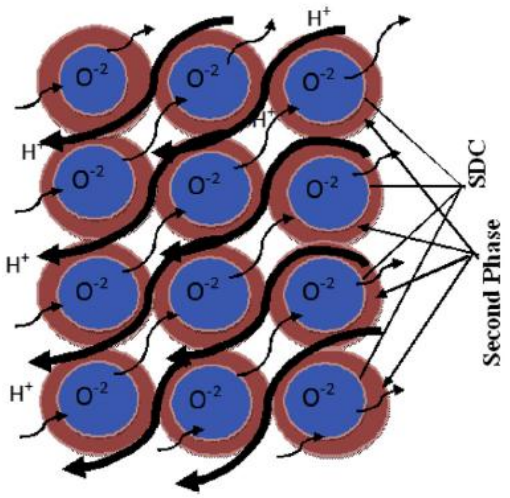

Figure 1.9 Schematic diagram showing the ionic conduction pathway for oxygen ions and protons in doped ceria-carbonate composite electrolytes [179]

As mentioned above, doped ceria-carbonate composites are multi-ionic conductors (Figure 1.10). This property makes them promising electrolyte materials for many applications, including LT/IT-SOFCs [155, 164-169], water (steam) electrolysis [180], direct carbon fuel cells (DCFCs) [181, 182], carbon dioxide (CO_2) permeation membrane [183-185] and ammonia synthesis [186]. Recently, Zhu et al. [187] and Fan et al. [188] have reviewed the recent advances in doped ceria-carbonate composite electrolytes and their possible applications as illustrated in Figure 1.10.

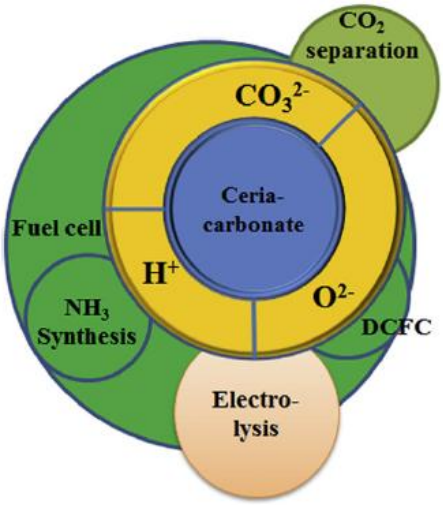

Figure 1.10 Schematic representation showing the advanced applications of doped ceria-carbonate composite electrolytes and their multi-ionic conduction behaviour [188]

1.2.2.5 Polymer-type electrolytes

Solid polymer electrolytes (SPEs), also known as proton exchange membranes (PEMs) are another type of proton conductors with the ability to conduct H^+ at low temperature [100].

In fact, the application of the low temperature proton conductor-based polymer membrane in electrolytic cells for ammonia synthesis dates back to the end of the 1980s. In 1988, Cook and Sammells [55] reported that ammonia was synthesised from H_2 and N_2 for the first time under ambient temperature and pressure using a solid polymer electrolyte type cell. In that study, an acidic membrane (Nafion), Ru-based catalyst and Pt were used as solid electrolyte, cathode and anode respectively. The maximum rate of ammonia formation was found to be 4.86×10^{-13} mol s^{-1} cm^{-2} at an applied current density of 3.12 mA cm^{-2}, corresponding to a Faradaic efficiency of 0.0015 %. This conversion indicates the difficulty of producing ammonia at ambient temperature. This can be ascribed to the slow kinetic reaction rates at low temperature. Kordali et al. [70] also synthesised ammonia using electrolytic cell based on solid polymer electrolyte from room temperature to 100 °C under atmospheric pressure. However, in this study, by using Nafion as electrolyte, Ru-based catalyst as cathode and Pt as anode, ammonia was synthesised for the first time from water and nitrogen. However, the maximum rate of ammonia formation was found to be 2.12×10^{-11} mol s^{-1} cm^{-2} with an applied voltage of -1.02 vs. Ag/AgCl at 90 °C at which the current efficiency reached 0.24 %. This low conversion was attributed to the nature of the working electrode (particle size and crystal structure), the low number of active catalytic sites where the reaction of interest takes place and the competitive reaction (H_2 evolution) [11, 70].

It is worth stressing that, in the above reported investigations, the precious metals such as Pt and Ru were used as anode and cathode primarily due to using an acidic membrane-based electrolytic cell (i.e. Nafion). However, these metals not generally preferred, because of their high costs. Thus, Wang et al. [119] demonstrated the synthesis of ammonia in solid polymer type cells using non-precious metal electrodes. In their study the electrolytic cell was composed of sulfonated polysulfone (SPSF) electrolyte, a perovskite-based catalyst, $Sm_{0.5}Sr_{0.5}CoO_{3-\delta}$,

(SSCo), as a cathode, and Ni-ceramet (Ni-SDC) as an anode. Moreover, ammonia was synthesised from H_2 and N_2 with a maximum rate of 6.5×10^{-9} mol s^{-1} cm^{-2} at 80 °C. In another study, Xu et al. [66] reported the synthesis of ammonia from H_2 and N_2 using an electrolytic cell consisting of Nafion, $SmFe_{0.7}Cu_{0.3x}Ni_xO_{3-\delta}$ (x = 0-0.3) and Ni-SDC as solid electrolyte, cathode and anode respectively. The $SmFe_{0.7}Cu_{0.1}Ni_{0.2}O_{3-\delta}$ (SFCN) cathode exhibited the highest rate of ammonia formation (1.13×10^{-8} mol s^{-1} cm^{-2}) with an applied voltage of 2 V and 80 °C under atmospheric pressure. This rate corresponds to a Faradaic efficiency of 90.4 % which is the highest value reported in the literature so far. Recently, Xu et al. [68] synthesised ammonia from its constituents (H_2, N_2) in an electrolytic cell composed of Nafion electrolyte, a Ni-SDC anode and K_2NiF_4-type cathode of the form $Sm_{1.5}Sr_{0.5}MO_4$ (M=Ni, Co, Fe). Unlike $Sm_{1.5}Sr_{0.5}FeO_4$ and $Sm_{1.5}Sr_{0.5}CoO_4$, the catalyst oxide with a composition of $Sm_{1.5}Sr_{0.5}NiO_4$ (SSN) displayed that highest rate of ammonia production which was found to be up to 1.05×10^{-8} mol s^{-1} cm^{-2} at 80 °C and 2.5 V. Recently, Liu et al. [120] investigated the synthesis of ammonia using an electrolytic cell based on SPSF and Nafion membranes. In this study the cathode and anode were $Sm_{1.5}Sr_{0.5}NiO_4$ (SSN) and Ni-SDC respectively. However, despite that fact that the protonic conductivity of Nafion is higher than that of SPSF, the two membranes exhibited similar rates. The rates were found to be 1.05×10^{-8} and 1.03×10^{-8} mol s^{-1} cm^{-2} for Nafion and SPSF respectively, with an applied voltage of 2.5 V at 80 °C under atmospheric pressure. This indicates that SPSC-based membrane can replace Nafion as an electrolyte in ammonia production cells.

In addition to the perovskite and K_2NiF_4-type catalysts, double perovskites can also be employed for electrochemical synthesis of ammonia. Recently, Zhang et al. [67] reported that ammonia was synthesised in electrolytic cell using Nafion, Ni-SDC and double perovskite-based catalyst $SmBaCuMO_{5+\delta}$ (M=Fe, Co, Ni) as electrolyte, anode and cathode respectively. The rate obtained using $SmBaCuNiO_{5+\delta}$ (SBCN) catalyst (8.7×10^{-9} mol s^{-1} cm^{-2}) was higher than that of $SmBaCuFeO_{5+\delta}$ (SBCF) and $SmBaCuCoO_{5+\delta}$ (SBCC) catalysts with an applied voltage of 2.5 V at 80 °C under atmospheric pressure.

1.2.3 Electrochemical synthesis of ammonia based on oxygen ion conducting electrolytes

Analogously to proton conducting electrolytes, oxygen ion conducting ceramics have been successfully employed in the electrochemical synthesis of ammonia at atmospheric pressure. These solid electrolytes have the ability to conduct oxygen ions (O^{2-}) and are known as oxygen-ion conducting electrolytes [189]. In 2009, Skodra and Stoukides [10] were the first to report that ammonia had been successfully produced in an electrolytic cell using an oxygen ion conductor (8 mol% yttria-stabilised zirconia, YSZ) as solid electrolyte, Ag as an anode and Ru-MgO catalyst as a cathode. The ammonia was synthesised from nitrogen and water (steam) rather than molecular hydrogen. The maximum formation rate was ~ 3.75×10^{-13} mol s^{-1} cm^{-2} with a current efficiency of 0.0012 % at 650 °C with an applied voltage of 2 V. The low conversion of nitrogen and water into ammonia was attributed to the poor electronic conductivity of the working electrode (Ru-MgO) as well as the rate of ammonia decomposition due to the high operating temperature. The principle is as follows (Figure 1.2b):

Cathode reaction:

$$3H_2O + N_2 + 6e^- \rightarrow 3O^{2-} + 2NH_3 \qquad \text{Equation 1.18}$$

Anode reaction:

$$3O^{2-} \rightarrow \tfrac{3}{2}O_2 + 6e^- \qquad \text{Equation 1.19}$$

The overall reaction is the same as in the case of the H^+ cell (Equation 1.14).

1.2.4 Factors affecting the rate of ammonia formation

The key parameters affecting the rate of ammonia formation are quite complex and include electrode materials, electrical conductivity of the working electrode (catalyst), the cell operating temperature, electrolyte materials and conductivities, applied current, applied voltages and the rate of ammonia decomposition. These factors will be discussed in detail in the following subsections.

1.2.4.1 Effect of the applied current and voltage

As discussed previously, the reaction of gaseous H_2 and N_2 to produce ammonia is thermodynamically unfavourable at temperature as high as 200 °C. Thus the ammonia synthesis process should be done under electrolysis conditions.

Guo et al. [104] investigated the effect of the applied current on the ammonia formation rate by keeping the operating temperature at a constant value (500 °C) and varying imposed current through the electrolytic cell. Under open-circuit condition (I = 0), no ammonia was synthesised. On the other hand, upon imposing a current through the cell (closed-circuit), ammonia was detected and a significant increase in the rate of ammonia formation was observed with increasing the applied current up to 0.75 mA. The rate remained almost the same when further increasing the applied current above 0.75 mA, as shown in Figure 1.11. Wang et al. [75] studied the effects of applied current on ammonia production rate and a volcano-type behaviour was observed as illustrated in Figure 1.12. Firstly, the rate increased with an increase in the imposed current up to 1 mA and then declined significantly above 1 mA. This could be ascribed to the competitive adsorption between N_2 and H_2 over the electrocatalyst surface (cathode), as reported by Sclafani et al. [41] and Kordali et al. [70]. This means that the hydrogen evolution reaction was the predominant process on the cathode surface when a current higher that 1 mA was applied (Figure 1.12).

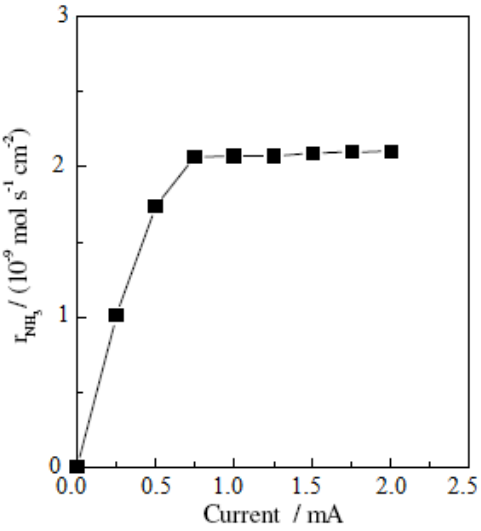

Figure 1.11 Dependence of the ammonia formation rate on the applied current. The electrolytic cell was: Wet H_2, Ag-Pd |BCY| Ag-Pd, dry N_2 and at operating temperature 500 ºC [104]

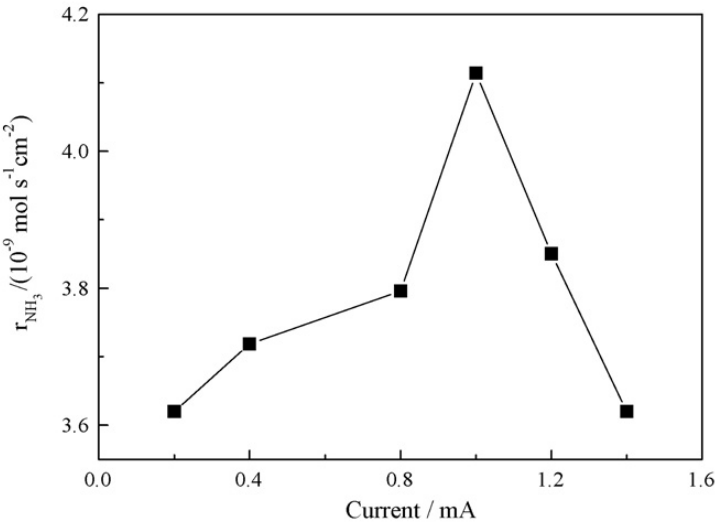

Figure 1.12 Dependence of the ammonia formation rate on the applied current. The electrolytic cell was: Wet H_2, Ni-BCY |BCY| BSCF, dry N_2 and the operating temperature 530 ºC [75]

The dependence of the ammonia formation rates on the applied voltage has also been investigated [64, 72, 76, 77, 96]. Li et al. [72] found that rates are voltage dependent, as illustrated in Figure 1.13. As can be seen, no ammonia was detected when no potential was imposed through the electrolytic cell. However, by applying a potential, the formation rate increased significantly and reached a maximum value at 0.6 V and plateaued up to 1.0 V. This behaviour is similar to that reported in the case of applied current, as described above.

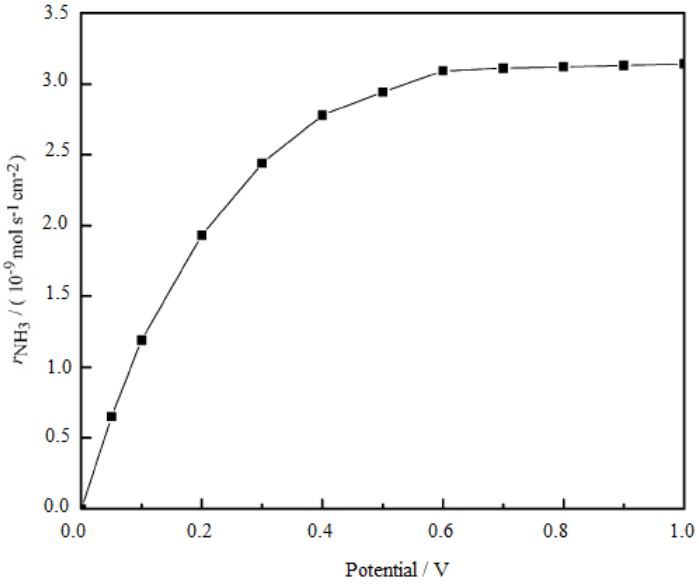

Figure 1.13 Effect of imposed potential on the ammonia formation rate. The electrolytic cell was: H_2, Ag-Pd |BCGO| Ag-Pd, N_2 and the operating temperature 480 ºC [72]

1.2.4.2 Effects of cathode catalyst materials and conductivity

As mentioned previously, the cathode (electrocatalyst) is the component of the cell at which the electrochemical reaction of interest takes place, poor electronic conductivity of the working electrode being one of the main obstacles to obtaining high ammonia formation rates [75]. Thus, different materials have been utilised as electrocatalysts to investigate their effects on ammonia formation rate. The influence of the working electrode materials on the ammonia formation rate was investigated by Xu and Liu [68]. In this study, three electrodes with different composition—

$Sm_{1.5}Sr_{0.5}FeO_4$ (SSF), $Sm_{1.5}Sr_{0.5}NiO_4$ (SSN) and $Sm_{1.5}Sr_{0.5}CoO_4$ (SSC)—were compared. It was found that the ammonia formation rate using SSN cathode is higher than that for SSC and SSF (Table 1.2). This difference in the formation rates was attributed to high electronic conductivity of SSN compared to SSC and SSF. Recently, Skodra and Stoukides [10] investigated the electrocatalytic activity of the industrial Ru-MaO catalyst for ammonia synthesis and the results indicated that the formation rate was rather low (4×10^{-13} mol s^{-1} cm^{-2} at 650 °C). This was attributed to its poor electronic conductivity, despite the fact that Ru-MaO catalyst is very active for ammonia synthesis. In order to enhance its electronic conductivity, a thin layer of Ag was deposited on the electrolyte surface before adding the active catalyst. However, some of the electrochemically supplied H^+ recombined to gaseous H_2 on the Ag layer and never reached the catalyst surface to react with the adsorbed N_2 to form ammonia. Thus, the fabrication and electrocatalyst design are of crucial importance to enhance the ammonia formation rate.

1.2.4.3 Effect of operating temperature

In terms of the impact played by the operating temperature on the ammonia formation rates, several studies in the literature have attempted to explain this effect [68, 73, 76, 101]. Chen and Ma [73] investigated the dependence of the formation rates on the operating temperature from 400 to 560 °C and a volcano-type behaviour was observed. It was found that with an increase in the operating temperature, the rate increased significantly and reached a maximum value at 480 °C, which could be attributed to the increase of the protonic conductivity of the employed electrolyte. However, the rates declined significantly when the operating temperature was further increased up to 560 °C, which certainly results from the ammonia decomposition, as illustrated in Figure 1.14.

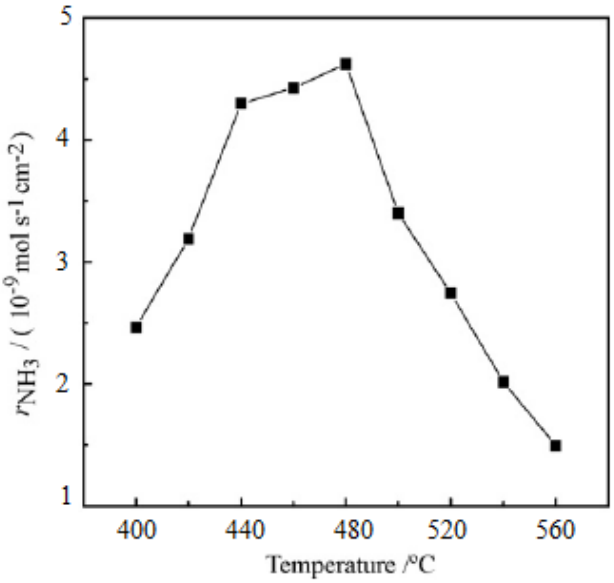

Figure 1.14 The relationship between the rate of ammonia formation and the synthesis temperature. The cell was H_2, Ni-BCGO |BCGO| Ag-Pd, N_2 [73]

The effect of the operating temperature on ammonia formation rates has also been investigated at low temperature (25 to 100 °C). Liu et al. [120] utilised acidic membranes (Nafion and SPSF) as solid electrolytes and studied the effect of operating temperature on production rate. In that study, volcano-type curves (Figure 1.15) were also observed, as mentioned above in the case of high temperature solid oxide proton conductors. The increase in the formation rates with temperature could also be ascribed to the increase in the protonic conductivity of the solid polymer electrolytes. The rates decreased significantly, however, with further increase in the operating temperature above 77 °C, which was attributed to the decrease of the electrolytes' proton conductivity as result of water loss. This means that ammonia decomposition did not play important role on decreasing the formation rates, since the operating temperature was quite low. The decomposition of ammonia happens above 175 °C [11]. Despite the fact that the ammonia decomposition could be reduced using low temperature proton conducting materials, the lack of stability of these acidic membranes (e.g. Nafion) in the presence of ammonia (weak base) is one of the main limitations of their usage as electrolytes in ammonia synthesis cells [11, 13].

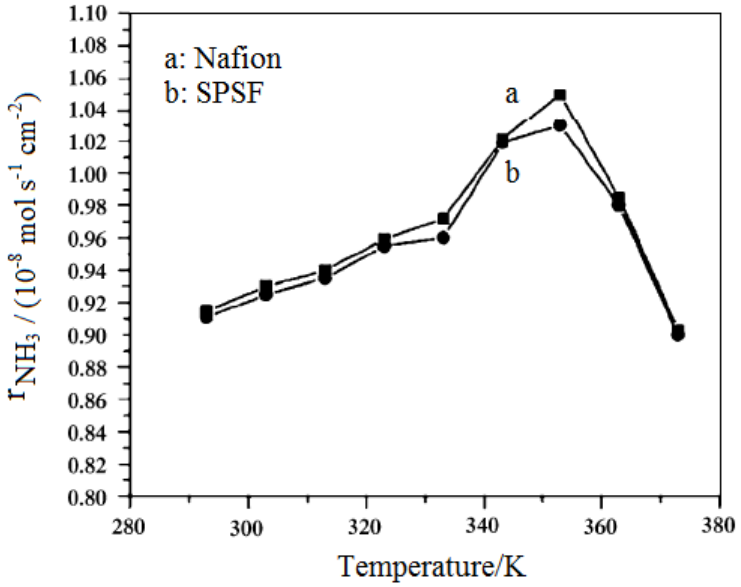

Figure 1.15 Dependence of ammonia formation rate on the operating temperature when polymers used as electrolytes. The electrolytic cells were (a) Wet H_2, Ni-SDC |Nafion| SSN, dry N_2; (b) Wet H_2, Ni-SDC |SPSF| SSN, dry N_2 [120]

1.2.4.4 Effects of electrolyte materials and thickness

The electrolyte materials and thickness are other factors that play an important role on enhancing the rate of ammonia formation. Generally, the formation rates varied significantly when using different electrolyte materials as summarised in Table 1.2. In addition, the maximum rates of ammonia formation according to the type of electrolyte were in the following order: solid polymers > YDC-phosphate composites > fluorites > perovskites > pyrochlores. Cheng et al. [105] investigated the effect of the electrolyte materials on the ammonia formation rate. In this study, three electrolytes with different composition—$La_{0.9}Sr_{0.1}Ga_{0.8}Mg_{0.2}O_{3-\delta}$ (LSGM), $La_{0.9}Ba_{0.1}Ga_{0.8}Mg_{0.2}O_{3-\delta}$ (LBGM) and $La_{0.9}Ca_{0.1}Ga_{0.8}Mg_{0.2}O_{3-\delta}$ (LCGM)—were compared. It was found that the formation rate using LSGM was higher than those of LBGM and LCGM, as listed in Table 1.2. This difference in the rates was ascribed to high protonic conductivity of LSGM compared to LBGM and LCGM as listed in Table 1.1.

In addition to the electrolyte materials, the electrolyte thickness plays an important role in improving the rates of ammonia formation. The operating temperature of the electrolytic cell could be lowered by reducing the thickness of the electrolyte which is beneficial in enhancing the formation rates. Practically, operating electrochemical devices at low or intermediate temperatures is desirable because it offers significant advantages, including more flexible choice of materials, lower manufacturing costs and a longer lifetime [108]. The downside of lowering the operating temperature is the significant decrease in the ionic conductivity of the electrolyte, which in turn results in high ohmic losses across the electrolyte. The ohmic losses can be overcome or minimised by reducing the thickness of the electrolyte or using electrolyte materials that exhibit high ionic conductivities at low/intermediate temperature [190, 191]. Guo et al. [104] reported that ammonia was successfully synthesised at intermediate temperature using perovskite-based proton conductors ($BaCe_{0.85}Y_{0.15}O_{3-\delta}$) with thickness of 0.8 mm. In this case, the maximum rate was found to be 2.1×10^{-9} mol s^{-1} cm^{-2} at 500 °C. However, recently, Wang et al. [75] reported that by reducing the thickness of the electrolyte ($BaCe_{0.85}Y_{0.15}O_{3-\delta}$) to about 0.03 mm, the rate of ammonia formation almost doubled (4.1×10^{-9} mol s^{-1} cm^{-2} at 530 °C).

1.3 Aims and thesis outlines

To summarise the previous discussion, the rate of ammonia formation is affected by several factors including; catalytic activity of electrode materials, electrode polarisation, synthesis temperature, applied current or voltage, the rate of ammonia decomposition, electrolyte materials and thickness of the electrolyte. The vast majority of the studies conducted focused on the performance of high temperature solid state proton conducting materials (HTPC) in the synthesis of ammonia, whereas only a few reports have been published on the performance of the catalytic (cathode) materials. In addition, H_2 and N_2 were the most widely used reactants for ammonia although there are many problems associated with using pure H_2, such as its production, transportation and storage. Therefore, the scopes of conducting this research are as follows;

- Investigate the synthesis of ammonia using three different types of catalysts (cathodes) namely; molybdenum containing nitrides (e.g. Co_3Mo_3N), spinel-type oxides (e.g. $CoFe_2O_4$) and perovskite-type oxides (e.g. $La_{0.6}Sr_{0.4}FeO_{3-\delta}$).
- Develop new electrolyte materials based on oxide-carbonate composites for applications at low and intermediate temperatures (300-600 °C) and explore their applications in electrochemical synthesis of ammonia, aiming to reduce the ammonia decomposition effect.
- Investigate the electrochemical synthesis of ammonia directly from water and N_2 rather than pure H_2.

The thesis comprises 8 chapters which can be classified into five parts. The first part deals with ammonia synthesis, applications and an overview of the previous work on solid state electrochemical synthesis of ammonia (Chapter 1). The second part is about synthetic methods and the techniques which have been used for sample characterisation (Chapter 2). The electrochemical synthesis of ammonia from its elements H_2 and N_2 using solid state electrolytic cells is discussed in Chapters 3 and 4 (the third part). The fourth part is about electrochemical synthesis of ammonia from water and nitrogen without the need for molecular hydrogen (Chapters 5-7). The synthesis of ammonia directly from air and water will be also discussed in Chapter 7. The fifth part provides a summary of the major findings of the thesis and discusses the potential future work (Chapter 8).

2 Experimental

2.1 Powder synthesis

In general, many different methods can be used to synthesise the materials of interest including conventional solid state method, sol-gel process, combustion, hydrothermal and co-precipitation etc. The discussion below will be restricted only to the methods employed in this thesis.

2.1.1 Solid state synthesis

Solid state reaction (SSR) or ceramic method is the simplest and the most widely employed synthesis process to prepare solid materials. This method involves mixing and heating the non-volatile solid reactants at high temperature (500-2000 ºC) to yield the required product [192]. The advantages of SSR are including; suitability for high mass production of powders, simplicity and low manufacturing cost. However, this process suffers from the following drawbacks; the requirements for high calcination temperature, formation of secondary phases, low surface area, poor sinterability, and poor compositional homogeneity [193].

2.1.2 Co-precipitation method

Co-precipitation is one of the oldest synthetic methods for preparing solid materials. In this method, stoichiometric amounts of soluble salts containing the desired metal ions are dissolved in an aqueous media and then mixed with the required amount of a precipitation agent solution. The material could be precipitated as hydroxides, oxalates, citrates, etc., depending on the precipitation agent (e.g. ammonia, oxalic acid, etc). The precipitate usually undergoes filtering, washing, drying and grinding steps before being heated to decompose, giving the final product. Unlike the ceramic method, well defined and less-agglomerated oxide powders with a small particle size can be obtained using co-precipitation method [192-195].

2.1.3 Combined EDTA-citrate complexing sol-gel process

Another attractive route to prepare ultrafine ceramic powders is the sol-gel process. Unlike conventional ceramic method, in this process, the synthesis is carried out at low temperatures. In addition, the sol-gel process is advantageous in that the possibility of changing the stoichiometry of the desired materials can be avoided since there are no washing and filtration steps at which one or more ions may stay in the solution as in the case of co-precipitation process [192, 196].

In this study, EDTA-citrate complexation route is adopted to prepare the desired materials because of its advantages such as obtaining final compounds of high purity, homogeneous, carbonate-free and ultrafine particle size. In this process citric acid and ethylenediaminetetraacetic acid (EDTA) are used as combined complexing (chelating) agents. This process involves complexation of metal ions in EDTA/citric acid and the pH of the solution is adjusted to the desired value (~ 6) using ammonia solution, followed by a gel formation step by evaporating the excess water. Finally, the thermal decomposition of the dried gel at much higher temperature, removes the residual organic materials and to form the desired ceramic powder [193, 194, 197].

2.1.4 Glycine-nitrate combustion process

Combustion synthesis (CS) is developed as alternative route to the conventional ceramic method [198, 199]. In the combustion synthesis, highly exothermic and explosive redox reaction is used to prepare many materials including ceramics, nitrides, etc [192]. Solution combustion synthesis (SCS) which is characterised by the combination of combustion and reactive solution approaches are considered as an important class of combustion synthesis. This process involves a self-sustained reaction in homogeneous solution of different oxidisers (e.g. metal nitrates) and fuels (e.g. urea, glycine, citric acid) [200, 201].

One of the simplest solution combustion synthesis methods is the glycine nitrate process (GNP) [202]. By using this synthetic method, ultra-fine ceramic oxide powders with improved powder characteristics in short process time (seconds) at a relatively low calcination temperature can be obtained [203]. This process involves a

stoichiometric mixing of metal nitrates with glycine in an aqueous solution followed by a gentle heating to evaporate the excess water and form a viscous liquid. By further heating this latter to about 180 ºC, an atuo-ignition occurs with rapid self-sustaining combustion yielding an oxide ash. Finally, a calcination step is carried out in order to burn out the residual organic materials and forming the desired ceramic powder.

As described above different methods have been used to synthesise the desired materials and more details will be given in the relevant Chapters.

2.2 Powder processing

2.2.1 Calcination

Once the wanted materials are synthesised via one of the above mentioned synthetic methods, it is necessary to calcine the resultant solid in order to obtain the final product. Calcination process can be defined as a heat treatment of the desired product precursor whereby it decomposes leaving a solid oxide of interest and librating gases. Thus calcination plays important roles in removing any remaining by-products and obtaining a single phase crystalline material. In addition, the particle size and surface area depend strongly on the calcination temperature. Therefore, this temperature needs to be carefully controlled to improve the materials properties (e.g. surface area). For obtaining very fine powders with high surface area, the calcination temperature should be as low as possible. However, if the materials are calcined at high temperature, low surface area powders would be obtained as a result of increasing the particle size and forming hard agglomerates which can affect the powders pressing and sinterability. Milling step can be used to break up the agglomerates and reduce the particle size. This can also improve the green density and enhance sinterability [204].

2.2.2 Ball mill mixing and grinding

In ceramic processing, it is important to remove agglomerates and aggregates, to reduce the average particle size of materials, to achieve the desired particle size distribution and modify the shape of particles, because these play very important role on pressing and sintering behaviours of ceramic powders and also on their final microstructures [204-206]. Ball milling is one of the most common techniques which can be utilised for these purposes.

In ball milling, the particles to be mixed and ground are placed with grinding media (balls, rods or short cylinders) in a closed rotating cylindrical container (Figure 2.1a). Smaller particles are obtained as a result of moving the ceramic particles between the grinding media and the wall of the container (mill). The most commonly used media are steel, WC, Al_2O_3, SiO_2 and ZrO_2. It is to be noted that, wearing of the mill walls and milling media are the common sources of contamination in milling. However, this can be avoided or controlled by using wear-resistant mill linings and media [204-206]. Practically, either wet or dry ball milling can be carried out. Dry milling is advantageous in that there is no need for separating the liquid from the resulting powder (i.e. drying), reaction between the powder and liquid can be avoided and milling can be started and stopped at any time. However, in dry milling the powder pack far from corners of the mill and avoid milling which is the major concern in this process. On contrary, wet milling offers the following advantages; no dust problems, good homogenisation and smaller particle size can be obtained [205].

In this study, the ball milling was performed using a planetary ball mill (Pulverisette 6, Fritsch (Figure 2.1b). The powder to be ball milled was placed with zirconia balls into the sample container. Then an appropriate amount of isopropanol is added as a liquid medium for milling. Then the container is placed in the ball miller instrument and the rotating speed is set at 400 rpm for several hours. After milling, the resultant mixture is dried on hot-plate and then ground thoroughly for subsequent use.

(a) (b)

Figure 2.1 (a) Grinding bowls and grinding balls; (b) Planetary mono mill Pulverisette 6

2.2.3 Dry pressing of powder

Dry pressing or powder compaction is one of the simplest and most common process of obtaining the desired shape of material [207]. This process can be divided into isostatic pressing and uniaxial die pressing [208]. In isostatic compaction or isopressing, a rubber bag is used as a container for the powdered materials and the pressure is applied isostatically by means of fluid. Unlike uniaxial die pressing, more complicated shapes can be formed using isostatic pressing. However, the isostatic pressing is an expensive and more time-consuming technique [209].

In uniaxial dry pressing, the powder to be pressed (containing 0-5 wt % binder) is fed into a rigid die and the pressure is applied through a rigid punch in a single axial direction [204, 205, 207]. In this process the powder compacts take the die configuration which allows the fabrication of shapes with accurate dimensions. In addition, the uniaxial pressing is inexpensive and large quantities can be produced in short time (i.e. high production rate) [207-209]. Uniaxial powder pressing is accomplished by the three following stages [206, 208]; die filling, powder compaction and finally the ejection of green compact as illustrated schematically in Figure 2.2c. In the first stage, free-flowing powder is fed into the die cavity and high

green density can be achieved by uniform distribution of the powder particle size inside the die. This could be accomplished with the aid of sieve. By doing this, the gaps between the large particles will be filled by the small ones which play an important role on packing the particles in the next step. In the second stage, the filled powder is compacted by applying pressure on the top of upper punch. Finally, the pressed compact is ejected by pushing up the lower punch [208, 209].

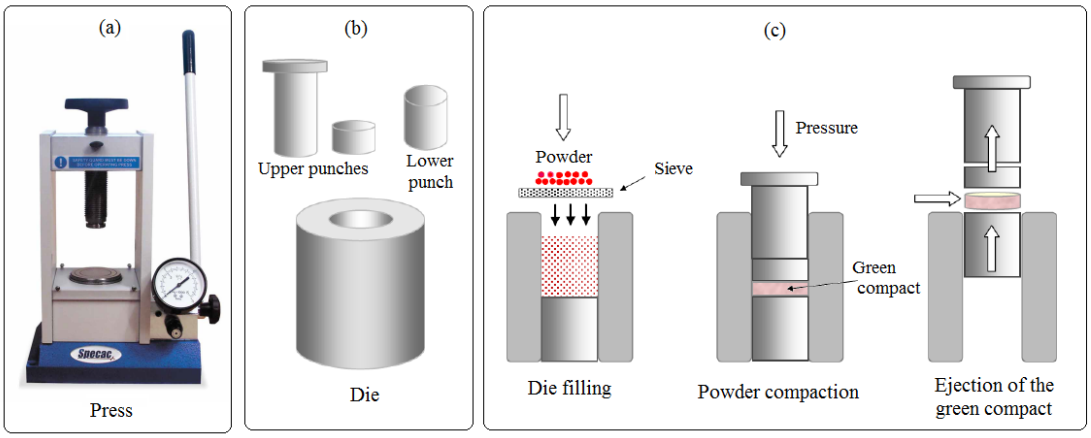

Figure 2.2(a) Press; (b) Schematic representation of stainless steel die and punches; (c) stages in uniaxial die pressing

In this study, uniaxail dry-pressing technique was used to prepare the pellets using stainless steel dies. For conductivity measurements, 13 mm die was used to prepare the pellets. While either 13 mm or 19 mm were used to prepare the single cells for ammonia synthesis experiments. In the case of multi-layered single cells, a cost-effective one-step dry-pressing method was adopted. The cell components (anode, electrolyte and cathode) were fed into the die, layer by layer, with the aid of sieve to ensure uniform particle size distribution and then uniaxailly co-pressed. In both cases the applied pressure was typically 121-259 MPa. Once the pellets are ready, further sintering step is followed which will be described in detail in the relevant Sections.

2.2.4 Powder sintering

Sintering is a heat treatment process by which a powder compact is converted into a dense ceramic component [210, 211]. During the sintering process, most of the pores between the starting particles can be removed or eliminated accompanied by shrinkage of the component, grain growth and strong bonds between the adjacent particles are formed [204, 212]. Sintering can be classified into liquid phase sintering and solid state sintering. In the presence of liquid phase is called liquid phase sintering (LPS), while is referred to as solid state sintering (SSS) in absence of the liquid phase [211]. In this study, sintering was used for preparation of cells (Figure 2.3a) for electrochemical synthesis of ammonia. This sintering process was carried out in muffle furnaces (Figure 2.3b) with programmable controllers.

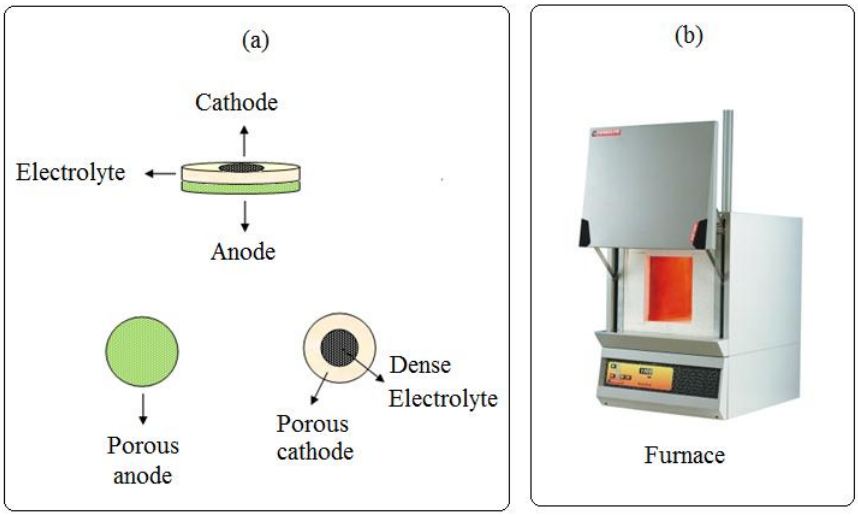

Figure 2.3 (a) Schematic representation of a tri-layer cell after sintering; (b) Furnace

2.3 Sample characterisation techniques

2.3.1 X-Ray Diffraction (XRD)

Powder X-ray diffraction (XRD) is a powerful and the most widely used technique to determine the crystal structure, phase purity and composition of polycrystalline materials. X-rays are a type of electromagnetic radiation of wavelength ~ 1 Å (10^{-10} m). The wavelengths of the X-rays are of the same order of magnitude as the distances between atoms in solids [192, 195, 213].

Crystals are defined as three-dimensional arrangement of atoms or molecules that are situated in fixed positions in a repeating pattern. These atoms are arranged in a series of parallel planes with varying interplanar distances, *d*, known also as d-spacing [213]. When monochromatic X-ray beams strike a crystalline sample, they will be diffracted by the lattice planes in all directions. At specific directions, the diffracted X-rays will interfere constructively resulting in a strong reflection. The constructive interference of two reflected beams occurs when Bragg's law is satisfied (Equation 2.1). The constructive interference occurs only when the reflected beams are in phase. The Bragg's condition for the reflection of X-ray from parallel planes within the crystal is shown schematically in Figure 2.4 [192, 195, 209].

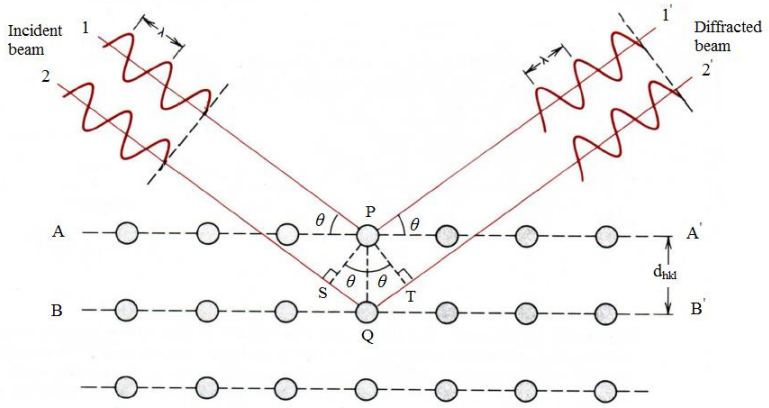

Figure 2.4 Diffraction of X-rays by a set of crystal planes with a spacing d_{hkl} [209]

$$2d_{hkl}\sin\theta = n\lambda \qquad \text{Bragg's law} \qquad \text{Equation 2.1}$$

From the Bragg's law, the spacing between the crystal planes (d_{hkl}) can be calculated once the angle of reflection (θ) has been determined. For crystal structures having cubic symmetry the interplanar, d_{hkl}, is given by Equation 2.2 [192, 209].

$$d_{hkl} = \frac{a}{\sqrt{h^2 + k^2 + l^2}} \qquad \text{Equation 2.2}$$

In which *h*, *k*, and *l* are the miller indices and *a* is the lattice parameters.

In addition to the aforementioned applications of the PXRD, it is also useful technique of determining crystalline size using Debye-Scherrer formula (Equation 2.3) [195].

$$\tau = \frac{0.9\lambda}{(\beta \cos\theta)} \qquad \text{Equation 2.3}$$

Where τ is the crystallite size, λ is the wavelength of the X-ray, β is the full width at half maximum (FWHM) of the peak in radiance and θ is the Bragg angle.

In this study two XRD instruments were used for data collection. One is a Bruker-AXS (D8Advance) machine, controlled by DIFFRACT plus™ software, in the Bragg-Brentano reflection geometry with a Ni-filtered CuKα radiation (λ=1.5405 Å), fitted with a LynxEye^{TM} detector. XRD patterns were recorded in the 2θ range 5-85º. The second is a Panalytical X'Pert Pro diffractometer with a Ni-filtered CuKα radiation (λ=1.5405 Å), using 40 kV and 40 mA, fitted with a X'Celerator detector. Absolute scans were recorded in the 2θ range 5-100º.

2.3.2 Simultaneous Thermal Analysis

Thermal analysis (TA) is a group of well established analytical techniques by which the change in the properties of materials (i.e. physical and chemical) is studied as a function of temperature. These techniques are useful in solid state science for investigating phase changes (e.g. melting), solid state reactions, thermal decompositions, losses of water or oxygen, etc [192, 195, 214]. There are different kinds of thermal analysis but the discussion below will be restricted only on thermogravimeric analysis (TGA), differential scanning calorimetry (DSC) and their combination (TGA-DSC).

In the thermogravimeric analysis (TGA), the change in weight of a sample is measured as function temperature or time. Differential scanning calorimetry (DSC) measures the difference in heat flow into the sample and reference as function of temperature or time [192, 195, 214]. It is to be noted that either TGA or DSC alone

rarely provides all the information required to permit a complete interpretation of the behaviour of the material being investigated. Thus, complementary information from another thermal technique or other form of analysis is usually needed. Therefore, it is advantageous if two or more measurements on the same sample could be carried out simultaneously [214, 215].

Simultaneous Thermal Analysis (STA) generally refers to the combination of two thermal analysis techniques in one unique instrument by which measurements on a single sample could be carried out at the same time and under identical experimental conditions. STA measurement not only save time and materials but also simplifies data interpretation. From the obtained complementary information, one can differentiate between endothermic and exothermic events which have no associated weight loss (e.g. melting and crystallisation) and those involve a weight loss (e.g. degradation). In simultaneous thermogravimetric analysis and differential scanning calorimerty (TGA-DSC), both weight changes and heat flow in a material are measured simultaneously as a function of temperature or time and in a controlled atmosphere [214-217].

TGA/DSC analyses were performed using a Stanton Redcroft STA/TGH series STA 1500 operating through a Rheometric Scientific system interface controlled by the software RSI Orchestrator.

2.3.3 Scanning Electron Microscopy (SEM)

Electron microscopy (EM) is most widely used technique in characterisation of solids to study structure, morphology and crystallite size, to examine defects and to determine the distribution of elements. An electron microscope is similar in principle to an optical microscope, except that a beam of electrons is used instead of a visible light [192]. EM is of two types, scanning electron microscopy (SEM) and transmission electron microscopy (TEM). The schematic of scanning electron microscope is shown in Figure 2.5.

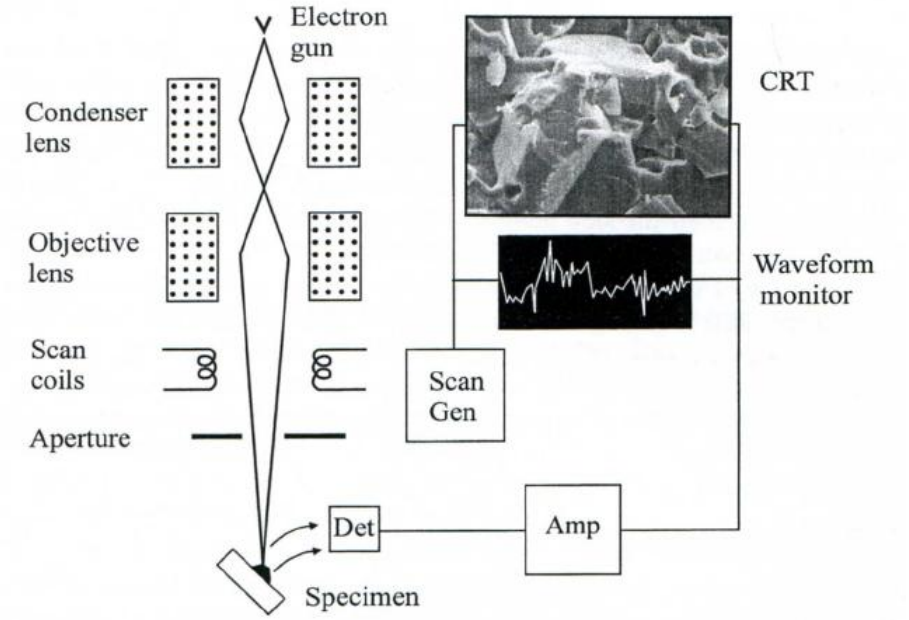

Figure 2.5 Schematic diagram of scanning electron microscope [218]

In SEM, the electron beams are emitted from an electron gun fitted with a tungsten filament cathode. The generated electron beams are accelerated by a voltage typically 0.5-30 kV between the cathode and the anode forming a smallest beam with diameter of about 10-50 μm which is too large to form a high-resolution image. Thus, a series of electromagnetic condenser lenses are used to focus the electron beams to a small spot typically 1-100 nm in diameter. The beam is swept across the surface of the sample by a set of scan coils before being focused onto the sample. As the incident electron beam strikes the sample, a series of signals are generated as a result of the interaction between the incident electron beam and a thin surface layer of the sample as shown in Figure 2.6. These signals including secondary electrons (SE), backscattered electrons (BSE), characteristic X-rays and cathodoluminescence can be collected by appropriate detectors and then displayed on a monitor after suitable amplification. For SEM imaging, the low energy secondary electrons (~ 5 eV) are the most commonly used [192, 218-220].

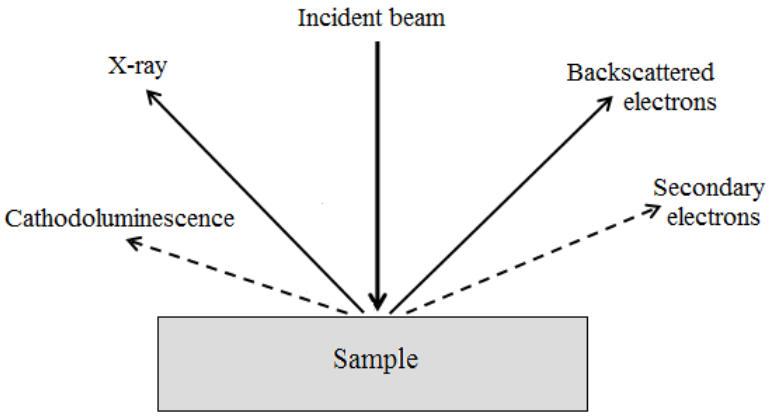

Figure 2.6 Schematic representation showing possible signals emitted by an electron beam

In this study, the microstructures of the prepared catalysts and the cross-sectional areas of the single cells were examined either using a Quanta 3D FEG (FEI Company) or with a Hitachi SU6600 Scanning Electron Microscopes (SEM)

2.4 Electrochemical Measurements

2.4.1 Conductivity measurements

After shaping and sintering, the pellets are coated on both sides by Ag paste as electrodes and then placed in the conductivity measurement jig. The electrical conductivities of the materials were measured using two different techniques (i.e. AC and DC). The AC was used to measure the ionic conductivities of the composite electrolyte, whereas the electronic conductivity of the cathode material was measured by the DC technique. Both conductivities were measured using a pseudo 4-point configuration (i.e. two contacts, 4 electrical leads), as shown in Figure 2.7.

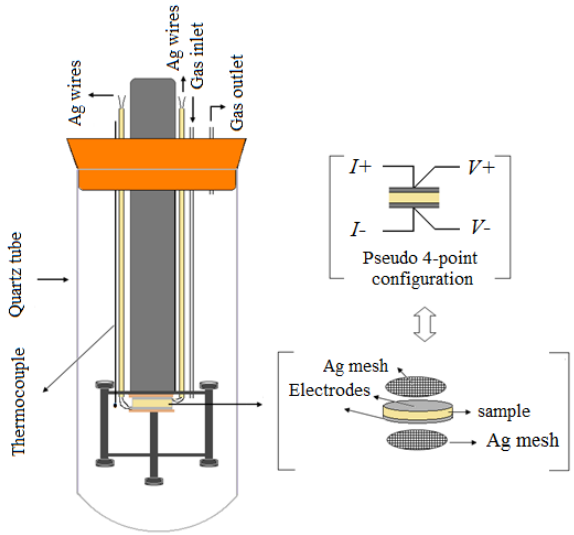

Figure 2.7 Schematic representation of experimental set up for conductivity measurement

The ionic conductivity measurements of the electrolyte was carried out using the AC impedance spectroscopy (IS), known also as electrochemical impedance spectroscopy (EIS). EIS is a powerful technique for characterising the electrical properties of materials and their interfaces [221, 222].

Impedance can be defined as a measure of material's opposition to the flow of alternating current (AC) at a given frequency [223]. Impedance ($Z(\omega)$) is usually measured by applying a small AC sinusoidal voltage perturbation and monitoring the system's resultant current response (Equation 2.4). This measurement is carried out over wide range of frequency typically from 10^{-2} to 10^{7} Hz [222, 224, 225].

$$Z(\omega) = \frac{V(t)}{I(t)} = \frac{V_0 \sin(\omega t)}{I_0 \sin(\omega t + \varphi)} = Z_0 \frac{\sin(\omega t)}{\sin(\omega t + \varphi)} \qquad \text{Equation 2.4}$$

Here, $V(t)$ and $I(t)$ are time-dependant voltage and current, V_0 and I_0 are their amplitudes. ω is the radial frequency $(\omega = 2\pi f)$ in rad/s, φ is the phase shift (rad) and f is frequency (Hz).

The impedance is complex quantity therefore it is represented by complex plane (Nyquist plot) by plotting the imaginary part (Z'') against the real part (Z') as shown in Figure 2.8.

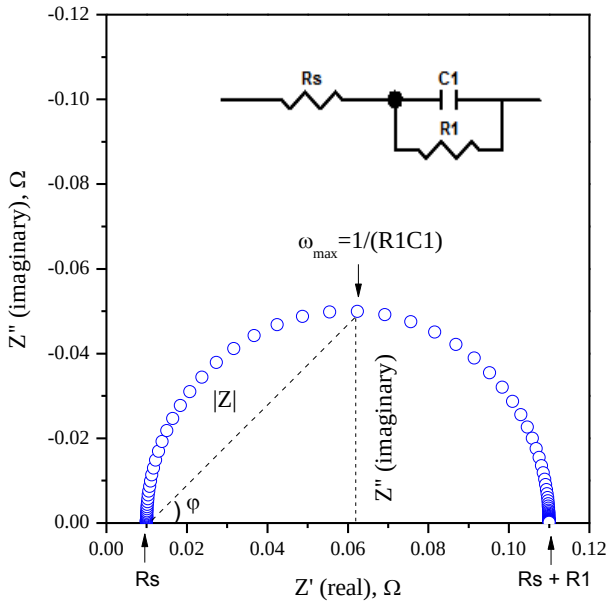

Figure 2.8 Impedance represented in complex plane. Rs = 0.01 Ω, R1 = 0.1 Ω, C1 = 0.02 F

The AC impedance data is commonly analysed by fitting it to an equivalent circuit (EC) model as shown in the inset of Figure 2.8. The EC is a combination of common circuit elements including resistors, capacitors and inductors, etc. The proposed circuit should be as simple as possible and provides a reasonable explanation for the electrochemical system under investigation. In addition, by fitting the impedance data to a good equivalent circuit model, useful information can be extracted about ohmic conduction processes, mass transport, reaction kinetics, etc [224, 226, 227].

In the DC conductivity, a constant current is applied between the two contacts while the voltage is measured across contacts. The conductivities (AC and DC) were calculated using Equation 2.5 [211].

$$\sigma = \frac{L}{RA}$$ Equation 2.5

Where σ is the conductivity (S/cm), R is the resistance (Ω), L is the sample thickness (cm) and A is the cross-sectional area of the specimen (cm^2).

$$\sigma = A\exp(-\frac{E_a}{kT})$$ Equation 2.6

Where E_a is the activation energy, A is the pre-exponential factor, T is the absolute temperature and k is the Bolzmann's constant (1.38×10^{-23} J/K).

The AC and DC conductivity measurements were carried out using a computer-controlled Solartron Analytical 1470E controlled by software CellTest for automatic data collection. In the case of AC conductivity, the impedance spectra were recorded with AC amplitude of 100 mV over the frequency range 1 MHz-0.01 Hz and 10 points per decade.

2.4.2 Ammonia synthesis and detection

The fabricated single cells for ammonia synthesis are placed in either self-designed two-chamber (Figure 2.9a) or single-chamber (Figure 2.9b). The chamber is situated inside a tube furnace and the temperature was monitored by a K-type thermocouple which is placed around the single cell. The operating temperature is increased or decreased gradually to the desired one and the measurements are carried out after at least 30 min so that the temperature reaches a stable state. The voltage was applied by a Solartron 1287A electrochemical interface, controlled by software CorrWare/CorrView for automatic data collection. A constant voltage is applied and the ammonia synthesised is absorbed by diluted acid (e.g. H_2SO_4, 0.001 M). AC impedance spectroscopy (IS) measurements were performed using a Schlumberger Solartron SI 1250 analyser coupled with a SI 1287 Electrochemical Interface controlled by Z-plot/Z-view software. The AC impedance spectra were recorded over

the frequency range 65 kHz to 0.01 Hz. More detail will be given in the relevant Chapters.

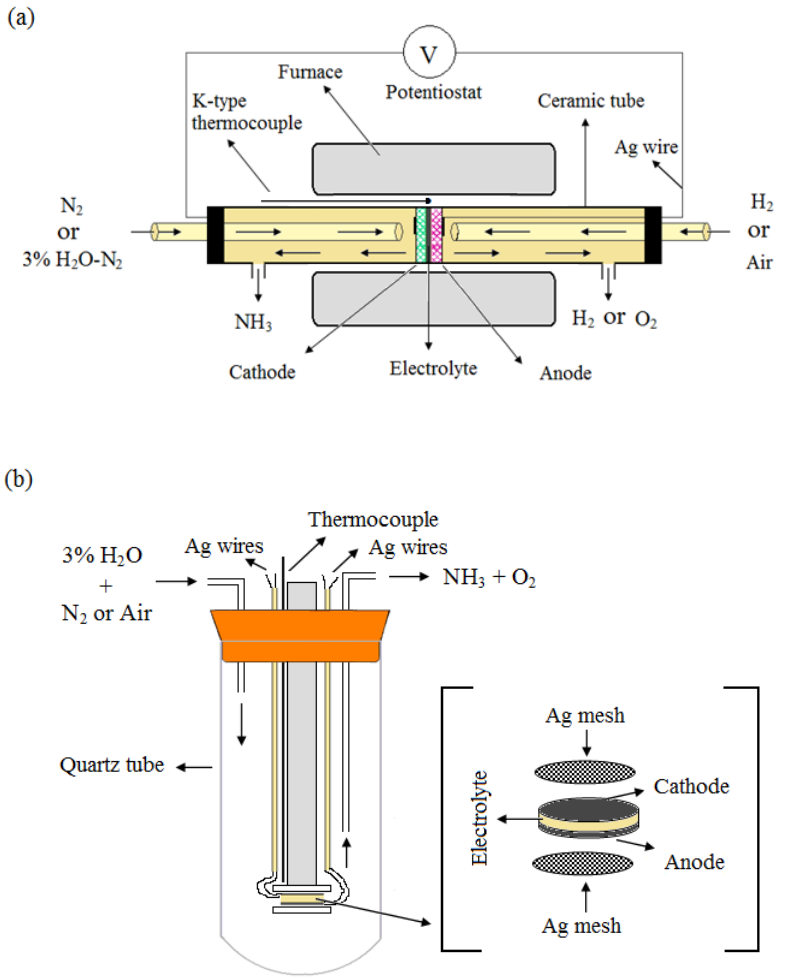

Figure 2.9 Schematic representation of the apparatus used for ammonia synthesis: (a) two-chamber reactor; (b) single-chamber reactor

The produced ammonia was detected by nesslerisation, the classical colorimetric method, or ion selective electrode.

The nesslerisation method involves reaction of Nessler's reagent, a strong alkaline solution of (K_2HgI_4), and ammonia to give a stable yellowish-brown colour. The intensity of the colour is proportional to the concentration of ammonia which can be measured using a spectrophotometer (a device to measure the absorbance of the light as function of wavelength). According to Beer's law (Equation 2.7), the

absorbance, *A*, is directly proportional to the concentration of the absorbing species [228-230].

$$A = \varepsilon bc \qquad \text{Equation 2.7}$$

Where ε is the molar absorpivity (L mol^{-1} cm^{-1}), *c* is the concentration of the absorbing species (mol L^{-1}) and *b* is the pathlength of the absorbing medium (cm).

Ion selective electrodes (ISEs) are a type of membrane electrodes which are used to measure selectively the concentration of certain ions or dissolved gases in solution. These electrodes exhibit a potential that is linearly proportional to the logarithm of the ionic activity of specific ion (Equation 2.8). ISEs are non-destructive, give short time response, non-contaminating and unaffected by colour or turbidity [228, 231]. The ion selective electrode that is used to measure the concentration of the dissolved gases (e.g. NH_3 or CO_2) in solution, known as gas-sensing electrodes [228, 230].

$$E = E^o + 2.303\frac{RT}{nF}\log A \qquad \text{Equation 2.8}$$

Where *E* is the measured electrode potential (i.e. potential difference between the gas-sensing electrode and reference electrode), E^o is standard electrode potential, *R* is gas constant (8.314 J/K mol), *T* the absolute temperature (K), *n* is number of moles of electrons, *F* is Faraday constant and *A* is the ionic activity of the sample.

In this study, either ammonia meter (Palintest 1000) or ion selective electrode ISE (Thermo Scientific Orion Star A214) were used for ammonia detection. The rate of ammonia formation was calculated using Equation 2.9.

$$r_{NH_3} = \frac{[NH_4^+] \times V}{t \times A} \qquad \text{Equation 2.9}$$

Where $[NH_4^+]$ is the measured NH_4^+ ion concentration, V is the volume of the diluted acid used for ammonia collection, t is the absorption time and A is the effective area of the catalysts.

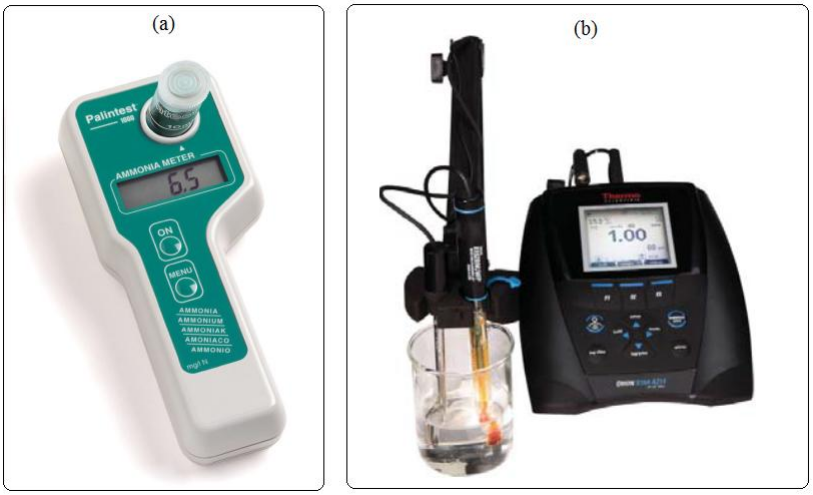

Figure 2.10 (a) ammonia meter; (b) ion selective electrode

3 Electrochemical synthesis of ammonia from hydrogen and nitrogen under atmospheric pressure based on $LiAlO_2$-carbonate composite electrolyte

This research investigated the electrochemical synthesis of ammonia from its elements (H_2 and N_2) using an electrolytic cell based on oxide-carbonate composite electrolyte ($LiAlO_2$-carbonate) and two different cathode materials (i.e. nitride and spinel). The ionic conductivity and thermal stability of the composite electrolyte were studied under different atmospheres (air, dry O_2 and wet 5% H_2-Ar). The ammonia formation rate related to each catalyst will be discussed in detail below in the relevant sections.

3.1 Ammonia synthesis based on $LiAlO_2$-$(Li/Na/K)_2CO_3$ composite electrolyte and nitride-type cathodes

3.1.1 Introduction

As mentioned in Chapter 1, composite solid electrolytes (CSEs) represent an important class of highly ionic conducting electrolyte materials in which the conductivity occurs via interfaces [153, 232]. Basically, composites are mixtures of two or more phases with a combination of different properties, such as high conductivity and enhanced mechanical properties (e.g. higher strength) [153, 232]. These properties make them promising electrolytes for solid state electrochemical devices. Composite electrolytes have been successfully used as solid electrolytes in devices for the electrochemical synthesis of ammonia. Wang et al. [78, 118] reported that ammonia was synthesised in an electrolytic cell based on a composite electrolyte composed of Y-doped ceria-binary phosphate (YDC-$Ca_3(PO_4)_2/K_3PO_4$) as a solid electrolyte.

In addition to the oxide-phosphate composites, oxide-carbonate based electrolytes are also of particular interest, due to their high ionic conductivity (10^{-2} - 1 S cm^{-1}) in the intermediate/low temperature (IT/LT) region [164-167, 180].

However, in the literature, the main focus has been on doped ceria-carbonate composites (e.g., SDC-$(La/Na)_2CO_3$). Recently, non-ceria/carbonate composites have also been proposed as potential electrolytes in IT/LT applications. These composite electrolytes include $LiAlO_2$-$(Li/Na)_2CO_3$, $BaZr_{0.8}Y_{0.2}O_{3-\delta}$-$(Li/Na)_2CO_3$ and $La_{0.9}Sr_{0.1}Ga_{0.8}Mg_{0.2}O_{2.85}$-$(Li/Na)_2CO_3$ [177, 233, 234]. However, in the aforementioned composites, binary carbonate ($(Li/Na)_2CO_3$), which melts at ~ 500 °C, was used as a second phase. However, the melting point of the ternary carbonate ($(Li/Na/K)_2CO_3$) is ~ 400 °C, which is almost a 100 °C lower than that of the binary carbonate [235]. Recently, Xia et al. [172] demonstrated a stable performance of IT-SOFC based on a doped ceria-ternary carbonate composite electrolyte (SDC-$(Li/Na/K)_2CO_3$). It has also been reported that lithium aluminate ($LiAlO_2$) is thermally stable, therefore it has been widely used as an electrolyte matrix ($LiAlO_2$-$(Li/Na)_2CO_3$) in molten carbonate fuel cells (MCFCs) [236, 237]. Based on these findings, it is expected that the combination between $LiAlO_2$ and the ternary carbonate ($(Li/Na/K)_2CO_3$) would result in a composite electrolyte with high ionic conductivity which can be used in ammonia synthesis at low temperature (~ 400 °C). Reducing the cell operating temperature is advantageous in that the thermal decomposition of ammonia can be minimised.

In terms of the cathode materials, in the literature, the main focus has been on the precious metal based catalysts (e.g. Pt, Pd and Ag-Pd). Transition metal nitrides (TMNs) have attracted considerable attention recently and have been used in a wide range of applications due to their interesting properties, including optical, magnetic, mechanical and catalytic properties [238-243]. These materials, such chromium nitride (CrN) and molybdenum nitride (Mo_2N), have been proposed as potential electrocatalysts for application in proton exchange membrane fuel cells (PEMFCs) to replace noble-metal based catalysts, such as the Pt group, that involve high cost and limited supply [244-246].

In the literature, it has been reported that the metallic molybdenum has a high ability to dissociate the dinitrogen molecule (N_2) and also to form a stable nitride under ammonia synthesis conditions [242, 247]. It has been reported that molybdenum-containing nitrides such as Mo_2N, Ni_2Mo_3N, Co_3Mo_3N and Fe_3Mo_3N exhibit high catalytic activities in ammonia synthesis [248-251]. Therefore, the main

aim of this section is to investigate their electrocatalytic activity for ammonia synthesis in an electrolytic cell based on $LiAlO_2$-carbonate composite electrolyte and Ag-Pd anode.

3.1.2 Experimental

3.1.2.1 Synthesis of $LiAlO_2$-carbonate composite electrolyte

The ternary eutectic salt ($(Li/Na/K)_2CO_3$) was prepared by solid state reaction. Lithium carbonate (Li_2CO_3, Alfa Aesar, 98 %), sodium carbonate (Na_2CO_3, Aldrich, 99.5+ %) and potassium carbonate (K_2CO_3, Alfa Aesar, 99 %) were mixed with a molar ratio of 43.5:31.5:25 respectively. The mixture was ground and then calcined in air at 600 °C for 1h and quenched directly to room temperature. The composite electrolyte was made by mixing the commercial Lithium aluminium oxide ($LiAlO_2$, Alfa Aesar) powder with the ternary carbonate salts ($(Li/Na/K)_2CO_3$) at weight ratio 50:50. The mixture was ground thoroughly with an agate mortar then calcined in air at 600 °C for 1h and quenched directly to room temperature. The calcined composite electrolyte ($LiAlO_2$-carbonate) was re-ground thoroughly for subsequent use.

3.1.2.2 Synthesis of nitride-based catalysts

Fe_3Mo_3N catalyst was synthesised by nitriding the corresponding precursor according to the procedure reported by Mckay et al [252]. The precursor was obtained by mixing an aqueous solution of iron nitrate ($Fe(NO_3)_3 \cdot 9H_2O$, Alfa Aesar, 98 %) with an aqueous solution of ammonium heptamolybdate ($(NH_4)_6Mo_7O_{24} \cdot H_2O$, Alfa Aesar, 99 %) in equimolar amounts (Fe/Mo= 1). The mixed solution was evaporated over a hot-plate under stirring to dryness after which a yellowish-brown solid product was obtained. The solid product was dried in the oven at 150 ºC for 2-3 hours then ground. Approximately 2 g of the product was placed into a quartz tube and then was put in a tube furnace (Figure 3.1). Pure NH_3 gas (BOC, 100 %) was introduced to the quartz tube. The tube furnace was programmed to heat the precursor powder in three steps as follows: the temperature was increased from room

temperature to 357 ºC at a rate of 5.6 ºC min^{-1}, and then slowly from 357 to 447 ºC at 0.5 ºC min^{-1}, then to 785 ºC at 2.1 ºC min^{-1} and then held for 5 hours at this temperature. The furnace was then cooled to room temperature at a rate of 5 ºC min^{-1} in flowing ammonia. Since the nitrided material is air sensitive, it was passivated for 1 h in flowing N_2 gas to avoid oxidation. Finally, an ultrafine black powder of Fe_3Mo_3N was obtained.

Co_3Mo_3N catalyst was synthesised by nitriding a cobalt molybdate hydrate precursor ($CoMoO_4 \cdot nH_2O$). The oxide precursor was obtained by mixing an aqueous solution of cobalt nitrate ($Co(NO_3)_2 \cdot 6H_2O$, Sigma Aldrich, 98 + %) with an aqueous solution of ammonium heptamolybdate ($(NH_4)_6Mo_7O_{24} \cdot H_2O$, Alfa Aeser, 99 %) in equimolar amounts (Co/Mo = 1). The mixed solution was evaporated to dryness on a hot-plate under magnetic agitation and a purple solid product was obtained. The resultant solid product was nitrided using the same procedure described above for Fe_3Mo_3N synthesis.

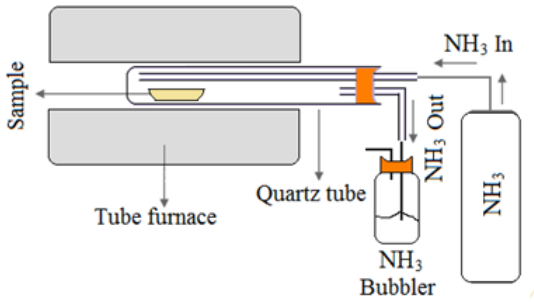

Figure 3.1 Schematic representation of the apparatus used for nitridation

3.1.2.3 Materials characterisation

Phase purity of the prepared materials was studied by powder X-ray diffraction (PXRD) using a Bruker-AXS (D8Advance) machine. The thermal behaviour of the composite electrolyte was studied under different atmospheres (air, O_2 and 5% H_2-Ar) from room temperature to 600 °C with a heating/cooling rate of 10 °C/min. The microstructures of Co_3Mo_3N and Fe_3Mo_3N catalysts were examined using a Quanta

3D FEG (FEI Company) Scanning Electron Microscope (SEM). It should be noted that, in order to obtain better image definition, the samples were coated by a thin layer of gold.

3.1.2.4 Fabrication of the single cell for ammonia synthesis

The electrolyte supported cell was fabricated by uniaxial dry-pressing the composite electrolyte powder ($LiAlO_2$-carbonate 50:50 wt %) into a 19 mm pellet under 121 MPa. The green pellet was sintered in air at 600 °C. The composite cathode was prepared by mixing the Fe_3Mo_3N catalyst with Ag paste to increase its conductivity and adhesion to the electrolyte surface. Then the Fe_3Mo_3N-Ag composite was pasted on one side of the composite electrolyte as the cathode, with a surface area of 0.64 cm^2. Ag-Pd (Johnson Matthey, 20 wt % Pd) paste was painted on the other side as the anode. Ag wires were used as output terminals for both electrodes. The single cell, consisting of a Co_3Mo_3N-Ag composite cathode with a surface area of 0.98 cm^2, was prepared as described for the Fe_3Mo_3N-Ag composite cathode.

3.1.2.5 Pellet preparation for conductivity measurement

The AC conductivity measurements were carried out using a computer-controlled Solartron Analytical 1470E plus 1455A FRA with AC amplitude of 100 mV over the frequency range 1 MHz-0.01 Hz and 10 points per decade. The $LiAlO_2$-$(Li/Na/K)_2CO_3$ composite powder was uniaxially dry-pressed under 295 MPa into pellets with diameter of 13 mm and thickness of 2 mm. The green pellets were sintered in air at 600 ºC for 2 h, at a rate of 2 ºC/min heating/cooling. The pellets were brushed on both sides with Ag paste. AC impedance measurements were performed in three atmospheres, namely; air, dry O_2 (dried through a 98% H_2SO_4 solution) and wet (~ 3% H_2O, passing through room temperature water) 5% H_2-Ar. The measurements were in the temperature range 300-600 ºC.

3.1.2.6 Ammonia synthesis

The fabricated single cell was placed in a self-designed double-chamber reactor. The two electrolytic cells for ammonia were constructed as follows: H_2, Ag-Pd|$LiAlO_2$-carbonate|Fe_3Mo_3N-Ag, N_2, and H_2, Ag-Pd|$LiAlO_2$-carbonate|Co_3Mo_3N-Ag, N_2. The cathode chamber was fed with oxygen-free N_2 (BOC Gas), whereas the anode chamber was fed with wet, highly pure H_2 (BOC, 99.995). Constant voltage was applied through the electrolytic cell over a period of 1 or 2 h. The ammonia synthesised at the cathode chamber was absorbed by 25 ml of dilute sulphuric acid (0.001 M). The concentration of NH_4^+ in the absorbed solution was analysed using Nessler's reagent (Aldrich). The produced ammonia was detected using an ammonia meter (Palintest 1000) and the rate of ammonia formation was calculated using Equation 2.9 (Section 2.4.2).

3.1.3 Results and discussion

3.1.3.1 X-ray analysis

Figures 3.2a-c show the XRD patterns of the ternary carbonate ($(Li/Na/K)_2CO_3$), commercial lithium aluminate ($LiAlO_2$) and $LiAlO_2$-carbonate composite electrolyte. As can be seen from Figure 3.2a, the ternary carbonates show a complicated phase composition. In the case of commercial $LiAlO_2$, the main detected peaks are indexed to γ-$LiAlO_2$ (JCPDS card no. 38-1464) with some unknown weak peaks (Figure 3.2b). The composite electrolyte is mainly composed of γ-$LiAlO_2$, Li_2CO_3 (JCPDS card no. 01-0996), $LiNaCO_3$ (JCPDS card no. 21-0954), $LiKCO_3$ (JCPDS card no. 34-1148), as shown in (Figure 3.2c). Figure 3.3 represents the XRD pattern of the Fe_3Mo_3N after nitridation. As can be seen, the most intense peaks match quite well with the cubic cell of Fe_3Mo_3N (JCPDS card no. 48-1408). A small peak at 37.4º was observed, however, indicating a minor impurity, which was identified as MoO_2 (JCPDS card no. 01-0615). Figure 3.4 shows the XRD pattern for the Co_3Mo_3N catalyst. A single phase of Co_3Mo_3N was obtained and was indexed as the cubic cell

of Co_3Mo_3N (ICSD code 162273).The crystallite sizes of the nitride catalysts were in the range of 29 nm, estimated from Sherrer's formula (Equation 2.3).

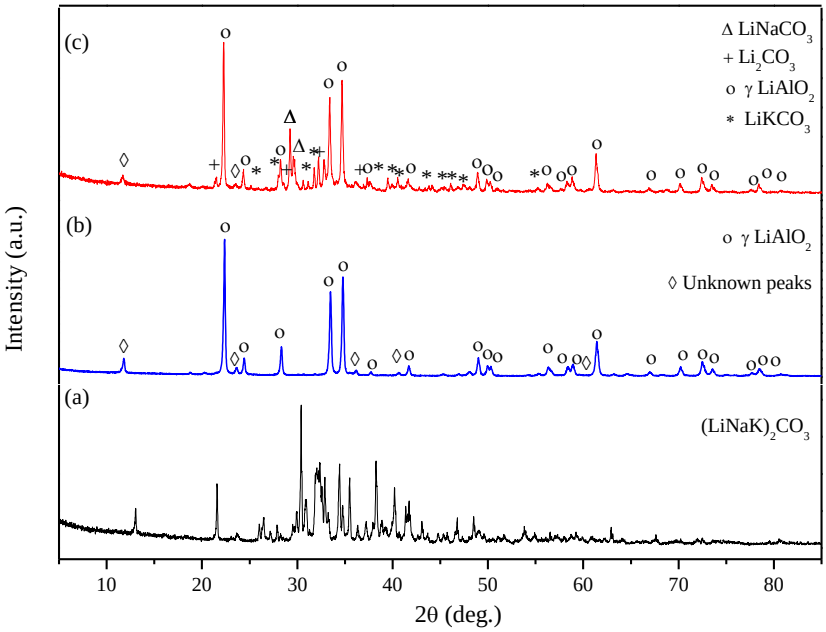

Figure 3.2 Powder X-ray diffraction pattern of (a) $(Li/Na/K)_2CO_3$; (b) $LiAlO_2$; (c) $LiAlO_2$-carbonate composite electrolyte

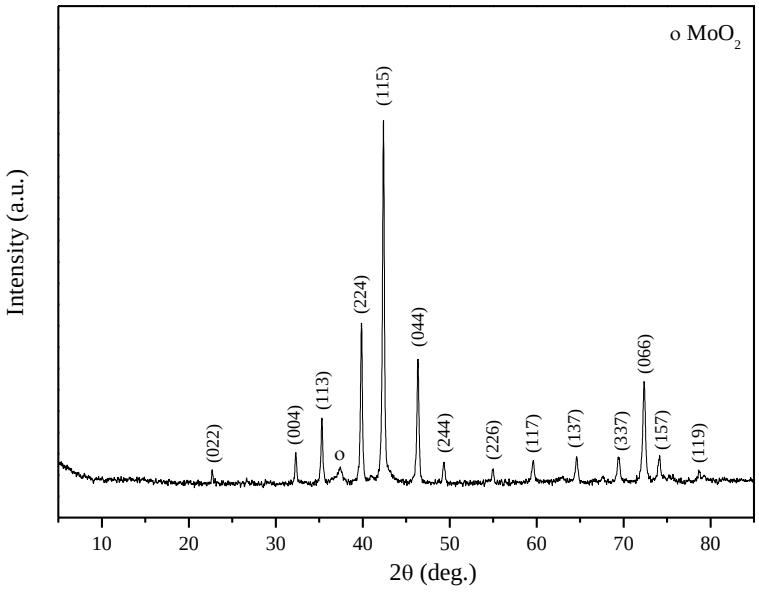

Figure 3.3 Powder X-ray diffraction pattern of Fe_3Mo_3N, after nitridation

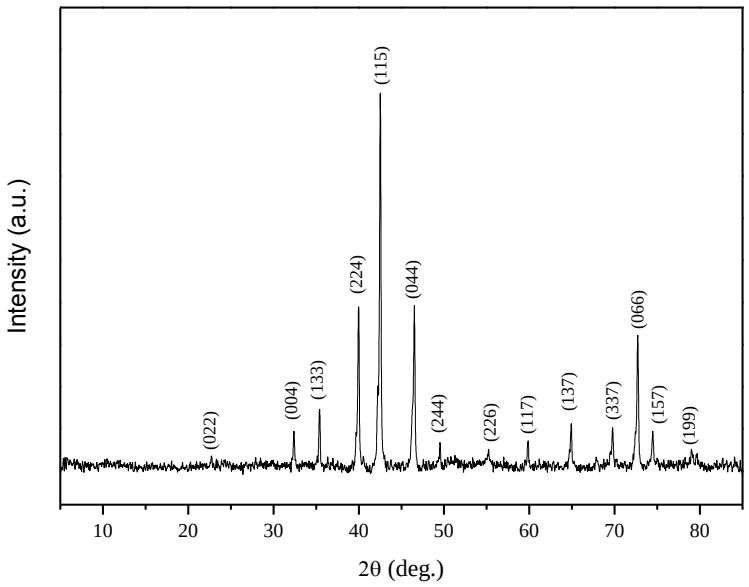

Figure 3.4 Powder X-ray diffraction pattern of Co_3Mo_3N

3.1.3.2 SEM analysis

The microstructures of Co_3Mo_3N and Fe_3Mo_3N catalysts were investigated by SEM, as shown in Figure 3.5. Figure 3.5a represents the morphology of Co_3Mo_3N at × 4000 magnification, showing rod-like particles with many void spaces. Figure 3.5b shows that Fe_3Mo_3N (× 30000 magnification) consists of homogenously-distributed nano-sized particles.

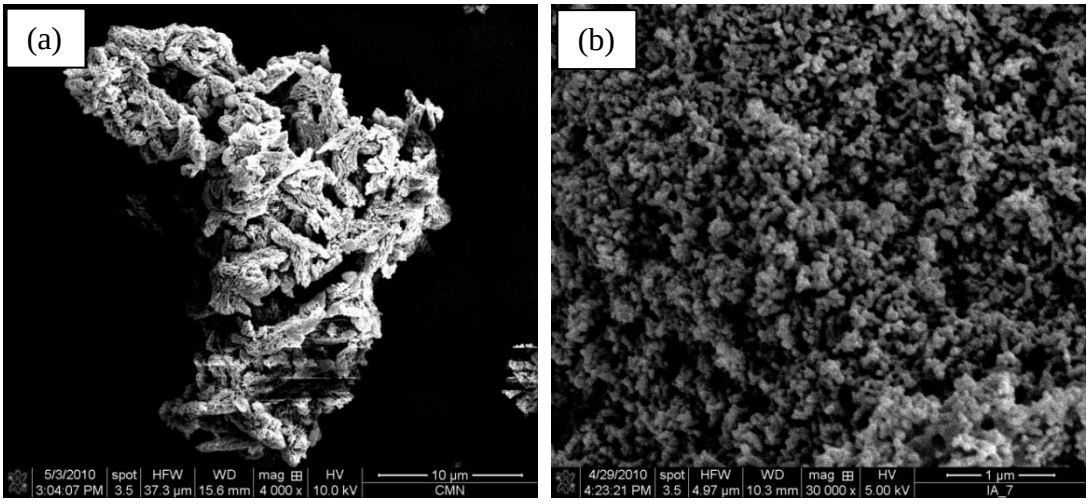

Figure 3.5 SEM images of the nitride based catalysts: (a) Co_3Mo_3N; (b) Fe_3Mo_3N

3.1.3.3 Thermal analysis

Figure 3.6 represents TGA/DSC curves of the ternary carbonate ($(Li/Na/K)_2CO_3$ 43.5:31.5:25 mol %) in air atmosphere. Upon heating, there was no significant weight loss observed from room temperature to 400 ºC. By further heating to 800 ºC, weight loss, accompanied by a strong endothermic peak at ~ 402 ºC, was observed, which was due to the melting point of the ternary carbonate (~ 400 ºC) [235]. Upon cooling, a strong exothermic event was observed at 380.34 ºC, which can be attributed to the solidifying of the ternary carbonate. In addition, there was a total weight loss of ~ 6.98 %. This could be related to the partial decomposition of carbonate [171].

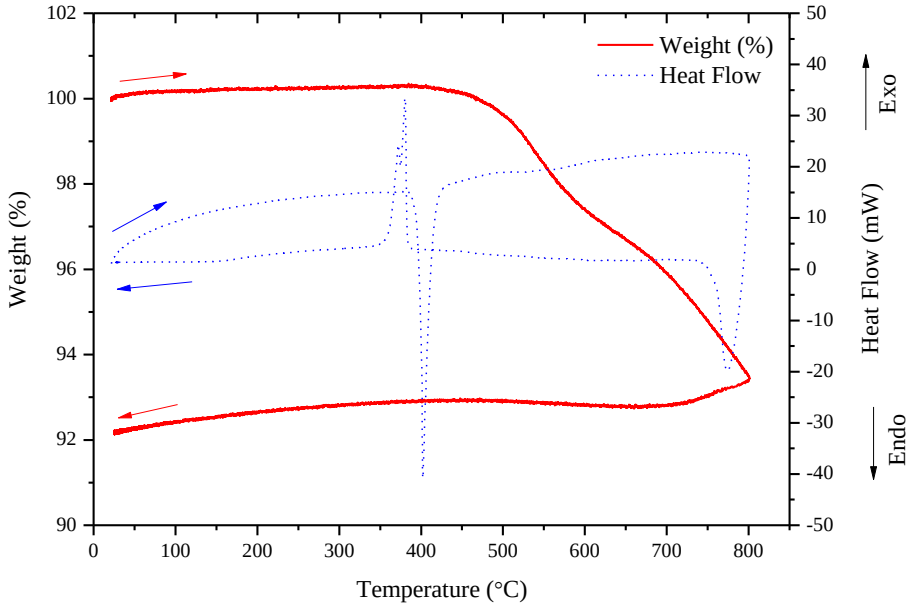

Figure 3.6 TGA-DSC curve of the ternary carbonate $(Li/Na/K)_2CO_3$ (43.5:31.5:25 mol %) in air atmosphere

The thermal behaviour of $LiAlO_2$-carbonate composite electrolyte was investigated in different atmospheres (air, O_2 and 5% H_2-Ar), as shown in Figure 3.7. It is to be noted that almost similar behaviour was observed for the composite electrolyte in each of the atmospheres under investigation. Upon heating, at least two endothermic peaks, accompanied by several stages of weight losses, depending on the atmosphere used, were observed, from room temperature to 250 ºC. This could be

attributed to the loss of adsorbed water. Between 300-600 ºC, endothermic peaks were observed at 402.44, 403.02 and 402.60 ºC, in air, O_2 and 5% H_2-Ar respectively, which are in good agreement with the melting point of the ternary carbonate, as described previously. Upon cooling, a small endothermic peak was observed at 511.34, 512.44 and at 509.53 ºC, when the sample was measured in air, O_2 and 5% H_2-Ar respectively. In addition, only one strong exothermic event was observed on cooling, at 386.28 and 378.03 ºC for air and O_2 respectively. In the case of 5% H_2-Ar, two exothermic peaks can be noticed, a strong peak at 379.88 and another small one at 305.20 ºC. These strong exothermic peaks correspond to recrystallisation of the ternary carbonate. Moreover, the total weight loss was approximately 3 % under all atmospheres which could be related to the partial decomposition of the carbonates. This slight weight change showing a good stability of the $LiAlO_2$-carbonate composite electrolyte. In addition, the observed peak at ~ 520 ºC upon cooling is not related to a phase change and it is due to the fact the sample was heated and cooled directly without a dwelling step as described in Chapter 5 (Figure 5.6b). Figures 3.8a-c show the XRD patterns of the composite electrolyte after the thermal analysis in different atmospheres (air, O_2 and 5% H_2 respectively). As can be seen, the composite electrolyte retains the same pattern observed before thermal analysis (Figure 3.2c) and no new phase was formed.

(a)

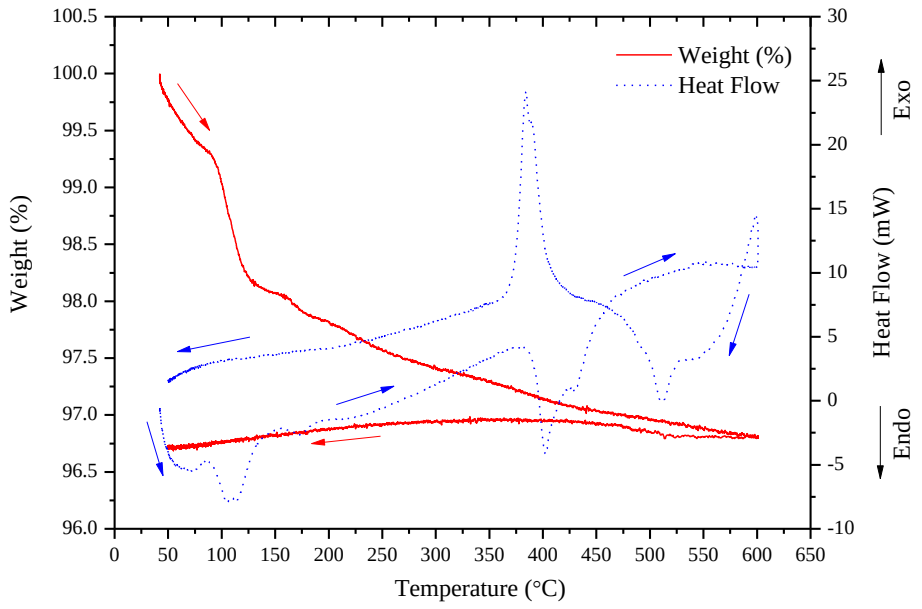

(b)

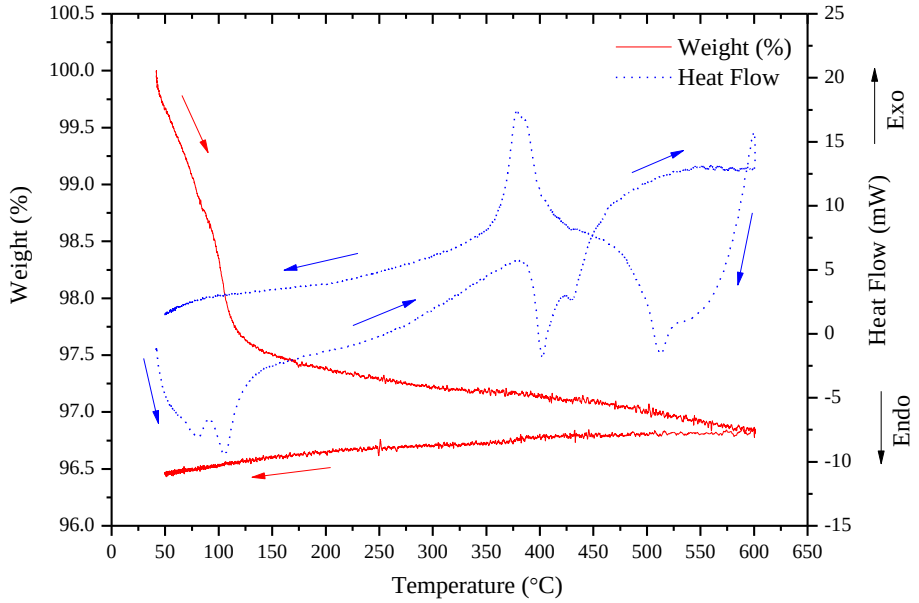

(c)

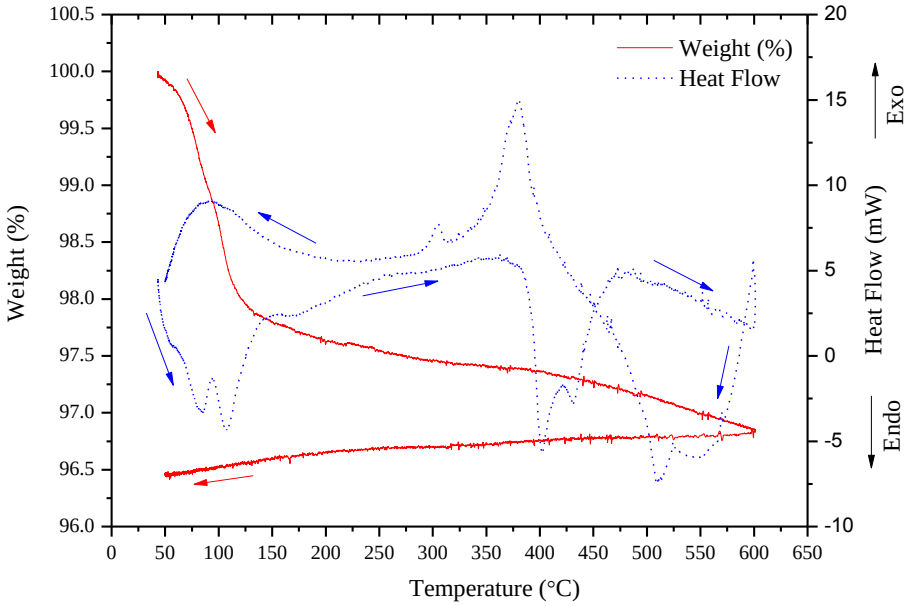

Figure 3.7 TGA-DSC curve of $LiAlO_2$-carbonate composite electrolyte: (a) in air; (b) in O_2; (c) in 5% H_2-Ar

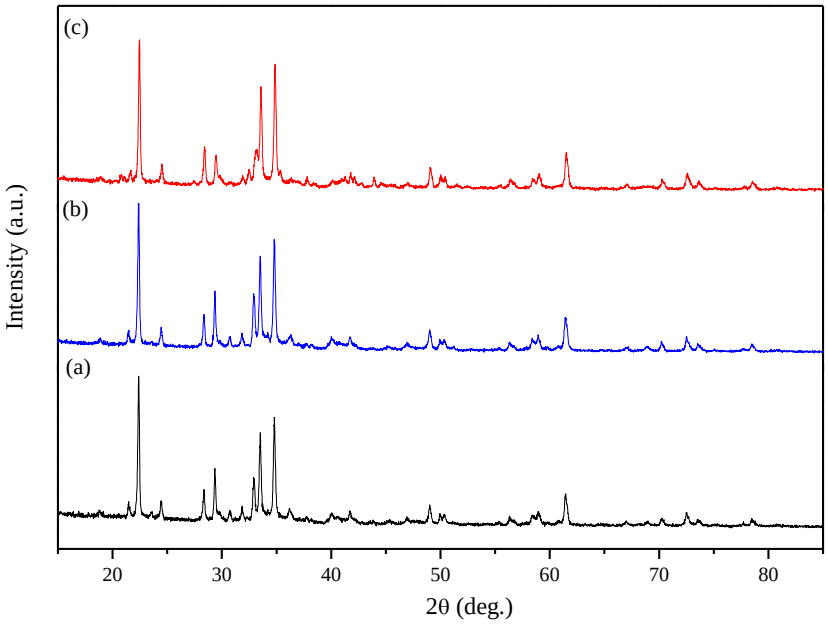

Figure 3.8 XRD pattern of $LiAlO_2$-carbonate after thermal analysis at 600 ºC in different atmospheres: (a) air; (b) O_2; (c) 5% H_2-Ar

3.1.3.4 The ionic conductivity of the composite electrolyte

The conductivity of the composite electrolyte was measured by AC impedance spectroscopy within the temperature range of 600-300 ºC. Figure 3.9 shows the typical impedance plots of the composite electrolyte at 500 ºC in three different atmospheres (air, O_2 and 5% H_2-Ar). As can be seen, in all atmospheres, only small part of the high frequency semicircle can be resolved which is attributed to the electrolyte contribution (Figure 3.9b). At low frequency, large depressed semicircles related to electrode contribution are observed in all cases. The low frequency semicircle is usually large because the barrier between the electronic conduction in the electrode and the ionic conduction in the electrolyte [155, 156]. The high frequency intercept with real axis was used to calculate total resistance value.

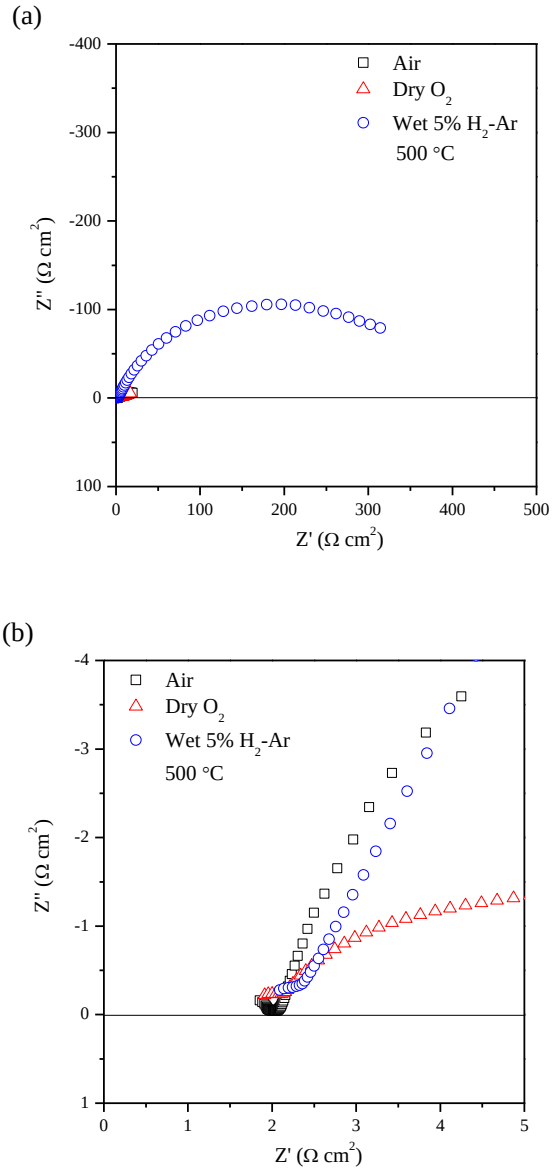

Figure 3.9 (a) Impedance spectra of $LiAlO_2$-carbonate under different atmospheres; (b) enlarged spectra

The AC conductivity of the composite electrolyte in three different atmospheres (air, dry O_2 and wet 5% H_2-Ar) as function of temperature is shown in Figure 3.10. As can be seen, the ionic conductivities of the composite electrolyte increase with increasing the operating temperature in all atmospheres under investigation. In addition, it can be clearly noticed that the conductivities changed at two different regions below and above ~ 400 ºC, which is the melting point of the ternary carbonate ($(Li/Na/K)_2CO_3$) [235]. This conductivity jump phenomenon above the

carbonate melting point has also been observed for doped ceria-ternary carbonate composite (SDC-$(Li/Na/K)_2CO_3$) [172], doped ceria-binary carbonate composite (e.g. SDC- or GDC-$(Li/Na)_2CO_3$) [165, 253] and non-ceria-binary carbonate composite (e.g. $LiAlO_2$- or LSGM-$(Li/Na)_2CO_3$) [177, 234].

Within the temperature range 600-400 ºC, the total conductivities were 0.215-0.048 S cm^{-1}, 0.218-0.037 S cm^{-1} and 0.217-0.047 S cm^{-1} in air, dry O_2 and wet 5% H_2-Ar respectively. It is well known that $LiAlO_2$ is an insulator [177]; therefore the ionic conduction in $LiAlO_2$-carobonate composite is likely to be due the composite effect. The apparent activation energies (E_a) of the composite electrolyte at high temperature (600-400 ºC) under different atmospheres were extracted from the slope of each series of points in the Arrhenius plots of conductivity, as shown in the inset of Figure 3.10. The activation energies were found to be 0.35(5) eV, 0.37(9) eV and 0.45(7) eV for the composite electrolyte in air, dry O_2 and wet 5% H_2-Ar respectively.

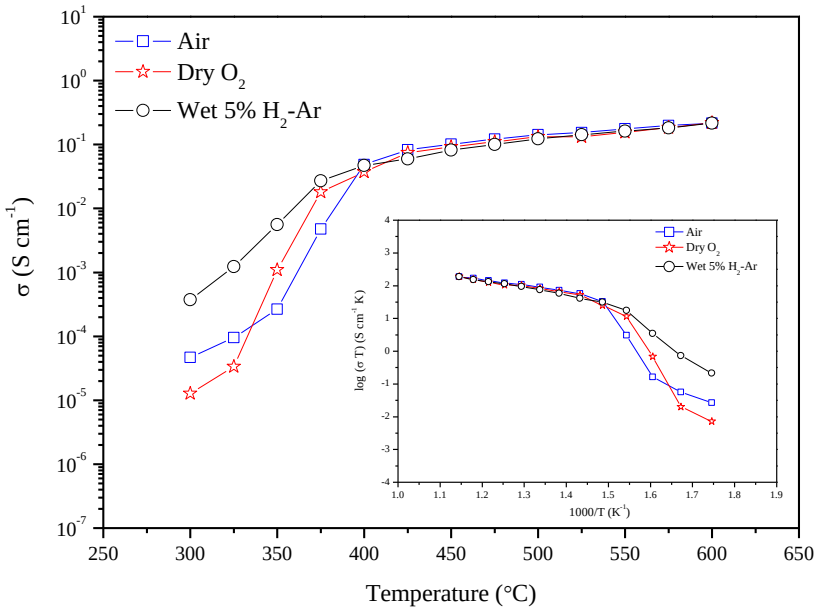

Figure 3.10 AC conductivity plot against temperature of $LiAlO_2$-$(Li/Na/K)_2CO_3$ composite electrolyte in air, dry O_2 and wet 5% H_2-Ar

As mentioned above, enhancement in the ionic conductivities has been observed above the melting point of the ternary carbonate. At high temperature, the ternary

carbonate in the composite will melt, which greatly enhances the mobility of both anions and cations, leading to superionic conduction. This means that all mobile ions (i.e. Li^+, Na^+, K^+, O^{2-}, H^+, HCO_3^- and CO_3^{2-}) contribute to the overall measured ionic conductivity and the contribution of H^+ or O^{2-} cannot be distinguished [177]. Therefore, 4-probe DC measurement is preferred to measure the contribution of these ions (H^+ and O^{2-}) while the other ions are blocked at the electrodes. In addition, it has been demonstrated that, during the electrolysis, only H^+ or O^{2-} are transported through the doped ceria-carbonate composite electrolyte, depending on the mode of operation (i.e. H^+ or O^{2-} conduction in the electrolyte) and the other mobile ions (i.e. Li^+, Na^+, K^+, HCO_3^- and CO_3^{2-}) are blocked at the electrodes [180]. Similar behaviour is expected in the case of electrochemical of ammonia synthesis in an electrolytic cell based on $LiAlO_2$-carbonate composite electrolyte, in which only protons will be transported through the electrolyte, whereas other mobile ions will be blocked.

At low temperature (375-300 ºC), the ionic conductivities of the composite electrolyte dropped significantly and were found to be 0.005-4.653 × 10^{-5}, 0.018-1.235 × 10^{-5} and 0.027-3.719 × 10^{-4} S cm^{-1} in air, dry O_2 and wet 5% H_2-Ar respectively. This could be due to the fact that the conducting ions are less mobile below the melting point of the carbonates, leading to low ionic conductivities in the region. It is also to be noted that, below the carbonate melting point, the conductivities of the composite electrolyte in wet 5 % H_2-Ar were higher than those obtained in air and dry O_2. This could be due to the fact that proton conduction can be easily activated at low temperature, compared to oxygen-ion conduction [169, 180].

It has been reported that the conductivity enhancement of the composites or two phase system occurs via the interface at which the ionic transport is fast [254]. Unlike doped ceria-carbonate composite electrolytes (e.g. SDC-carbonate), in which O^{2-} could be conducted through both the SDC phase and the interface between the two phases, lithium aluminate ($LiAlO_2$) is not an oxygen ion conductor and the O^{2-} conduction in the $LiAlO_2$-$(Li/Na/K)_2CO_3$) composite is likely to occur only through

the interface between the two phases (i.e. $LiAlO_2$ and carbonate). This indicates that the O^{2-} conduction mechanism in $LiAlO_2$-carbonate composite is different from that in the doped ceria-carbonate composite electrolytes [177]. On the other hand, the H^+ conduction in the $LiAlO_2$-$(Li/Na/K)_2CO_3$) composite is similar to that of doped ceria-carbonate composites, which is believed to occur through the interface between the two phases (i.e. the oxide and carbonate). In H_2 containing atmosphere, some bicarbonates (HCO_3^-) may be formed through the reaction between the carbonates (CO_3^{2-}) and H_2. Thus, protons may be transported between CO_3^{2-} ions in the form of HCO_3^-, which may cause proton conduction [169, 177].

3.1.3.5 Synthesis of ammonia at different temperatures

Figures 3.11a and b show the electrolytic cell performance stabilities during the synthesis of ammonia at different temperatures (400-450 °C) with an applied voltage of 0.8 V for two electrolytic cells based on Fe_3Mo_3N-Ag and Co_3Mo_3N-Ag composite cathodes respectively. It was noticed that both electrolytic cells demonstrated almost stable performance at all temperatures under investigation. In the case of Fe_3Mo_3N-Ag, it is obvious from Figure 3.11a that the generated current densities increased with an increase in the cell operating temperature and reached a maximum value of 4.97 mA/cm^2 at 450 °C, as listed in Table 3.1. This increase in current densities with temperature could be also speculated to be due to the increase in the proton conductivity of the working electrolyte. This means that more protons were transported through the electrolyte to the cathode surface. In the case of, the electrolytic cell based on Co_3Mo_3N-Ag, at low operating temperature (400 °C) the generated current density decreased significantly during the first 60 min, after which almost stable current was generated as shown in Figure 3.11b. At a higher operating temperature (425 and 450 °C), the electrolytic cell exhibited a stable performance and generated almost the same current density (~ 3.2 mA/cm^2), as listed in Table 3.1.

(a)

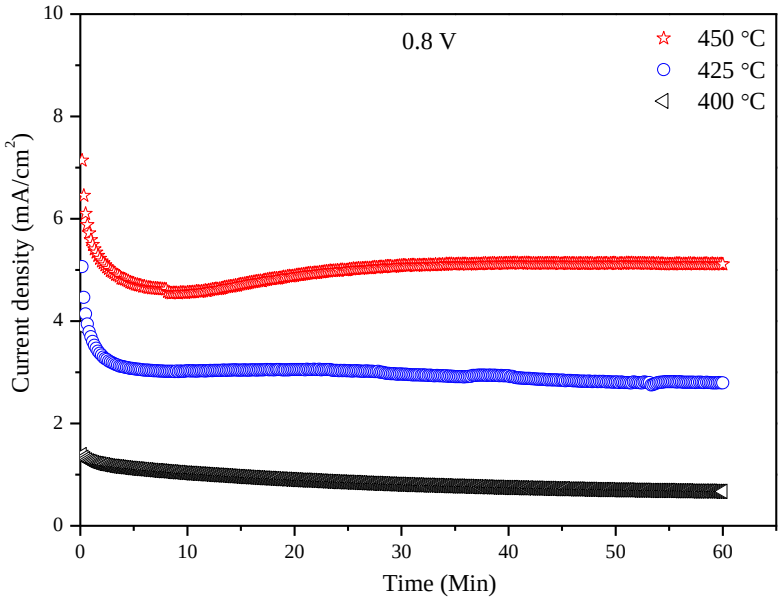

(b)

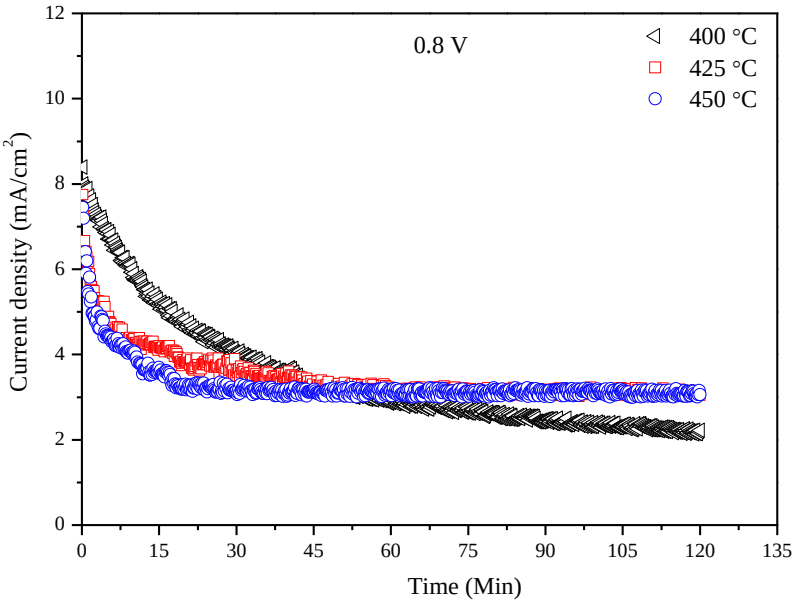

Figure 3.11 Electrolytic cell performance stability at 400, 425 and 450 °C at 0.8 V: (a) Fe_3Mo_3N-Ag cathode composite; (b) Co_3Mo_3N-Ag composite cathode

Figures 3.12a and b show the AC impedance spectra for two electrolytic cells based on Fe_3Mo_3N-Ag and Co_3Mo_3N-Ag composite cathodes respectively, at different temperatures (400-450 °C) under open circuit conditions. It should be noted that two depressed semicircles were observed in both cases, suggesting that there are at least two electrode processes. The impedance data were fitted using Zview software with an equivalent circuit model of the type LRs(R1CPE1)(R2CPE2), as shown in Figure 3.12c. Here, L represents the inductance caused by the equipment and wire connections, Rs is the series resistance, which comprises the resistances of the electrolyte, electrode materials and the contact resistance at the electrode/electrolyte interface; the two components (R1CPE1) and (R2CPE2) in series are associated with the electrode processes at high and low frequency arcs respectively. R1 and R2 represent the polarisation resistance while CPE is a constant phase element which represents a non-ideal capacitor (C).

In both electrolytic cells, the characteristic capacitances for the high frequency semicircles (HF) were found to be in the range of 10^{-5}-10^{-4} F/cm^2, which could be attributed to the charge transfer processes at the electrode/electrolyte interface. The low frequency semicircle (LF) with the associated capacitances of 10^{-4}-10^{-2} F/cm^2 could be ascribed to the mass transfer processes at the electrode [46, 255, 256]. In addition, the Rs resistance, which mainly related to the ohmic resistance of the electrolyte, decreased significantly when increasing the cell operating temperature from 400 to 450 °C. This could be speculated as pertaining to the improvement in ionic conductivity with increasing the electrolytic cell's operating temperature. However, the Rs values in the electrolytic cell based on the Co_3Mo_3N-Ag composite cathode were lower than those of the Fe_3Mo_3N-Ag composite cathode, which could be due to the contact resistance. With increasing the operating temperature of the electrolytic cell, there was also a significant decrease in the total polarisation resistance (Rp), which is the sum of R1 and R2 which could be due to the improvement in the catalytic activity of the cathode with temperature. However, the Rp values in the electrolytic cell based on the Co_3Mo_3N-Ag composite cathode were lower than those of the Fe_3Mo_3N-Ag composite cathode. For example, at 450 °C, the Rp value for Co_3Mo_3N-Ag was 31.52 Ω cm^2 while that for Fe_3Mo_3N-Ag was 37.47 Ω cm^2. This indicates a better activity of Co_3Mo_3N-Ag compared to Fe_3Mo_3N-Ag.

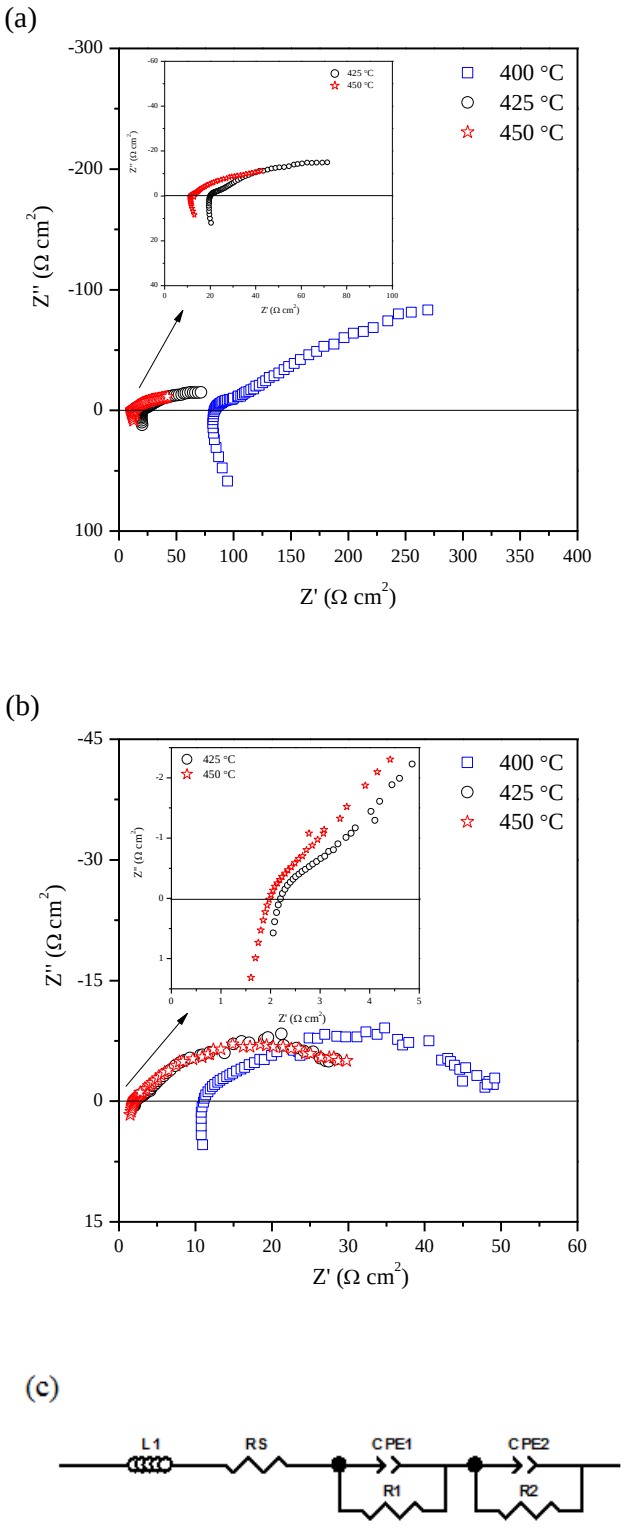

Figure 3.12 Impedance spectra under open circuit conditions at 400-450 °C: (a) Fe3Mo3N-Ag composite cathode; (b) Co_3Mo_3N-Ag composite cathode; (c) An equivalent circuit for the impedance data

Figures 3.13a and b represent the effect of cell operating temperature on the rate of ammonia production in two electrolytic cells based on Fe_3Mo_3N-Ag and Co_3Mo_3N-Ag composite cathodes respectively. This effect was investigated by varying the operating temperature (400-450 °C) and keeping the cell voltage at constant value of 0.8 V over a period of 1 h or 2 h. The ammonia produced in the cathode chamber was absorbed by 25 ml of diluted sulphuric acid. When Nessler's reagent was added to the absorbed solution, its colour immediately changed to yellow. This indicates that NH_4^+ is present in the absorbed solution and thus that ammonia was successfully synthesised. In the case of the Fe_3Mo_3N-Ag system (Figure 3.13a), the rate of ammonia formation increased significantly with increasing electrolytic cell operating temperature and reached a maximum value of 1.88×10^{-10} mol s^{-1} cm^{-2} at 425 °C, at which the generated current density and the corresponding Faradaic efficiency were 2.96 mA/cm^2 and 1.84 % respectively. This increase in the ammonia formation rate could be ascribed to the increase of the proton conductivity of $LiAlO_2$-carbonate composite electrolyte as the cell operating temperature increased [115]. However, when the operating temperature was further increased to 450 °C, the rate of ammonia formation declined, although the electrolyte ionic conductivity increases with temperature. It could be speculated that this is due to the decomposition of ammonia, which dominates at high temperature [75]. In theory, the decomposition of ammonia may start at temperature above 175 ºC [11], but it was reported that ammonia starts to decompose at ~ 500 °C [257].

In the case of the Co_3Mo_3N-Ag composite cathode (Figure 3.13b), the rate of ammonia formation decreased slightly when the operating temperature was raised from 400 ºC to 425 ºC. Moreover, a significant increase in the rate of ammonia formation was obtained by further increasing the temperature to 450 ºC. The maximum rate was found to be 3.27×10^{-10} mol s^{-1} cm^{-2} at 450 ºC, at which the generated current density and the corresponding Faradaic efficiency were 3.21 mA/cm^2 and 2.95 % respectively, as listed in Table 3.1. This could also be ascribed to the protonic conductivity, which increases as the temperature is increased [115]. The NH_3 formation rate is in general one order of magnitude lower than the one reported by Li et al. [72] (3.09×10^{-9}) when Ag-Pd alloy was used as a cathode

catalyst, which could be related to the low electrocatalytic activity of Co_3Mo_3N for ammonia synthesis.

Table 3.1 lists the generated current densities and the corresponding Faradaic efficiencies for ammonia formation at different temperatures, using two electrolytic cells, based on either Fe_3Mo_3N-Ag or Co_3Mo_3N-Ag as cathode. It is to be noted that, in both cases, the Faradaic efficiency decreased with an increase in current generated. In addition, the best Faradaic efficiencies were found to be only 4.28 % and 2.95 %, at which the corresponding current densities were 0.85 mA/cm^2 and 3.21 mA/cm^2 for Fe_3Mo_3N-Ag and Co_3Mo_3N-Ag respectively. These low Faradaic efficiencies indicate that not all protons transported through the electrolyte to the cathode surface reacted with the adsorbed N_2 to form ammonia. This means that competitive hydrogen evolution reaction (HER) is the predominant process over the cathode surface [41, 70]. This reaction occurs according to Equation 3.1:

$$2H^+ + 2e^- \rightarrow H_2 \qquad \text{Equation 3.1}$$

(a)

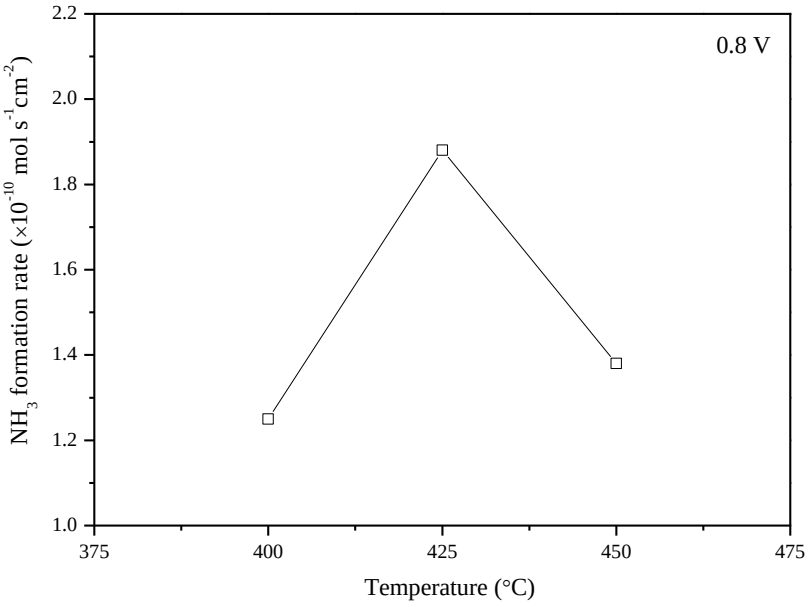

(b)

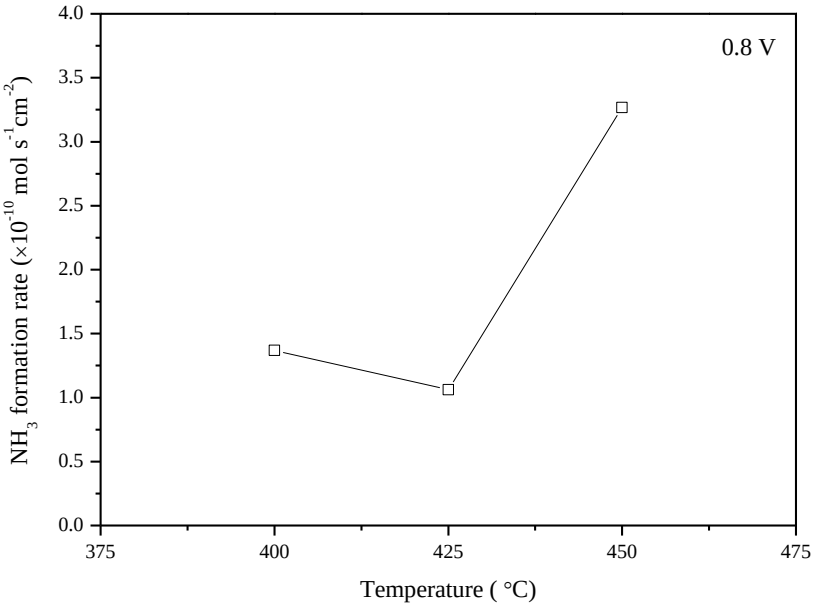

Figure 3.13 Dependence of ammonia formation rate on operating temperature: (a) Fe_3Mo_3N-Ag composite cathode; (b) Co_3Mo_3N-Ag composite cathode

Table 3.1 The corresponding current densities and Faradaic efficiencies of ammonia formation over Fe_3Mo_3N-Ag and Fe_3Mo_3N-Ag composite cathodes at different working temperatures and 0.8 V

Temperature (°C)	**Fe_3Mo_3N-Ag**		**Co_3Mo_3N-Ag**	
	Current density (mA/cm^2)	**Faradaic efficiency (%)**	**Current density (mA/cm^2)**	**Faradaic efficiency (%)**
400	0.85	4.28	2.53	1.57
425	2.96	1.84	3.24	0.95
450	4.97	0.80	3.21	2.95

3.1.3.6 Synthesis of ammonia at different applied voltages

Figures 3.14a and b represent the performance of two electrolytic cells based on Fe_3Mo_3N-Ag and Co_3Mo_3N-Ag at constant temperature and different applied voltages (0.4-1.2 V) respectively. It is important to note that the generated current

densities remain almost constant at all applied voltages, indicating a stable electrochemical process. In the case of Fe_3Mo_3N-Ag (Figure 3.14a), the generated current densities increased with applied voltage and the highest value of 2.96 mA/cm^2 was obtained when the cell operated with 0.8 V, as listed in Table 3.2. This indicates that more protons were transported through the electrolyte to the cathode. However, when the applied voltage was further increased (> 0.8 V), the generated current density decreased, which indicates the difficulty of transporting more H^+ through the electrolyte to the cathode. This could be due to the blocking effect of Li^+, Na^+ and K^+ ions. These positively charged ions will move under the presence of electric filed and accumulate at the cathode/electrolyte interface forming a layer, thus partially block the transfer of protons (H^+) and resulting in low current densities [258, 259]. In the electrolytic based on Co_3Mo_3N-Ag, the generated current density increased with an increase in the applied voltage and reached its highest value with an applied voltage of 1.2 V, as shown Figure 3.14b and listed in Table 3.2. It could be speculated that this increase in the current density with the voltage could be due to more protons being transported to the cathode as described above.

(a)

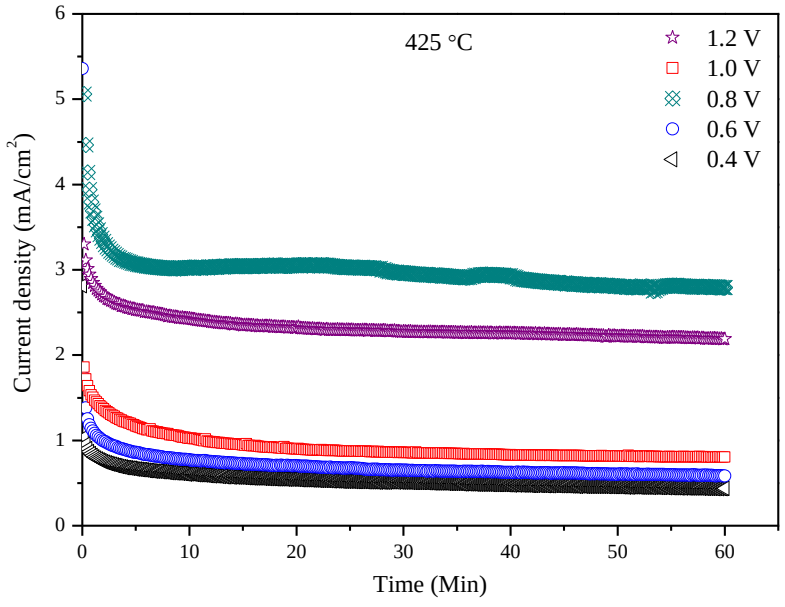

(b)

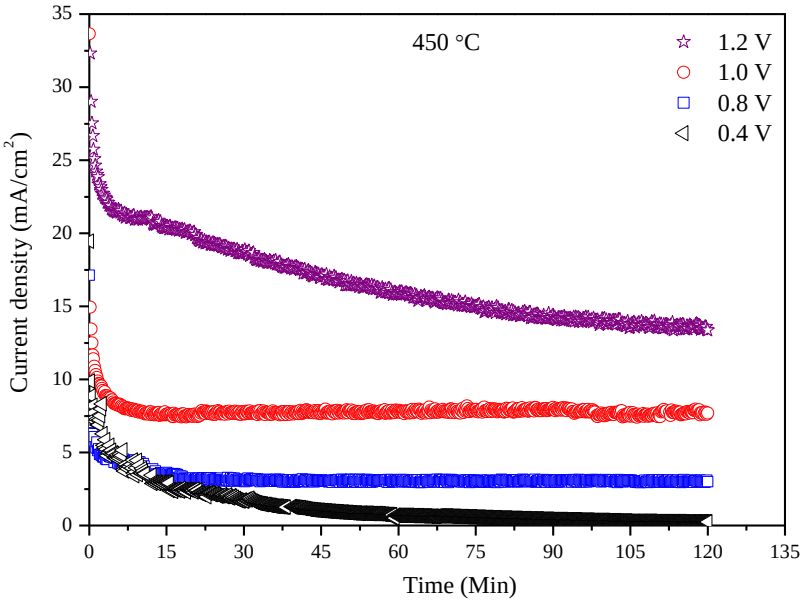

Figure 3.14 Electrolytic cell performance stability under different applied voltage at (a) Fe_3Mo_3N-Ag composite cathode; (b) Co_3Mo_3N-Ag composite cathode

To investigate the effect of the applied voltage on the rate of ammonia formation, the operating temperature of the two electrolytic cells was kept at constant value and the applied voltage varied from 0.4 to 1.2 V, as shown in Figure 3.15. In both cells, the rate of ammonia production increased significantly with increasing the applied voltages and reached the maximum values when 0.8 V was applied, as shown Figures 3.15a and b. In the case of the Fe_3Mo_3N-Ag composite cathode, the highest rate of ammonia formation was found to be 1.88×10^{-10} mol s^{-1} cm^{-2} with an applied voltage of 0.8 V at 425 °C, as presented in Figure 3.15a. This rate corresponds to a Faradaic efficiency of 1.84 % at current density of 2.96 mA/cm^2, as listed in Table 3.2. For the Co_3Mo_3N-Ag composite cathode (Figure 3.15b), however, the maximum rate of ammonia production was much higher, 3.27×10^{-10} mol s^{-1} cm^{-2} with an applied voltage of 0.8 V at 450 ºC, at which the generated current density and Faradaic efficiency were 3.21 mA/cm^2 and 2.95 % respectively, as listed in Table 3.2. However, by further increasing the applied to values above 0.8 V, there was a significant decrease in the rates of ammonia formation which reached the lowest value when 1.2 V was applied. This could be attributed to the competitive adsorption

between N_2 and H_2 over the cathode surface. Moreover, these low Faradaic efficiencies indicate that there is more than one reaction occurring over the cathode surface and that the competitive hydrogen evolution reaction is the dominant one [41, 70].

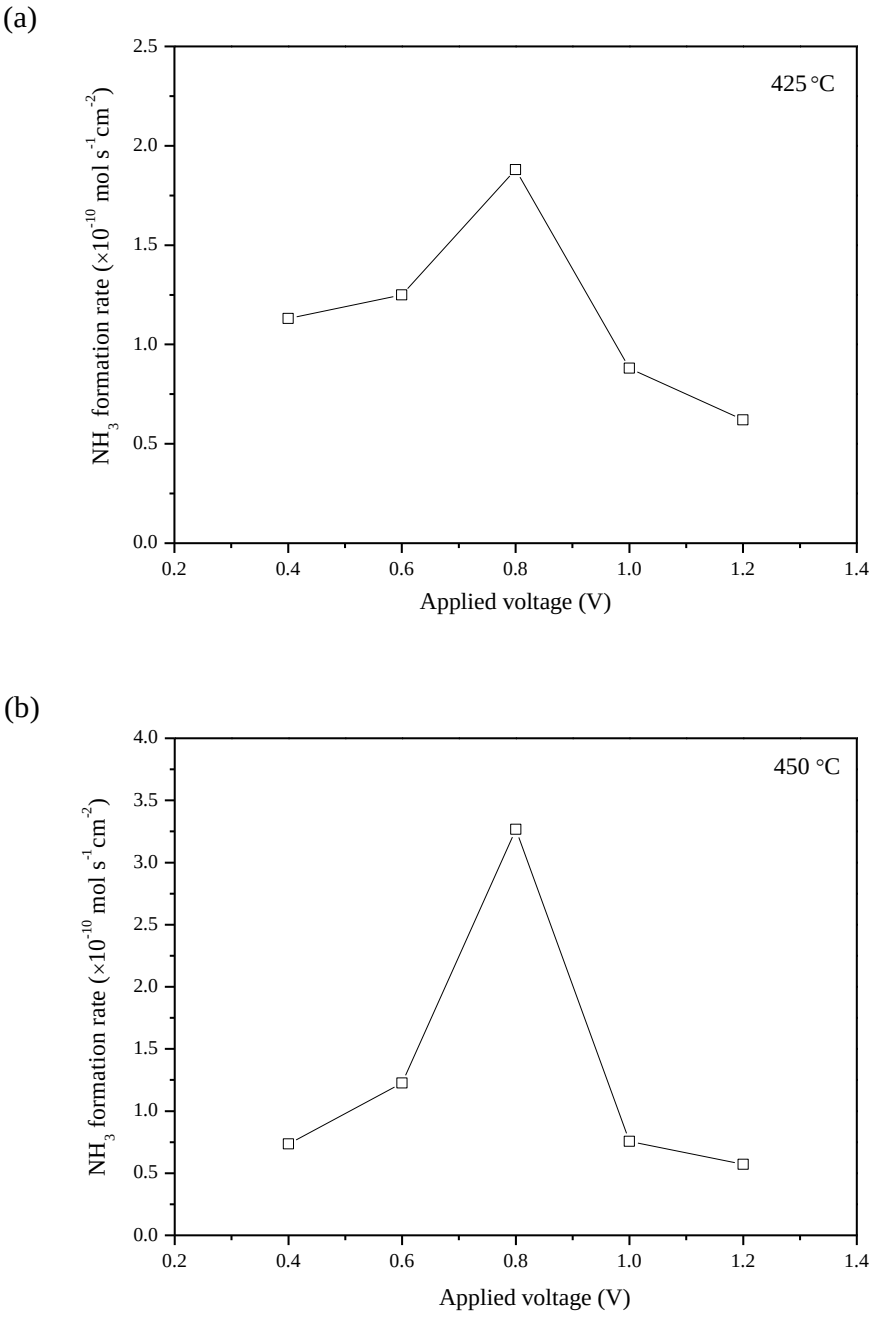

Figure 3.15 Dependence of the rate of ammonia formation on the applied voltage: (a) Fe_3Mo_3N-Ag composite cathodes; (b) Co_3Mo_3N-Ag composite cathodes

Table 3.2 The corresponding current densities and Faradaic efficiencies of ammonia formation over Fe_3Mo_3N-Ag and Co_3Mo_3N-Ag composite cathodes

Applied voltage (V)	Fe_3Mo_3N-Ag (425 °C)		Co_3Mo_3N-Ag (450 °C)	
	Current density (mA/cm^2)	Faradaic efficiency (%)	Current density (mA/cm^2)	Faradaic efficiency (%)
0.4	0.52	6.28	0.56	3.83
0.6	0.68	5.32	1.73	2.06
0.8	2.96	1.84	3.21	2.95
1.0	0.84	3.03	7.76	0.28
1.2	2.35	0.76	15.48	0.11

3.2 Ammonia synthesis based on $LiAlO_2$-$(Li/Na/K)_2CO_3$ composite electrolyte and spinel oxide type cathode

3.2.1 Introduction

Mixed transition metal oxides with the general formula AB_2O_4 are called spinels. These metal oxides take their name from the mineral spinel ($MgAl_2O_4$). Generally, A ions that occupy the tetrahedral sites are divalent cations (Fe^{2+}, Zn^{2+}, Co^{2+}, Ni^{2+}, Mn^{2+}, Mg^{2+}, Cd^{2+}, etc.), whereas B ions that occupy the octahedral sites are trivalent cations (Co^{3+}, Fe^{3+}, Cr^{3+}, Al^{3+}, Mn^{3+}, Ga^{3+} etc.) [192, 260, 261]. When spinels with the AB_2O_4 formula adopt the inverse-spinel structure, their formula can be written as $B(AB)O_4$, which means that half of the B ions occupy the tetrahedral sites whereas the other half share the octahedral sites with A ions. $Fe(MgFe)O_4$ is an example of an inverse-spinel [262].

In the literature, these materials have been investigated for a wide range of applications due to their optical, magnetic, electric, gas sensing, and catalytic properties [263-266]. In addition, the spinel-type oxides are also interesting owing to their electrocatalytic activities. Thus, these materials have been investigated as potential electrodes for many reactions, including the oxygen evolution reaction (OER) [267, 268], the electrochemical reduction of NO_x and the oxygen reduction reaction (ORR) [269] and have also been proposed as alternative anode materials to replace the precious metal-based catalysts for methanol oxidation in a direct methanol fuel cell (DMFC) [270].

Cobalt-iron spinel oxides ($Co_xFe_{3-x}O_4$) are regarded as promising materials for application in many different technologies. In addition to the above mentioned properties, these materials are chemically and thermally stable [271]. These mixed transition metal oxides, in particular $CoFe_2O_4$, have exhibited great potential for application in gas sensors [272], heterogeneous catalysis, such as removal of NO_x [266] and ammonia synthesis [273-275], and electrocatalysis, such as electrochemical reduction of NO_x [276] etc. Based on those properties, it is expected that $CoFe_2O_4$ would be a very promising electrocatalyst (cathode) in ammonia synthesis.

3.2.2 Experimental

3.2.2.1 Catalyst preparation

A $CoFe_2O_4$ spinel catalyst was prepared by a co-precipitation method. The oxide precursor was obtained by mixing an aqueous solution of cobalt nitrate ($Co(NO_3)_2 \cdot 6H_2O$, Sigma Aldrich) with an aqueous solution of iron nitrate ($Fe(NO_3)_3 \cdot 9H_2O$, Alfa Aesar) at the molar ratio Co:Fe of 1:2. A dilute ammonia solution was then slowly added into the mixed solution under stirring, until the pH value was about 7. A brown precipitate was obtained after vacuum filtration, washed several times with deionised water and ethanol, and then dried at 100 °C overnight. The powder obtained was calcined in air at 450 °C for 4 h with a heating/cooling rate of 2 °C min^{-1}. Finally, an ultrafine powder of $CoFe_2O_4$ was obtained.

3.2.2.2 Fabrication of the single cell for ammonia synthesis

An electrolyte supported cell was fabricated by uniaxially dry-pressing the composite electrolyte ($LiAlO_2$/carbonate 50:50 wt %) into a 19 mm pellet under 121 MPa. The green pellet was sintered in air at 600 °C. The composite cathode was prepared by mixing the $CoFe_2O_4$ catalyst with Ag paste to increase its conductivity and adhesion on the electrolyte surface. Then the $CoFe_2O_4$-Ag composite was pasted on one side of the composite electrolyte as cathode, with surface area 0.45 cm^2. Ag-Pd (Johnson Matthey, 20 wt % Pd) paste was pasted on the other side as the anode. Ag wires were used as output terminals for both electrodes.

3.2.2.3 Ammonia synthesis

The fabricated single cell was placed in a self-designed double-chamber reactor. The electrolytic cell used for ammonia synthesis was constructed as follows: wet H_2, Ag-Pd|$LiAlO_2$-Carbonate|$CoFe_2O_4$-Ag, dry N_2, NH_3. The cathode chamber was fed with oxygen-free N_2 (BOC Gas), whereas wet highly pure H_2 (BOC, 99.995) was fed into the anode chamber. Constant voltage was imposed through the cell over a period

of 2 h. The ammonia synthesised in the cathode chamber was absorbed by 25 ml of dilute sulphuric acid (0.001 M). The ammonia formed was detected as described in Section 3.1.2.6 and the rate of ammonia formation was calculated using Equation 2.9.

3.2.2.4 Materials characterisation

X-ray diffraction (XRD), TGA/DSC and the microstructure analysis of the $CoFe_2O_4$ catalyst were carried out following the same procedures and instruments as described in Section 3.1.2.3.

3.2.3 Results and discussion

3.2.3.1 XRD analysis

Single-phase spinel oxide with the form $CoFe_2O_4$ was obtained when the precursor was calcined in air at 450 °C for 4 h. The XRD pattern is in good agreement with the standard pattern for cobalt ferrite with cubic spinel structure (JCPDS card no. 22-1086) and the cell constant of a = 8.3592 Å (Figure 3.16). The crystallite size of $CoFe_2O_4$ is about 15.93 nm, estimated from Sherrer's formula (Equation 2.3). Figures 3.17a-c show the XRD patterns of the commercial $LiAlO_2$ and carbonate-$LiAlO_2$ composite electrolyte before and after the ammonia synthesis, respectively. As can be seen from Figures 3.17b and c, there was no change in the composite electrolyte composition before and after ammonia synthesis. Furthermore, only peaks corresponding to the composite electrolyte (γ-$LiAlO_2$, Li_2CO_3, $LiNaCO_3$ and $LiKCO_3$) and $CoFe_2O_4$-Ag were observed, indicating that the $LiAlO_2$-carbonate electrolyte is stable and that there was no obvious reaction between $CoFe_2O_4$ cathode and the composite electrolyte.

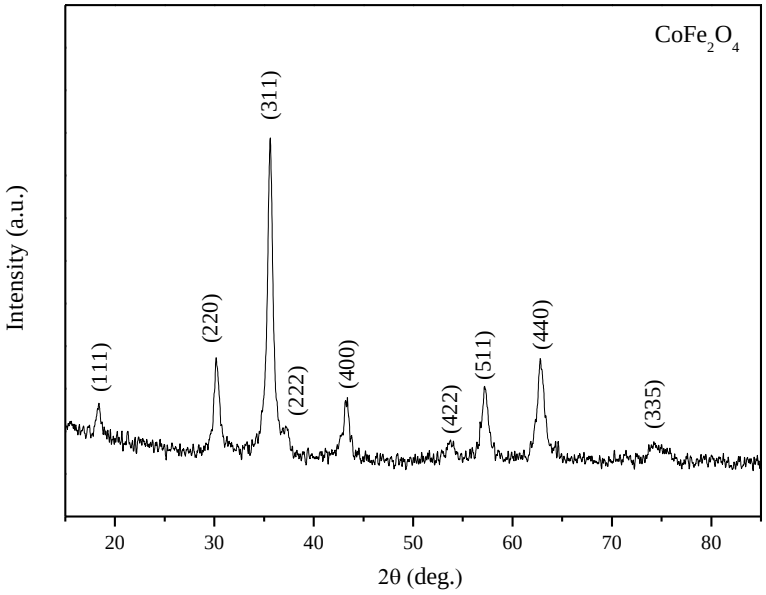

Figure 3.16 Powder X-ray diffraction pattern of $CoFe_2O_4$ calcined at 450 °C for 4 h

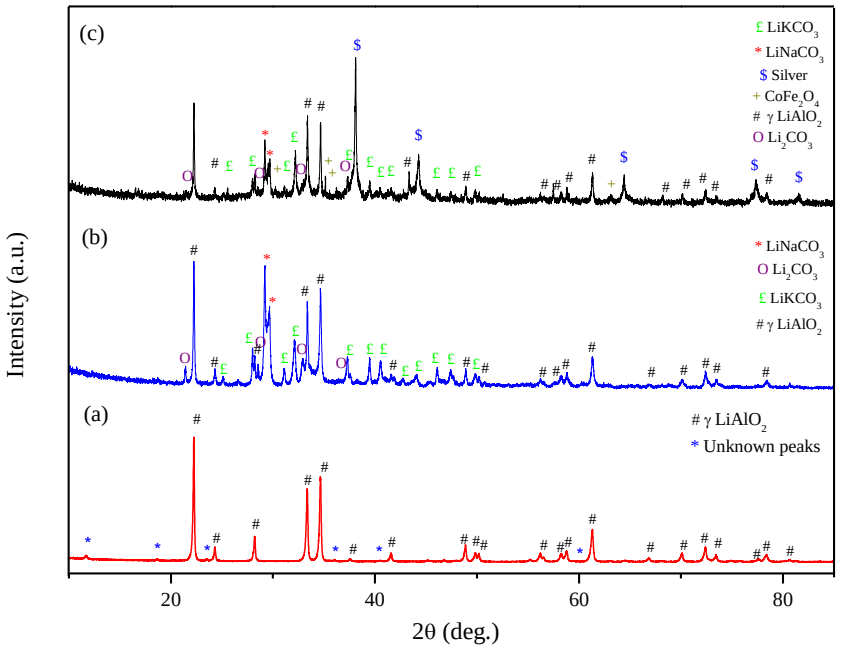

Figure 3.17 Powder X-ray diffraction patterns of (a) γ-$LiAlO_2$; (b) $LiAlO_2$-carbonate before ammonia synthesis; (c) $LiAlO_2$-carbonate after ammonia synthesis

3.2.3.2 SEM analysis

The microstructure of $CoFe_2O_4$ powder was investigated by SEM. Figures 3.18a and b show the SEM images of the $CoFe_2O_4$ catalyst at ×20,000 and at ×40,000 magnification, respectively. After calcination at 450 °C for 4 h, the microstructure of $CoFe_2O_4$ consists of large grains surrounded by small, homogenous primary grain particles with particle size 10-20 nm.

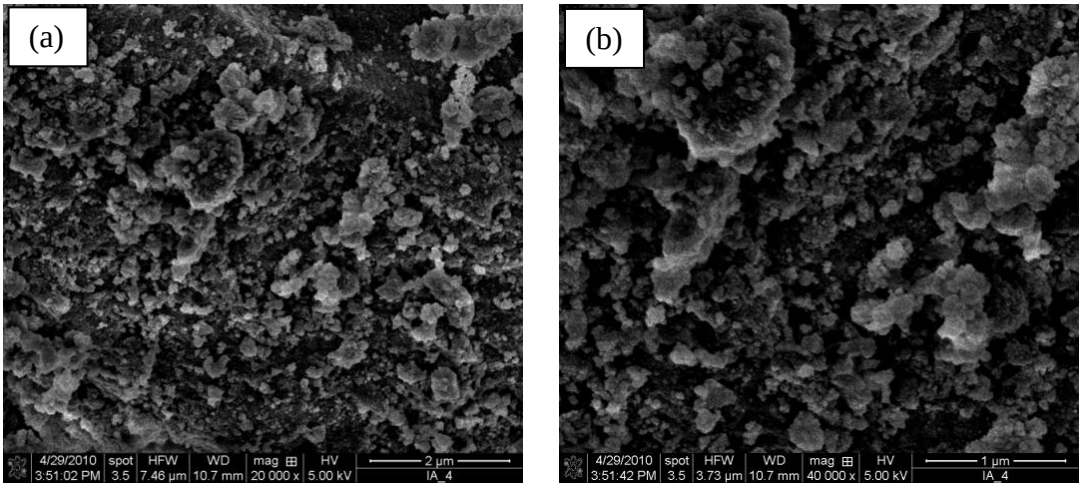

Figure 3.18 SEM images of $CoFe_2O_4$ calcined at 450 °C for 4 h. (a) at × 20000 magnification; (b) at × 40000 magnification

3.2.3.3 Thermal analysis

Figure 3.19 shows the TGA-DSC curves of $CoFe_2O_4$ in N_2 atmosphere from room temperature up to 500 °C, at a rate of 10 °C/min. Upon heating, the TGA trace shows a 0.4 % weight loss between room temperature and 500 °C, which is due to the desorption of water and adsorbed gases. In addition, there are no obvious thermal effects shown in the DSC curve, indicating that there is no observable phase transition and there is no reaction between $CoFe_2O_4$ and N_2. This suggests the thermal stability of $CoFe_2O_4$ cathode in N_2 within the measured temperature range. Figure 3.20b shows the XRD pattern of the $CoFe_2O_4$ catalyst after thermal analysis in N_2 atmosphere. As can be seen, the oxide retains the same spinel structure and

there are no extra peaks are observed, indicating the thermal stability of cathode under N_2 within the measured temperature range.

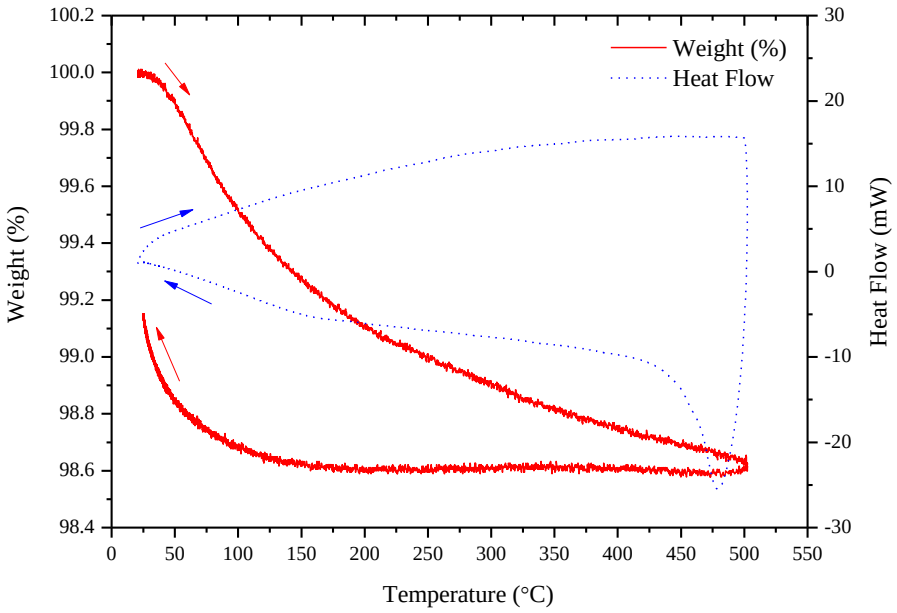

Figure 3.19 TGA-DSC curve of $CoFe_2O_4$ in nitrogen up to 500 ºC

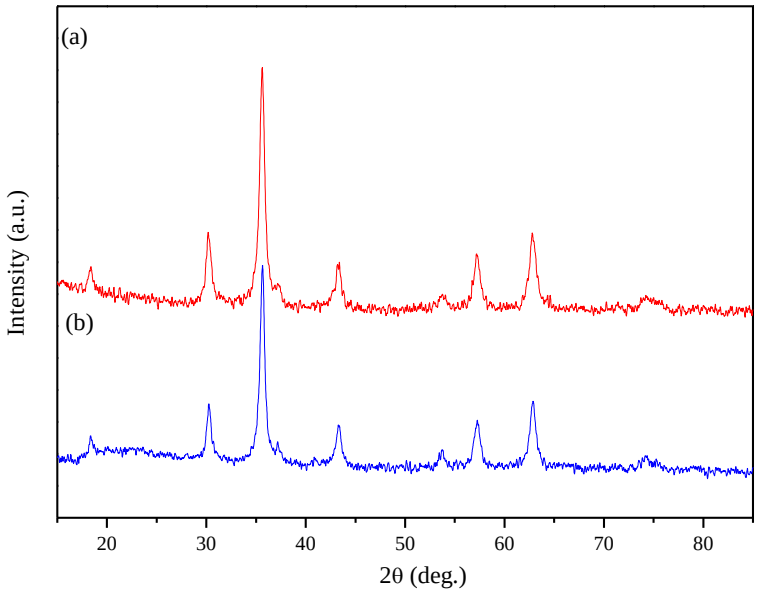

Figure 3.20 XRD pattern of $CoFe_2O4$: (a) before thermal analysis; (b) after thermal analysis in N_2 at 500 ºC

3.2.3.4 Ammonia synthesis at different temperatures

Figure 3.21 represents the electrolytic cell stability during the ammonia synthesis process at three operating temperatures, 400, 425 and 450 °C, respectively at 0.8 V over a 2 h period. As can be seen, at 400 °C, the generated current density dropped significantly, during first 20 min, after which it started to stabilise as the experiment proceeded. However when the electrolytic cell operating temperature was increased to 425 °C and 450 °C, the cell exhibited almost stable current densities, indicating stable electrochemical process.

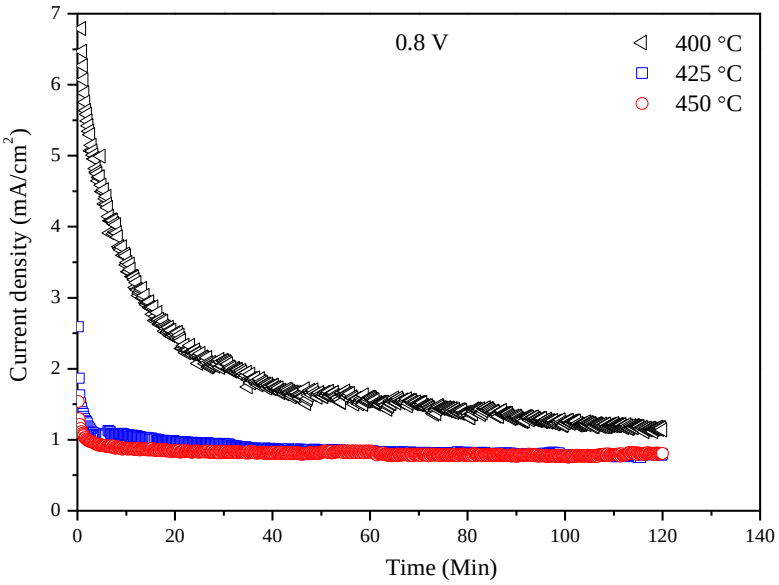

Figure 3.21 Electrolytic cell performance stability at 400, 425 and 450 °C at 0.8 V. The electrolytic cell was: wet H_2, Ag-Pd |$LiAlO_2$-carbonate|$CoFe_2O_4$-Ag, dry N_2

AC impedance spectra at different temperatures (400-425 °C) under open circuit conditions are shown in Figure 3.22. As can be seen from Figure 3.22a, at 400 and 425 °C, the spectra are composed of two depressed semicircles, whereas at 450 °C a depressed semicircle and straight line with an angle not equal to 45° were observed at high and low frequency respectively. Therefore, the impedance spectra at 400 and 425 °C were fitted to an equivalent circuit shown in Figure 3.22b, while the circuit shown in Figure 3.22c was used for fitting the spectra recorded at 450 °C. The capacitances of high frequency semicircles were found to be in the range of 10^{-6}-10^{-3}

F/cm^2, which is related to charge transfer processes at the electrode/electrolyte interface. The low frequency (LF) semicircles at 400 and 425 °C, with associated frequency (10^{-2} F/cm^2), and the straight line at 450 °C could be related to the mass transfer process at the electrode surface [46, 255, 256].

It can be also seen from Figure 3.22a, that the Rs, which is mainly related to the ohmic resistance of the electrolyte, decreased significantly with an increase in the cell operating temperature and reached a lowest value of 0.38 Ω cm^2 at 450 °C. In addition, there was a significant decrease in the total polarisation resistance (Rp) as the cell operating temperature increased, which could be due to the improvement of the cathode catalytic activity with temperature [46].

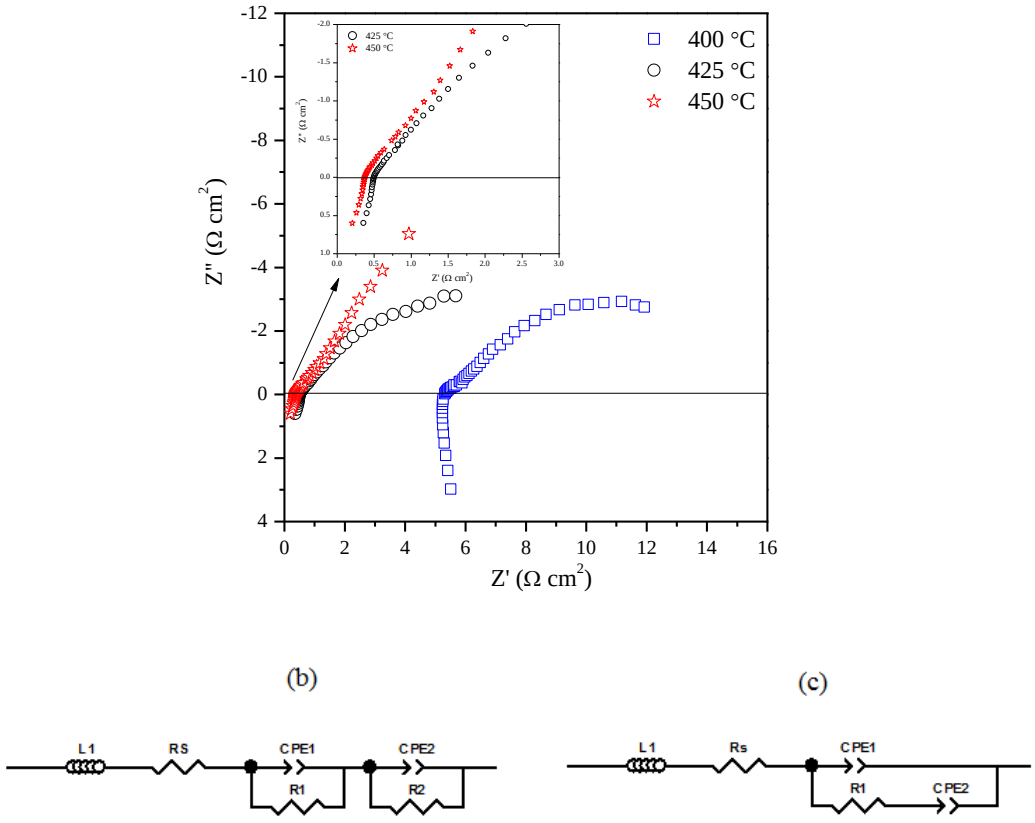

Figure 3.22 (a) Impedance spectra under open circuit conditions for $CoFe_2O_4$-Ag; (b) equivalent circuit for the spectra at 400 and 425 ºC and (c) equivalent circuits for the spectra at 450 ºC

The effect of the operating temperature on the rate of ammonia formation was investigated by varying the cell operating temperature from 400 ºC to 450 ºC and keeping the cell voltage at a constant value of 0.8 V over a period of 2 h. When Nessler's reagent was added to the absorption solution (H_2SO_4, 0.001M), its colour changed immediately to yellow. This indicates that NH_4^+ is present in the absorbed solution and that ammonia was synthesised at atmospheric pressure using $CoFe_2O_4$ as a catalyst. As shown in Figure 3.23, the rate of ammonia formation decreased significantly with an increase in the cell operating temperature, which could be attributed to ammonia decomposition at higher temperatures [75]. Furthermore, the rate reached a maximum value of 2.32×10^{-10} mol s^{-1} cm^{-2} when the cell operated at 400 °C, at which the corresponding current density and Faradaic efficiency were 1.59 mA/cm^2 and 4.17 % respectively. The generated current densities and corresponding Faradaic efficiencies for the ammonia synthesis are listed in Table 3.3. This low Faradaic efficiency may indicate that not all protons transported through the electrolyte to the cathode surface reacted with the adsorbed N_2 to form ammonia. This means that the competitive hydrogen evolution reaction (HER) is the predominant process on the cathode surface [41, 70].

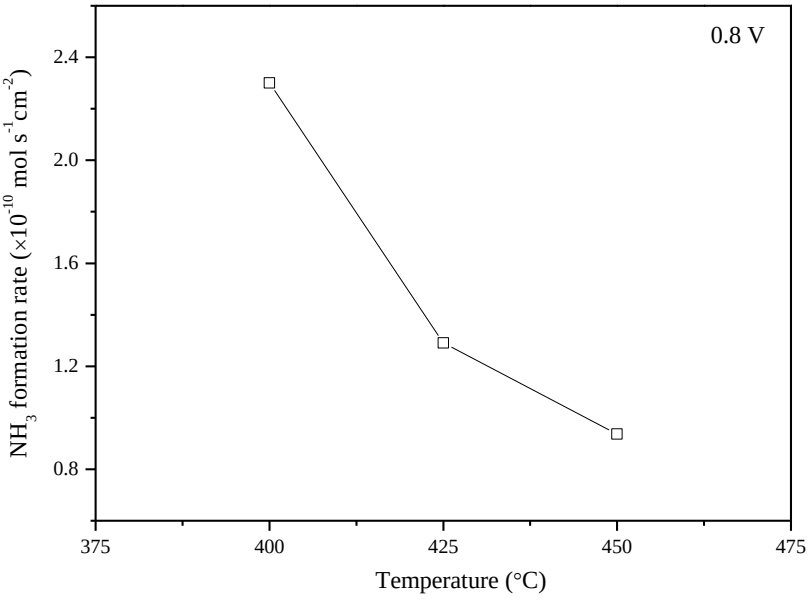

Figure 3.23 Dependence of ammonia formation rate on operating temperature. The applied voltage was 0.8 V: wet H_2, Ag-Pd |$LiAlO_2$-carbonate|$CoFe_2O_4$-Ag, dry N_2

Table 3.3 The corresponding current densities and Faradaic efficiencies of ammonia formation over $CoFe_2O_4$-Ag composite cathode at different working temperatures and 0.8 V

Temperature (°C)	**Current density (mA/cm^2)**	**Faradaic efficiency (%)**
400	1.59	4.17
425	0.86	4.33
450	0.81	3.36

3.2.3.5 Ammonia synthesis at different applied voltages

Figure 3.24 shows the electrolytic cell stability during the ammonia synthesis process at different applied voltages ranging from 0.4 to 1.2 V at 450 °C over a period of 2 h. As can be seen, the cell exhibited almost stable performance under the applied voltages, indicating a stable electrochemical process. In addition, the generated current densities increased with an increase in the applied voltage and reached a maximum value of 2.97 mA/cm^2 at 1.2 V as listed in Table 3.4. This means that more protons were transported to the cathode surface as the cell operating voltage increased [277].

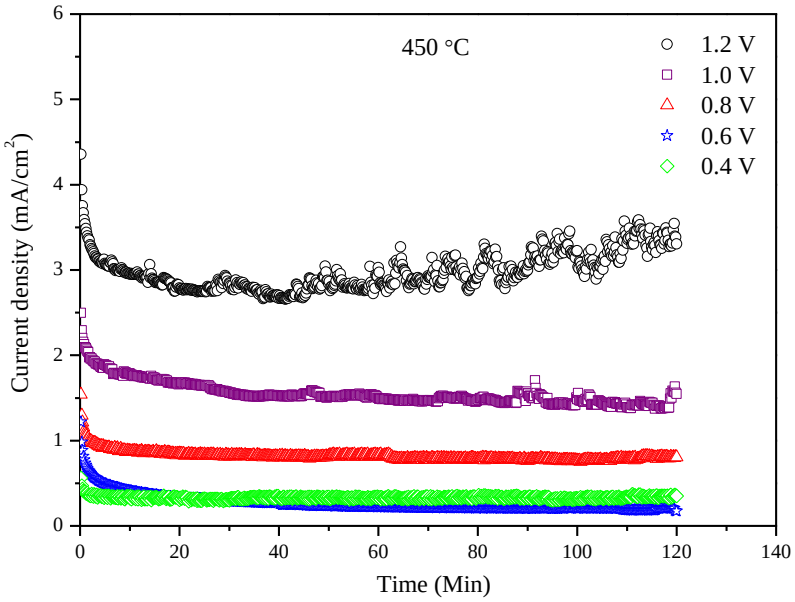

Figure 3.24 Electrolytic cell performance stability under different applied voltages at 450 °C: wet H_2, Ag-Pd |$LiAlO_2$-carbonate|$CoFe_2O_4$-Ag, dry N_2

The effect of the applied voltage on the rate of ammonia formation was investigated at 450 °C. As can be seen in Figure 3.25, there was significant increase in the rate of ammonia formation with an increase in the cell applied voltage, reaching a maximum value of 9.4×10^{-11} mol s^{-1} cm^{-2} at 0.8 V, at which the corresponding current density and Faradaic efficiency were 0.81 mA/cm^2 and 3.36 % respectively, as listed in Table 3.4. However, by further increasing the cell applied voltage, the rate of ammonia formation dropped significantly and reached a minimum value of 5.35×10^{-11} mol s^{-1} cm^{-2} at 1.2 V, at which the corresponding current density and Faradaic efficiency were 2.97 mA/cm^2 and 0.52 % respectively (Table 3.4). This decrease in ammonia formation at higher voltages, although the generated current densities increased could be attributed to the competitive adsorption between N_2 and H_2 over the cathode surface. This means that, when a voltage higher than 0.8 V is applied, the hydrogen evolution reaction is the predominant process over the cathode surface. A similar behaviour was also reported by Sclafani et al. [41] and Kordali et al. [70] and the above stated explanation was proposed.

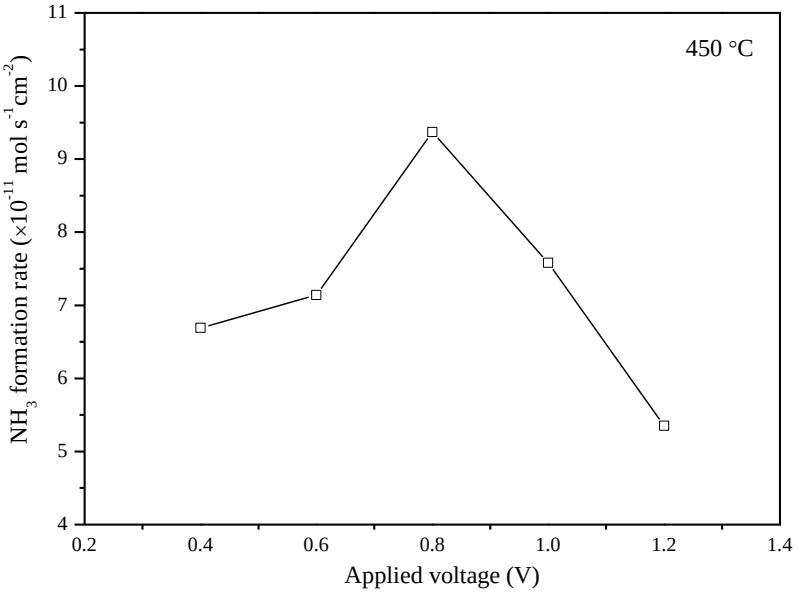

Figure 3.25 Relationship between the rate of ammonia production and the applied voltage at 450 °C: wet H_2, Ag-Pd |$LiAlO_2$-carbonate|$CoFe_2O_4$-Ag, dry N_2

Table 3.4 The corresponding current densities and Faradaic efficiencies of ammonia formation over $CoFe_2O_4$-Ag composite cathode at 450 °C

Applied voltage (V)	**Current density (mA/cm^2)**	**Faradaic efficiency (%)**
0.4	0.33	5.87
0.6	0.25	8.19
0.8	0.81	3.36
1.0	1.52	1.44
1.2	2.97	0.52

3.3 Conclusion

A composite electrolyte consists of $LiAlO_2$-$(LiNaK)_2CO_3$ (50:50 wt %) was prepared via a solid state reaction. The thermal behaviour and the ionic conductivity of the composite electrolyte were investigated under three different atmospheres (air, O_2 and 5% H_2-Ar). The ionic conductivity of the composite electrolyte was in the range of $0.22\text{-}10^{-5}$ S/cm with the measured temperature of 600-300 °C. Nitride- (Fe_3Mo_3N and Co_3Mo_3N) and spinel- ($CoFe_2O_4$) based catalysts were prepared and applied for electrochemical synthesis of ammonia. Electrolyte supported cells were fabricated using Ag-Pd as the anode, $LiAlO_2$-$(Li/Na/K)_2CO_3$ as the electrolyte and one of the following catalysts Fe_3Mo_3N-Ag, Co_3Mo_3N-Ag $CoFe_2O_4$-Ag as the cathode. In all these cases, ammonia was successfully synthesised from H_2 and N_2 at atmospheric pressure. The maximum rates of ammonia formation were found to be 1.88×10^{-10} mol s^{-1} cm^{-2} for Fe_3Mo_3N-Ag, 3.27×10^{-10} mol s^{-1} cm^{-2} for Co_3Mo_3N-Ag and for 2.32×10^{-10} mol s^{-1} cm^{-2} for $CoFe_2O_4$-Ag at 425, 450 and 400 °C with an applied voltage of 0.8 V.

4 Ammonia synthesis based on Sm-doped ceria-carbonate composite electrolyte and Sr and Cu doped lanthanum ferrite cathode

4.1 Introduction

Perovskite is a mineral with chemical composition $CaTiO_3$ which is named after the Russian mineralogist Count Lev Aleksevich Von Perovski. The perovskite-type oxides have the general formula ABO_3 in which A is either a rare-earth or alkaline earth element (e.g. La, Sr, Ba) whereas B is a transition metal cation (e.g. Fe, Cr, Co). In addition, the total charge of A and B cations is +6 [192, 278-280]. These oxides have attracted considerable interest due to their ease of synthesis, high thermal stability, good catalytic activity and low cost [281]. Basically, the properties of such oxides depend on the nature of the cations that occupy the A and B sites and their valence states. In general, the catalytic and electrocatalytic activities of the perovskite-type oxides are determined by the B-site elements (i.e. transition metals) which exhibit multiple oxidation states [280, 282, 283]. The removal of nitrogen oxides are among the various catalytic reactions that have been investigated using perovskite based catalysts. For example, Voorhoeve et al. [284] demonstrated that $La_{0.7}Pb_{0.3}MnO_3$ is an active catalyst for the reduction of NO.

In addition, the perosvkite-type oxides have been widely used as electrocatalysts (electrodes) in many applications, including solid oxide fuel cells (SOFCs) [285, 286], solid oxide steam electrolysis cells (SOECs) [287, 288] and electrochemical synthesis of ammonia [66, 75, 119]. Due to its high electronic conductivity, thermal stability and chemical compatibility with a YSZ-based electrolyte, strontium doped lanthanum manganite (LSM) is the most commonly used cathode material for high temperature SOFCs (700-900 °C) [289]. At low operating temperatures (< 700°C), mixed ionic-electronic conductors (MIECs), including $Ba_{0.5}Sr_{0.5}Co_{0.8}Fe_{0.2}O_{3-\delta}$ (BSCF) [286], $La_{0.6}Sr_{0.4}Co_{0.8}Fe_{0.2}O_{3-\delta}$ (LSCF) [290], $Sm_{0.5}Sr_{0.5}CoO_{3-\delta}$ (SSCo) [285], $Sm_{0.5}Sr_{0.5}Fe_{0.8}Cu_{0.2}O_{3-\delta}$ (SSFCu) [291] and $La_{0.7}Sr_{0.3}Fe_{0.8}Cu_{0.2}O_{3-\delta}$ (LSFCu) [292] are preferred due to their high electronic and ionic conductivities.

In terms of electrochemical synthesis of ammonia from its elements (H_2 and N_2), Wang et al. [119] reported that ammonia was successfully synthesised at low temperature (80 °C) using the perovskite oxide with the form of $Sm_{0.5}Sr_{0.5}CoO_{3-\delta}$ (SSCo). Xu et al. [66] also demonstrated the synthesis of ammonia at low temperature using a cobalt-free perovskite oxide in the form of $SmFe_{0.7}Cu_{0.1}Ni_{0.2}O_{3-\delta}$ (SFCN), by which the highest rate of ammonia formation reported so far was achieved (1.13×10^{-8} mol s^{-1} cm^{-2} at 80 °C). In addition, the electrocatalytic activity of the perovskite-type oxides for ammonia synthesis has been also studied at intermediate temperature (400-600 °C). Recently, Wang et al. [75] successfully synthesised ammonia electrochemically from H_2 and N_2 in an electrolytic cell in which $Ba_{0.5}Sr_{0.5}Co_{0.8}Fe_{0.2}O_{3-\delta}$, (BSCF) was used as a cathode.

Doped ceria based electrolytes like samarium doped ceria (SDC) and gadolinium doped ceria (GDC) exhibit high ionic conductivity within the temperature range 500 to 700 °C. However, these materials show electronic conduction due the partial reduction of Ce^{4+} to Ce^{3+} in a reducing atmosphere or at elevated temperature.

As discussed previously in Chapters 1 and 3, the composite electrolytes are a class of materials which exhibit high ionic conductivities and enhanced mechanical properties. Among these electrolytes are doped ceria-salt composite electrolytes, which consist of two phases, a host oxide phase and a salt phase such as carbonates, halides or phosphates [78, 154, 155]. In recent years, doped-ceria-carbonate composites have drawn considerable interest, owing to their potential applications as electrolytes for intermediate/low temperature (300-600 °C) fuel cells (LT/IT-FCs) [165-167]. In addition, these materials exhibit high ionic conductivity (> 0.1 S cm^{-1}) below 600 °C, which is higher that of pure doped ceria (10^{-2} S cm^{-1}) at 600 °C [166, 173]. This conductivity enhancement is related to the fast ionic transport at the interface region between the two phases [293]. In addition to the enhanced ionic conductivity and stability, the addition of the carbonate phase is found to suppress the electronic conduction of doped ceria arising from the partial reduction of Ce^{4+} to Ce^{3+} in a reducing atmosphere. Furthermore, it has been reported that doped ceria-

carbonate composite electroytes are co-ionic (O^{2-}/H^{+}) conductors in H_2/air fuel cell [156, 165].

It is to be noted that most the above mentioned electrolytes are based on doped ceria-binary carbonate composites such as SDC-$(Li/Na)_2CO_3$. Recently, Xia et al. [172] reported a composite material based on samarium doped ceria (SDC) and ternary carbonate ($(Li/Na/K)_2CO_3$), in which the ternary carbonate melts at ~ 400 °C, which is almost a 100 °C lower than the melting point of the binary carbonate ($(LiNa)_2CO_3$). The ionic conductivity of this composite electrolyte varied from 10^{-4} to 10^{-1} S cm^{-1} in the temperature range of 300-650 °C. Based on the aforementioned properties of perovskite-type catalysts and doped ceria-carbonate composite electrolytes, the aim of this chapter is to explore their applications in the electrochemical synthesis of ammonia from H_2 and N_2.

4.2 Experimental

4.2.1 Synthesis of perovskite catalysts

$La_{0.6}Sr_{0.4}Fe_{0.8}Cu_{0.2}O_{3-\delta}$ (LSFCu) catalyst was synthesised via a combined EDTA-citrate complexing sol-gel process [291]. Lanthanum oxide (La_2O_3, Alfa Aesar, 99%), strontium nitrate ($Sr(NO_3)_2$, Alfa Aesar, 99%), iron nitrate nonahydrate ($Fe(NO_3)_3 \cdot 9H_2O$, Alfa Aesar, 98%) and copper nitrate hemi (pentahydrate) ($Cu(NO_3)_2 \cdot 2.5H_2O$, Alfa Aesar, 98%) were used as starting materials. La_2O_3 was heated at 700 °C for 1-2 h before weighing, in order to remove moisture. It was then dissolved in diluted nitric acid to form lanthanum nitrate. Calculated amounts of $Sr(NO_3)_2$, $Fe(NO_3)_3 \cdot 9H_2O$ and $Cu(NO_3)_2 \cdot 2.5H_2O$ were dissolved in deionised water and then added to the lanthanum nitrate solution. Citric acid and EDTA (ethylenediaminetetraacetic acid) were then added as complexing agents, with a ratio of citric acid: EDTA: metal cations of 1.5 : 1 : 1. Dilute aqueous ammonia solution was then added to the mixed solution to adjust the pH value to around 6. Under heating and stirring, the solution was evaporated on a hot-plate, and then gradually changed into a black sticky gel before complete drying. The as-prepared powder was ground and subsequently calcined in air at 950 °C for 2 h with heating/cooling rates of 5 °C min^{-1} to obtain a single phase of LSFCu.

4.2.2 Synthesis of $Ce_{0.8}Sm_{0.2}O_{2-\delta}$

SDC powder with a composition of $Ce_{0.8}Sm_{0.2}O_{2-\delta}$ was synthesised by a glycine-nitrate process (GNP) [294]. Samarium oxide (Sm_2O_3, Alfa Aesar, 99%) and cerium nitrate hexahydrate ($Ce(NO_3)_3 \cdot 6H_2O$, Alfa Aesar, 99%) were used as starting materials. Sm_2O_3 was heated at 700 °C for 1-2 h before weighing, in order to remove absorbed water. It was then dissolved in nitric acid to form samarium nitrate. A calculated amount of $Ce(NO_3)_3 \cdot 6H_2O$ was dissolved in deionised water and mixed with the samarium nitrate solution. Subsequently, glycine (NH_2CH_2COOH) was added to the solution with a molar ratio of glycine/salt = 2:1, and stirred until completely dissolved. The mixed solution was then evaporated under stirring on a hot-plate, converted into a viscous gel and further heated until combustion occurred, resulting in a pale yellow and porous ash. The ash was calcined in air at 800 °C at a heating rate of 5 °C min^{-1}, maintained for 2 h and cooled down to room temperature at a rate of 5 °C min^{-1} to form SDC powder.

4.2.3 Preparation of the composite electrolyte

The ternary eutectic salt ($(Li/Na/K)_2CO_3$) was prepared by solid state reaction. Lithium carbonate (Li_2CO_3, Alfa Aesar, 98 %), sodium carbonate (Na_2CO_3, Aldrich, 99.5+ %) and potassium carbonate (K_2CO_3, Alfa Aesar, 99 %) were mixed with a molar ratio of 43.5:31.5:25 respectively. The mixture was ground and then calcined in air at 600 °C for 1 h and quenched directly to room temperature. The composite electrolyte was made by mixing the SDC powder with ternary carbonate salts (43.5 mol % Li_2CO_3, 31.5 mol % Na_2CO_3 and 25 mol % K_2CO_3) at weight ratio 70:30. The mixture was ground thoroughly with an agate mortar and acetone. The material was fired in air at 600 and 680 °C for 1 h in sequence before being quenched to room temperature. The powders obtained were ground thoroughly for subsequent use.

4.2.4 Pellet preparation for conductivity measurements

The AC and DC conductivities measurements were carried out using a computer-controlled Solartron Analytical 1470E controlled by software CellTest for automatic

data collection. The impedance spectra were recorded with AC amplitude of 100 mV over the frequency range 1 MHz-0.01 Hz and 10 points per decade. The composite electrolyte was uniaxially dry-pressed at pressure of 259 MPa into a pellet with diameter of 13 mm and thickness of ~ 2 mm. The green pellet was sintered in air at 600 ºC for 2 h at rate of 2 ºC heating/cooling. The pellet was brushed on both sides with Ag paste to serve as electrodes. AC impedance measurements were performed in three atmospheres, namely, air, dry O_2 (dried through 98% a solution of H_2SO_4 at 98%) and wet (~ 3% H_2O, pass through room temperature water) 5% H_2-Ar in the temperature range 300-600 ºC.

The LSFCu powder was uniaxially dry-pressed at pressure of 259 MPa into a pellet with 13 mm in diameter and 2 mm in thickness. The pellet was sintered in air at 1200 ºC for 5 h at a rate of 2 ºC/min heating/cooling, then Ag paste was painted on both sides. The relative density of the LSFCu pellet was about 80.39 %. The DC conductivity of the LSFCu pellet was measured using the pseudo-four probe method, in air, within the temperature range of 50 to 600 ºC. The applied current was 100 mA.

4.2.5 Fabrication of the single cell

A tri-layer single cell was fabricated by a cost-effective one-step dry-pressing. The anode material was a mixture of nickel oxide (NiO, Aldrich, 99%), SDC and starch, as pore former, in the weight ratio of 60:40:10. The cathode was made by mixing the LSFCu, SDC and starch, with a weight ratio of 70:30:10. The composite anode, composite electrolyte and composite cathode were fed into the die, layer by layer, with the aid of a sieve to ensure uniform powder distribution, and then uniaxially pressed at pressure of 121 MPa. The green pellet was sintered in air at 600 °C for 2 h. The catalyst surface area of the cathode was 0.785 cm^2. Silver paste was painted on each electrode surface of the cell as a current collector. Ag wires were used as output terminals for both electrodes.

4.2.6 Ammonia synthesis

The fabricated cell for ammonia synthesis was placed in a self-designed double-chamber reactor, using ceramic paste (Aremco, Ceramabond 552) as a sealant. The electrolytic cell constructed was as follows: wet H_2, Ni-SDC|SDC-carbonate|LSFCu-SDC dry N_2. The cathode chamber was fed with oxygen-free N_2 (BOC), whereas wet, highly pure H_2 (~3 % H_2O) (BOC, 99.995) was fed to the anode chamber. A constant voltage was applied over a period of 30 min. The ammonia synthesised at the cathode chamber was absorbed by 25 ml of diluted sulphuric acid (0.001 M). The concentration of NH_4^+ in the absorbed solution was analysed using Nessler's reagent (Aldrich). The produced ammonia was detected using an ammonia meter (Palintest 1000) and the rate of ammonia formation was calculated using Equation 2.9 (Section 2.4.2).

4.2.7 Materials characterisation

Phase purity was studied by powder X-ray diffraction using a Panalytical X'Pert Pro diffractometer. The thermal behaviour of the perovskite catalyst (LSFCu) was studied in N_2 atmosphere from room temperature to 500 °C with a heating/cooling rate of 10 °C/min. The thermal behaviour of the composite electrolyte was investigated under different atmospheres (air, O_2 and 5% H_2-Ar), from room temperature to 600 °C with a heating/cooling rate of 10 °C/min. A platinum crucible was used for carbonate containing samples. The microstructures of the prepared catalyst and the cross-sectional area of single cell were examined using Hitachi SU6600 Scanning Electron Microscope (SEM).

4.3 Results and discussion

4.3.1 XRD analysis

Figure 4.1 shows the XRD pattern of $La_{0.6}Sr_{0.4}Fe_{0.8}Cu_{0.2}O_{3-\delta}$ (LSFCu) powder after calcination in air at 950 ºC for 2 h. As can be seen, a single phase with typical cubic perovskite oxide structure was obtained, which is in good agreement with

JCPDS file 39-1083. The crystallite size of LSFCu catalyst is about 30 nm, estimated from Sherrer's formula (Equation 2.3).

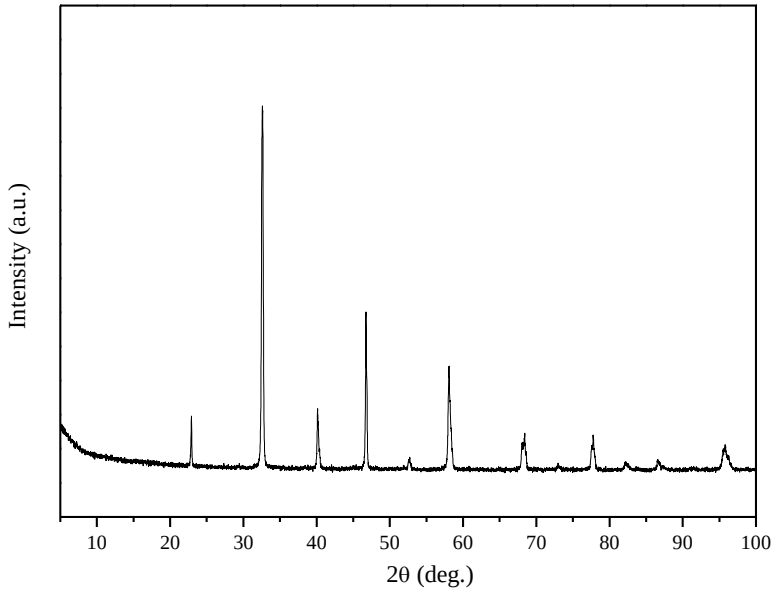

Figure 4.1 Powder X-ray diffraction pattern of LSFCu calcined air at 950 °C for 2 h

Figure 4.2 shows the XRD patterns of the ternary carbonate, pure SDC and the composite electrolyte (SDC-Li/Na/K)$_2$CO$_3$ 70:30 wt%). As can be seen from Figure 4.2a, after firing the ternary carbonate in air at 600 °C for 1 h, a complicated phase composition was observed. A single phase of SDC with a cubic fluorite structure was obtained when SDC ash was calcined in air at 800 °C for 2 h, which is in good agreement with JCPDS file 34-0394, as presented in Figure 4.2b. The powder XRD patterns of SDC-carbonate composite fired in air for 1 h at 600 and 680 °C are shown in Figures 4.2c and d respectively. As can be seen, the composite electrolyte shows the major characteristic peaks of pure SDC when it was fired in air at 600 °C, but a small peak, which could be ascribed to the carbonate phase ((Li/Na/K)$_2$CO$_3$), was observed at 31.99º (Figure 4.2c). On the other hand, no extra peaks were observed when the SDC-carbonate composite was fired in air at 680 °C, indicating that the carbonate exists as an amorphous phase co-existing with the SDC, and there is no interaction between the SDC and the ternary carbonate (Figure 4.2d), which was also observed before, by Zhang et al. [295], for GYDC-(Li/Na)$_2$CO$_3$ composite

electrolyte. The crystallite size of pure SDC is about 29 nm, while that of SDC-carbonate composite is about 36 nm, estimated from Sherrer's formula (Equation 2.3).

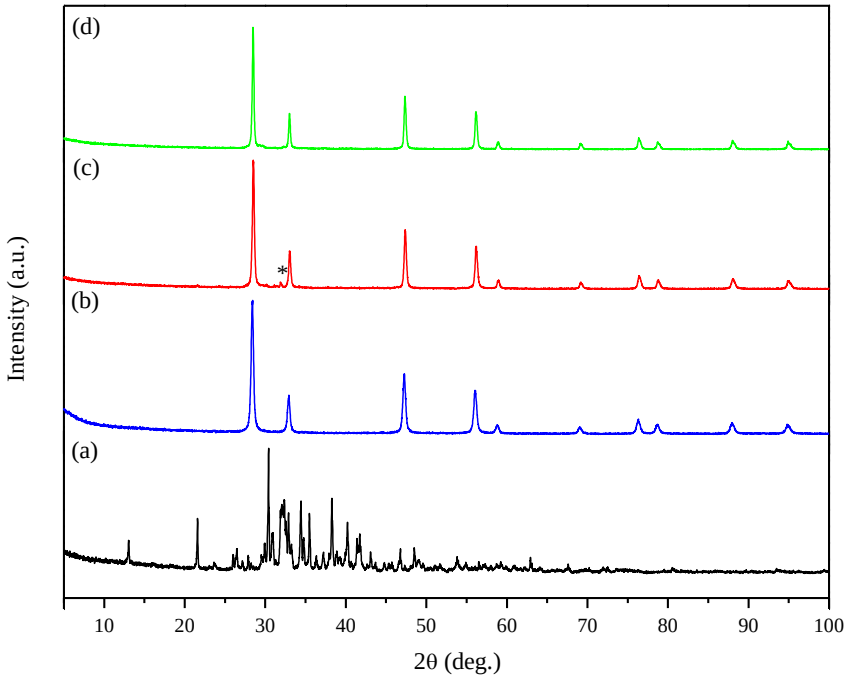

Figure 4.2 XRD patterns of (a) (Li/Na/K)2CO3, (b) SDC calcined in air at 800 °C for 2h, (c) 70 wt% SDC-30 wt% carbonate calcined in air at 600 °C for 1h, * ternary carbonate, (d) 70 wt% SDC-30 wt% carbonate calcined in air at 680 °C for 1 h

In order to investigate the chemical compatibilities between the LSFCu and NiO with SDC, the composite cathode (LSFCu-SDC, 70:30 wt %) and the composite anode (NiO-SDC, 60:40 wt %) were fired at 600 °C, which is the sintering temperature for the fabricated single cell. As can be seen from Figure 4.3c, the XRD pattern of the composite cathode (LSFCu-SDC) displays only the peaks that correspond to the pure LSFCu (Figure 4.3a) and pure SDC (Figure 4.3b). In the case of the composite anode (Figure 4.4c), the observed peaks correspond only to NiO (Figure 4.4a) and SDC (Figure 4.4b). As discussed above, no additional diffraction peaks were observed when the composite cathode and the composite anode were fired at 600 °C. This indicates that NiO and LSFCu materials are chemically compatible with SDC, at the single cell sintering temperature.

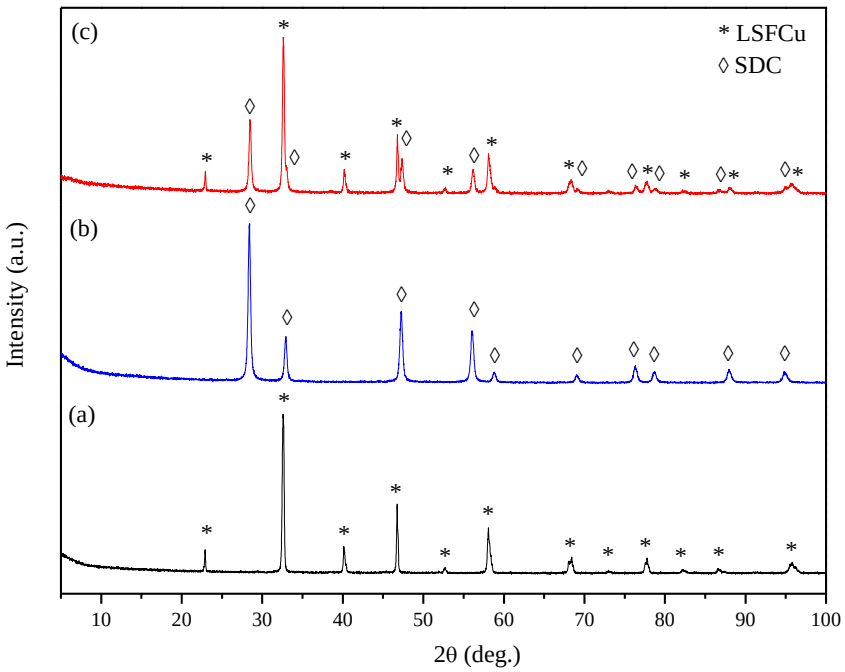

Figure 4.3 XRD patterns of (a) pure LSFCu; (b) pure SDC; (c) LSFCu-SDC composite cathode

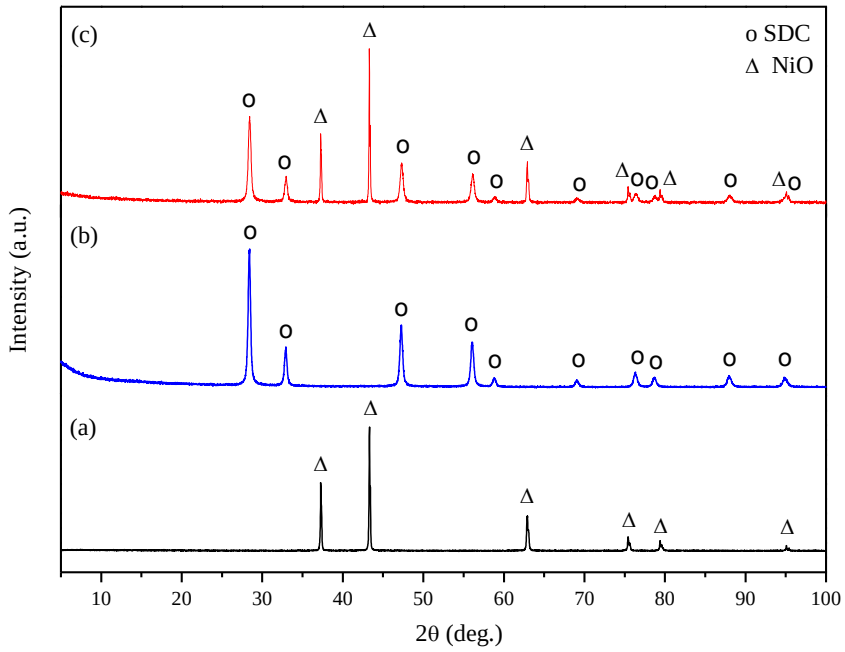

Figure 4.4 XRD patterns of (a) commercial NiO; (b) pure SDC; (c) NiO-SDC composite anode

4.3.2 SEM

Figure 4.5a shows the morphology of the LSFCu powder calcined in air at 950 ºC for 2 h. As can be seen, the microstructure of LSFCu powder consists of large grains in a homogenous matrix of small particles. Figure 4.5b represents the microstructure of the cross-sectional area of the single cell sintered in air at 600 ºC for 2 h, before ammonia synthesis. A good adhesion between the electrodes (cathode and anode) and the SDC-carbonate composite electrolyte was observed. This indicates a good thermal compatibility between the single cell components at the sintering temperature.

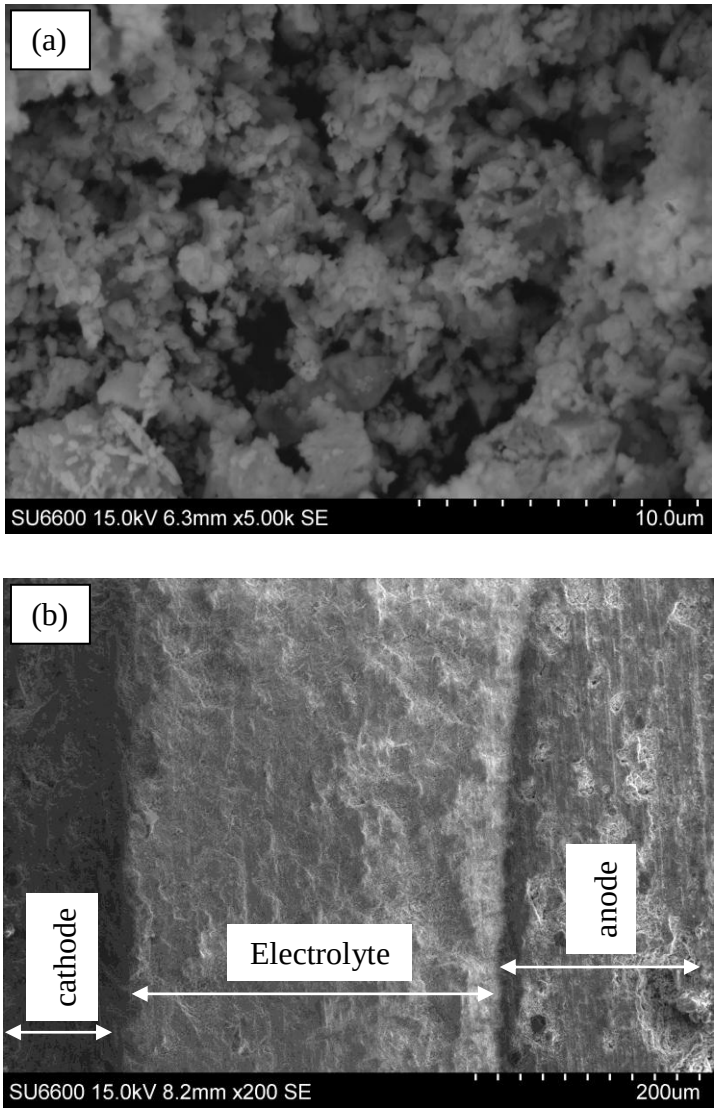

Figure 4.5 SEM images of (a) LSFCu calcined in air at 950 ºC; (b) The cross-sectional area of the single cell before ammonia synthesis

4.3.3 Thermal analysis

The thermal behaviour of SDC-carbonate composite calcined in air at 680 °C for 1 h was investigated in three different atmospheres (air, O_2 and 5% H_2-Ar), as shown in Figure 4.6. As can be seen, the composite electrolyte exhibits almost similar behaviour in each of the atmospheres under investigation. Upon heating, endothermic peaks were observed, accompanied by several stages of weight loss, depending on the atmosphere used. In the temperature range from room temperature to 280 ºC, an endothermic event was observed, which could be due to the loss of adsorbed water. Within the temperature range from 300 to 600 ºC, endothermic peaks were observed at 398.91, 397.91 and 403.8 ºC in air, O_2 and 5% H_2-Ar respectively. These could be ascribed to the melting point of the ternary carbonate (~ 400 ºC) [235]. Upon cooling, only one exothermic event was observed in each atmosphere, which can be attributed to the solidifying of the ternary carbonate. These exothermic peaks are located at 375.34, 371.94 and 365.34 ºC for air, O_2 and 5% H_2-Ar respectively. In addition, upon cooling, the observed peak at ~ 525 ºC is not related to a phase change and it is due to the fact the sample was heated and cooled directly without a dwelling step as described in Chapter 5 (Figure 5.6b). Furthermore, the total weight losses were approximately 0.5 %, 0.7 % and 2.8 % in air, O_2 and 5% H_2-Ar atmospheres respectively. This indicates the thermal stabilities of the composite electrolytes in the atmospheres under investigation within the measured temperature.

Figures 4.7a-c show the XRD patterns of the composite electrolyte after thermal analysis in different atmospheres (air, O_2 and 5% H_2-Ar respectively). As can be seen, the composite electrolyte retains the same fluorite structure after thermal analysis and no phase change was observed, suggesting its thermal stabilities, as discussed above.

(a)

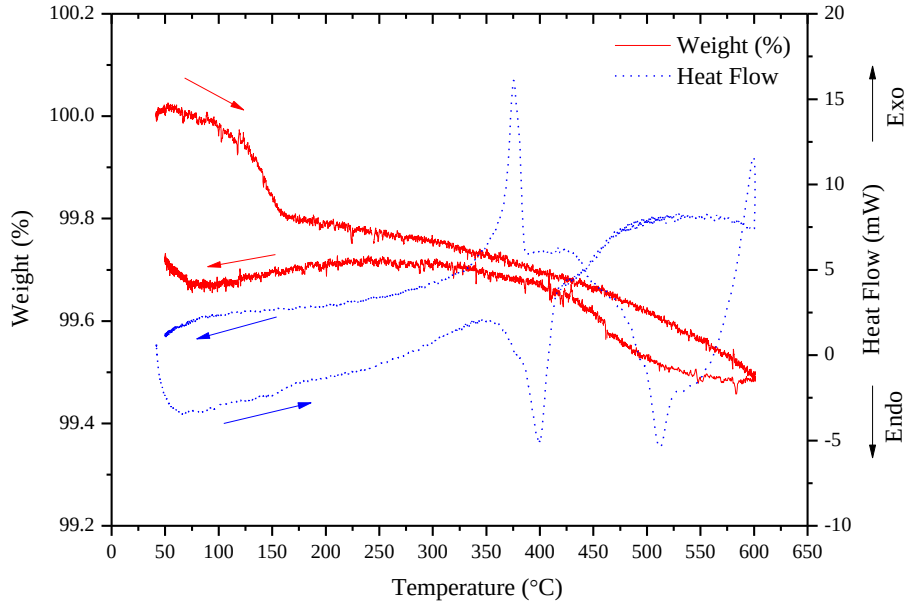
Weight (%)
Heat Flow
Exo
Endo
Weight (%)
Heat Flow (mW)
Temperature (°C)
100.2
100.0
99.8
99.6
99.4
99.2
20
15
10
5
0
-5
-10
0
50
100
150
200
250
300
350
400
450
500
550
600
650

(b)

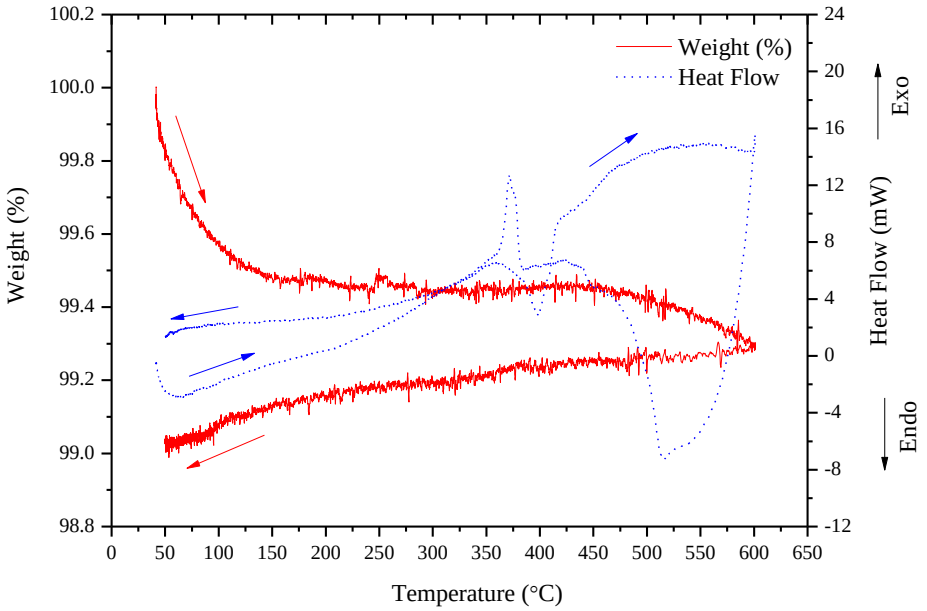
Weight (%)
Heat Flow
Exo
Endo
Weight (%)
Heat Flow (mW)
Temperature (°C)
100.2
100.0
99.8
99.6
99.4
99.2
99.0
98.8
24
20
16
12
8
4
0
-4
-8
-12
0
50
100
150
200
250
300
350
400
450
500
550
600
650

(c)

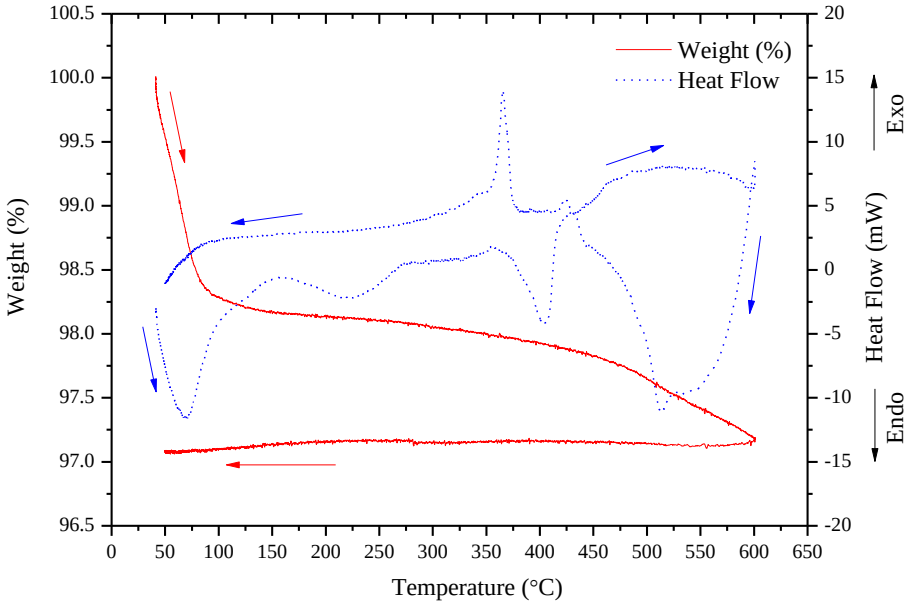

Figure 4.6 TGA-DSC curves of (a) SDC-carbonate composite in air; (b) SDC-carbonate composite in O_2; (c) SDC-carbonate composite in 5% H_2-Ar

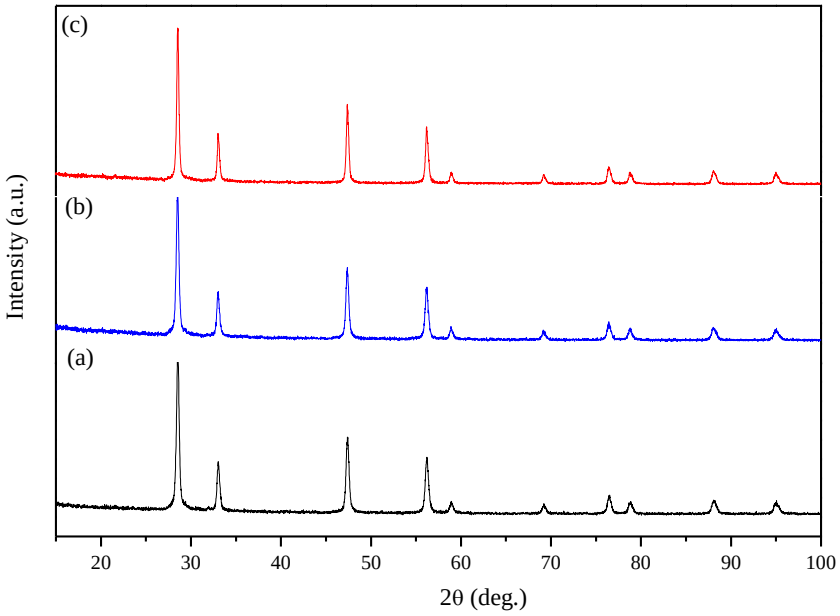

Figure 4.7 XDR patterns of SDC-carbonate composite after thermal analysis in different atmospheres: (a) air; (b) O_2; (c) 5% H_2-Ar

During the ammonia synthesis process, the cathode is supplied by N_2, thus its stability in this atmosphere is of crucial importance. Figure 4.8 shows TGA-DSC curves of the perovskite oxide (LSFCu) in N_2 atmosphere from room temperature up to 500 °C. As can be seen, within the range of room temperature to 350 °C, a slight weight gain of about 0.25 % was observed, which is mainly related to the buoyancy effect of air, which also appears on cooling. In addition, a slight weight loss of about 0.45 wt % was observed within the range 350 to 500 °C. This could be ascribed to the loss of oxygen from the structure of $La_{0.6}Sr_{0.4}Fe_{0.8}Cu_{0.2}O_{3-\delta}$ in N_2, as the pO_2 in N_2 is lower than that in air. The DSC curve shows no obvious thermal effects, indicating that there is no phase transition or sample decomposition and there is no reaction between the $La_{0.6}Sr_{0.4}Fe_{0.8}Cu_{0.2}O_{3-\delta}$ catalyst and N_2 in the measured temperature range. Figures 4.9a and b respectively show the XRD pattern of LSFCu catalyst before and after the thermal analysis in N_2 atmosphere from room temperature up to 500 °C. As can be seen, the oxide (LSFCu) retains the same perovskite structure (Figure 4.9a), indicating its thermal stability in a N_2 atmosphere in the measured temperature range.

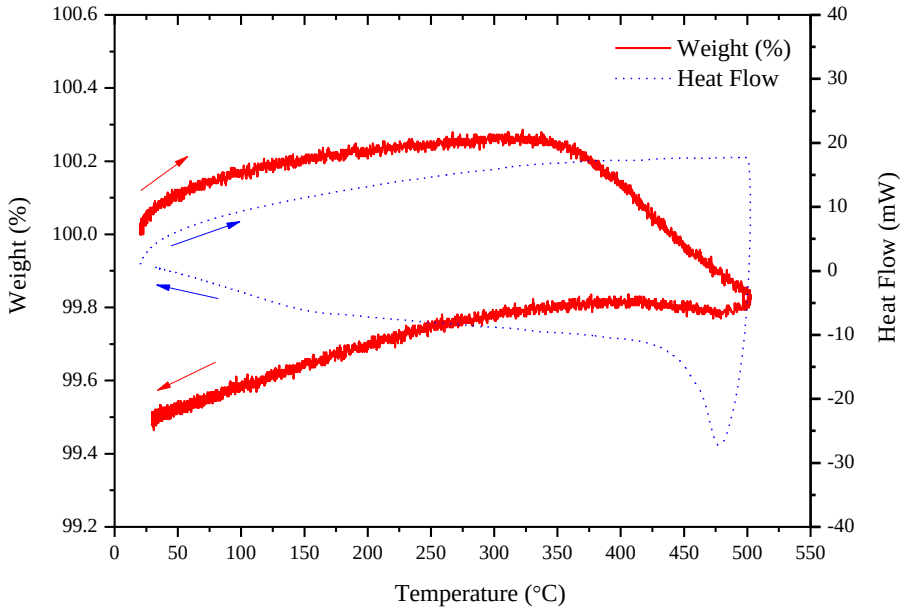

Figure 4.8 TGA-DSC curve of LSFCu cathode in nitrogen, up to 500 ºC

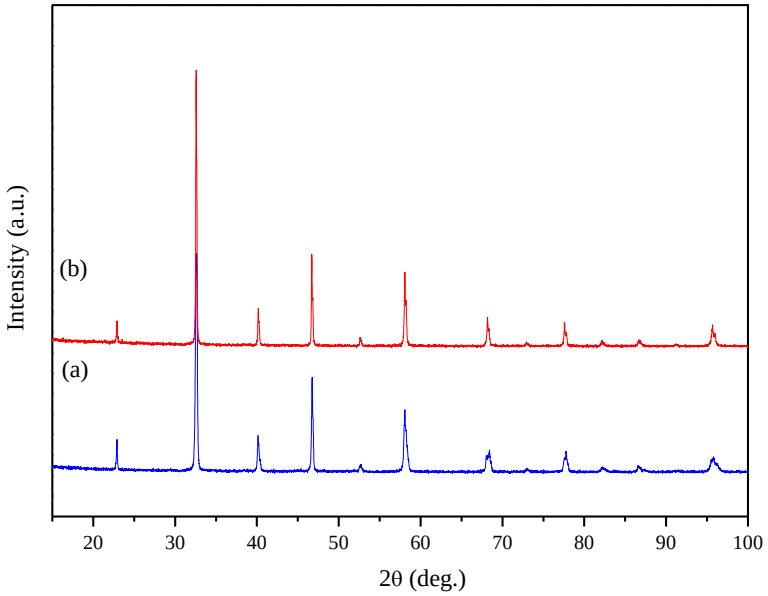

Figure 4.9 XRD patterns of LSFCu: (a) before thermal analysis; (b) after thermal analysis in N_2 at 500 ºC

4.3.4 Conductivity

4.3.4.1 The ionic conductivity of the composite electrolyte

The ionic conductivity of the SDC/(Li/Na/K)$_2$CO$_3$ was measured by electrochemical impedance spectroscopy (EIS) within the temperature range of 600-300 ºC in three different atmospheres (air, O_2 and 5% H_2-Ar). Figure 4.10 shows the typical impedance plots of the composite electrolyte at 600 ºC in three different atmospheres (air, O_2 and 5% H_2-Ar). As can be seen, only small part of the high frequency semicircle which is attributed to the electrolyte contribution was observed in each of the atmospheres under investigation (Figure 4.10b). At low frequency, large depressed semicircles related to electrode contribution are observed in all cases. The high frequency intercept with real axis was used to calculate total resistance value.

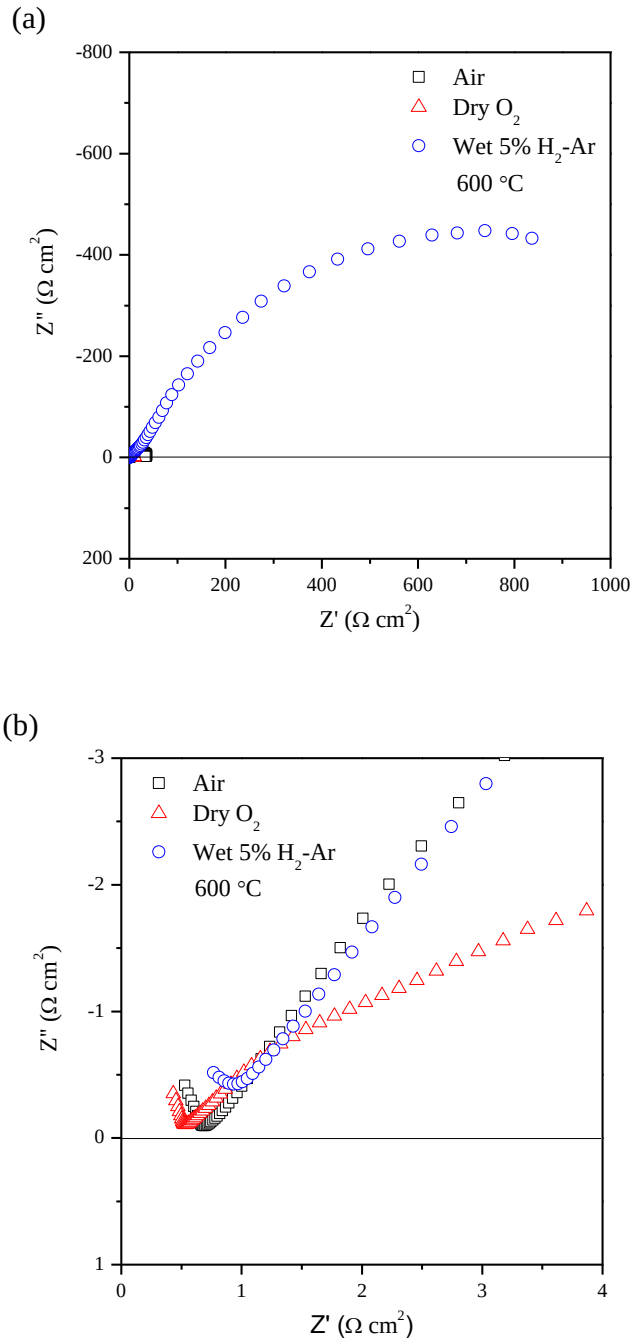

Figure 4.10 (a) Impedance spectra of SDC-carbonate under different atmospheres; (b) enlarged spectra

The AC conductivity of the composite electrolyte (SDC-$(Li/Na/K)_2CO_3$) in three different atmospheres (air, dry O_2 and wet 5% H_2-Ar) as a function of temperature are shown in Figure 4.11. It can be clearly noticed that the ionic conductivities of the

composite electrolyte under all used atmospheres increase with increasing temperature. In addition, it is obvious that the conductivities changed at two different regions below and above ~ 375 ºC, which is ~ 25 ºC lower than the melting point of the ternary carbonate (~ 400 ºC) [235]. According to Bodén et al. [170], the carbonate in the composite electrolyte partially melts below the bulk melting point of the salt, which is enough to enhance the conductivity. In addition, the phenomenon of conductivity jump above the carbonate melting point was previously reported by Huang et al. [165] for SDC-$(Li/Na)_2CO_3$ and by Chockalingam et al. [253] for GDC-$(Li/Na)_2CO_3$.

At high temperature (600-400 ºC), the total conductivities were found to be 0.35-3.26 × 10^{-2}, 0.37-2.44 × 10^{-2} and 0.24-3.97 × 10^{-2} S cm^{-1} in air, dry O_2 and wet 5% H_2-Ar respectively. These values are higher than those reported by Fu et al. [173] for pure SDC (1.59 × 10^{-2} S cm^{-1}) and by Xia et al. [296] for SDC-carbonate composite (9.10 × 10^{-2} S cm^{-1}) in air at 600 ºC. The apparent activation energies (E_a) of the composite electrolyte at high temperature (600-400 ºC) under different atmospheres were extracted from the linear part of the Arrhenius plots of conductivity, as shown in the inset of Figure 4.11. The calculated activation energies were found to be 0.69(18) eV, 0.76(10) eV and 0.51(23) eV for the composite electrolyte in air, dry O_2 and wet 5% H_2-Ar respectively.

It can be also seen from Figure 4.11 that at high temperature (> 450 ºC), the measured conductivity in wet 5% H_2-Ar (H^+ conductivity) is lower than those measured in air and dry O_2 (O^{2-} conductivity), indicating that oxygen-ion conduction (O^{2-}) is dominant in the SDC-carbonate composite electrolyte. This could be explained by the fact that proton ions (H^+) are extrinsic or non-structural in the carbonate phase; thus their existence and concentration in the sample are limited by the in situ environment. By contrast, oxygen ions (O^{2-}) are intrinsic, or structural, in both phases (SDC and carbonate) and therefore their concentration is higher than that of proton ions [180, 297].

The enhancement in the ionic conductivities above the melting point of the ternary carbonate could be ascribed to the so-called the composite effect. As

discussed previously in Chapter 3, the ternary carbonate softens or becomes molten at high temperature (400-600 ºC), which enhances the mobility of all ions (i.e. Li^+, Na^+, K^+, O^{2-}, H^+, HCO_3^- and CO_3^{2-}) leading to a superionic conducting region at the interface between the two phases. Thus, all these mobile ions contribute to the overall measured AC ionic conductivity [177]. However, only H^+ or O^{2-} can transfer through the composite electrolyte during electrolysis, whereas other mobile ions (i.e. Li^+, Na^+, K^+, HCO_3^- and CO_3^{2-}) are blocked at the electrodes [180].

At low temperature (375-300 ºC), the composite electrolyte ionic conductivities dropped significantly (Figure 4.11) and were found to be 8.81×10^{-3}-4.91×10^{-6} in air, 1.87×10^{-2}-4.61×10^{-5} in dry O_2 and 3.36×10^{-2}-4.14×10^{-4} S cm^{-1} in wet 5% H_2-Ar. Below the carbonate melting point, the ions are not highly activated and less mobile, due to the activation barrier, leading to low ionic conductivities within this temperature range [170]. Furthermore, at low temperature, the conductivity of the composite electrolyte in wet 5% H_2-Ar is higher than that obtained in air and dry O_2, as seen from Figure 4.11. This could be due to the fact that proton conduction can be easily activated at low temperature, compared to oxygen-ion conduction [169, 180].

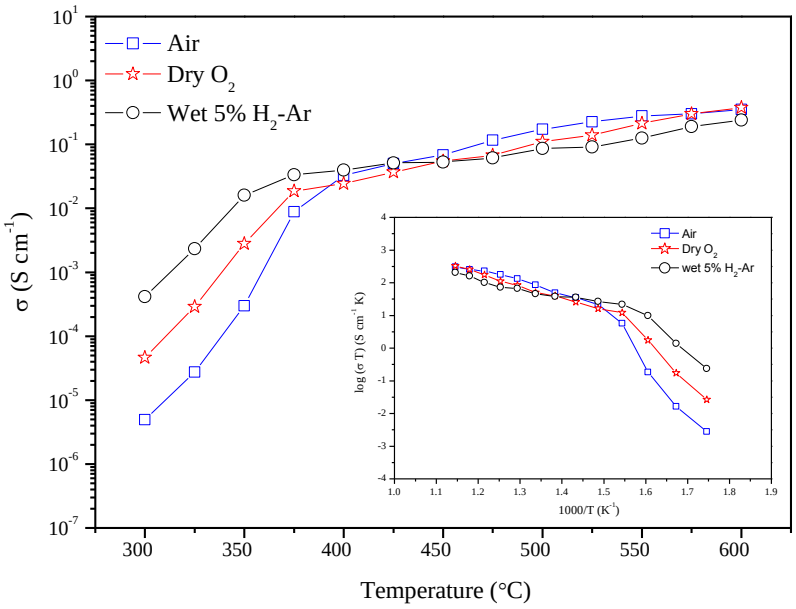

Figure 4.11 AC conductivity plot against temperature for SDC-$(Li/Na/K)_2CO_3$ composite in air, dry O_2 and wet 5% H_2-Ar atmospheres

As mentioned previously, doped ceria-carbonate composite electrolytes are co-ionic (O^{2-}/H^{+}) conductors [156, 165]. In the SDC-carbonate composite, oxygen ions (O^{2-}) can transfer through the SDC phase and the interfacial region between the two phases (SDC and carbonate). On the other hand, protons (H^{+}) can transfer through the interface between SDC and carbonate via an intermediate proton carrier (HCO_3^-), which is formed by combining H^{+} with CO_3^{2-} [169, 177].

4.3.4.2 The electronic conductivity of LSFCu

Figure 4.12a shows the electrical conductivity of LSFCu in air, as a function of temperature. As can be seen, there was an increase in the conductivity with increasing temperature and a maximum value of about 18.77 S cm^{-1} was attained when the temperature reached 470 ºC (semiconducting behaviour). This value of conductivity is higher than that of $La_{0.2}Sr_{0.8}Cu_{0.2}Fe_{0.8}O_{3-\delta}$, LSFCu (10 S cm^{1}) [298] and that of $Ba_{0.5}Sr_{0.5}Zn_{0.2}Fe_{0.8}O_{3-\delta}$, BSZF (9.4 S cm^{-1}) [299], but much lower than that of $La_{0.7}Sr_{0.3}Cu_{0.2}Fe_{0.8}O_{3-\delta}$, LSFCu (~ 100 S cm^{-1}) [300]. However, when the temperature is increased above 470 ºC, the conductivity begins to decrease and reaches a value of about 3 S cm^{-1} at 600 ºC. This is due to semi-conductor to metal transition. This decrease in the electrical conductivity could be ascribed to the loss of the lattice oxygen and formation of oxygen vacancies at high temperatures [299, 301]. The activation energy (E_a) for the conduction was extracted from the slope of the linear part of the Arrhenius plot shown in Figure 4.12b. The calculated activation energy was found to be 0.23(1) eV between ~ 50 and 450 °C , which is slightly lower than that of BSZF (~ 0.33 eV) [299].

(a)

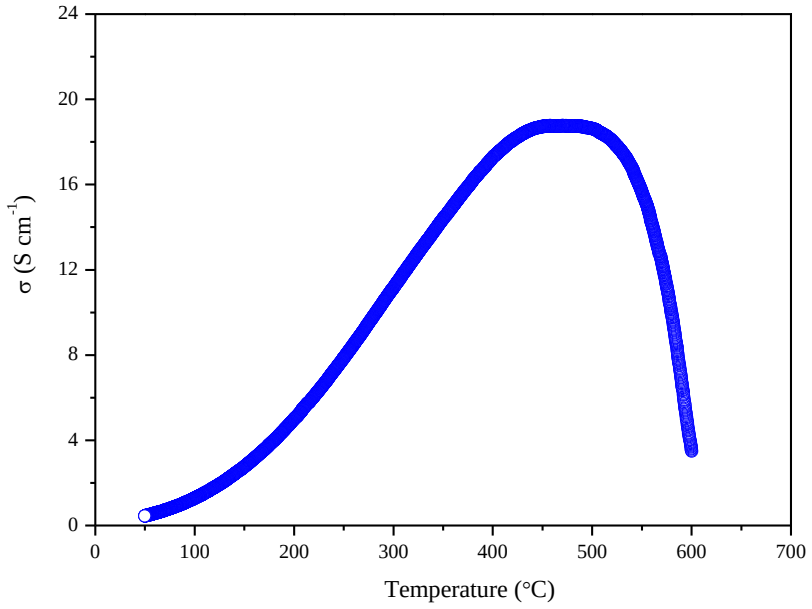

(b)

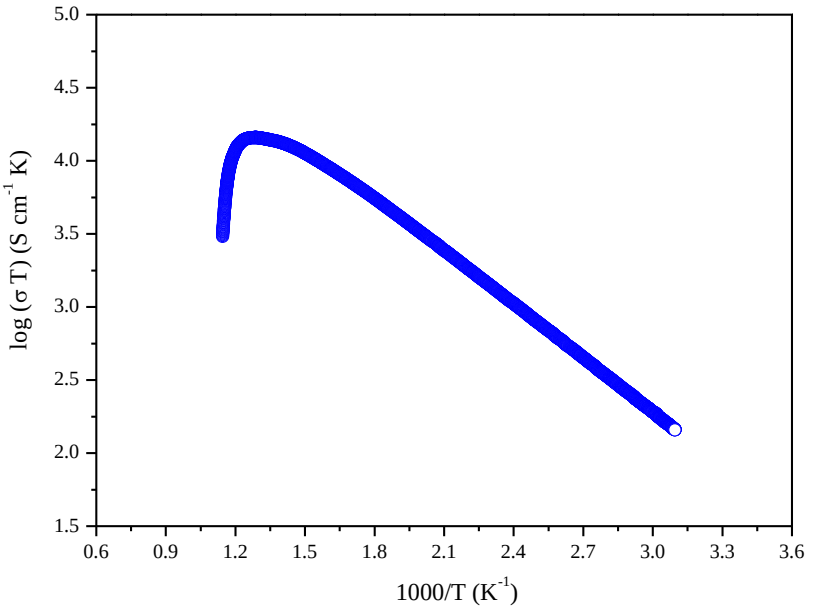

Figure 4.12 Electrical conductivity of $La_{0.6}Sr_{0.4}Fe_{0.8}Cu_{0.2}O_{3-\delta}$ (LSFCu) pellet in air: (a) conductivity as a function of measuring temperature; (b) Arrhenius plot

4.3.5 Synthesis of ammonia at different temperatures

Figure 4.13 represents the electrolytic cell stabilities during the ammonia synthesis process at different temperatures (400-475 ºC), at 0.8 V over a period of 30 min. As can be seen, the electrolytic cell was almost stable at synthesis temperatures of 425-475 ºC. However, at low temperature (400 ºC), the electrolytic cell seems to be unstable and the generated current density decreased with time. Furthermore, it was found that the current density increased with increasing the operating temperature and reached a maximum value of 62.56 mA/cm^2 at 475 °C, as listed in Table 4.1. This means that more protons were transported to the cathode surface as a result of the enhancement in ionic conductivity with an increase in the operating temperature, as mentioned above.

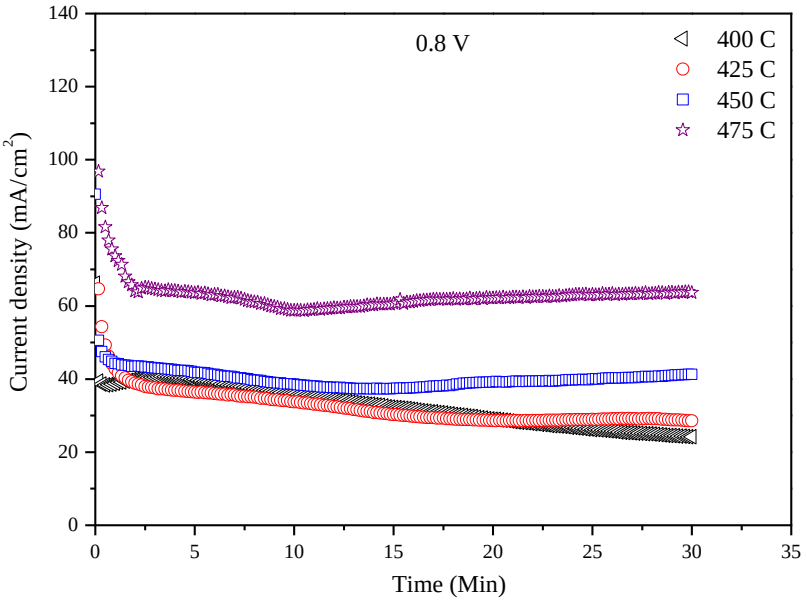

Figure 4.13 Electrolytic cell performance stability at 0.8 V and 400-475 °C. The electrolytic cell was wet H_2, NiO-SDC|SDC-carbonate|LSFCu-SDC, dry N_2

The AC impedance spectra of the electrolytic cell based on a LSFCu-SDC composite cathode at different temperatures (400-475 °C) under open circuit condition are shown in Figure 4.14a. As can be seen, the spectra consist of two depressed semicircles, suggesting that there are two corresponding electrode

processes. The impedance data were fitted using Zview software and the equivalent circuit is shown in Figure 4.14b. The circuit consists of LRs(R1CPE1)(R2CPE2), where L represents inductance caused by the instrument and contact leads, Rs is the series resistance, including the resistance contributions of the electrolyte, electrodes, current collectors and contact resistance at the electrode/electrolyte interface, the remaining two components, (R1CPE1) and (R2CPE2), are associated with electrode processes. R1 and R2 represent the polarisation resistances, whereas CPE1 and CPE2 are the constant phase elements. In this study, CPE which represents a non-ideal capacitor was used in place of a pure capacitor (C).

The capacitances of the high frequency (HF) semicircles were found to be 10^{-4}-10^{-3} F/cm^2, which are related to the charge transfer processes at the electrode/electrolyte interface. The low frequency (LF) semicircles, with associated frequencies of 10^{-2}-2 F/cm^2, could be related to the mass transfer process at the electrode surface [46, 255, 256].

As can be seen from Figure 4.14a, the Rs, which is mainly attributed to the ohmic resistance of the electrolyte, decreased significantly with the increase in the cell operating temperature and reached 2.19 Ω cm^2 at 475 ºC. This means that ionic conductivity is increased at higher operating temperatures. In addition, as the operating temperatures increased, there was significant decrease in the total polarisation resistance (Rp), which is defined as the sum of R1 and R2, and the best Rp value (5.84 Ω cm^2) was obtained when the electrolytic cell operated at 475 ºC.

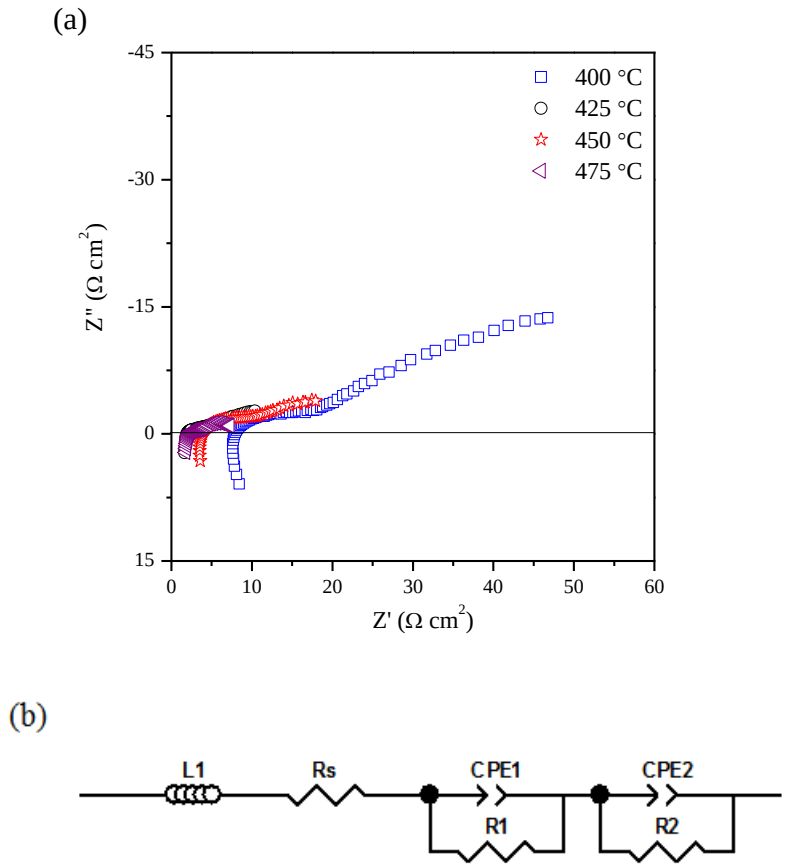

Figure 4.14 (a) Impedance spectra under open circuit conditions of the cell at 400-475 °C; (b) An equivalent circuit for the impedance data

The effect of the operating temperature on the rate of ammonia formation was investigated by varying the cell operating temperature from 400 ºC to 475 ºC and keeping the cell voltage at a constant value of 0.8 V over a period of 30 min. The ammonia produced in the catalyst (cathode) chamber was absorbed by 25 ml of diluted sulphuric acid (0.001 M). When Nessler's reagent was added to the solution, its colour changed immediately to yellow. This indicates that NH_4^+ and/or neutral NH_3 are present in the absorbed solution and that ammonia was successfully synthesised at atmospheric pressure using the LSFCu-SDC composite as a catalyst. As shown in Figure 4.15, the ammonia formation rate (r_{NH_3}) increased with an increase in working temperature and then decreased significantly when further

increasing the working temperature to over 450 °C. Furthermore, the maximum ammonia formation rate was found to be up to 5.39×10^{-9} mol s^{-1} cm^{-2} when the cell operated at 450 °C, at which temperature the corresponding current density and Faradaic efficiency were 39.16 mA/cm^2 and 3.93 % respectively. This increase in formation rate could be ascribed to the enhancement of the electrolyte ionic conductivity as the operating temperature increased. However, the decrease in the ammonia formation rate above 450 °C could be attributed to the decomposition of ammonia, although the composite electrolyte exhibited high ionic conductivity at high temperature. Table 4.1 lists the generated current densities and the corresponding Faradaic efficiencies for ammonia formation at different temperatures and constant voltage (0.8 V). It is to be noted that the generated current densities increase with an increase in the operating temperature which could be attributed to the decrease in the cell resistance (i.e. the increase in the electrolyte ionic conductivity). This means that more protons were transported through the electrolyte to the cathode surface. Similarly, the Faradaic efficiencies increase with increasing the generated current to a certain value (39.61 mA/cm^2 at 450 °C) and then the current efficiency decreased (1.50 %) although the generated current density reached a high value of 62.56 mA/cm^2 at 475 °C. These low Faradaic efficiencies indicate that there is more than one process over the cathode surface and not all protons transported to the cathode surface react with the adsorbed N_2 to generate ammonia. This means that the competitive hydrogen evolution reaction is the dominant process over the cathode surface.

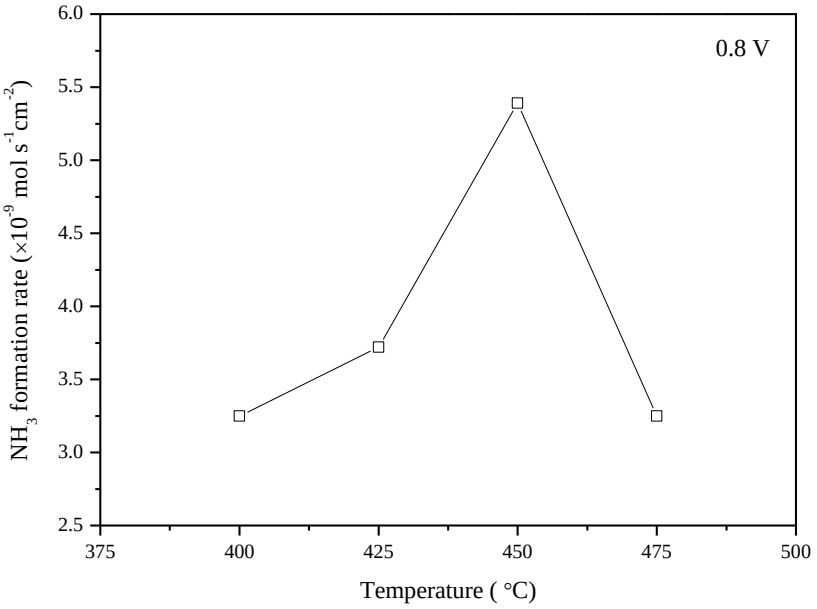

Figure 4.15 Dependence of ammonia formation rate on operating temperature. The electrolytic cell was: wet H_2, NiO-SDC|SDC-carbonate| LSFCu-SDC, dry N_2

Table 4.1 The corresponding current densities and Faradaic efficiencies of ammonia formation over LSFCu-SDC composite at different working temperatures and 0.8 V

Temperature (°C)	**Current density (mA/cm^2)**	**Faradaic efficiency (%)**
400	30.31	3.10
425	31.20	3.44
450	39.61	3.93
475	62.56	1.50

4.3.6 Synthesis of ammonia at different applied voltages

Figure 4.16 shows the electrolytic cell stability during the ammonia synthesis process at different potentials (0.2-1.2 V) at 450 °C over a period of 30 min. As can be seen, the electrolytic cell demonstrated good stability under the applied voltages, indicating stable electrochemical process. Furthermore, it was found that the current density increased with increased applied potential and reached a highest value of 56.14 mA/cm^2 when the electrolytic cell operated with an applied voltage of 1.2 V, as listed in Table 4.2. These increases in the generated current densities imply that more protons were supplied to the cathode surface.

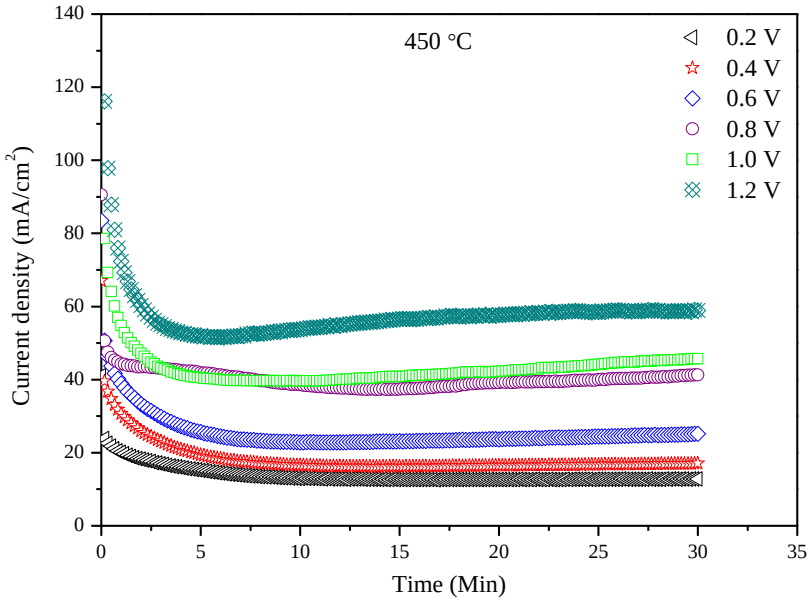

Figure 4.16 Electrolytic cell performance stability at 450 °C and 0.2-1.2 V. The electrolytic cell was wet H_2, NiO-SDC|SDC-carbonate|LSFCu-SDC, dry N_2

The effect of the applied potential on the rate of ammonia formation was investigated at 450 °C. As shown in Figure 4.17, the rate of ammonia formation increased with increasing applied potential and reached a maximum of 5.39×10^{-9} mol s^{-1} cm^{-2} at 0.8 V, at which the generated current density and current efficiency were 39.61 mA/cm^2 and ~ 4% respectively, as listed in Table 4.2. However, the rate of ammonia formation decreased significantly when further increasing the applied potential above 0.8 V and reached a lowest value of 3.35×10^{-9} mol s^{-1} cm^{-2} with an applied potential of 1.2 V. This low rate of ammonia formation corresponds to a current efficiency of 1.73 % at current density of 56.14 mA/cm^2. As described above, the low current efficiencies indicate that there is more than one process occurring and the hydrogen evolution reaction is the dominant one [41, 70]. In this study, the maximum formation rate was 5.39×10^{-9} mol s^{-1} cm^{-2} at 450 °C with an applied potential of 0.8 V. This is comparable to that reported by Wang et al. [75] using $Ba_{0.5}Sr_{0.5}Co_{0.8}Fe_{0.2}O_{3-\delta}$ (BSCF) and $BaCe_{0.85}Y_{0.15}O_{3-\delta}$ (BCY) as cathode and electrolyte respectively (4.1×10^{-9} mol s^{-1} cm^{-2}).

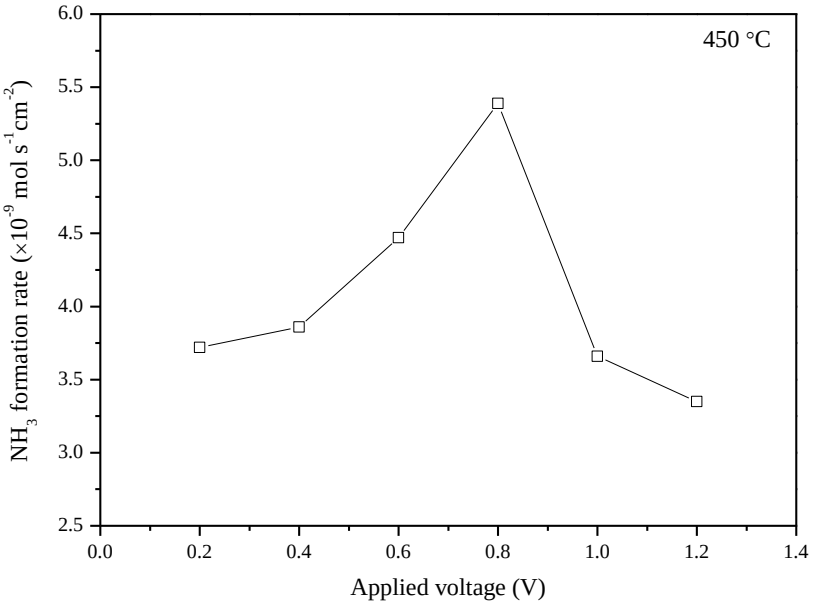

Figure 4.17 Dependence of the rate of ammonia formation on the applied voltage at 450 °C. The electrolytic cell was wet H_2, NiO-SDC|SDC-carbonate| LSFCu-SDC, dry N_2

Table 4.2 The corresponding current densities and Faradaic efficiencies of ammonia formation over LSFCu-SDC composite at 450 °C

Applied voltage (V)	**Current density (mA/cm^2)**	**Faradaic efficiency (%)**
0.2	13.40	8.03
0.4	17.27	6.47
0.6	24.18	5.35
0.8	39.61	3.93
1.0	41.95	2.52
1.2	56.14	1.73

4.4 Conclusion

In this study, $La_{0.6}Sr_{0.4}Fe_{0.8}Cu_{0.2}O_{3-\delta}$ (LSFCu) and $Ce_{0.8}Sm_{0.2}O_{2-\delta}$ (SDC) were synthesised via a combined EDTA-citrate complexing sol-gel process and glycine nitrate process, respectively. A composite electrolyte consisting of SDC-

$(Li/Na/K)_2CO_3$ (70:30 wt %) was prepared via solid state reaction. The properties of these materials, including phase compositions, microstructure, electronic conductivities and thermal behaviours were investigated. The highest DC electrical conductivity of LSFCu in air was found to be ~ 19 S cm^{-1} at 470 °C. The ionic conductivity of the composite electrolyte (SDC-carbonate) was studied under three different atmospheres (air, dry O_2 and wet 5% H_2-Ar). The ionic conductivity was found to 0.35-4.91 × 10^{-6}, 0.37-4.61 × 10^{-5} and 0.24-4.14 × 10^{-4} S cm^{-1} with the measured temperature range of 600-300 °C in air, dry O_2 and wet 5% H_2-Ar respectively. A tri-layer electrolytic cell was successfully fabricated by a cost-effective one-step dry-pressing and co-firing process. Ammonia was successfully synthesised from wet hydrogen and dry nitrogen under atmospheric pressure, using NiO-SDC, SDC-$(Li/Na/K)_2CO_3$ and LSFCu-SDC composites as anode, electrolyte and cathode, respectively. The maximum rate of ammonia production was found to be 5.39×10^{-9} mol s^{-1} cm^{-2} at 450 °C and 0.8 V. This rate formation is higher than those of Co_3Mo_3N-Ag, $CoFe_2O_4$-Ag and Fe_3Mo_3N-Ag composite cathodes (10^{-10} mol s^{-1} cm^{-2}), presented previously in Chapter 3.

5 Ammonia synthesis from water and nitrogen, based on spinel type cathode and Ca and Gd co-doped ceria-carbonate composite electrolyte

5.1 Introduction

The conversion of molecular nitrogen into ammonia is a very important chemical process. Ammonia is predominantly synthesised on a large-scale via the Haber-Bosch process and its global production in 2011 was 136 million metric tons [5, 20]. Currently, the production of hydrogen gas for ammonia synthesis relies entirely on steam reforming of natural gas or coal, which consumes approximately 84 % of the energy required for ammonia industry. In addition, approximately 2.3 tons of fossil-derived CO_2 are released per ton of NH_3 produced [6, 7] and more than 300 million metric tons of CO_2 are generated per year from industrial ammonia production [302].

As discussed previously in Chapter 1, the electrochemical synthesis of ammonia is an attractive alternative to the Haber-Bosch process [8, 41, 43]. In the literature, most attention is focused on the use of H_2 and N_2 to produce ammonia. However, the use of H_2 is not preferred, due to the problems associated with its production, purification, transportation and storage [161, 162]. The synthesis of ammonia from other non-fossil resources hydrogen sources without the need for the steam reforming step would be more favourable for the future ammonia industry [9]. Water is considered as the most abundant and cleanest hydrogen source. Therefore, the synthesis of ammonia directly from water and nitrogen is advantageous because hydrogen production stage has been by-passed [9-11]. However, there are few reports in the literature of ammonia being synthesised electrochemically from H_2O and N_2 without the need for molecular hydrogen [9, 10, 70].

As mentioned in Chapters 1 and 4, doped ceria based materials are among the promising electrolytes for the applications in the intermediate temperature regions. The most effective dopants for ceria (CeO_2) are Sm and Gd cations, by which its ionic conductivity is enhanced [107, 146, 303]. In addition, several studies have shown that the ionic conductivities of singly-doped ceria oxides (e.g. SDC or GDC) could be further improved by a co-doping strategy. Wang et al. [304] reported that

Gd and Sm co-doped ceria exhibit much higher ionic conductivity compared to singly-doped ceria solid solution. Guan et al. [305] have also investigated the co-doping effect on the conductivity of Gd-doped ceria (GDC) and it was found out that the ionic conductivity (0.013 S cm^{-1} at 500 °C) of Gd and Y co-doped CeO_2 is three times higher than that of GDC ($Ce_{0.8}Gd_{0.2}O_{1.9}$). However, the above studied co-dopants are very expensive. Therefore, from the point of view of material cost, exploring new and more cost-effective electrolyte materials with stable compositions and improved properties is of practical importance. On the other hand, calcium (Ca^{2+}), the divalent cation, is economically viable and readily available [306]. In addition, it has been reported that the grain boundary conduction in doped ceria oxides (e.g. GDC and YDC) can be enhanced by the addition of 2 mol % CaO. This was attributed to that the presence of CaO will eliminate the impurities located at the grain boundary in particular SiO_2 [307-309]. However, the drawbacks of the pure ceria phase, such as electronic conduction, could not be eliminated either by single- or co-doping approaches [168].

In the literature, it has been reported that doped ceria-carbonate composite electrolytes exhibit high ionic conductivity (> 0.1 S cm^{-1}) below 600 °C, which higher than that of pure doped ceria. The conductivity enhancement of the composite electrolyte is believed to be due to the composite effect [157, 165-167]. In addition, the presence of the carbonate as second phase is found to suppress the electronic conduction of the pure ceria phase that is caused by the partial reduction of Ce^{4+} to Ce^{3+} in a reducing atmosphere [156, 165]. In recent years, a combination between the two approaches (i.e. co-doping and composite effects) has been proposed to prepare materials with improved properties (e.g. high ionic conductivity). Recently, several studies have demonstrated that co-doped ceria-carbonate composite electrolytes, including $Ce_{0.8}Gd_{0.05}Y_{0.15}O_{2-\delta}$-$(Li/Na)_2CO_3$ [167], $Ce_{0.8}Sm_{0.1}Nd_{0.1}O_{2-\delta}$-$(Li/Na)_2CO_3$ [310] and $Ce_{0.8}Sm_{0.18}Ca_{0.02}O_{2-\delta}$-$Na_2CO_3$ [168] exhibit high ionic conductivities at low and intermediate temperatures.

As mentioned earlier in Chapter 4, $Sm_{0.5}Sr_{0.5}CoO_{3-\delta}$ (SSCo) is one of the perovskite-based oxides which have been used as a cathode in solid oxide fuel cells and electrochemical synthesis of ammonia applications [119, 285]. In addition,

because of its activity for oxygen evolution, it was used as an anode (oxygen electrode) in solid oxide steam electrolysis cells [311]. The aim of this chapter is to investigate the electrochemical synthesis of ammonia from water and nitrogen, using spinel type catalyst, an oxygen-ion conducting electrolyte (Ca and Gd co-doped ceria-carbonate composite) and a perovskite-based anode (SSCo).

5.2 Experimental

5.2.1 Synthesis of materials

5.2.1.1 Synthesis of CFO catalyst

$CoFe_2O_4$ (CFO) spinel was synthesised via a combined EDTA-citrate complexing sol-gel process [291]. ($Fe(NO_3)_3 \cdot 9H_2O$, Alfa Aesar, 98%) and cobalt nitrate ($Co(NO_3)_2 \cdot 6H_2O$, Sigma Aldrich, 98 + %) were used as starting materials. Calculated amounts of $Fe(NO_3)_3 \cdot 9H_2O$ and $Co(NO_3)_2 \cdot 6H_2O$ were dissolved in deionised water. Citric acid and EDTA were then added as complexing agents, with molar ratio of citric acid:EDTA:metal cations of 1.5:1:1. Ammonia solution was added to the mixed solution to adjust the pH value to around 6. The solution was evaporated under heating and stirring on a hot-plate, and then gradually changed into a black sticky gel before complete drying. The as-prepared powder was ground and subsequently calcined in air at 900 ºC for 3 h with heating/cooling rates of 5 ºC min^{-1} to obtain a pure phase of CFO catalyst without carbon residue.

5.2.1.2 Synthesis of SSCo

$Sm_{0.5}Sr_{0.5}CoO_{3-\delta}$ catalyst (SSCo) was also synthesised via a combined EDTA-citrate complexing sol-gel process as described above. Samarium oxide (Sm_2O_3, Alfa Aesar, 99.9 %), strontium nitrate ($Sr(NO_3)_2$, Alfa Aesar, 99 %) and cobalt nitrate ($Co(NO_3)_2 \cdot 6H_2O$, Sigma Aldrich, 98 + %) were used as starting materials. Sm_2O_3 was dissolved in diluted nitric acid to form samarium nitrate. The resultant powder

was ground and subsequently fired in air at 900 ºC for 2 h, with heating/cooling rates of 5 ºC min^{-1}, to obtain a pure phase of SSCo catalyst without carbon residue.

5.2.1.3 Synthesis of GDC and CGDC powders

Gd-doped ceria (GDC) powder with a composition of ($Ce_{0.8}Gd_{0.2}O_{2-\delta}$) was synthesised via a combined EDTA-citrate complexing sol-gel process. Gadolinium oxide (Gd_2O_3, Alfa Aesar, 99.9 %) and cerium nitride hexahydrate ($Ce(NO_3)_3 \cdot 6H_2O$, Alfa Aesar, 99 %) %) were used as starting materials. Gd_2O_3 was dissolved in diluted nitric acid to form gadolinium nitrate. Calculated amounts of $Ce(NO_3)_3 \cdot 6H_2O$ was dissolved in deionised water and mixed with gadolinium nitrate solution. Citric acid (Alfa Aesar, 99 %) and EDTA (, Alfa Aesar, 99 %) were then added as complexing agents, with a ratio of citric acid: EDTA: metal cations of 1.5:1:1. Dilute aqueous ammonia solution was then added to the mixed solution, to adjust the pH value to around 6. The solution was evaporated under heating and stirring on a hot-plate and then gradually changed into a brown sticky gel before complete drying, leaving a porous yellow ash. Finally, the resultant ash was ground and subsequently calcined in air at 700 °C for 2 h, with heating/cooling rates of 5 °C min^{-1}, to obtain a single phase of GDC.

Gd and Ca co-doped ceria (CGDC) powder with a composition of ($Ce_{0.8}Gd_{0.18}Ca_{0.02}O_{2-\delta}$) was also synthesised via a combined EDTA-citrate complexing sol-gel process as described above. Gadolinium oxide (Gd_2O_3, Alfa Aesar, 99.9 %), cerium nitride hexahydrate ($Ce(NO_3)_3 \cdot 6H_2O$, Alfa Aesar, 99 %) and calcium nitrate tetrahydrate ($Ca(NO_3)_2 \cdot 4H_2O$, Alfa Aesar, 99 %) were used as starting materials. The resultant ash was ground and subsequently calcined in air at 700 °C for 2 h, with heating/cooling rates of 5 °C min^{-1}, to obtain a single phase of CGDC.

5.2.2 Preparation of the composite electrolyte

The ternary eutectic salt ($(Li/Na/K)_2CO_3$) was prepared by solid state reaction. Lithium carbonate (Li_2CO_3, Alfa Aesar, 98 %), sodium carbonate (Na_2CO_3, Aldrich,

99.5+ %) and potassium carbonate (K_2CO_3, Alfa Aesar, 99 %) were mixed with molar ratios of 43.5:31.5:25, respectively. The mixture was ball milled in isopropanol for 9 h and dried on a hot-plate and then ground and calcined in air at 600 °C for 1 h and air quenched directly to room temperature. The composite electrolyte CGDC-$(Li/Na/K)_2CO_3$ was also prepared by solid state reaction. The prepared CGDC powder was mixed with the previously prepared ternary carbonate salt, at weight ratio of 70:30. The mixture was ball milled in isopropanol for 9 h. The material was fired in air at 600 °C for 1 h, before being quenched to room temperature. The resultant mixture was dried and then ground thoroughly for subsequent use.

5.2.3 Characterisation of materials

X-ray diffraction (XRD) data were collected at room temperature using a Panalytical X'Pert Pro diffractometer. The microstructures of the prepared catalyst and the cross-sectional area of a single cell were examined using a Hitachi SU 6600 Scanning Electron Microscope (SEM). The thermal behaviour (TGA/DSC) of the composite electrolyte was studied in three different atmospheres (air, O_2 and 5% H_2-Ar), from room temperature to 600 ºC, with a heating/cooling rate of 10 ºC/min. The thermal behaviour of CFO catalysts was studied in N_2 atmosphere from room temperature to 500 ºC, with heating/cooling rates of 10 ºC/min. A platinum crucible was used for carbonate containing samples

5.2.4 Fabrication of the single cells

A tri-layer single cell was fabricated by a cost-effective one-step dry-pressing method. The composite anode was prepared by mixing in a mortar SSCo, CGDC and starch as pore former, with weight ratio of 70:30:15. The electrolyte was CGDC/$(Li/Na/K)_2CO_3$ composite (70:30 wt %). The composite cathode was prepared by mixing CFO and CGDC and starch, with weight ratio of 70:30:15, in a mortar. The composite anode, composite electrolyte and composite cathode were fed into the

die, layer by layer, with the aid of a sieve to ensure uniform powder distribution, and then uniaxially pressed at pressure of 121 MPa. The freshly made green pellet was sintered in air at 700 °C for 2 h at a rate of 2°C/min heating/cooling. The active surface area of the cathode was 0.785 cm^2. Silver paste was painted in a grid pattern on each electrode surface of the cell, as a current collector. Ag wires were used as output terminals for both electrodes.

5.2.5 Pellet preparation for conductivity measurement

The composite electrolyte powder (CGDC-carbonate) was uniaxially dry-pressed at pressure of 259 MPa into pellets with diameter of 13 mm and thickness of ~ 2 mm. The green pellets were sintered in air at 600 and 700 ºC for 2 h, at a rate of 2 ºC heating/cooling. The pellets were brushed on both sides with Ag paste to serve as electrodes. AC impedance measurements were performed in three atmospheres, namely, air, dry O_2 (dried through a solution of H_2SO_4 at 98%) and wet 5% H_2-Ar. The GDC and CGDC powders were uniaxially dry-pressed at pressure of 259 MPa into pellets with diameter of 13 mm and thickness of ~ 2 mm. The pellets were sintered in air at 1300 ºC for 4 h. The relative density of both pellets was ~ 94 %. The pellets were brushed on both sides with Ag paste to serve as electrodes and the conductivity was measured in air within the temperature range of 300-600 ºC (Section 2.4.1).

5.2.5.1 Synthesis of ammonia

The fabricated single cell for ammonia synthesis was sealed into a self-designed double chamber reactor using ceramic paste (Aremco, Ceramabond 552). The electrolytic cell constructed was as follows: Air, SSCo-CGDC|CGDC-carbonate|CFO-CGDC, 3% H_2O-N_2. The cathode chamber was fed with 3%H_2O-N_2 (BOC). The water vapour (3% H_2O) was supplied to the cathode chamber by bubbling a N_2 stream through a liquid water container, at 25°C. The anode was exposed to air. A constant voltage (1.2-1.8 V) was applied for a period of 30 min. The ammonia synthesised at the cathode chamber was absorbed by 20 ml of diluted

HCl (0.01 M). The concentration of NH_4^+ in the absorbed solution was analysed using ion selective electrode (ISE) and the rate of ammonia formation was calculated using Equation 2.9 (Section 2.4.2).

5.3 Results and discussion

5.3.1 XRD analysis

Single phase fluorite oxides of $Ce_{0.8}Gd_{0.2}O_{2-\delta}$ (GDC) and $Ce_{0.8}Gd_{0.18}Ca_{0.02}O_{2-\delta}$ (CGDC) were obtained when their ashes were calcined in air at 700 °C for 2 h. The X-ray diffraction patterns of GDC (Figure 5.1a) and CGDC (Figure 5.1b) show a typical cubic fluorite oxide structure, which is in good agreement with JCPDS file 34-0394. The calculated lattice parameters, *a*, from the XRD patterns of the samples were found to be 5.4196 Å for GDC and 5.4213 Å for CGDC. At co-ordination number of 8, the ionic size of Ca^{2+} (1.12 Å) is slightly larger than those of Ce^{4+} (0.97 Å) and Gd^{3+} (1.06 Å). Therefore, adding CaO will result in a slight increase in the lattice parameters [308]. The crystallite size of GDC is ~ 18.56 nm while that of CGDC is ~ 21.03 nm, estimated from Sherrer's formula (Equation 2.3).

The powder XRD patterns of the ternary carbonate, pure CGDC and CGDC-$(Li/Na/K)_2CO_3$ composite electrolytes are shown in Figure 5.2a-c. As can be seen from Figure 5.2a, the ternary carbonate which was calcined in air at 600 ºC for 1 h shows a complicated phase composition. The XRD pattern of CGDC-carbonate composite calcined in air at 600 ºC for 1 h and quenched directly to room temperature is presented in Figure 5.2c. As can be seen, the major peaks could be ascribed to the pure CGDC phase (Figure 5.2b), indicating that the ternary carbonates in the composite electrolyte are present in an amorphous phase. The lattice parameter, *a*, for CGDC after the addition of the ternary carbonate ($(Li/Na/K)_2CO_3$) was 5.4202 Å which slightly smaller than that of pure CGDC (5.4213 Å). The possible reason is that some large Gd^{3+}/Ca^{2+} ions are replaced by smaller Li^+ ions [312]. The crystallite size of CGDC-carbonate composite is ~ 24.49 nm, estimated from Sherrer's formula (Equation 2.3).

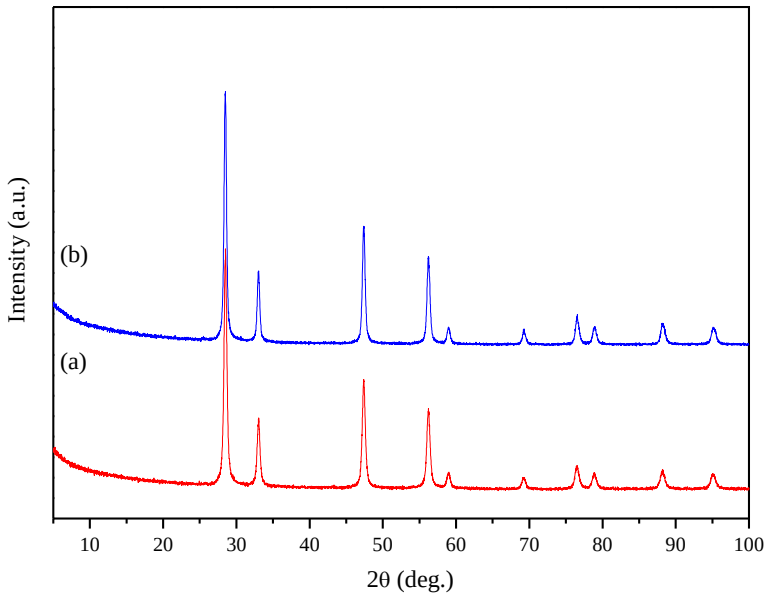

Figure 5.1 The XRD patterns of: (a) (GDC); (b) CGDC fired in air at 700 ºC for 2 h

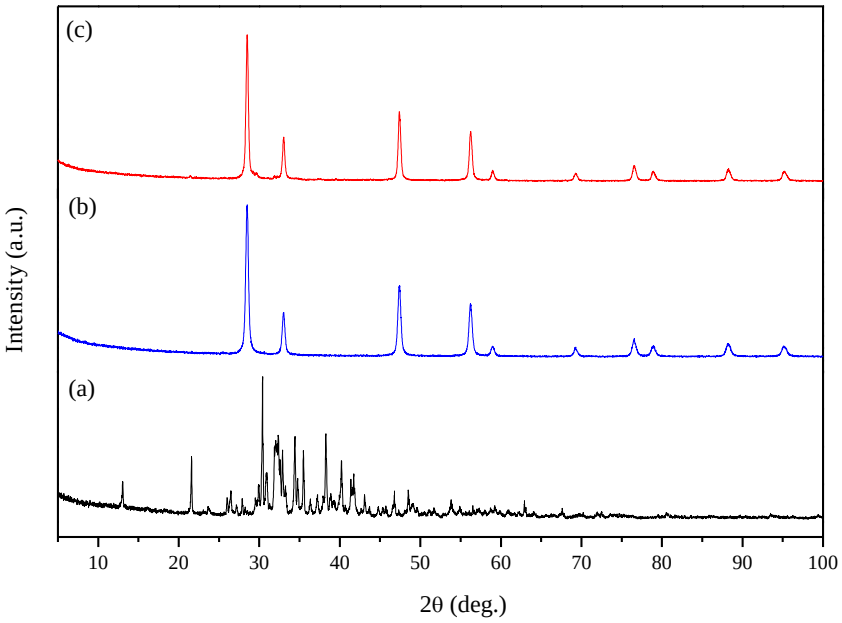

Figure 5.2 XRD patterns of (a) $(Li/Na/K)_2CO_3$ calcined in air at 600 ºC for 1 h; (b) pure CGDC; (c) CGDC-$(Li/Na/K)_2CO_3$ (70:30 wt%) calcined in air at 600 ºC for 1 h

The powder XRD patterns of the pure CFO and CFO-CGDC composite cathode respectively are shown in Figures 5.3a-c. As can be seen from Figure 5.3b, a single phase of spinel (CFO) was obtained after firing the precursor in air at 900 ºC for 3 h. This pattern is in good agreement with the standard XRD pattern for cobalt ferrite with cubic structure (JCPDS no. 22-1086). The XRD patterns of CGDC, SSCo and the composite anode are shown in Figures 5.4a-c. As can be seen from Figure 5.4, single phase perovskite oxide of SSCo was obtained by firing the ash in air at 900 ºC for 2 h. The crystallite size of CFO and SSCo were found to be 47.69 and 27.30 nm respectively, estimated from Sherrer's formula (Equation 2.3). In order to investigate the chemical compatibility of the cathode (CFO) and the anode (SSCo) materials with the CGDC, the composite cathodes and composite anode containing CGDC were fired in air at the single cell sintering temperature (700 ºC). The XRD patterns of the composite cathode (CFO-CGDC) and the composite anode (SSCo-CGDC) are shown in Figures 5.3c, and 5.4c respectively. In all cases, no extra peaks were found and the only peaks detected correspond to the individual component of the cathode and the anode composites. This indicates that both CFO and SSCo are chemically compatible with CGDC at the single cell sintering temperature.

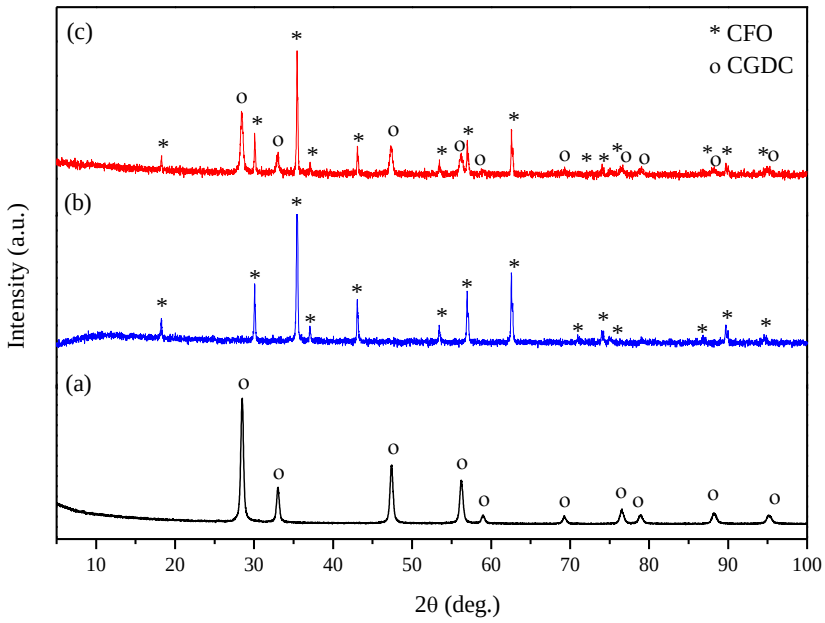

Figure 5.3 XRD patterns of (a) pure CGDC; (b) CFO fired in air at 900 ºC for 3 h; (c) CFO-CGDC composite cathode fired in air at 700 ºC

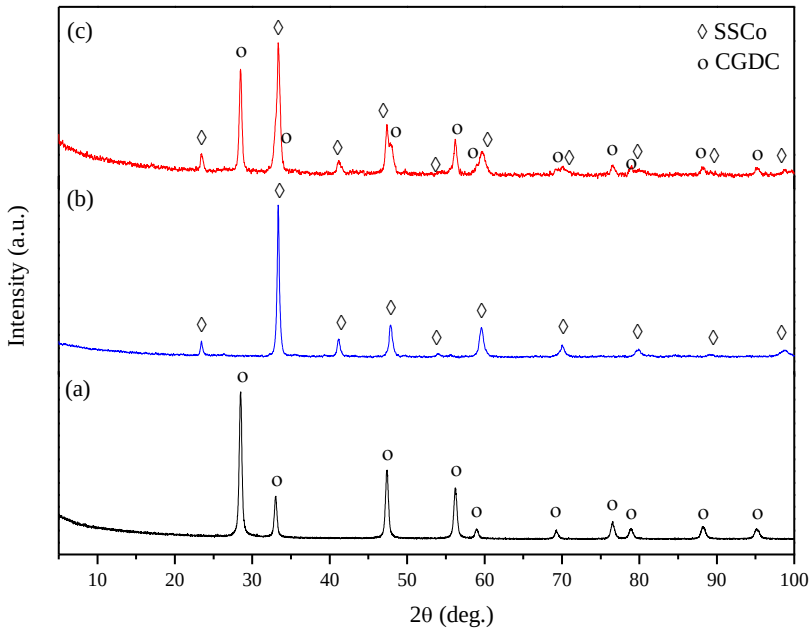

Figure 5.4 XRD patterns of (a) pure CGDC; (b) SSCo fired in air at 900 ºC for 2 h; (c) SSCo-CGDC composite anode fired in air at 700 ºC

5.3.2 Microstructure of spinel-type catalyst

The microstructures of CFO powder calcined in air at 900 ºC for 3 h was investigated by SEM, as shown in Figure 5.5a. As can be seen, the catalyst morphology consists of large grains surrounded by small homogenous primary grain particles and many pores. Figure 5.5b represents the microstructure of the cross-sectional area of single cell (before testing) based on CFO-CGDC composite cathode, sintered in air at 700 ºC for 2 h. As can be seen, the sintered cell shows good adhesion at the interface between the porous electrodes (anode and cathode) and the dense electrolyte (CGDC-carbonate composite).

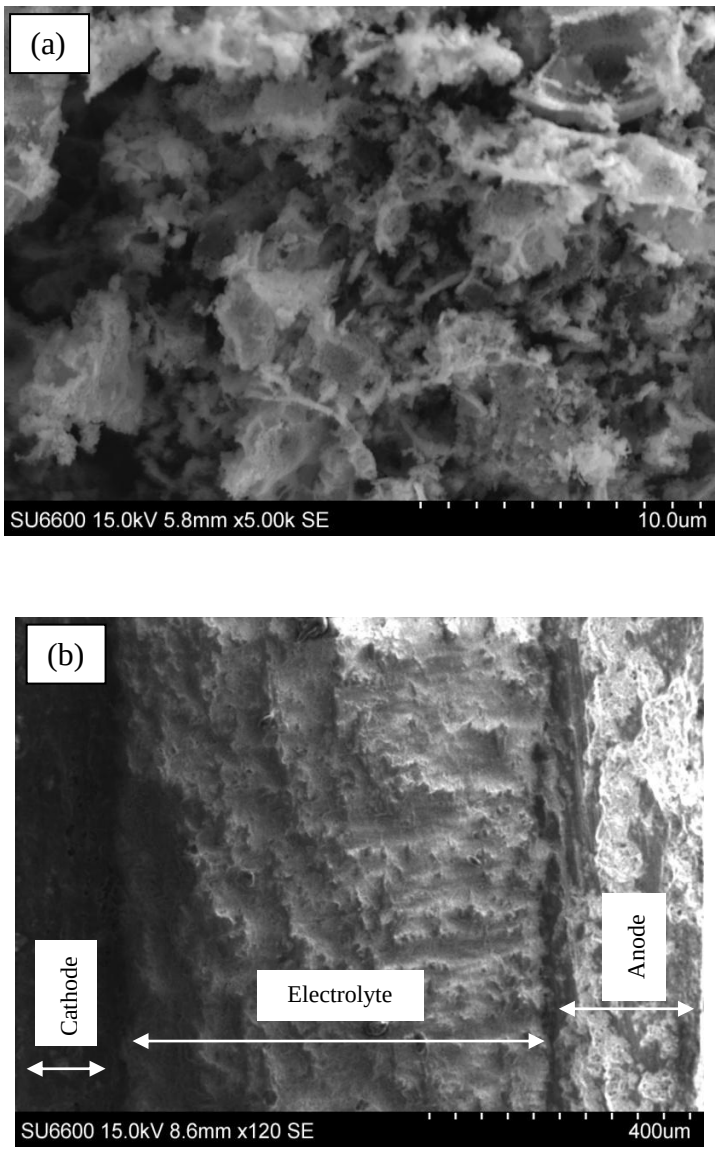

Figure 5.5 SEM images of: (a) CFO calcined in air at 900 ºC for 3 h; (b) cross-sectional areas of a single cell based on a CFO-CGDC composite cathode sintered in air at 700 ºC for 2 h

5.3.3 Thermal analysis

The thermal behaviour of CGDC-$(Li/Na/K)_2CO_3$ composite electrolyte calcined in air at 600 ºC for 1 h was studied in different atmospheres (air, O_2 and 5% H_2-Ar), as shown in Figures 5.6a-d. As can be seen, the composite electrolyte exhibits almost similar thermal behaviour in each of the atmospheres under investigation. Upon

heating, some endothermic peaks were observed, accompanied by several stages of weight loss, depending on the atmosphere used. In the temperature range from room temperature to 200 ºC, small endothermic peaks were observed, which could be attributed to the loss of adsorbed water. Within the temperature range of 300-600 ºC, strong endothermic peaks were observed at 397.24, 388.03 and 387.27 ºC in air, O_2 and 5% H_2-Ar respectively. These could be ascribed to the melting point of the $(Li/Na/K)_2CO_3$ ternary carbonate (~ 400 ºC) [235]. Upon cooling, a strongly exothermic event was observed in each atmosphere, which can be attributed to the solidifying of the ternary carbonate. These exothermic peaks are located at 379.95, 349.04 and 336.97 ºC for air, O_2 and 5% H_2-Ar respectively. Furthermore, the total weight loss in air was about 1.01 %, whereas in O_2 and H_2-Ar atmospheres weight losses were approximately 0.87 % and 1.21 % respectively. This suggests that the composite electrolyte is quite stable in the atmospheres under investigation.

In addition, the thermal behaviour of the composite electrolyte was studied in air at 800 ºC (Figure 5.6b) in order to investigate if the observed peak on cooling at ~ 525 ºC when the sample was heated in air up 600 ºC (Figure 5.6a) is related to a phase change. As can be seen from Figure 5.6b, the sample heated up to 800 ºC exhbits the similar behaviour of the sample heated up to 600 ºC, but no peak was observed at ~ 525 ºC. This indicates this peak is not related to phase change and this peak appeared due the to the fact that the sample was heated and cooled directly without the dwelling step.

Figures 5.7a-c show the XRD patterns of the composite electrolyte after thermal analysis in different atmospheres (air, O_2 and 5% H_2-Ar respectively). As can be seen, the composite electrolyte retains the same fluorite structure after thermal analysis and no phase change was observed, suggesting its thermal stabilities

(a)

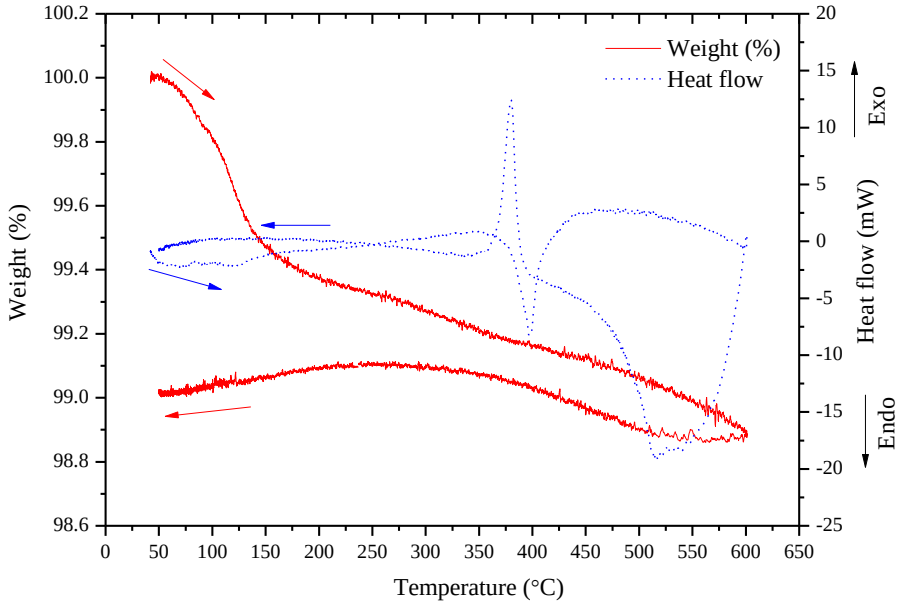
Weight (%)
Heat flow
Exo
Endo
Weight (%)
Heat flow (mW)
Temperature (°C)
100.2
100.0
99.8
99.6
99.4
99.2
99.0
98.8
98.6
20
15
10
5
0
-5
-10
-15
-20
-25
0
50
100
150
200
250
300
350
400
450
500
550
600
650

(b)

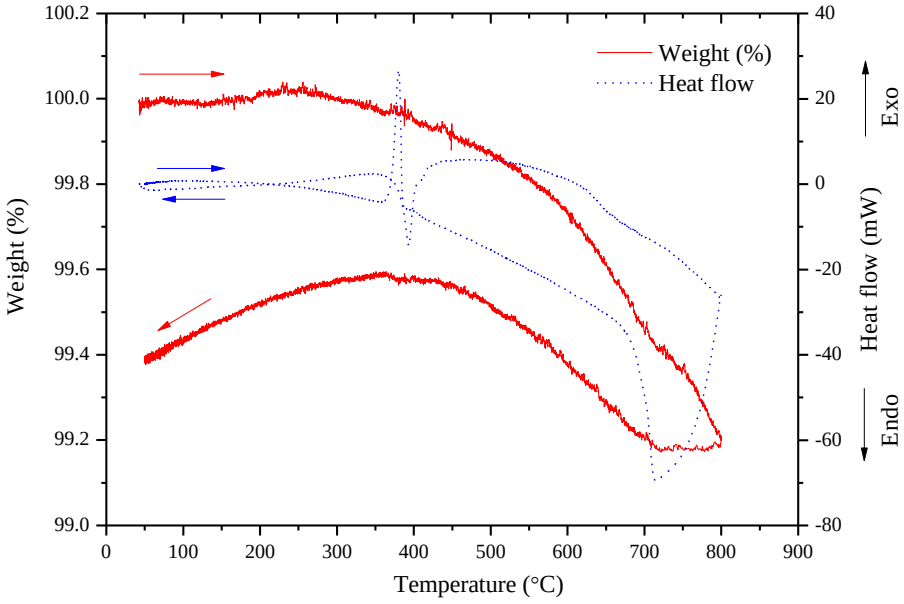
Weight (%)
Heat flow
Exo
Endo
Weight (%)
Heat flow (mW)
Temperature (°C)
100.2
100.0
99.8
99.6
99.4
99.2
99.0
40
20
0
-20
-40
-60
-80
0
100
200
300
400
500
600
700
800
900

(b)

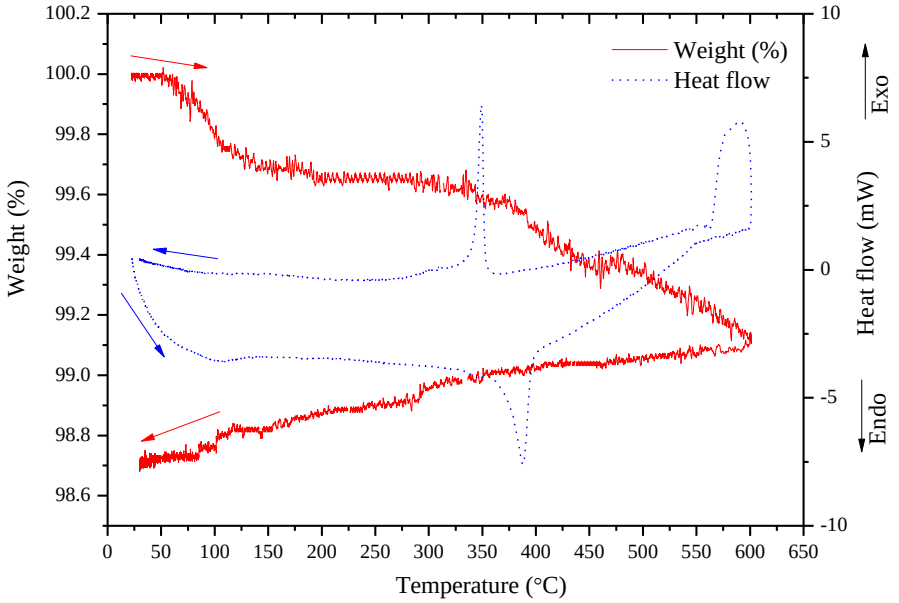

(c)

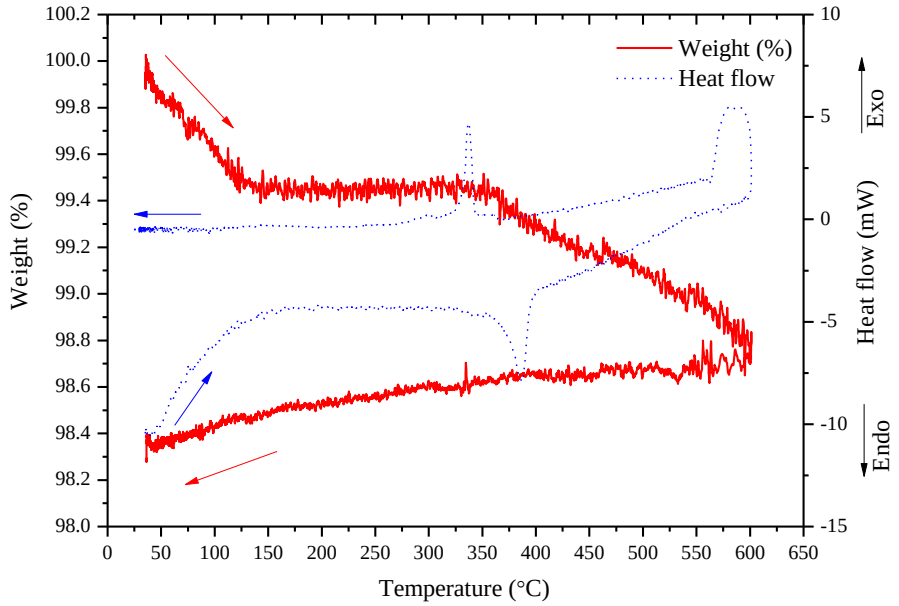

Figure 5.6 TGA-DSC curves of CGDC-carbonate composite in different atmospheres: (a) air at 600 ºC; (b) air at 800 ºC; (c) O_2; (d) 5% H_2-Ar

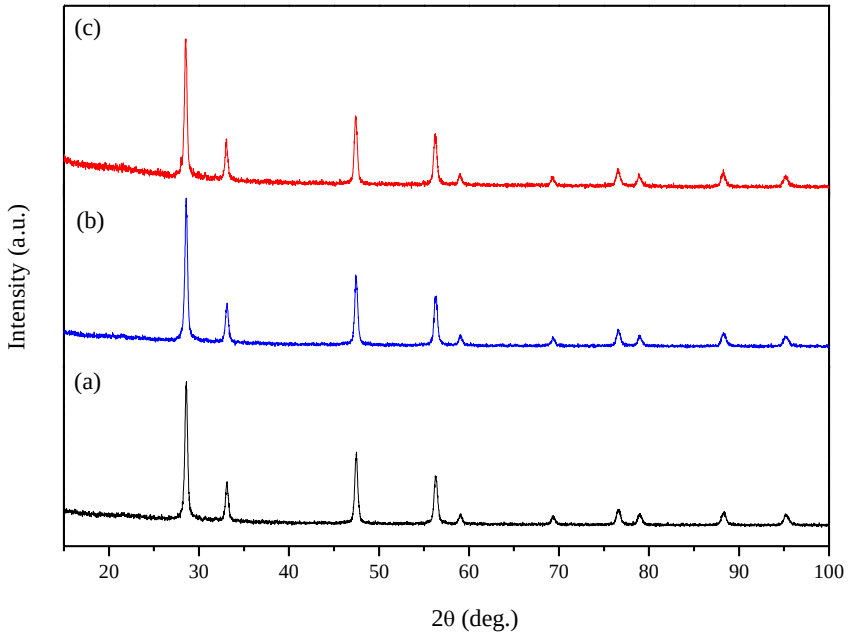

Figure 5.7 XDR patterns of CGDC-carbonate composite after thermal analysis in different atmospheres: (a) air; (b) O_2; (c) 5% H_2-Ar

The thermal behaviour of CFO cathode was also investigated under N_2, as the cathode is exposed to this atmosphere during the ammonia synthesis. Figure 5.8 shows TGA-DSC curves of CFO cathode in N_2 atmosphere from room temperature up to 500 °C, at a heating/cooling rate of 10 °C/min. In the temperature range from room temperature up to 200 ºC, small endothermic peak was observed at ~ 75 ºC, accompanied by weight losses of about 0.28 % which could be attributed to the loss of adsorbed water. Between 200 and 500 ºC, no significant weight loss was observed and the total weight loss was about 0.37 %. The DSC curve shows no obvious thermal effects, indicating that there are no phase transitions or sample decomposition and there is no reaction between the spinel cathode (CFO) and N_2 in the measured temperature range. This suggests that CFO is thermally stable in N_2 within the measured temperature range. Figure 5.9 shows the XRD pattern of CFO after thermal analysis. As can be seen, the oxide retains the same spinel structure, indicating its thermal stabilities in a N_2 atmosphere in the measured temperature range.

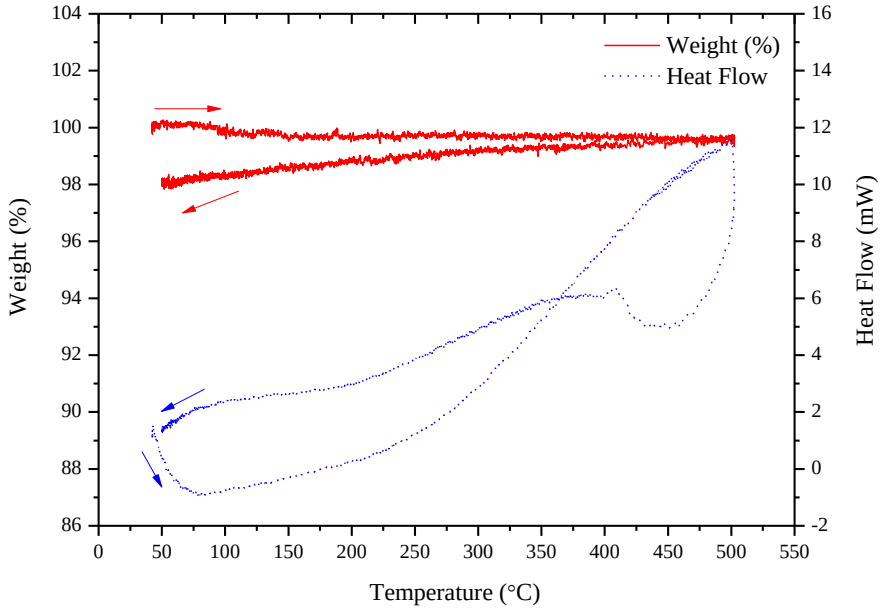

Figure 5.8 TGA-DSC curves of CFO in nitrogen up to 500 ºC.

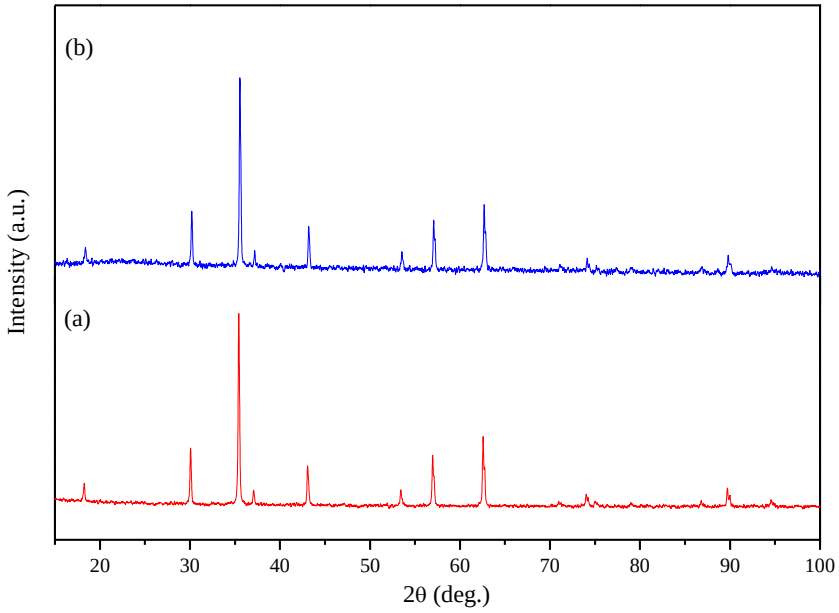

Figure 5.9 XDR patterns of CFO: (a) before thermal analysis; (b) after thermal analysis

5.3.4 The ionic conductivity of the composite electrolyte

The conductivity of CGDC-$(Li/Na/K)_2CO_3$ was measured by EIS in air within the temperature range of 300-600 ºC. For comparison, the conductivities of pure GDC and CGDC were measured under the same condition. Figure 5.10 shows the typical impedance spectra of the GDC, CGDC and CGDC-carbonate composite at 600 ºC in air. As can be seen, only the electrode contribution was observed in all cases. The dependence of the total ionic conductivity on temperature is shown in Figure 5.11. As can be seen, the conductivity of the composite electrolyte was higher than those of singly (GDC) and co-doped ceria (CGDC). At 600 ºC, the conductivity of the composite electrolyte reached a value of ~ 0.49 S cm^{-1}, while those for GDC and CGDC were 8.13×10^{-3} and 1.12×10^{-2} S cm^{-1} respectively. The enhancement of the ionic conductivity composite electrolyte compared to GDC and CGDC is due to the composite effect which will be discussed below.

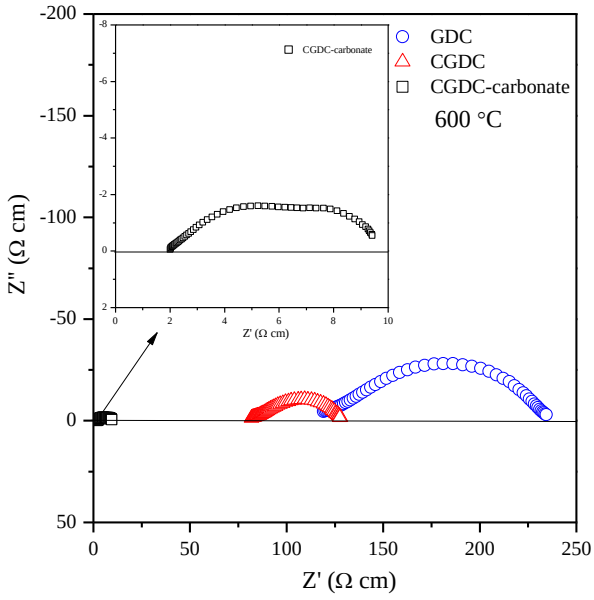

Figure 5.10 Impedance spectra in air at 600 ºC

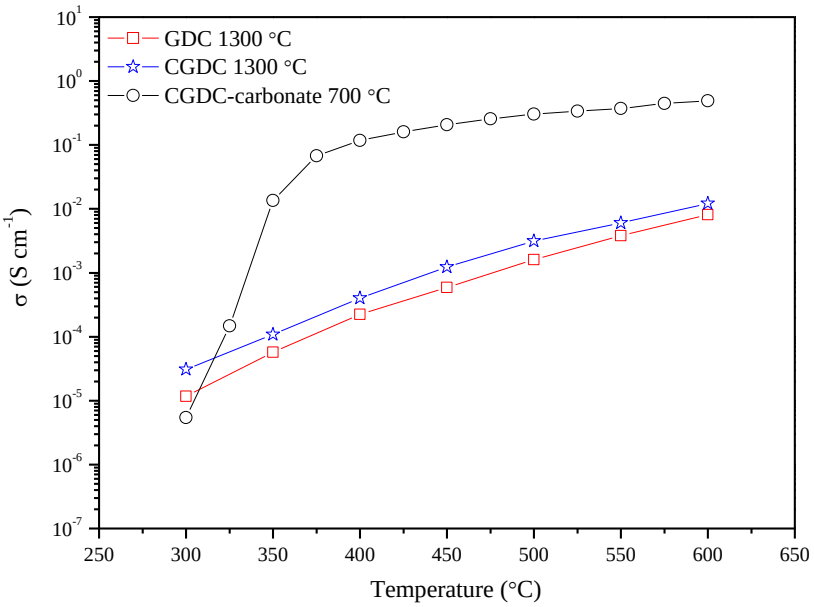

Figure 5.11 AC conductivity plot in air against temperature for CGDC-$(Li/Na/K)_2CO_3$ compared to GDC and CGDC

The AC ionic conductivities of the composite electrolyte (CGDC-carbonate) were also investigated under different atmospheres (air, dry O_2 and wet 5% H_2-Ar). In addition, the effect of the sintering temperature on the ionic conductivities was also investigated. Figures 5.12a and b show the AC conductivity of CGDC-carbonate composite sintered at different temperatures, 600 ºC and 700 ºC respectively. As can be seen, the ionic conductivity in both cases increased with temperature. Furthermore, it can be clearly seen that the conductivity changed at two regions below and above ~ 375 ºC, which is 25 ºC lower than melting point of the ternary carbonate (~ 400 ºC) [235]. In air, for the sample sintered at 600 ºC (Figure 5.12a), the conductivity changed from 0.31 S cm^{-1} to 2.88 × 10^{-5} S cm^{-1} at 600 ºC and 300 ºC respectively. The sample sintered at 700 ºC (Figure 5.12b) exhibits the highest ionic conductivity, ranging from 0.49 S cm^{-1} to 7.31 × 10^{-6} S cm^{-1} at 600 ºC and 300 ºC respectively. These values are higher than those of CGDC (1.22 × 10^{-2} S cm^{-1}) and GDC (8.13 × 10^{-3} S cm^{-1}) in air at 600 ºC.

A similar behaviour to that described above, in which the ionic conductivity increases with temperature, was also observed when the measurements were

performed in dry O_2 and wet 5% H_2-Ar atmospheres, as shown in Figures 5.12a and b for sample sintered at 600 and 700 ºC respectively. In dry O_2, the conductivity was in the range of 0.38 - 2 × 10^{-5} S cm^{-1} and 0.50-3.34 × 10^{-5} S cm^{-1} at 600-300 ºC, for the samples sintered at 600 ºC (Figure 5.12a) and 700 ºC (Figure 5.12b) respectively. For measurements in wet 5% H_2-Ar, it can be seen that the conductivity for the sample sintered at 600 ºC (Figure 5.12) changed from 0.38 S cm^{-1} to 6.87 × 10^{-4} S cm^{-1} at 600 ºC and 300 ºC respectively, while for the sample sintered at 700 ºC (Figure 5.12), the conductivity was in the range of 0.52-1.21×10^{-3} S cm^{-1} at 600 ºC and 300 ºC respectively. These values of conductivity are higher than those of $LiAlO_2$-carbonate (0.22 S cm^{-1} at 600 ºC in air) and SDC-carbonate (0.35 S cm^{-1} at 600 ºC in air) as demonstrated in Chapters 3 and 4 respectively.

It is to be noted that the conductivity of the composite electrolyte increased as the sample sintering temperature increased from 600 to 700 ºC in all atmospheres under investigation. This could be due to the higher sintering temperature resulting in better contact at the interfacial region between the two phases, which, in turn, provides a superionic highway for ion conduction [296].

As mentioned above, enhancement of ionic conductivity was observed above the melting point of the ternary carbonate in all atmospheres (air, dry O_2 and wet 5% H_2-Ar). This enhancement is believed to be due to the composite effect, by which the ionic transport at the interface region between the two phases is faster, which means that the interface provides a smooth pathway for ionic conduction. In other words, at high temperature (400-600 ºC), the ternary carbonate in the composite electrolyte will melt, which in turn greatly enhances the mobility of all ions (i.e. Li^+, Na^+, K^+, O^{2-}, H^+, HCO_3^- and CO_3^{2-}), leading to a superionic conducting region at the interface between the two phases. This means that all mobile ions contributed to the overall AC ionic conductivity. However, during the electrolysis, only H^+ or O^{2-} can be transported through the composite electrolyte, while the other mobile ions are blocked at the electrodes [177, 180].

It can also be seen from Figures 5.12a and b that, at high temperature (> 375 ºC), the composite electrolyte exhibits similar values of ionic conductivities under all

atmospheres (air, dry O_2 and wet 5% H_2-Ar). However, below the melting point of the ternary carbonate, the measured conductivity in wet 5% H_2-Ar was higher than those measured in air and dry O_2. This indicates that, at low temperature, proton conduction is dominant in CGDC-carbonate composite. This could be explained by the fact that proton conduction can be more easily activated at low temperature than oxygen-ion conduction [169, 180].

The activation energies (E_a) of the composite electrolyte under different atmospheres were extracted from the slope of each series of points in the Arrhenius plots of conductivity, as shown in the insets of Figures 5.12a and d. The activation energies of CGDC-carbonate composite at high temperature (600-400 ºC), for samples sintered in air at 600 ºC or 700 ºC, are listed in Table 5.1. It is to be noted that the composite electrolyte demonstrated similar values of activation energies in all atmospheres under investigation. For instance, in air, the activation energies were found to be 0.42 ± 0.07 eV and 0.42 ± 0.08 eV for samples sintered at 600 ºC and 700 ºC respectively. These values are similar to that reported by Menamira et al. [171] for GDC-$(Li/Na)_2CO_3$ composite (0.40 eV).

(a)

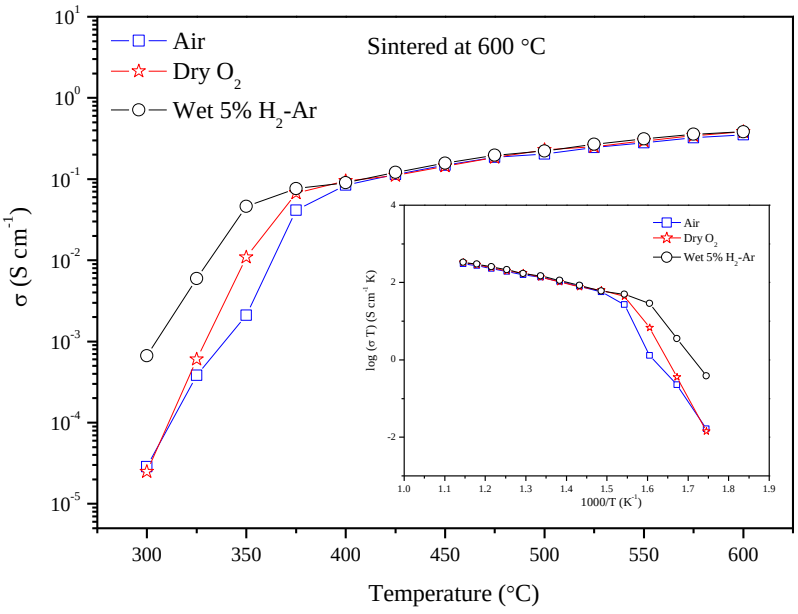

(b)

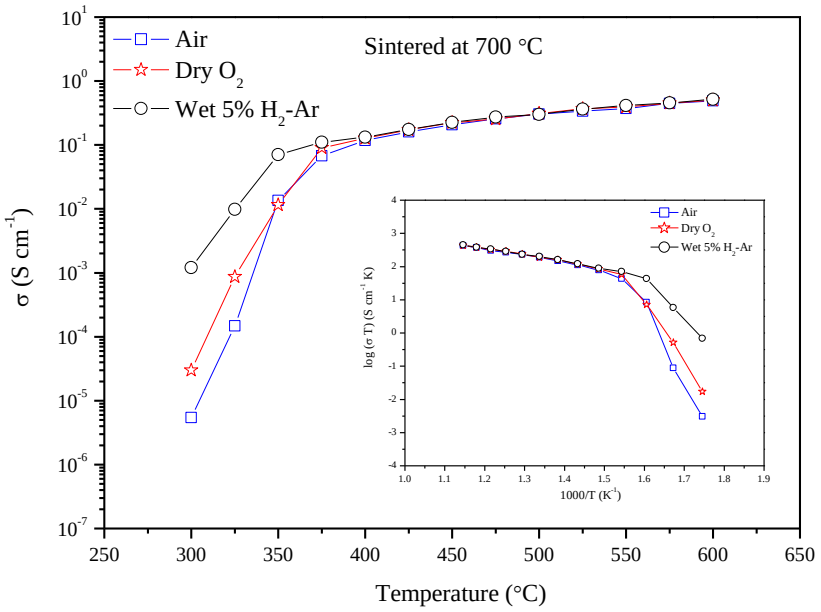

Figure 5.12 AC conductivity plot of CGDC-$(Li/Na/K)_2CO_3$ composite against temperature: (a) sample sintered at 600 C; (b) sample sintered at 700 C

Table 5.1 The activation energy of CGDC-carbonate composite pellets sintered at 600 ºC and 700 ºC

Sintering temperature (ºC)	**Activation Energy, E_a (eV) [600-400 ºC]**		
	Air	**Dry O_2**	**Wet 5% H_2-Ar**
600	0.42 ± 0.07	0.43 ± 0.06	0.43 ± 0.07
700	0.42 ± 0.08	0.40 ± 0.07	0.40 ± 0.06

Figures 5.13a and b show the XRD patterns of CGDC-carbonate composite electrolyte after AC conductivity measurements for samples sintered in air at 600 ºC and 700 ºC respectively. As can be seen, the composite electrolyte retains the fluorite structure and no phase change was observed after the conductivity measurement in both oxidising and reducing atmospheres. This indicates the stability of the CGDC-$(Li/Na/K)_2CO_3$ composite electrolyte.

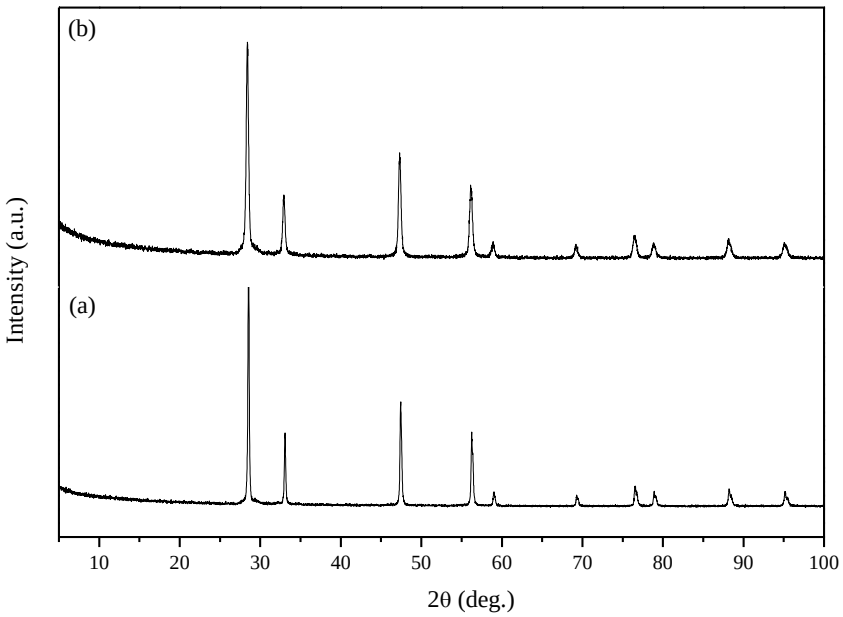

Figure 5.13 XRD patterns of CGCD-(Li/Na/K)$_2$CO$_3$ composite after AC conductivity measurements: (a) sintered at 600 ºC; (b) sintered at 700 ºC

5.3.5 Synthesis of ammonia at different temperatures

The performance stability of electrolytic cell based on CFO-CGDC composite cathode during the synthesis of ammonia at different temperatures (375-450 °C), with an applied voltage of 1.4 V over a period of 30 min, is shown in Figure 5.14. As can be seen, the cell demonstrated almost stable performance at the operating temperatures under investigation. In addition, the generated current densities increased with an increase in operating temperature and reached a maximum value when the electrolytic cell operated at 450 °C, as listed in Table 5.2. The increase in current densities with temperature could be also speculated to be due to the increase in the ionic conductivity of the composite electrolyte, which means that more oxygen-ions (O^{2-}) were transported through the electrolyte to the anode surface.

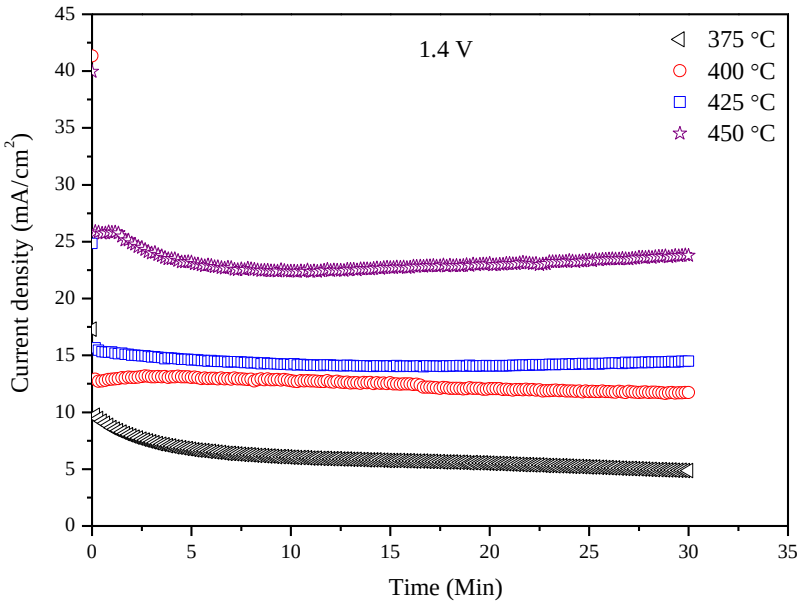

Figure 5.14 Electrolytic cell performance stability at 1.4 V and 375-450 °C: The electrolytic cell was; air, SSCo-CGDC|CGDC-carbonate|CFO-CGDC, 3% H_2O-N_2

Figure 5.15a shows the AC impedance spectra for the electrolytic cell based on CFO-CGDC composite cathode at different temperatures (375-450 °C), under open circuit conditions. As can be seen, the spectra were composed of two depressed semicircles at each of the operating temperatures (375-450 °C), suggesting that there are at least two electrode processes, and the data were fitted using the equivalent circuit shown Figure 5.15b. In these circuits, L is inductance, Rs is the series resistance, CPE1 and CPE2 are constant phase elements and R1 and R2 are polarisation resistances.

The characteristic capacitances of the high frequency semicircle (HF) are in the range of 10^{-6}-10^{-5} F/cm^2, which could be attributed to the charge transfer processes at the electrode/electrolyte interface. The low frequency semicircle (LF), with the associated capacitances of 10^{-3}-10^{-2} F/cm^2, could be ascribed to the mass transfer processes at the electrode [46, 255, 256]. In addition, the Rs resistance, which is mainly related to the ohmic resistance of the electrolyte, decreased significantly as the cell operating temperature increased from 375 to 450 °C. This could be attributed to the enhancement in the ionic conductivity of the composite electrolyte as the

operating temperature is increased. There was also a significant decrease in the total polarisation resistance (Rp) which is the sum of R1 and R2, with an increase in operating temperature, which could be due to the improvement in the catalytic activity of the cathode with temperature.

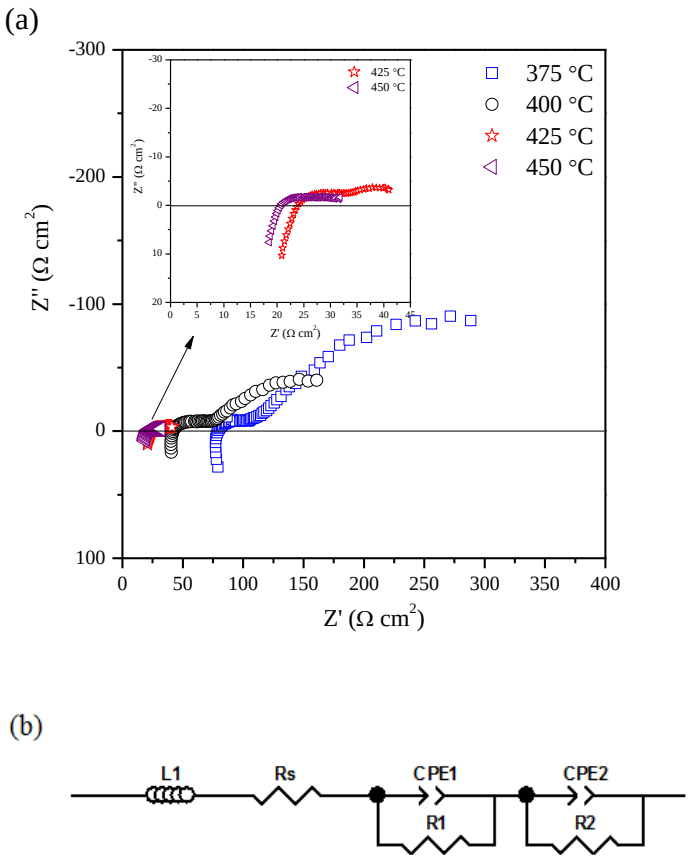

Figure 5.15 Impedance spectra under open circuit condition of the cell based on CFo-CGDC composite cathode at 375-450 °C; (b) An equivalent circuit for the impedance data

The dependence of the ammonia formation rate on the operating temperature was investigated by varying the cell operating temperature from 375 ºC to 450 ºC and keeping the cell voltage at a constant value of 1.4 V over a period of 30 min, as shown in Figure 5.16. As can be seen, the rate of ammonia formation increased as the cell operating temperature was increased and the maximum value was obtained at 400 ºC. The maximum rate was found to be up to 4.0 $\times 10^{-11}$ mol s^{-1} cm^{-2}, at which the generated current density was 12.22 mA/cm^2 and the corresponding Faradaic

efficiency was about 0.10 %, as listed in Table 5.2. This increase in the rate of ammonia formation with an increase in cell operating temperature could be attributed to the fact that the ionic conductivity of the electrolyte increases as the operating temperature is increased. However, when the electrolytic cell operated above 400 ºC, the ammonia formation rate declined [115]. This rate decrease at high temperature might be speculated to be due to the ammonia decomposition, although the ionic conductivity of the electrolyte increased with temperature [75].

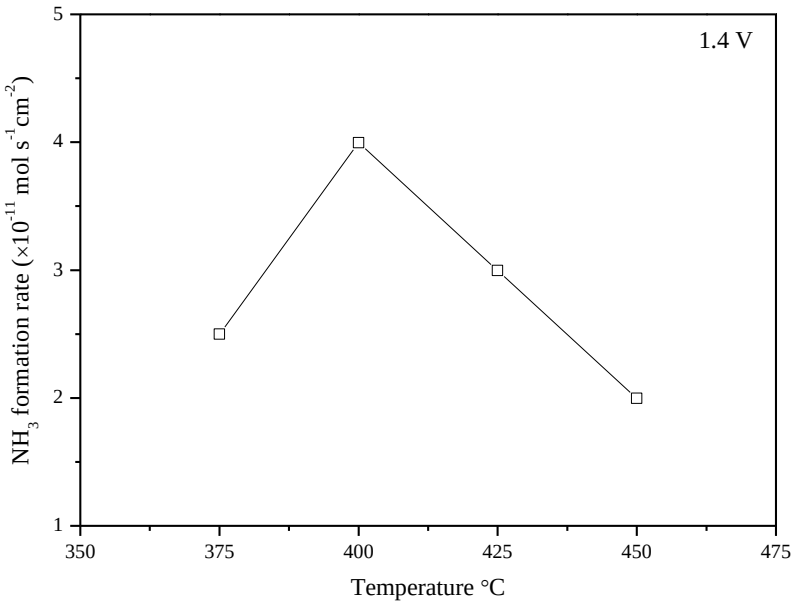

Figure 5.16 Dependence of the rate of ammonia formation on the operating temperature

Table 5.2 Corresponding current densities and Faradaic efficiencies of ammonia formation over CFO-CGDC composite cathode at 1.4 V

Temperature (°C)	**Current density (mA/cm^2)**	**Faradaic efficiency (%)**
375	5.60	0.13
400	12.22	0.10
425	14.31	0.06
450	23.14	0.03

5.3.6 Synthesis of ammonia at different applied voltages

Figure 5.17 shows the performance of the electrolytic cell at a constant temperature and different applied voltages (1.2-1.8 V), over a period of 30 min. As can be seen, the generated current densities remain almost constant at all applied voltages, indicating a stable electrochemical process. In addition, the generated current density increases with the applied voltage and reach a value of 12.22 mA/cm^2 at 1.4 V as shown in Table 5.3. This indicates that more oxygen-ions (O^{2-}) were transported through the electrolyte to anode. However, when the applied voltages were further increased, to values higher than 1.4 V, the generated current densities decreased and reached values of 11.28 mA/cm^2 at 1.6 V, as shown in Table 5.3. This indicates the difficulties of transporting more O^{2-} through the electrolyte to the anode surface at higher voltages (> 1.4 V). This may be due to the blocking effect of Li^+, Na^+, and K^+ ions. Under the presence of electric filed, these ions will move and accumulate at the cathode/electrolyte interface forming positively charged layer, thus partially block the transfer of O^{2-} and resulting in low current densities [258, 259].

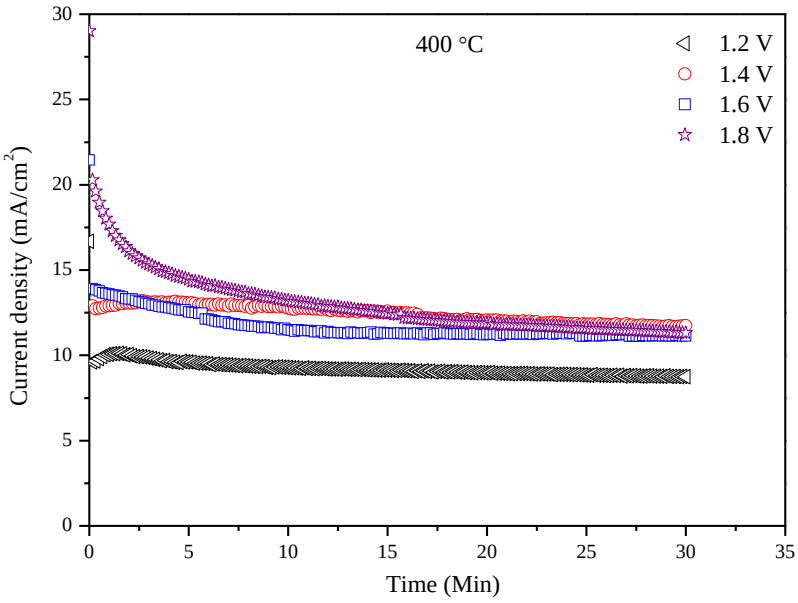

Figure 5.17 Electrolytic cell performance stability at 400 °C and 1.4-1.8 V: The electrolytic cell was; air, SSCo-CGDC|CGDC-carbonate|CFO-CGDC, 3% H_2O-N_2

Table 5.3 The corresponding current densities and Faradaic efficiencies of ammonia formation over CFO-CGDC composite cathode at 400 °C

Applied voltage (V)	Current density (mA/cm^2)	Faradaic efficiency (%)
1.2	9.13	0.11
1.4	12.22	0.10
1.6	11.28	0.17
1.8	12.18	0.02

The effect of the applied voltages on the rate of ammonia formation was investigated by keeping the cell operating temperature at a constant value (400 °C) and varying the applied voltage from 1.2 to 1.8 V, as shown in Figure 5.18. As can be seen, the rate of ammonia formation increased significantly with the increase in the applied voltage. The maximum rate of 6.5×10^{-11} mol s^{-1} cm^{-2} was obtained when the electrolytic cell operated at 1.6 V. This rate corresponds to a current density of about 11.28 mA/cm^2 at Faradaic efficiency of 0.17 %, as listed in Table 5.3. However, above 1.6 V, the rate decreased markedly and reached a minimum value of 1.0×10^{-11} mol s^{-1} cm^{-2} at 1.8 V. This decrease in the rate of ammonia formation at higher applied voltage might be due to the competitive adsorption between the N_2 and H_2 over the cathode surface [41, 70]. However, the low current efficiencies indicate that the hydrogen evolution reaction (HER) is the dominant process over the cathode surface. However, despite the low ammonia formation rates, these values are still higher than that reported previously when steam and nitrogen were used to produce ammonia in an electrolytic cell based on oxygen-ion (O^{2-}) conducting electrolyte (YSZ) and Ru based cathode (3.75×10^{-13} mol s^{-1} cm^{-2} at 650 °C) [10]. This difference in the ammonia formation rates could be related to higher ionic conductivity of the CGDC- carbonate composite electrolyte compared to YSZ. Another factor which could account for the difference in these results was the temperature, as the present study was carried out at a temperature of 400 °C, 250 °C lower than that in the earlier study, which would possibly reduce the effect of thermal decomposition of ammonia.

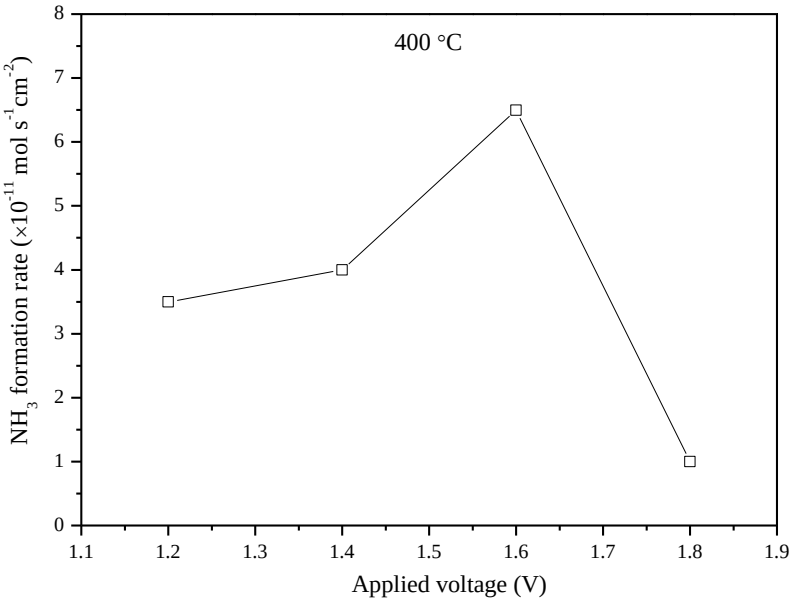

Figure 5.18 Dependence of the rate of ammonia formation on the applied voltage, at 400 °C

Figure 5.19 represents the microstructure of the cross-sectional area of the single cell after ammonia synthesis. No obvious change in morphology (see Figure 5.19a) was observed after testing and the cell is still in good condition, as shown in Figures 5.19b-d.

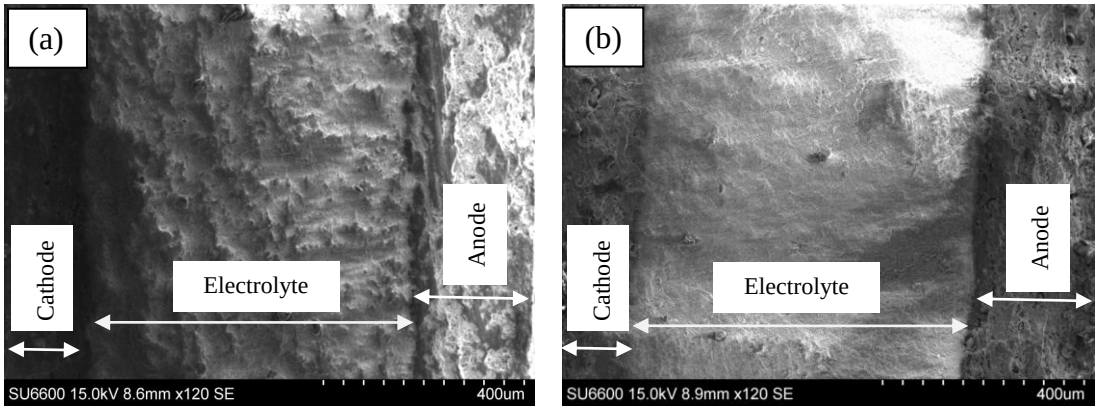

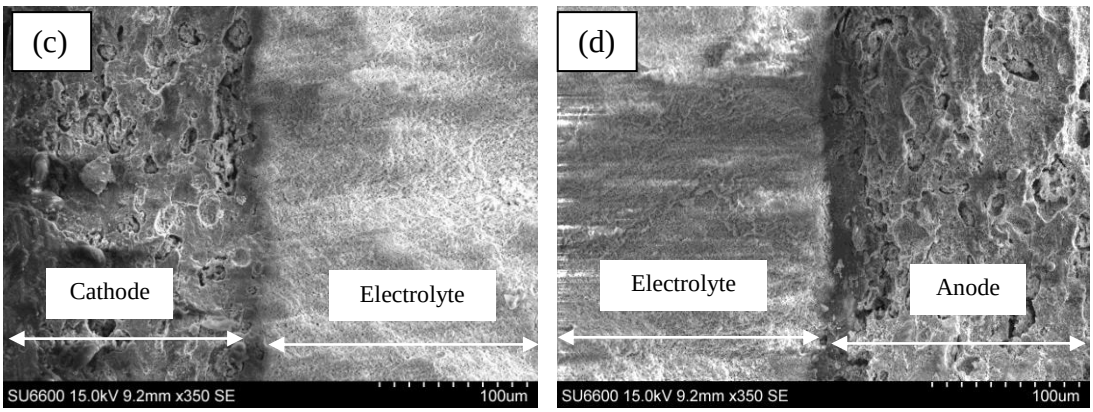

Figure 5.19 SEM images of cross-sectional areas of a single cell based on a CFO-CGDC cathode: (a) before ammonia synthesis; (b) after ammonia synthesis; (c) interface between cathode and electrolyte; (d) interface between anode and electrolyte

5.4 Conclusion

In these experiments, $CoFe_2O_4$ (CFO), $Ce_{0.8}Gd_{0.18}Ca_{0.02}O_{2-\delta}$ (CGDC) and $Sm_{0.5}Sr_{0.5}CoO_{3-\delta}$ (SSCo) were synthesised via a combined EDTA-citrate complexing sol-gel process. A new composite electrolyte was prepared by mixing $Ce_{0.8}Gd_{0.18}Ca_{0.02}O_{2-\delta}$ with the ternary carbonate ($(Li/Na/K)_2CO_3$, 70:30 wt %).

The composite electrolyte was thermally stable in both oxidising and reducing atmospheres. The ionic conductivities of the composite electrolyte were measured by AC impedance within the temperature range 600-300 ºC, under different atmospheres (Air, dry O_2 and wet 5% H_2-Ar). The ionic conductivity measured for samples sintered at two different temperatures (600 and 700 ºC), to investigate the effect of sintering temperature on conductivity. The conductivities of samples sintered at 700 ºC were higher than those obtained for samples sintered at 600 ºC. This could be probably because high sintering temperature improves the contact at the interfacial region between doped ceria and the carbonate phase, which in turn provides a superionic highway for ion conduction [296]. The ionic conductivities for samples sintered at 700 ºC were found to be 0.49-3.731 $\times 10^{-6}$, 0.50-3.34$\times 10^{-5}$ and 0.52-1.21$\times 10^{-3}$ S cm^{-1} in air, dry O_2 and wet 5% H_2-Ar respectively. After the

conductivity measurements, the composite electrolyte retained its fluorite structure, indicating its stability.

A tri-layer electrolytic cell was successfully fabricated by a cost effective one-step dry-pressing and co-firing process. Ammonia was synthesised directly from water and nitrogen in electrolytic cell based on CFO-CGDC composite as a cathode, CGDC-carbonate composite as an electrolyte and SSCo-CGDC composite as an anode. The maximum rate of ammonia formation was found to be up to 6.5×10^{-11} mol s^{-1} cm^{-2} at 400 ºC, with an applied voltage of 1.6 V.

6 Ammonia synthesis from water and nitrogen based on doped lanthanum ferrite cathodes

6.1 Introduction

Lanthanum ferrite ($LaFeO_3$) belongs to the family of perovskite oxides with the general formula ABO_3 (Chapter 4). $LaFeO_3$ based oxides, including Lanthanum strontium ferrite (LSF), Lanthanum strontium cobalt ferrite (LSFCo) and Lanthanum strontium copper ferrite (LSFCu), are known as mixed ionic-electronic conductors (MIECs) due to the presence of electron holes and oxygen vacancy [290, 292, 300, 313-315]. These oxides have high electronic conductivity (> 100 S/cm), high ionic conductivity and good catalytic activity for an oxygen reduction reaction (ORR) [300, 315, 316]. These properties make them promising electrode materials for solid oxide fuel cells and solid oxide steam electrolysis cells. In addition, such oxides have been used in other applications, including gas sensors, oxygen separation membranes and catalysis (e.g. methane oxidation) [317-319].

Lanthanum ferrite-based oxides such as $La_{0.6}Sr_{0.4}FeO_{3-\delta}$ (LSF), $La_{0.6}Sr_{0.4}Fe_{0.8}Co_{0.2}O_{3-\delta}$ (LSFCo), and $La_{0.7}Sr_{0.3}Fe_{0.8}Cu_{0.2}O_{3-\delta}$ (LSFCu) have gained considerable attention as cathode materials for intermediate temperature solid oxide fuel cells (IT-SOFCs), due to their aforementioned properties [292, 314, 315]. In addition, Marina et al. [320] and Kong et al. [321] have investigated LSF, LSFCo and LSFCu as anode materials for high temperature solid oxide steam electrolysis cells (HT-SOECs).

In Chapter 4, it was reported that ammonia was successfully synthesised from hydrogen and nitrogen in an electrolytic cell based on a $LaFeO_3$ based oxide with the form of $La_{0.6}Sr_{0.4}Fe_{0.8}Cu_{0.2}O_{3-\delta}$ (LSFCu) as cathode. In this chapter, the focus is set on the electrocatalytic activity of these oxides for ammonia synthesis from water and nitrogen. In addition to $La_{0.6}Sr_{0.4}Fe_{0.8}Cu_{0.2}O_{3-\delta}$ (LSFCu), the ferrite-based oxides $La_{0.6}Sr_{0.4}FeO_{3-\delta}$ (LSF) and $La_{0.6}Sr_{0.4}Fe_{0.8}Co_{0.2}O_{3-\delta}$ (LSFCo) will also be used as cathode materials in electrolytic cell based on oxygen-ion conducing cell.

6.2 Experimental

6.2.1 Synthesis of perovskite-type catalysts

$La_{0.6}Sr_{0.4}FeO_{3-\delta}$ catalyst (LSF) was synthesised via a combined EDTA-citrate complexing sol-gel process [291]. Lanthanum oxide (La_2O_3, Alfa Aesar, 99 %), strontium nitrate ($Sr(NO_3)_2$, Alfa Aesar, 99 %) and iron nitrate nanohydrate ($Fe(NO_3)_3 \cdot 9H_2O$, Alfa Aesar, 98 %) were used as starting materials. La_2O_3 was dissolved in diluted nitric acid to form lanthanum nitrate. Calculated amounts of $Sr(NO_3)_2$ and $Fe(NO_3)_3 \cdot 9H_2O$ were dissolved in deionised water and then added to the lanthanum nitrate solution. Citric acid and EDTA were then added as complexing agents, with molar ratio of citric acid:EDTA:metal cations of 1.5:1:1. $NH_3 \cdot H_2O$ was added to the mixed solution to adjust the pH value to around 6. Under heating and stirring, the solution was evaporated on a hot-plate, and then gradually changed into a black sticky gel before complete drying. The resultant powder was ground and subsequently fired in air at 900 ºC for 2 h with a heating/cooling rate of 5 ºC min^{-1} to obtain a pure phase of LSF catalyst without carbon residue.

$La_{0.6}Sr_{0.4}Fe_{0.8}Co_{0.2}O_{3-\delta}$ catalyst (LSFCo) was also synthesised via a combined EDTA-citrate complexing sol-gel process as described above. Lanthanum oxide (La_2O_3, Alfa Aesar, 99 %), strontium nitrate ($Sr(NO_3)_2$, Alfa Aesar, 99 %) ($Fe(NO_3)_3 \cdot 9H_2O$, Alfa Aesar, 98%) and cobalt nitrate ($Co(NO_3)_2 \cdot 6H_2O$, Sigma Aldrich, 98 + %) were used as starting materials. The resultant powder was ground and subsequently calcined in air at 900 ºC for 2 h with a heating/cooling rate of 5 °C min^{-1} to obtain a single phase of LSFCo. $La_{0.6}Sr_{0.4}Fe_{0.8}Cu_{0.2}O_{3-\delta}$ (LSFCu) was synthesised as described in Section 4.2.1.

6.2.2 Characterisation of materials

Phase purity was studied by powder X-ray diffraction using a Panalytical X'Pert Pro diffractometer. The microstructures of the prepared catalyst and the cross-sectional area of the single cell were examined using a Hitachi SU6600 Scanning Electron Microscope (SEM). The thermal behaviour of the perovskite based cathodes

(LSF and LSFCo) was investigated in N_2 atmosphere from room temperature to 500 ºC with a heating/cooling rate of 10 ºC/min.

6.2.3 Fabrication of the single cell

A tri-layer single cell was fabricated by a cost-effective, one-step, dry-pressing method. The composite anode was prepared by mixing in a mortar SSCo, prepared as described in section 5.2.1.2, CGDC, prepared as described in section 5.2.1.3, and a pore former (starch), with weight ratio of 70:30:15. The composite electrolyte CGDC/$(Li/Na/K)_2CO_3$ (70:30 wt %) was prepared as described in section 5.2.2. The composite cathode was prepared by mixing in a mortar LSF and CGDC and starch, with weight ratio of 70:30:15. The composite anode, composite electrolyte and composite cathode were fed into the die, layer by layer, with the aid of a sieve to ensure uniform powder distribution, and then uniaxially pressed at pressure of 121 MPa. This freshly made green pellet was sintered in air at 700 °C for 2 h, at a rate of 2°C/min heating/cooling. The active surface area of the cathode was 0.785 cm^2. Silver paste was painted in a grid pattern on each electrode surface of the cell, as a current collector. Ag wires were used as output terminals for both electrodes. The single cells consisting of either LSFCu-CGDC or LSFCo-CGDC composite cathodes were prepared as described for the LSF-CGDC composite cathode.

6.2.4 Synthesis of ammonia

The fabricated single cells for ammonia synthesis were sealed into a self-designed double-chamber reactor, using ceramic paste (Aremco, Ceramabond 552). The cathode chamber was fed with 3% H_2O-N_2 (BOC). The water vapour (3% H_2O) was supplied to the cathode chamber by bubbling a N_2 stream through a liquid water container, at 25°C. The anode was exposed to air. A constant voltage was applied over a period of 30 min. The ammonia synthesised at the cathode chamber was absorbed by 20 ml of diluted HCl (0.01 M) for 30 min. The concentration of NH_4^+ in the absorbed solution was analysed using an ion selective electrode (ISE) and the rate of ammonia formation was calculated using Equation 2.9 (Section 2.4.2).

The three electrolytic cells were constructed as follows:

- Air, SSCo-CGDC|CGDC-carbonate|LSF-CGDC, 3% H_2O-N_2
- Air, SSCo-CGDC|CGDC-carbonate|LSFCu-CGDC, 3% H_2O-N_2
- Air, SSCo-CGDC|CGDC-carbonate|LSFCo-CGDC, 3% H_2O-N_2

6.3 Results and discussion

6.3.1 XRD analysis

Single-phase perovskite oxides with the forms of $La_{0.6}Sr_{0.4}FeO_{3-\delta}$ (LSF) and $La_{0.6}Sr_{0.4}Fe_{0.8}Co_{0.2}O_{3-\delta}$ (LSFCo) were obtained when their ashes were calcined in air at 900 °C for 2 h. The X-ray diffraction patterns of LSF (Figure 6.1a) and LSFCo (Figure 6.1b) show a typical cubic perovskite oxide structure, which is in good agreement with JCPDS file 39-1083. The crystallite sizes of LSF and LSFCo are about 31.58 nm and 30.66 nm respectively, estimated from Sherrer's formula (Equation 2.3).

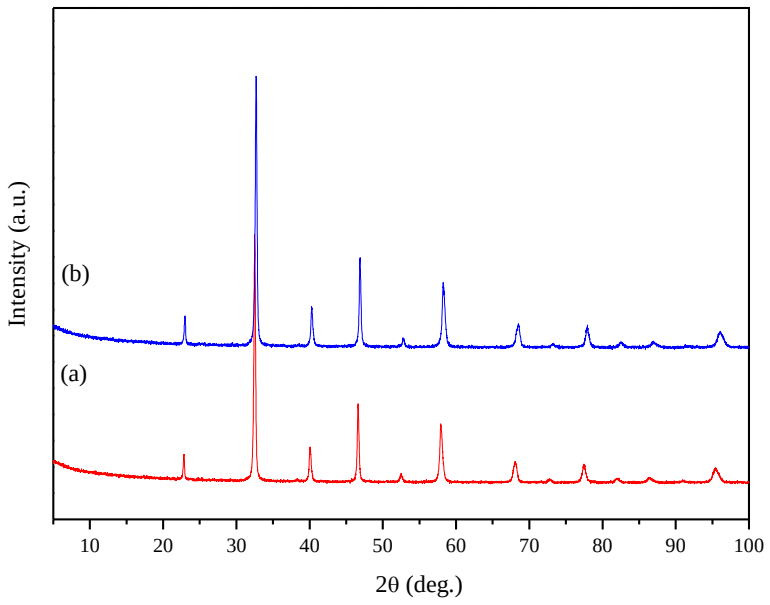

Figure 6.1 The XRD patterns of: (a) LSF; (b) LSFCo calcined at 900 °C for 2 h

In order to investigate the chemical compatibilities between the perovskite based oxides (LSF and LSFCo) and the CGDC, the composite cathodes containing CGDC were fired in air at 700 °C, which is the sintering temperature for the fabricated single cells for ammonia synthesis. Figures 6.2a-c show the XRD patterns of CGDC, LSF and the LSF-CGDC composite cathode respectively. As can be seen from Figure 6.2c, the XRD pattern of the composite cathode (LSF-CGDC, 70:30 wt %) displays only the characteristic peaks of pure CGDC (Figure 6.2a) and pure LSF (Figure 6.2b). The XRD patterns of CGDC, LSFCo and LSFCo-CGDC composite cathode (70:30 wt %), respectively, are shown in Figures 6.3a-c. As can be seen, the XRD pattern of the LSFCo-CGDC composite (Figure 6.3c) shows only the peaks that correspond to pure CGDC (Figure 6.3a) and pure LSFCo (Figure 6.3b). As discussed above, no additional diffraction peaks in either case were observed when the composite cathodes were fired in air at 700 °C. This indicates that both perovskite oxides (LSF and LSFCo) are chemically compatible with CGDC at the single cell sintering temperature.

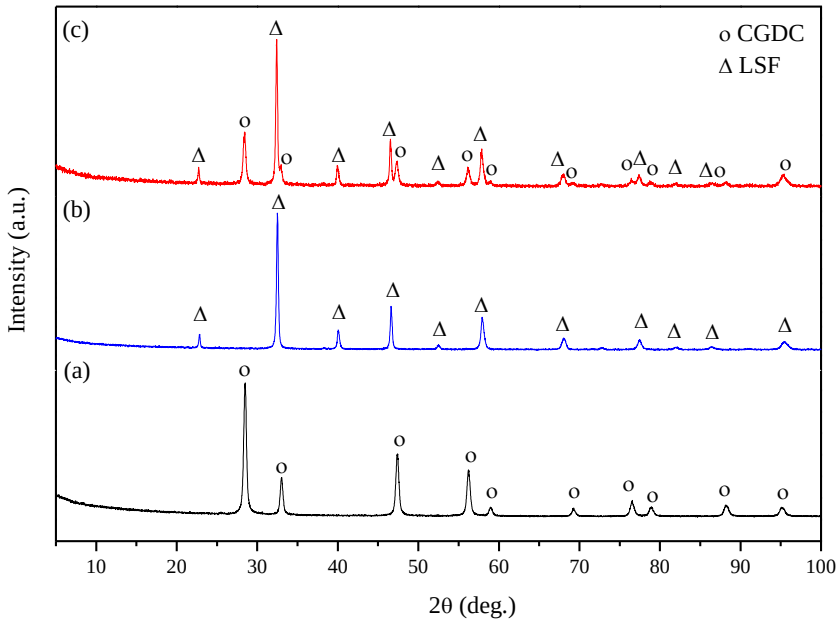

Figure 6.2 XRD patterns of (a) CGDC calcined in air at 700 ºC; (b) LSF calcined in air at 900 ºC; (c) LSF-CGDC composite cathode fired in at 700 ºC

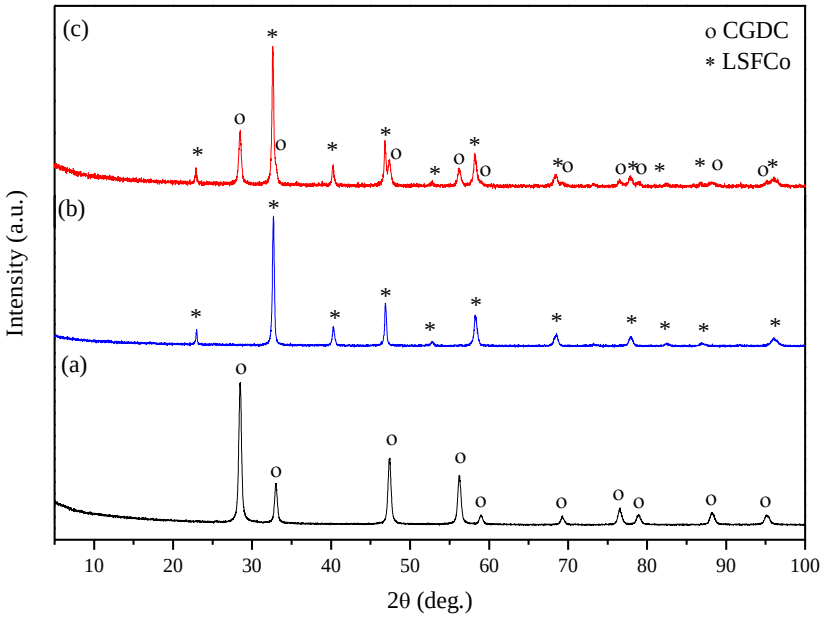

Figure 6.3 XRD patterns of (a) CGDC calcined in air at 700 ºC; (b) LSFCo calcined in air at 900 ºC; (c) LSFCo-CGDC composite cathode fired in at 700 ºC

6.3.2 SEM analysis

The microstructures of LSF and LSFCo powders calcined in air at 900 C for 2 h were examined by scanning electron microscopy (SEM), as shown in Figures 6.4a and b respectively. As can be seen, the SEM images of both oxides show microporous structures with fine agglomerated particles of different sizes and shapes.

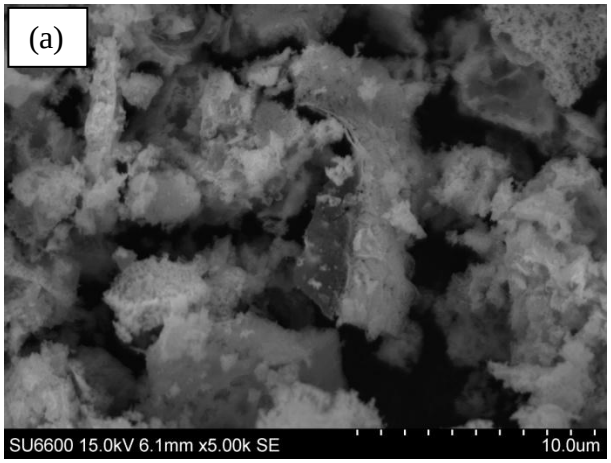

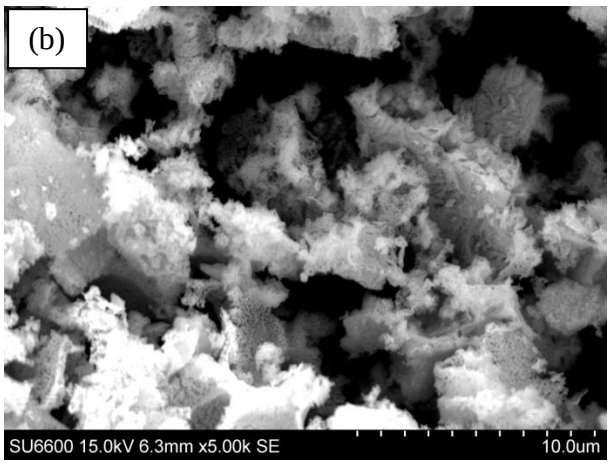

Figure 6.4 SEM images of the perovskite based catalyst powders calcined in air at 900 ºC: (a) LSF; (b) LSFCo

The SEM micrographs of the cross-section views of three single cells (before test) sintered in air at 700 ºC for 2 h are shown in Figure 6.5. In these cells, the anode was SSCo-CGDC composite and the electrolyte was CGDC-$(Li/Na/K)_2CO_3$, while the cathode was one of the following composites; LSF-CGDC, LSFCu-CGCD and LSFCo-CGDC, as presented in Figures 6.5a-c, respectively. As can be seen, in all cases, the CGDC-carbonate composite electrolyte is dense and adheres very well to the composite anode and the composite cathodes. This indicates that the composite electrolyte is thermally compatible with both composite electrodes (anode and cathode).

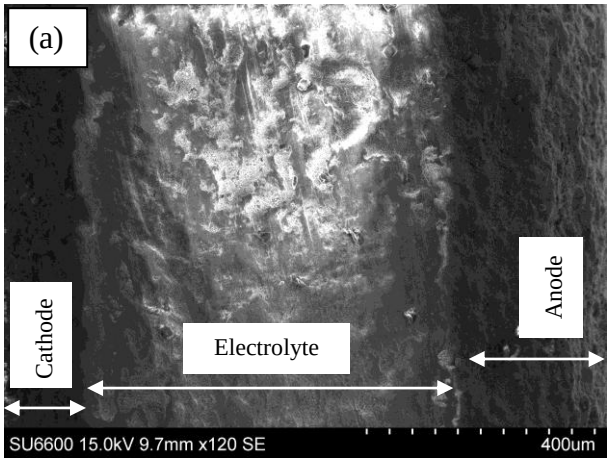

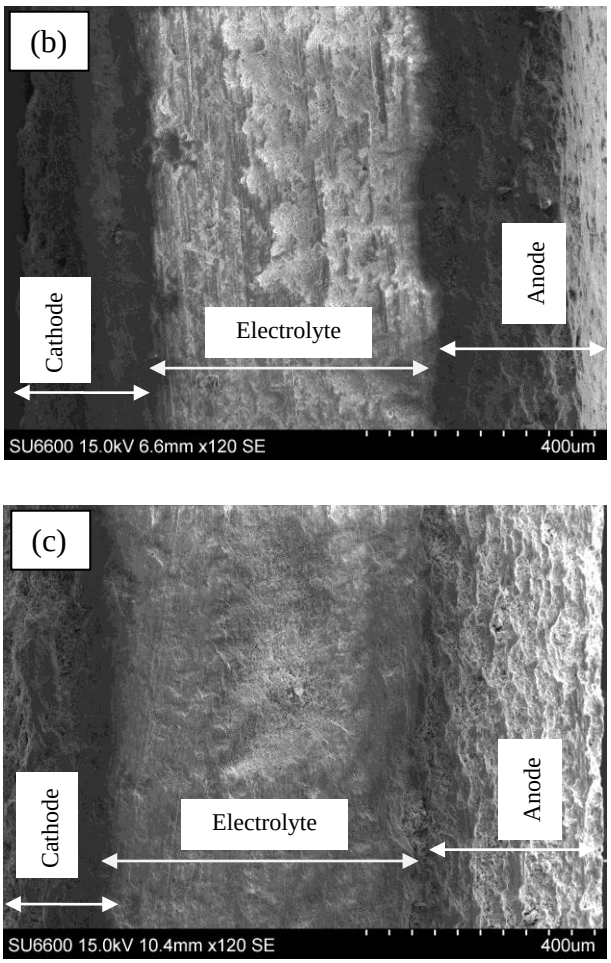

Figure 6.5 SEM images of cross-sectional areas of the single cells based on different composite cathodes, before ammonia synthesis: (a) LSF-CGDC; (b) LSFCu-CGDC; (c) LSFCo-CGDC

6.3.3 Thermal analysis

As the cathode materials are exposed to N_2 during the ammonia synthesis process, it is important to investigate their thermal stabilities under this atmosphere. The thermal behaviour of the perovskite based cathodes is shown in Figure 6.6.

The TGA-DSC curves of the LSF cathode in N_2, from room temperature up to 500 °C, at rate of 10 °C/min, is presented in Figure 6.6a. As can be seen, in the temperature range from room temperature to 200 ºC, a small endothermic peak was observed at ~ 60 ºC, accompanied by a weight loss of about 0.67 %, which could be attributed to the loss of adsorbed water. Within the temperature range from 200 to

500 ºC, a slight weight loss of about 0.25 % was observed, which could be due to the loss of lattice oxygen from the $La_{0.6}Sr_{0.4}FeO_{3-\delta}$ structure.

Figure 6.6b represents the TGA-DSC curves of the LSFCo cathode in N_2. A slight weight gain of about 0.05 % was observed between room temperature and 200 ºC, which might be due to the buoyancy effect. Within the temperature range from 200 to 500 ºC, a slight loss of about 0.29 % was observed, which could be ascribed to the loss of lattice oxygen from the $La_{0.6}Sr_{0.4}Fe_{0.8}Co_{0.2}O_{3-\delta}$ structure. In addition, in both cases, there are no obvious thermal effects shown in the DSC curves, indicating the thermal stability of both cathodes in N_2 within the measured temperature range.

Figure 6.7 show the XRD patterns of the perovskite based cathodes after thermal analysis in N_2 atmosphere. As can be seen, both oxides retain the same perovskite structure and there are no extra peaks are observed, indicating the thermal stability of LSF (Figure 6.7a) and LSFCo (Figure 6.7b) cathodes under N_2 atmosphere in the measured temperature range. It is to be noted that thermal analysis of LSFCu in a N_2 atmosphere was also studied for which more details were given in Chapter 4.

(a)

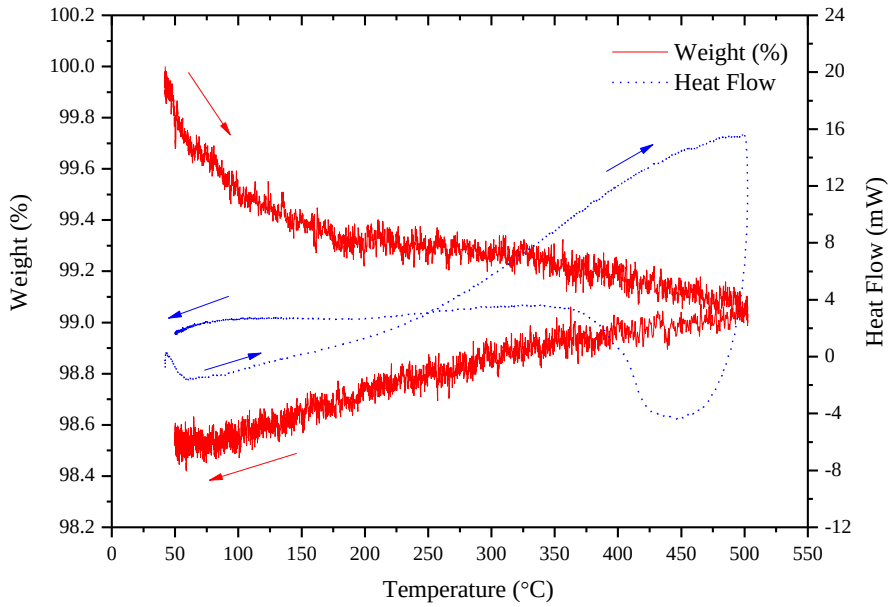

(b)

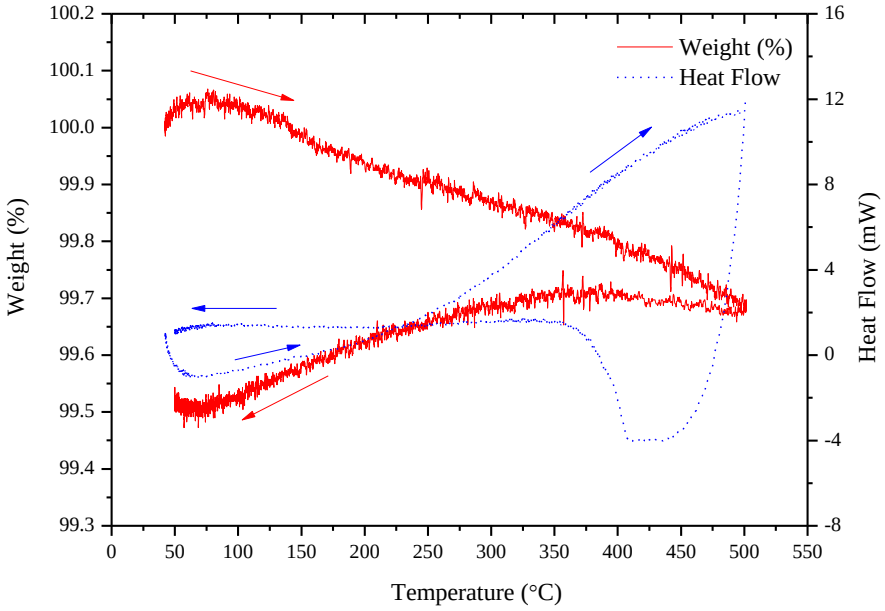

Figure 6.6 TGA-DSC curves for perovskite based catalysts in nitrogen, up to 500 ºC: (a) LSF; (b) LSFCo

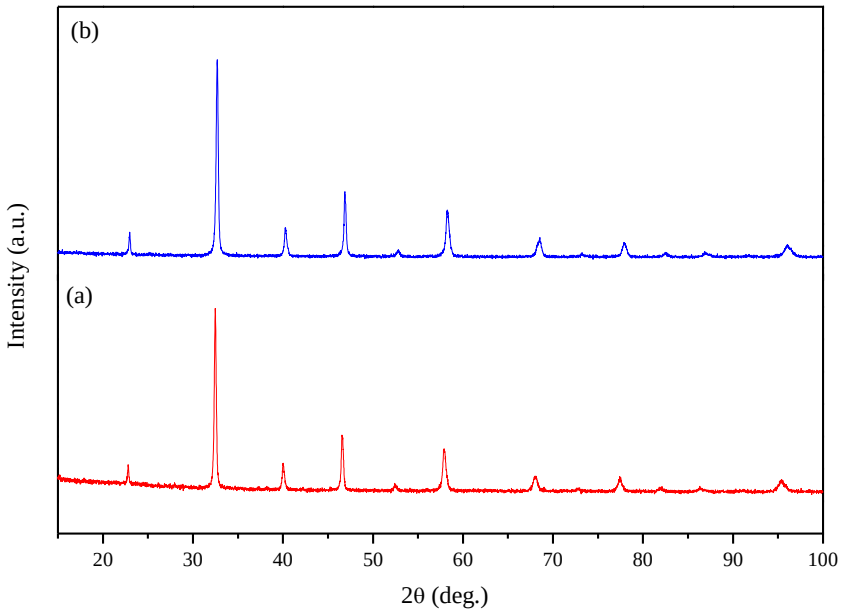

Figure 6.7 XDR patterns of perovskite based catalysts in nitrogen, up to 500 ºC: (a) LSF; (b) LSFCo

6.3.4 Synthesis of ammonia at different temperatures

Figures 6.8a-c represent the performance stabilities of electrolytic cells based on LSF-CGDC, LSFCu-CGDC and LSFCo-CGDC composite cathodes, during the synthesis of ammonia at different temperatures (375-450 °C), with an applied voltage of 1.4 V, over a period of 30 min. As can be seen, the electrolytic cells demonstrated stable performance at the operating temperatures under investigation. Furthermore, the generated current densities increased as the operating temperature increased and reached maximum values of 28.54, 19.72 and 40.61 mA/cm^2 at 450 °C, for LSF-CGDC, LSFCu-CGDC and LSFCo-CGDC composite cathodes respectively, as listed in Table 6.1. These increases in the generated current densities as the electrolytic cell operating temperature increased could be attributed to the enhancement of the ionic conductivity of the electrolyte at high temperature. This indicates that that more oxygen ions (O^{2-}) were transported through the electrolyte to the anode surface.

(a)

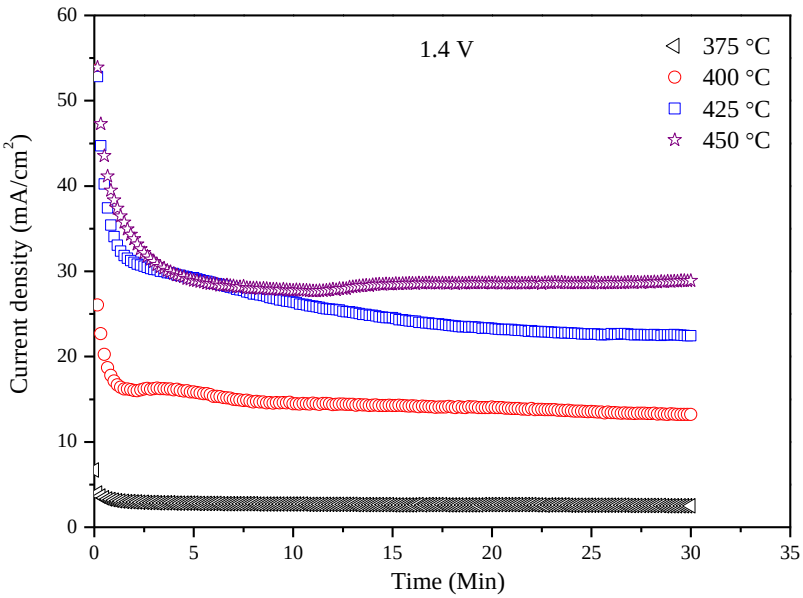

(b)

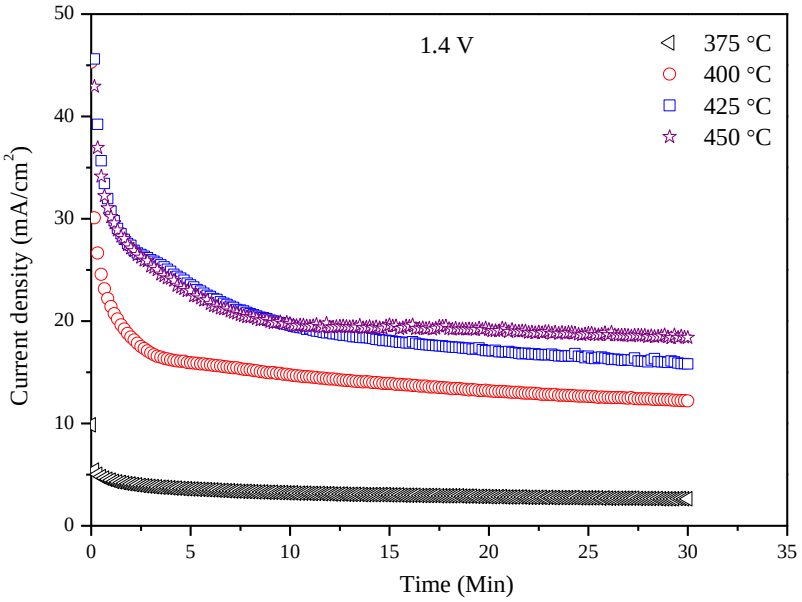

(c)

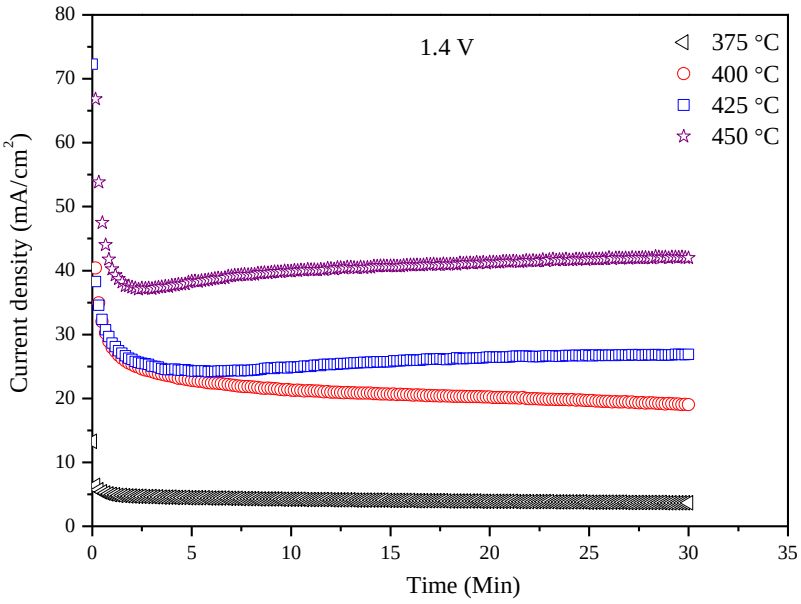

Figure 6.8 Electrolytic cell performance stability at 1.4 V and 375-450 °C: (a) LSF-CGDC composite cathode; (b) LSFCu-CGDC composite cathode; (c) LSFCo-CGDC composite cathode

Figures 6.9a-c show the in-situ AC impedance spectra under open circuit conditions at different temperatures (375-450 °C) of three electrolytic cells based on LSF-CGDC, LSFCu-CGDC and LSFCo-CGDC composite cathodes respectively. As can be seen, the spectra display different shapes, depending upon the operating temperature, thus three different equivalent circuits were used for data fitting, as shown in Figure 6.10. In these circuits, L is an inductance, Rs is series resistance, CPE is a constant phase element, Wo is a Warburg element and R1 and R2 are polarisation resistances.

In the case of the LSF-CGDC system, at 375 and 400 °C the spectra consist of one semicircle and a straight line with an angle not equal to 45°, at high and low frequencies respectively (Figure 6.9a), thus the equivalent circuit shown in Figure 6.10a was used for fitting this data. At high temperature (425 and 450 °C), two depressed semicircles were observed, at high and low frequencies, and the data were fitted using the circuit shown in Figure 6.10b. For the electrolytic cell based on the LSFCu-CGDC composite cathode (Figure 6.9b), at 375 °C, only one semicircle and a diagonal line with an angle equal to 45° were observed at high and low frequency respectively. In this case, a Warburg diffusion element was used instead of CPE for fitting the low frequency region (Figure 6.10c). Above 375 °C, two depressed semicircles were observed, at high and low frequencies, and the circuit shown in Figure 6.10b was used for data fitting. In the case of the LSFCo-CGDC composite cathode, the spectra were composed of two depressed semicircles, at high and low frequencies, as shown in Figure 6.9c. These impedance spectra suggest that there are at least two electrode processes. These data were also fitted using the equivalent circuit presented in Figure 6.10b.

The characteristic capacitances for the high frequency semicircles (HF) were found to be in the range of 10^{-5}-10^{-3} F/cm^2, which could be attributed to the charge transfer processes at the electrode/electrolyte interface. In the low frequency region (LF), either the semicircles with the associated capacitances of 0.1-0.7 F/cm^2 or the straight lines could be ascribed to mass transfer processes at the electrode [46, 255, 256].

It can also be seen from Figures 6.9a-c, that the series resistance (Rs), which is mainly related to the ohmic resistance of the electrolyte, decreased significantly with an increase the in cell operating temperature, and the lowest values, of 4.17, 4.41 and 3.95 Ω cm^2, were attained at 450 °C for LSF-CGDC, LSFCu-CGDC and LSFCo-CGDC composite cathodes respectively. This decrease in the ohmic resistance with temperature could be due to the increase in the ionic conductivity of the composite electrolyte with temperature. In the addition, the total polarisation resistances, Rp (R1 + R2) also decreased significantly when the operating temperature was increased, which could be due to the improvement in the catalytic activity of the composite cathodes with temperature. However, the Rp values in the electrolytic cell based on the LSFCo-CGDC composite cathode were lower than those of the LSF-CGDC and LSFCu-CGDC composite cathodes. At 450 °C, the total Rp value of LSFCo-CGDC was 11.03 Ω cm^2, while those for LSF-CGDC and LSFCu-CGDC composite cathodes were 19.66 Ω cm^2 and 21.37 Ω cm^2 respectively. This indicates that the catalytic activity of LSFCo-CGDC is better than that of LSF-CGDC and LSFCu-CGDC [75].

(a)

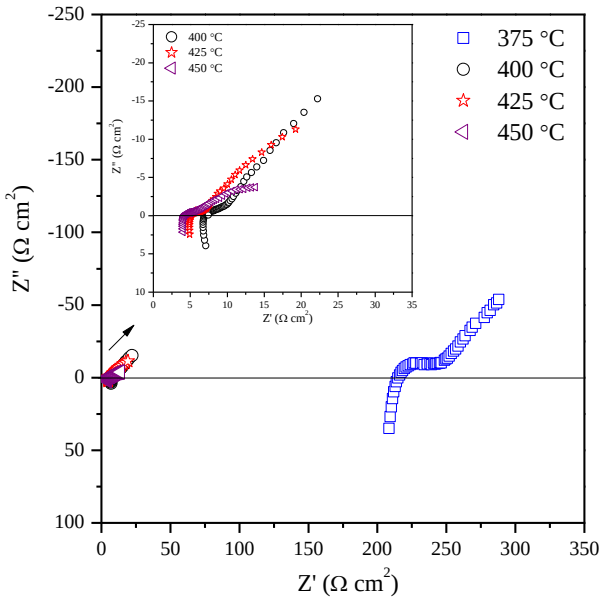

(b)

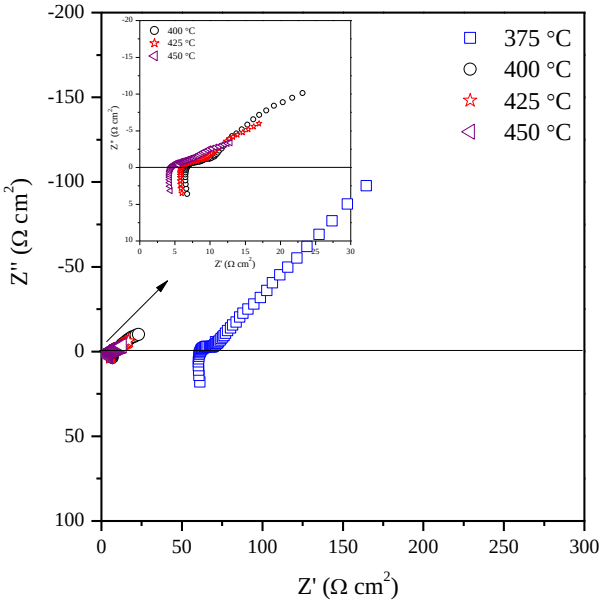

(c)

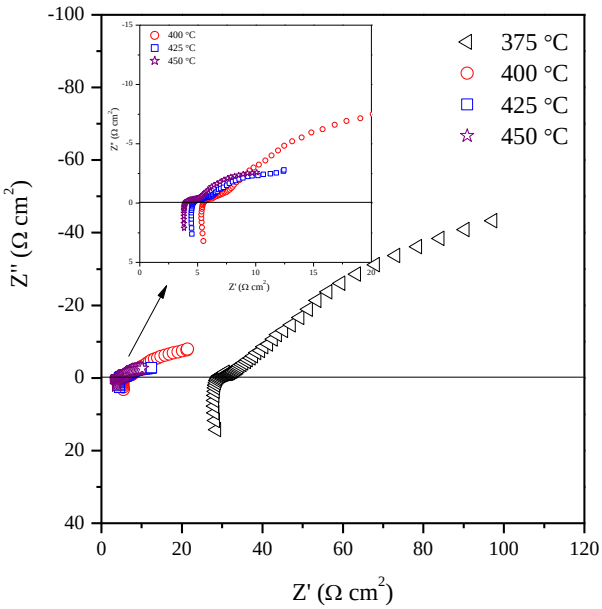

Figure 6.9 Impedance spectra: (a) LSF-CGDC; (b) LSFCu-CGDC; (c) LSFCo-CGDC

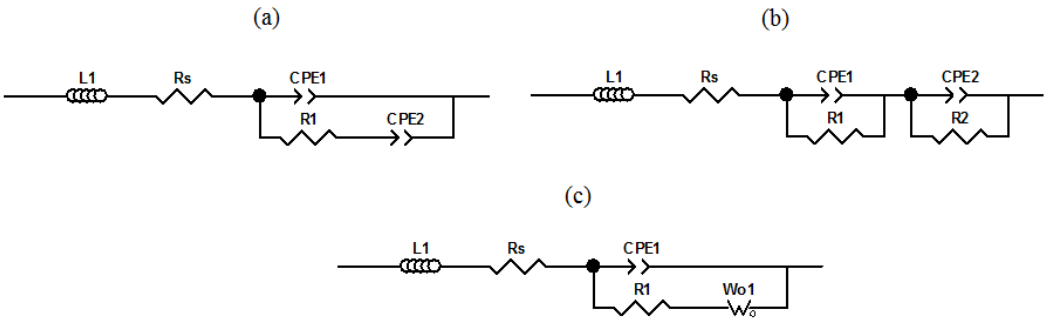

Figure 6.10 Equivalent circuits for impedance spectra fitting

The relationship between the rate of ammonia formation and the operating temperature was investigated under constant voltage (1.4 V) for three electrolytic cells based on LSF-CGDC, LSFCu-CGDC and LSFCo-CGDC composite cathodes, as shown in Figure 6.11. As can be seen, the rates of ammonia formation increased with an increase in the cell's operating temperature and the maximum values were attained when the electrolytic cells operated at 400 ºC. Moreover, the maximum rates of ammonia formation were found to be up to 0.7×10^{-10}, 0.5×10^{-10} and 1.5×10^{-10} mol s^{-1} cm^{-2}, at which the generated current densities were 14.25, 13.85 and 21.21 mA/cm^2 and the corresponding Faradaic efficiencies were about 0.14, 0.10 and 0.20 % for LSF-CGDC, LSFCu-CGDC and LSFCo-CGDC composite cathodes, respectively, as listed in Table 6.1. This indicates that the electrocatalytic activity of the LSFCo-CGDC composite cathode for ammonia synthesis is better than that of LSF-CGDC and LSFCu-CGDC. This could ascribed to the low polarisation resistance (Rp) of LSFCo-CGDC compared to LSF-CGDC and LSFCu-CGDC as described above [75]. In addition, the increase in the rates of production with an increase in operating temperature could be attributed to the increase in the ionic conductivity of the electrolyte with temperature [115]. However, when the electrolytic cells operated above 400 ºC, the ammonia formation rate declined. This decrease in the rates at high temperature might be due to the rate of ammonia decomposition, although the electrolyte ionic conductivity increases with temperature [75, 115].

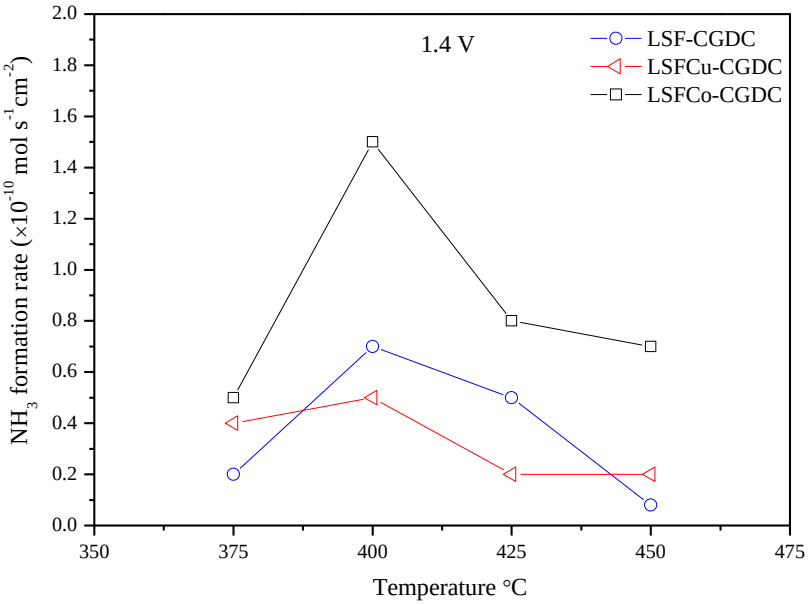

Figure 6.11 Dependence of the rate of ammonia formation on the operating temperature for LSF-CGDC, LSFCu-CGDC and LSFCo-CGDC composite cathodes

Table 6.1 Corresponding current densities and Faradaic efficiencies of ammonia formation over LSF-CGDC, LSFCu-CGDC and LSFCo-CGDC composite cathodes at 1.4 V

Temperature (°C)	**LSF-CDGC**		**LSFCu-CGDC**		**LSFCo-CGDC**	
	Current density (mA/cm^2)	**Faradaic efficiency (%)**	**Current density (mA/cm^2)**	**Faradaic efficiency (%)**	**Current density (mA/cm^2)**	**Faradaic efficiency (%)**
375	2.64	0.22	3.02	0.38	4.02	0.36
400	14.25	0.14	13.85	0.10	21.21	0.20
425	24.77	0.06	18.52	0.03	25.80	0.10
450	28.54	0.01	19.72	0.03	40.61	0.05

6.3.5 Synthesis of ammonia at different applied voltages

Figures 6.12a-c show performance stabilities of electrolytic cells based on LSF-CGDC, LSFCu-CGDC and LSFCo-CGDC composite cathodes respectively, at

constant temperature and different applied voltages (1.2-1.8 V) over a period of 30 min. It is to be noted that the three electrolytic cells demonstrated almost stable performance under the applied voltages (1.2-1.8 V), indicating a stable electrochemical process. In addition, the generated current densities increased with increasing the applied voltages from 1.2 to 1.4 V, which means that more oxide ions (O^{2-}) were transported through the electrolyte to the anode surface. When the electrolytic cell operated at 1.4 V, the generated current densities were found to be up to 14.25, 13.85 and 21.21 mA/cm^2 for LSF-CGDC, LSFCu-CGDC and LSFCo-CGDC composite cathodes respectively, as listed in Table 6.2. However, when the applied voltages were further increased, to values higher than 1.4 V, the generated current densities decreased and reached values of 13.43, 7.27 and 13.49 mA/cm^2 at 1.8 V, as listed in Table 6.2. This indicates the difficulties of transporting more O^{2-} through the electrolyte to the anode surface at higher voltages (> 1.4 V). This may be related to the blocking effect of Li^+, Na^+, and K^+ ions, as mentioned previously in Chapter 5. These ions will move and accumulate at the cathode/electrolyte interface forming positively charged layer, thus partially block the transfer of oxygen ions (O^{2-}) and resulting in low current densities [258, 259].

(a)

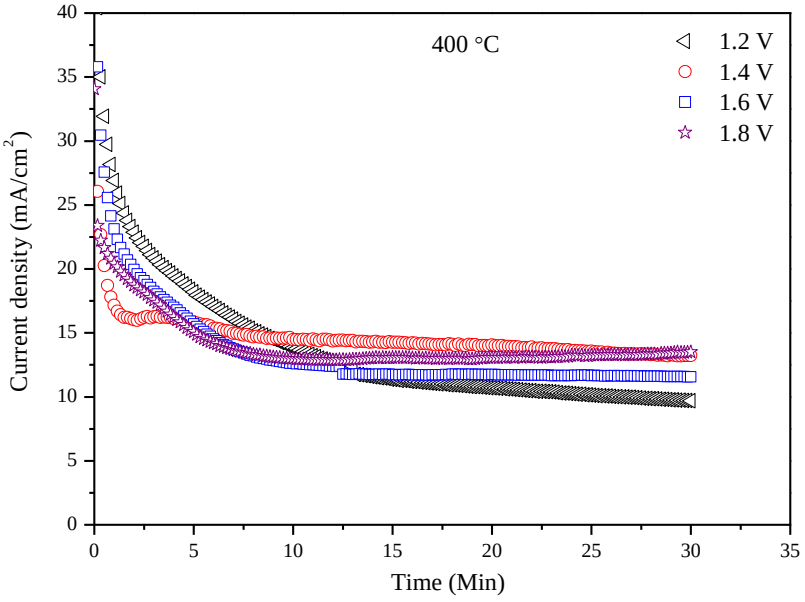

(b)

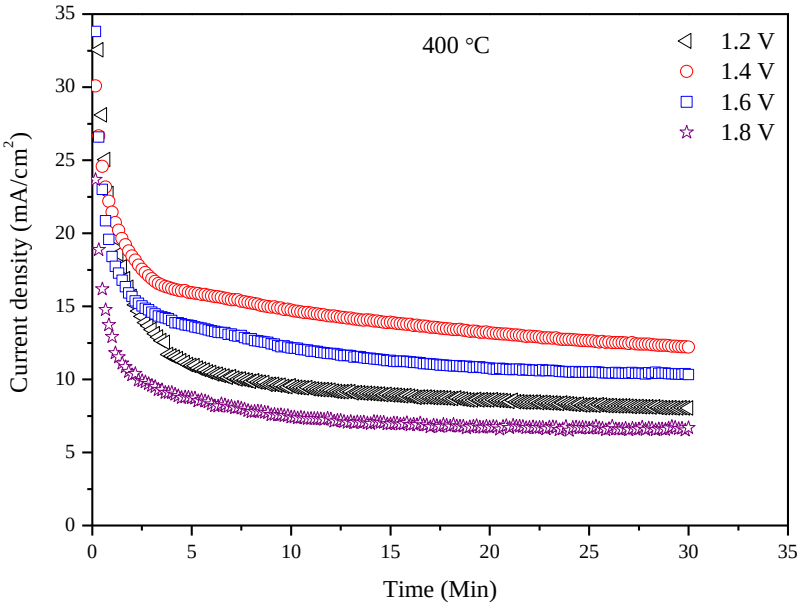

(c)

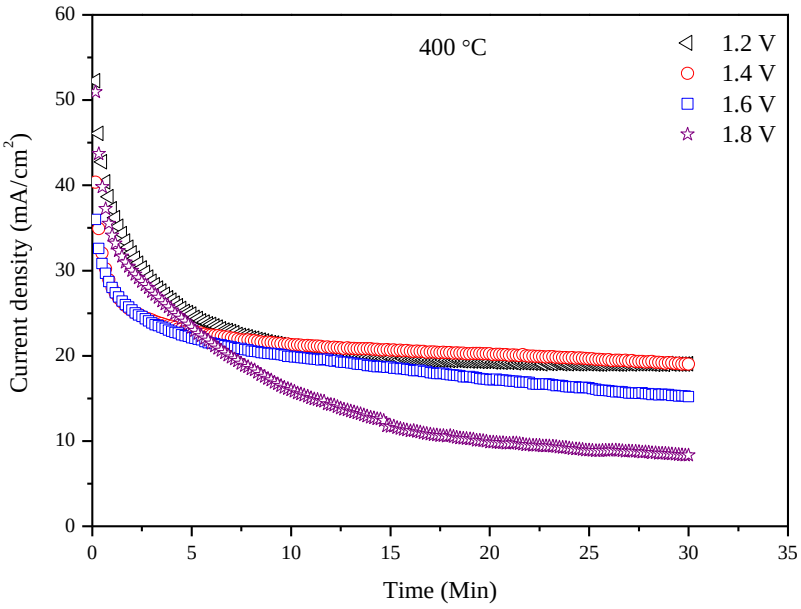

Figure 6.12 Electrolytic cell performance stability at 400 °C and 1.2-1.8 V: (a) LSF-CGDC composite cathode; (b) LSFCu-CGDC composite cathode; (c) LSFCo-CGDC composite cathode

In order to investigate the effect of the applied voltage on the rates of ammonia formation, the operating temperature of the electrolytic cells was kept at constant value (400 °C) and the applied voltages were varied from 1.2 to 1.8 V. Figure 6.13 shows the dependence of the rates of ammonia formation on the applied voltages of the electrolytic cells based on LSF-CGDC, LSFCu-CGDC and LSFCo-CGDC. As can be seen, there is an increase in the rate of ammonia formation as the applied voltage is increased from 1.2 to 1.4 V, accompanied by an increase in the generated current densities, as listed in Table 6.2. In addition, the rates of ammonia formation for LSFCo-CGDC were higher than that of LSF-CGDC and LSFCu-CGDC composite cathodes. These ammonia production rates were found to be 0.7×10^{-10}, 0.5×10^{-10} and 1.5×10^{-10} mol s^{-1} cm^{-2} for LSF-CGDC, LSFCu-CGDC and LSFCo-CGDC composite cathodes, respectively, at 400 °C with an applied voltage of 1.4 V. However, the rates of ammonia formation decreased significantly when the applied voltage was further increased to values higher than 1.4 V and reached the minimum values at 1.8 V. This could be attributed to the competitive adsorption of H_2 and N_2 over the cathode surface [41, 70]. These low rates of ammonia formation, with the corresponding current efficiencies (< 1%), indicate that there is more than one process over the cathode surface and that the competitive hydrogen evolution reaction (HER) is the dominant one. Although the rates of ammonia formation were rather low, these values are higher than those reported previously (3.75×10^{-13} mol s^{-1} cm^{-2} at 650 °C), when steam and nitrogen were used to produce ammonia in an electrolytic cell based on an oxide ion (O^{2-}) conducting electrolyte (YSZ) [10]. This difference in the ammonia formation rates could be due to the high ionic conductivity of the composite electrolyte (CGDC-carbonate) in comparison to YSZ and to operating at lower temperature, which in turn reduced the effect of thermal decomposition of ammonia, as discussed previously in Chapter 5.

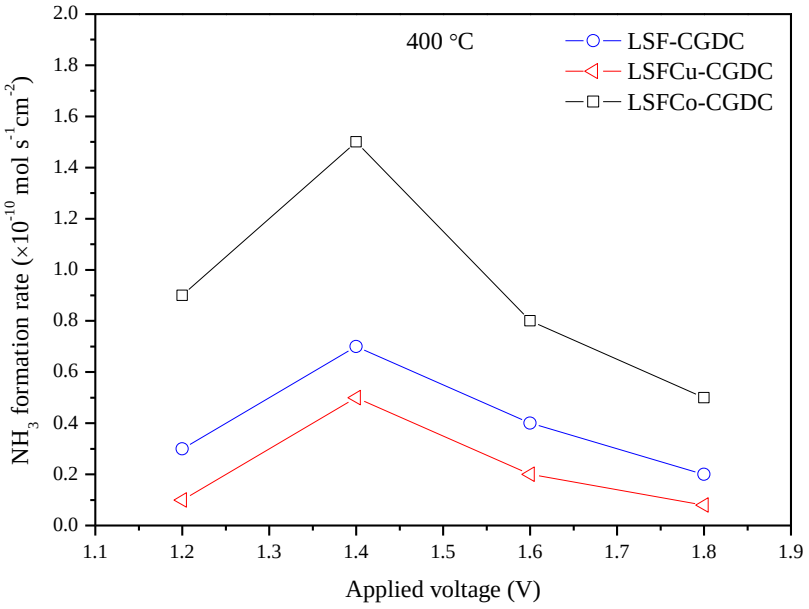

Figure 6.13 Dependence of the rate of ammonia formation on the applied voltage at 400 °C for LSF-CGDC, LSFCu-CGDC and LSFCo-CGDC cathodes

Table 6.2 The corresponding current densities and Faradaic efficiencies of ammonia formation over LSF-CGDC, LSFCu-CGDC and LSFCo-CGDC composite cathodes at 400 °C

Applied voltage (V)	**LSF-CDGC**		**LSFCu-CGDC**		**LSFCo-CGDC**	
	Current density (mA/cm^2)	Faradaic efficiency (%)	Current density (mA/cm^2)	Faradaic efficiency (%)	Current density (mA/cm^2)	Faradaic efficiency (%)
1.2	12.33	0.07	9.12	0.03	20.55	0.13
1.4	14.25	0.14	13.85	0.10	21.21	0.20
1.6	12.61	0.09	11.50	0.05	18.38	0.13
1.8	13.43	0.04	7.27	0.03	13.49	0.11

6.4 Conclusion

Three perovskite oxides, based on Sr doped-$LaFeO_3$ (LSF), Sr and Cu doped $LaFeO_3$ (LSFCu) and Sr and Co doped $LaFeO_3$ (LSFCo), were synthesised via a combined EDTA-citrate complexing sol-gel process. The properties of these

materials, including phase composition, microstructure, and thermal behaviour were investigated. It was found that the oxides were thermally stable in N_2 atmosphere within the measured temperature range (~ 25-500°C).

Tri-layer electrolytic cells were successfully fabricated by a cost-effective one-step dry-pressing and co-firing process. Ammonia was successfully synthesised directly from water and nitrogen in electrolytic cells based on LSF-CGDC, LSFCu-CGDC and LSFCo-CGDC as composite cathodes, CGDC-carbonate composite as an electrolyte and SSCo-CGDC composite as an anode. The maximum rates of ammonia formation were 0.7×10^{-10} mol s^{-1} cm^{-2} for LSF-CGDC, 0.5×10^{-10} mol s^{-1} cm^{-2} for LSFCu-CGDC and 1.5×10^{-10} mol s^{-1} cm^{-2} for LSFCo-CGDC at 400 °C with an applied voltage of 1.4 V. It is obvious from these figures that when LSF was doped with Co, the rate of ammonia formation almost doubled. However, there was a decrease in the rate of ammonia formation when LSF was doped with Cu. This indicates the catalytic activity of the LSFCo-CGDC composite cathode for ammonia synthesis is better than that of LSF-CGDC and LSFCu-CGDC. This could be attributed to the low polarisation resistance (Rp) of LSFCo-CGDC compared to LSF-CGDC and LSFCu-CGDC composite cathodes. It could be attributed to the better catalytic activity towards ammonia synthesis for LSFCo which needs further investigation. In addition, the rate of ammonia formation using the LSFCo-CGDC composite cathode was also higher than those obtained for the spinel type catalyst (6.5×10^{-11} mol s^{-1} cm^{-2} for CFO-CGDC) at similar experimental conditions (Chapter 5).

In general, although the rates of ammonia formation were rather low, these values are two or three order of magnitude higher than those previously reported by Skodra et al. [10], when ammonia was synthesised from H_2O and N_2 at 650 °C over a Ru-based catalyst.

7 Ammonia synthesis from water and nitrogen or air based on doped lanthanum chromite cathodes

7.1 Introduction

Lanthanum chromite ($LaCrO_3$) is among the perovskite-based oxides which have ABO_3 formula (see Chapter 4). $LaCrO_3$ is the most commonly used interconnect material for SOFCs owing to its high electronic conductivity and stability under both oxidizing and reducing environment at high temperature and its good compatibility with other adjacent cell components [322]. Furthermore, $LaCrO_3$-based perovskites have been also proposed as potential anode materials for SOFCs due to their aforementioned properties as well [323].

Within the $LaCrO_3$ family, Sr and Mn doped $LaCrO_3$ and Sr and Fe doped $LaCrO_3$ are the most promising. Tao and Irvine [324] investigated the catalytic properties of $La_{0.75}Sr_{0.25}Cr_{0.5}Fe_{0.5}O_{3-\delta}$ (LSCrF) for CH_4-reforming and its potential application as anode materials for direct methane fuel cell. In that study, it was found out that LSCrF exhibits good catalytic activity for methane-reforming. The electronic conductivity of LSCrF is approximately 14.3 in air and 0.21 S cm^{-1} in 5% H_2 at 900°C [325]. Tao and Irvine [326] demonstrated for the first time a fully redox-stable anode for SOFCs based on Sr and Mn doped $LaCrO_3$ with the form of $La_{0.75}Sr_{0.25}Cr_{0.5}Mn_{0.5}O_{3-\delta}$ (LSCM). The electronic conductivity of LSCM is about 38 and 1.5 S cm^{-1} in air and wet 5% H_2 at 900 ºC respectively [327]. In addition, due to its stability and conductivity in both reducing and oxidising atmospheres, LSCM was proposed as anode and cathode to fabricate symmetrical SOFCs [328]. These properties make LSCM a good candidate material to be used as electrodes in solid oxide electrolysis cell (SOECs) as well. Recently, Yang and Irvine [329] employed LSCM as a cathode for steam electrolysis in oxygen ion conducting SOECs and it was found that LSCM composite cathode performed much better with low steam content (3% H_2O) without the presence of protective H_2 gas as in the case of Ni/YSZ cathode. LSCM has been also used as anode material for steam electrolysis in proton conducting SOECs [288]. In addition, LSCM has been evaluated as a cathode in high temperature steam and carbon dioxide co-electrolysis [287].

As mentioned previously, doped $LaCrO_3$-based oxides are redox stable materials. This makes them a better choice as cathode materials for ammonia synthesis, since hydrogen is also produced at the cathode side. This reducing environment requires redox stable cathodes. Building on the above mentioned properties of doped $LaCrO_3$ based oxides, it is expected that such type of oxides might be good cathode and anode materials for the electrochemical synthesis of ammonia from water and nitrogen in oxygen-ion conducting electrolytic cells.

7.2 Ammonia synthesis based on LSCrF- and LSCM-CGDC composite cathodes

This research investigated the electrochemical synthesis of ammonia from water and nitrogen under atmospheric pressure in two chamber cell based on an oxygen-ion conducting electrolyte and either LSCrF-CGDC or LSCM-CGDC as composite cathodes.

7.2.1 Experimental

7.2.1.1 Synthesis of perovskite-type catalysts

$La_{0.75}Sr_{0.25}Cr_{0.5}Mn_{0.5}O_{3-\delta}$ catalyst (LSCM) was synthesised via a combined EDTA-citrate complexing sol-gel process [291]. Lanthanum oxide (La_2O_3, Alfa Aesar, 99 %), strontium nitrate ($Sr(NO_3)_2$, Alfa Aesar, 99 %) and chromium nitrate nonahydrate ($Cr(NO_3)_3 \cdot 9H_2O$, Sigma Aldrich, 99 %) and manganese acetate tetrahydrate ($(CH_3COO)_2Mn \cdot 4H_2O$, Sigma Aldrich, > 99 %) were used as starting materials. La_2O_3 was dissolved in diluted nitric acid to form lanthanum nitrate. Calculated amounts of $Sr(NO_3)_2$, $Cr(NO_3)_3 \cdot 9H_2O$ and $(CH_3COO)_2Mn \cdot 4H_2O$ were dissolved in deionised water and then added to the lanthanum nitrate solution. Citric acid and EDTA (ethylenediaminetetraacetic acid) were then added as complexing agents with molar ratio of citric acid:EDTA:metal cations of 1.5:1:1. $NH_3 \cdot H_2O$ was added to the mixed solution to adjust the pH value to around 6. Under heating and stirring, the solution was evaporated on a hot-plate, and then gradually changed into

a black sticky gel before complete drying. The as-prepared powder was ground and subsequently calcined in air at different temperatures from 900 to 1200ºC for 2 h with heating/cooling rates of 5 ºC min^{-1} to obtain a pure phase of LSCM catalyst without any carbon residue.

$La_{0.75}Sr_{0.25}Cr_{0.5}Fe_{0.5}O_{3-\delta}$ catalyst (LSCrF) was also synthesised via a combined EDTA-citrate complexing sol-gel process as described above. Lanthanum oxide (La_2O_3, Alfa Aesar, 99 %), strontium nitrate ($Sr(NO_3)_2$, Alfa Aesar, 99 %) and chromium nitrate nonahydrate ($Cr(NO_3)_3 \cdot 9H_2O$, Sigma Aldrich, 99 %) iron nitrate nanohydrate ($Fe(NO_3)_3 \cdot 9H_2O$, Alfa Aesar, 98 %) were used as starting materials. The resultant powder was ground and subsequently calcined in air at different temperatures from 900 to 1300 ºC for 2 h with heating/cooling rates of 5 °C min^{-1} to obtain a single phase of LSCrF.

7.2.1.2 Materials characterisation

Phase purity was studied by powder X-ray diffraction using Panalytical X'Pert Pro diffractometer. The thermal behaviour of both perovskite based cathodes (LSCM and LSCrF) was investigated in N_2 atmosphere from room temperature to 500 ºC with heating/cooling rates of 10 ºC/min. The microstructures of the prepared catalyst and the cross-sectional area of single cell were examined using Hitachi SU6600 Scanning Electron Microscope (SEM).

7.2.1.3 Fabrication of the single cell

A tri-layer single cell was fabricated by a cost-effective one-step dry-pressing method. The composite anode was prepared by mixing in a mortar SSCo, prepared as described in Section 5.2.1.2, CGDC, prepared as described in Section 5.2.1.3 and starch as pore former with weight ratio of 70:30:15. The composite electrolyte GDC/$(Li/Na/K)_2CO_3$ (70:30 wt %) was prepared as described in Section 5.2.2. The composite cathode was prepared by mixing in a mortar LSCM and CGDC and starch with weight ratio of 70:30:15. The composite anode, composite electrolyte and composite cathode were fed into the die, layer by layer, with the aid of a sieve to

ensure uniform powder distribution, and then uniaxially pressed at pressure of 121 MPa. This freshly made green pellet was sintered in air at 700 °C for 2 h at rates of 2°C/min heating/cooling. The active surface area of the cathode was 0.785 cm^2. Silver paste was painted in grid pattern on each electrode surface of the cell as a current collector. Ag wires were used as output terminals for both electrodes. The single cell consists of LSCrF- composite cathode was prepared as described above in for the LSCM-CGDC composite cathode.

7.2.1.4 Ammonia synthesis

The fabricated single cells for ammonia synthesis were sealed into a self-designed double chamber reactor using ceramic paste (Aremco, Ceramabond 552). The cathode chamber was fed with 3% H_2O-N_2 (BOC), whereas anode was exposed to air. The water vapour (3% H_2O) was supplied to the cathode chamber by bubbling N_2 stream through a liquid water container, at 25 °C. A constant voltage (1.2-1.8 V) was applied over a period of 30 min. The ammonia synthesised at the cathode chamber was absorbed by 20 ml of diluted HCl (0.01 M). The concentration of NH_4^+ in the absorbed solution was analysed using ion selective electrode (ISE) and the rate of ammonia formation was calculated using Equation 2.9 (Section 2.4.2). The two electrolytic cells were constructed as follows;

- Air, SSCo-CGDC|CGDC-carbonate|LSCM-CGDC, 3% H_2O-N_2
- Air, SSCo-CGDC|CGDC-carbonate|LSCrF-CGDC, 3% H_2O-N_2

7.2.2 Results and discussion

7.2.2.1 XRD analysis

The XRD patterns of LSCM and LSCrF calcined in air at different temperatures is shown in Figure 7.1 and Figure 7.2 respectively. As can be seen, a single-phase perovskite oxide of LSCM was obtained when the corresponding ash was fired at 1200 °C for 2 h (Figure 7.1c), whereas a calcination temperature 1300 °C and 2 h were needed to obtain a pure phase of LSCrF (Figure 7.2c). Below these

temperatures, a minor impurity of $SrCrO_4$ (JCPDS card no 35-734) was detected in both cases [330]. The crystallite size of LSCM is about 44.63 nm, while that of LSCrF is 46.75 nm, estimated from Sherrer's formula (Equation 2.3).

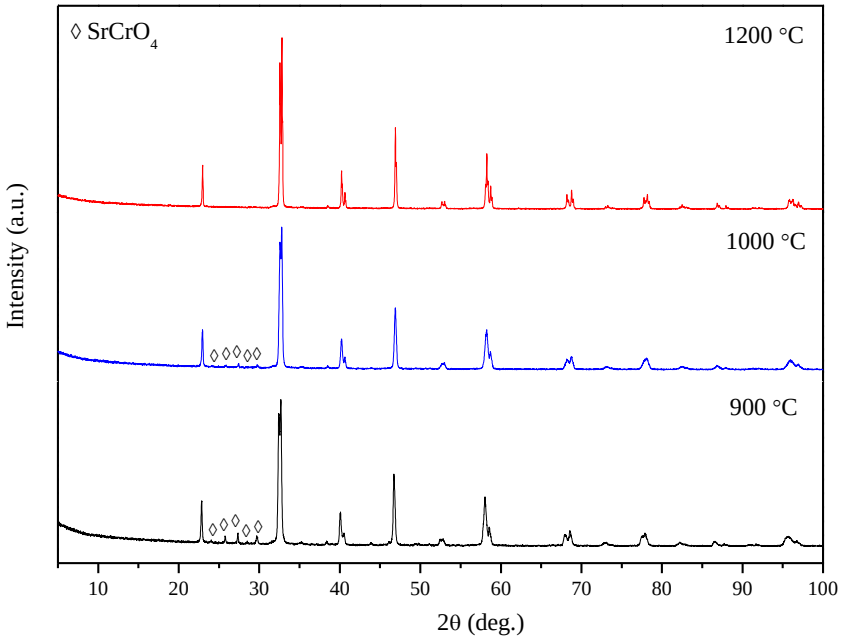

Figure 7.1 XRD patterns of LSCM

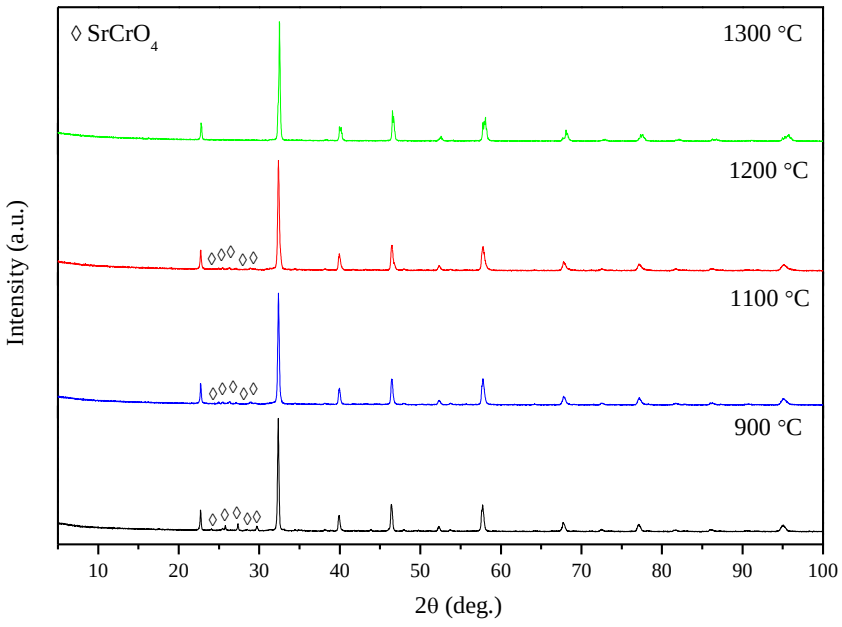

Figure 7.2 XRD patterns of LSCrF

In order to investigate the compatibility between the CGDC and the perovskite oxides (LSCM and LSCrF), both composite cathodes (LSCM-CGDC and LSCrF-CGDC) were fired in air at 700 °C which is the sintering temperature for the single cells. As can be seen from Figure 7.3, the XRD patterns of LSCrF-CGDC (Figure 7.3b) and LSCM-CGDC (Figure 7.3c) display only the corresponding peaks for LSCrF, LSCM and CGDC, no extra peaks were detected indicating that both oxides (LSCrF and LSCM) are chemically compatible with CGDC at the single cell sintering temperature.

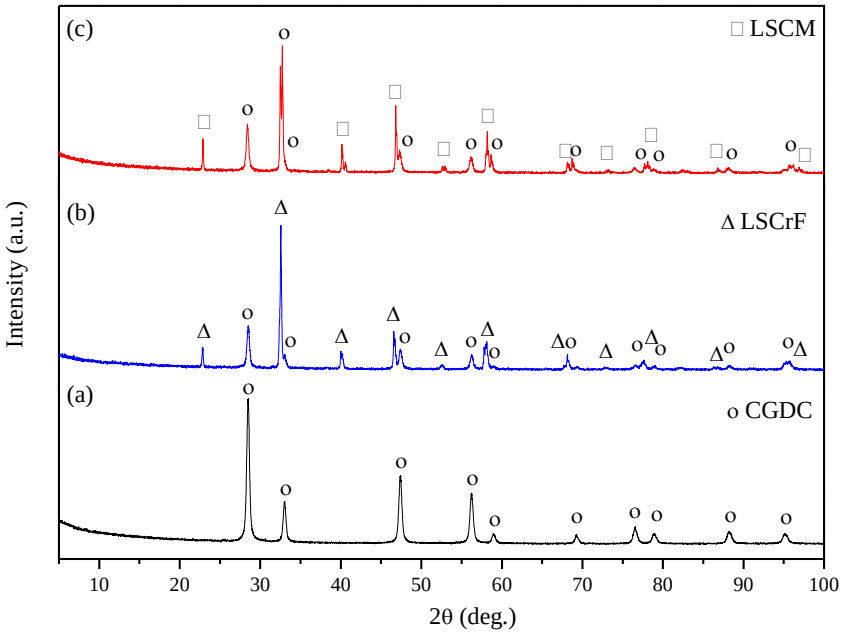

Figure 7.3 XRD patterns of (a) CGDC; (b) LSCrF-CGDC composite cathode fired at 700 ºC; (c) LSCM-CGDC composite cathode fired at 700 ºC

7.2.2.2 SEM

The SEM micrographs of the LSCM and LSCrF powders synthesised by sol-gel method and calcined in air at 1200 and 1300 ºC for 2 h are shown in Figure 7.4a and b respectively. As can be seen, both powders display similar morphology which is characterised by sphere-type particles with a slight agglomeration.

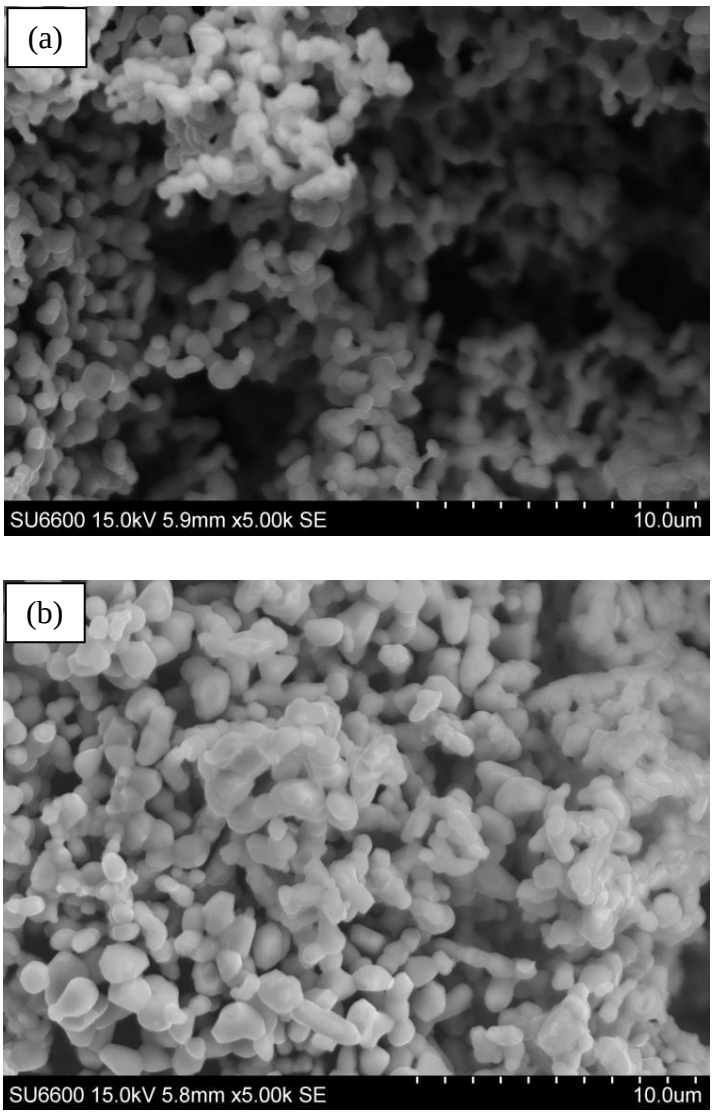

Figure 7.4 SEM images of the perovskite based catalysts powder: (a) LSCM calcined in air at 1200 ºC: (b) LSCrF calcined in air at 1200 ºC

Figure 7.5a and b shows the SEM micrographs of the cross-section views of two single cells (before test) sintered in air 700 ºC for 2 h. These cells compose of SSCo-CGDC composite as anode, CGDC-$(Li/Na/K)_2CO_3$ as an electrolyte and either LSCM-CGDC (Figure 7.5a) or LSCrF-CGDC (Figure 7.5b) composites as cathode. As can be seen, in both cases, the composite electrolyte is dense and adheres very well to the composite anode and the composite cathode, indicating its thermal compatibility with them.

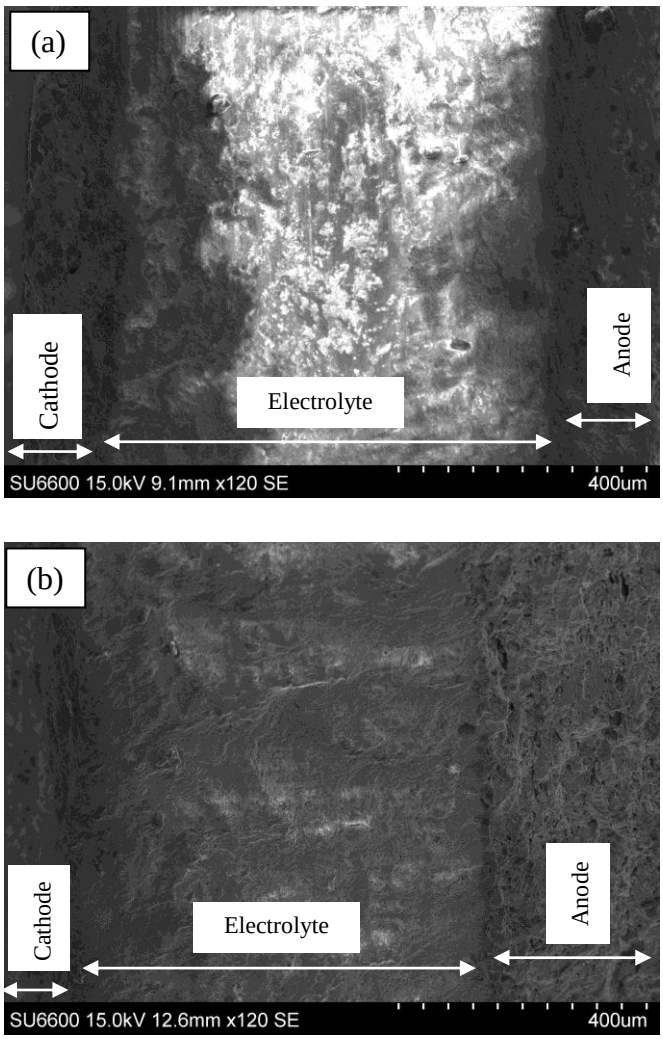

Figure 7.5 SEM images of cross-sectional areas of the single cells based on different composite cathodes before test: (a) LSCM-CGDC; (a) LSCrF-CGDC

7.2.2.3 Thermal analysis

The thermal behaviours of LSCM and LSCrF cathodes were investigated under N_2, as the cathode is exposed to this atmosphere during the ammonia synthesis. The TGA-DSC curves of LSCM and LSCrF catalysts in N_2 atmospheres from room temperature up to 500 °C are shown in Figures 7.6a and b respectively. As can be seen, a slight weight gain which is due to the buoyancy effect of air was observed in both cases. In the case of LSCM (Figure 7.6a), the weight gain was about 0.02 %, whereas for LSCrF (Figure 7.6b) was about 0.26 %. The DSC curves show no obvious thermal effects, indicating that there are no phase transitions or sample

decomposition or reaction between this perovskite-based cathodes and N_2 in the measured temperature range. This suggests that LSCM and LSCrF cathodes are thermally stable in N_2 within the measured temperature range.

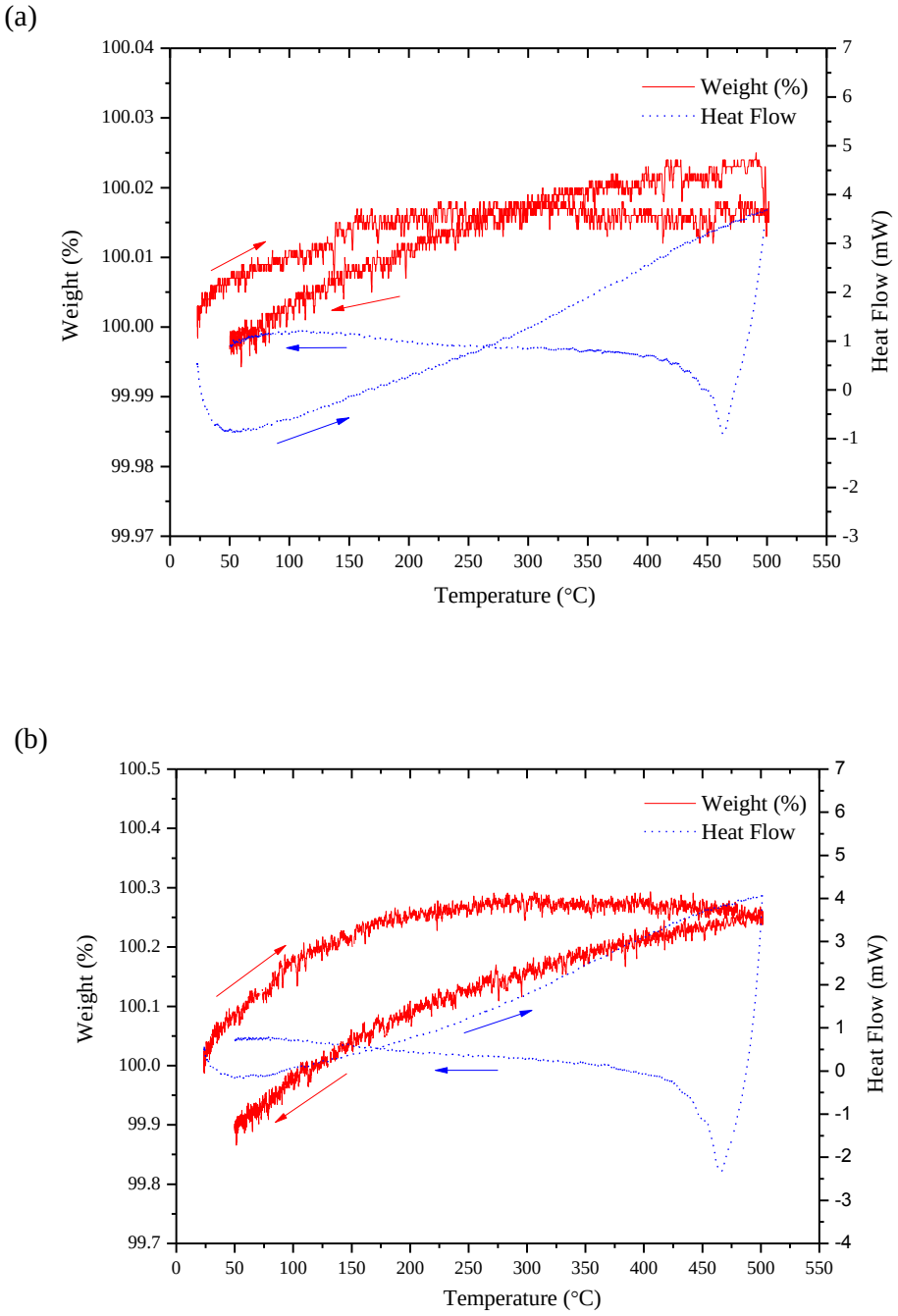

Figure 7.6 TGA-DSC curves for perovskite based catalysts in nitrogen, up to 500 ºC: (a) LSCM; (b) LSCrF

7.2.2.4 Synthesis of ammonia at different temperatures

Figures 7.7a and b show the performance stabilities during the ammonia synthesis at different temperatures (375-425 °C) with an applied voltage of 1.4 V over a period of 30 min for two electrolytic cells based on LSCM-CGDC and LSCrF-CGDC composite cathodes respectively. As can be seen, the performances of both electrolytic cells were stable under all measured temperatures. In addition, it is obvious that the generated current densities increase significantly as the cell operating temperature increased and reached maximum values of 21.90 and 23.13 mA/cm^2 at 425 ºC for LSCM-CGDC and LSCrF-CGDC systems respectively as listed in Table 7.1. This increase in the generated current densities with temperature indicates that more oxygen ions (O^{2-}) were transported through the electrolyte to the anode surface as stated previously.

(a)

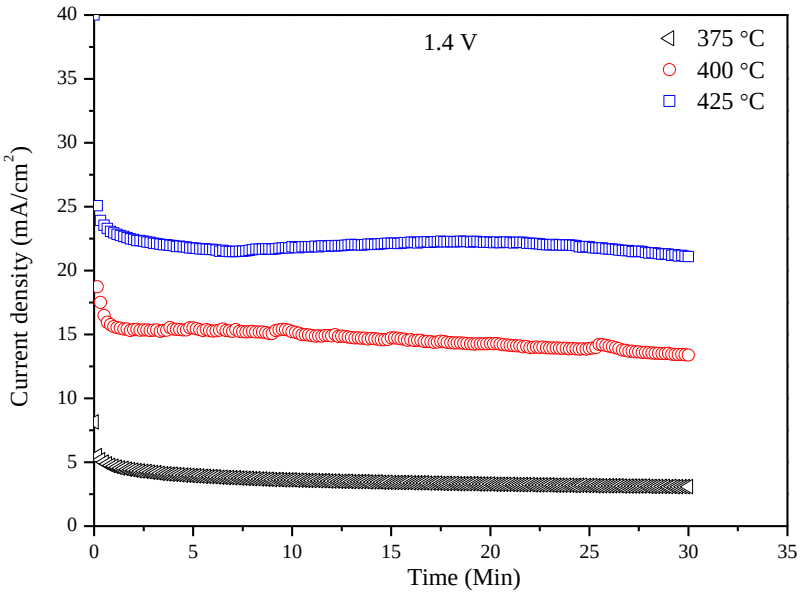

(b)

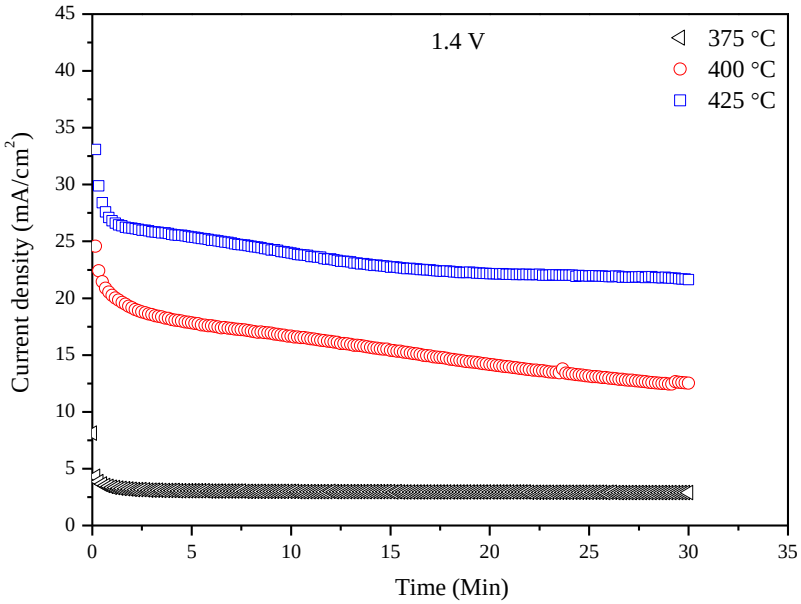

Figure 7.7 Electrolytic cell performance stability at 1.4 V and 375-425 °C. (a) LSCM-CGDC composite cathode; (b) LSCrF-CGDC composite cathode

Figures 7.8a and b show the in-situ AC impedance spectra under open circuit conditions at different temperatures (375-425 °C) of two electrolytic cells based on LSCM-CGDC and LSCrF-CGDC composite cathodes respectively. In the case of LSCM-CGDC (Figure 7.8a), the spectra display different shapes, depending upon the operating temperature, thus two different equivalent circuits were used for data fitting. At 375 and 400 °C, two depressed semicircles were observed. These data were fitted using the equivalent circuit shown in Figure 7.8c. In this circuit, L represents an inductance that caused by the instrument and connection wires, Rs is the series resistance (Rs) including resistances of the electrolyte, electrode materials and the contact resistance at the electrode/electrolyte interface, the two components (R1CPE1) and (R2CPE2) in series are associated to the electrode processes at high and low frequency arcs respectively. R1 and R2 represent the polarisation resistance while CPE is a constant phase element. At 425 °C, only one depressed semicircle at high frequency and diagonal line with an angle less than 45° at low frequency were observed. This spectrum was fitted to the equivalent circuit shown in Figure 7.8d. In

the case of LSCrF-CGDC composite cathode, two depressed semicircles were observed at all operating temperatures (375-425 °C). These data were also fitted using circuit shown in Figure 7.8c.

In both electrolytic cells, the capacitances related to electrodes contribution at high frequency semicircle were found to be in the range of 10^{-5}-10^{-4} F/cm^2 which could be attributed to the charge transfer processes at the electrode/electrolyte interface. The low frequency semicircle with the associated capacitances of 10^{-3}-10^{-1} F/cm^2 could be ascribed to the mass transfer processes at the electrode. The diagonal line at 425 °C in the case of LSCM-CGDC composite cathode could be also speculated to the mass transfer processes at the electrode [46, 255, 256].

As can be seen from Figures 7.8a and b, with increasing the cell operating temperature, the Rs which is mainly related to the ohmic resistance of the electrolyte decreased significantly. This could be attributed to the increase in the electrolyte conductivity with temperature. In the case of LSCM-CGDC system, the lowest Rs value of about 10.43 Ω cm^2 was attained at 425 °C as presented Figure 7.8a. Whereas for LSCrF-CGDC composite cathode, the lowest Rs value (7.86 Ω cm^2) was obtained at 400 °C after which the Rs value increased and reached 10.11 Ω cm^2 at 425 °C as shown in Figure 7.8b. This might be due to the contact resistance. In addition, in both electrolytic cells, the total polarisation resistance, Rp (R1 + R2) decreased significantly with increasing the operating temperature which could be due to the electrodes catalytic activity improvement with temperatures. However, the Rp values in the electrolytic cell based on the LSCrF-CGDC composite cathode were lower than those of the LSCM-CGDC composite cathode, indicating a better catalytic activity of LSCrF-CGDC compared to LSCM-CGDC [75]. For example, at 400 °C, the total polarisation resistance of LSCrF-CGDC was 72.72 (Ω cm^2), while that of LSCM-CGDC was 88.29 (Ω cm^2).

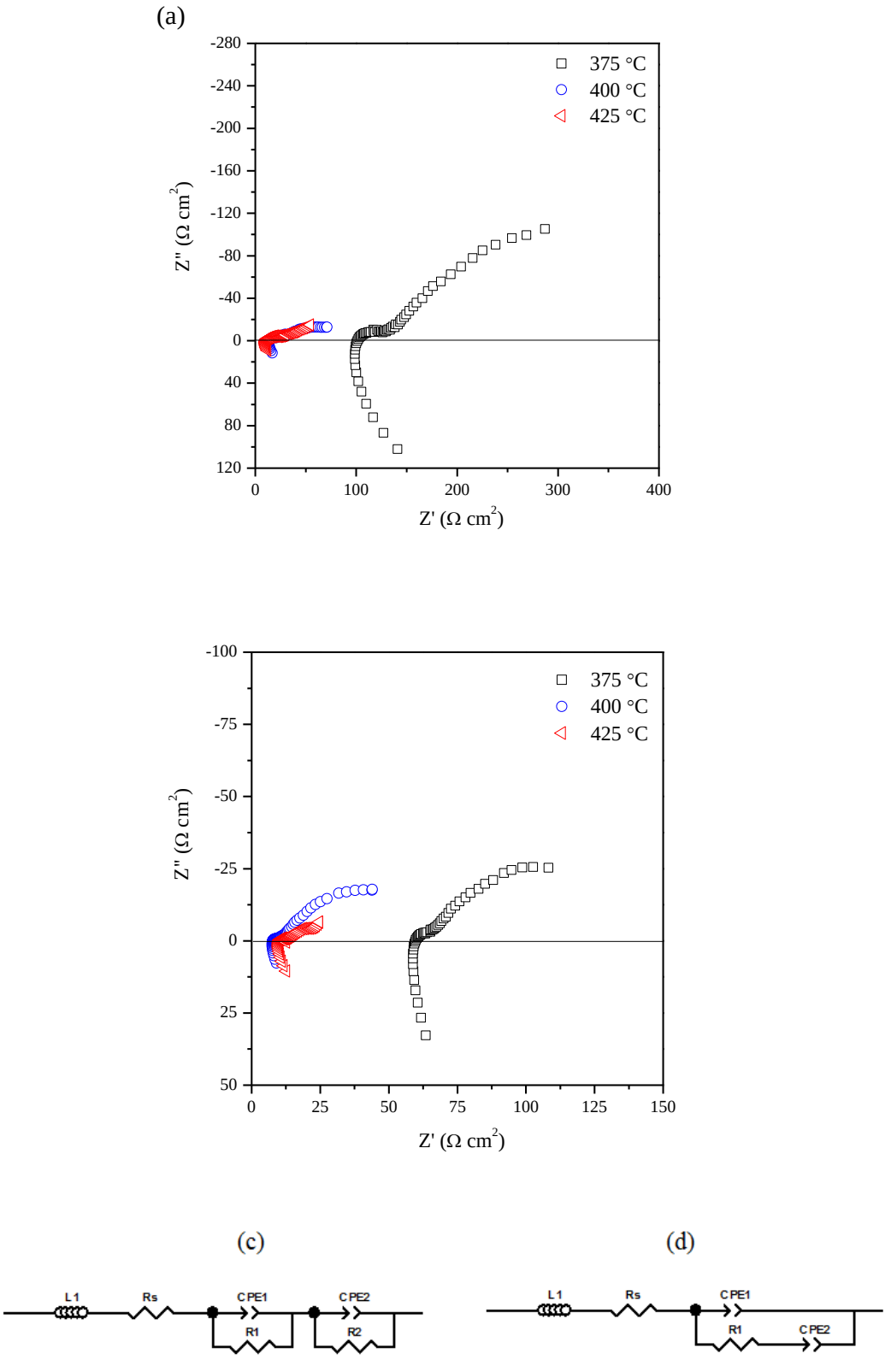

Figure 7.8 Impedance spectra under open circuit condition at 375-425 °C. (a) LSCM-CGDC composite cathode; (b) LSCrF-CGDC composite cathode; (c) and (d) equivalent circuits for the impedance data

The effect of the operating temperature on the rates of ammonia production was investigated under constant voltage (1.4 V) and varying the operating temperature from 375 to 425 ºC for two electrolytic cells based on LSCM-CGDC and LSCrF-CGDC composite cathodes as shown in Figure 7.9. In the case of LSCM-CGDC system (Figure 7.9a), there was an increase in the rate of ammonia formation as the cell operating temperature increased from 375 to 400 ºC and the maximum value of about 2.5×10^{-10} mol s^{-1} cm^{-2} was obtained at 400 ºC. At this rate of ammonia formation the generated current density and the corresponding Faradaic efficiency were found to be up to 14.55 mA/cm^2 and 0.52 % respectively as listed in Table 7.1. The observed increase in ammonia production rate with temperature could be ascribed to the increase the electrolyte ionic conductivity [73]. However, when the cell operating temperature was further increased to 425 ºC, the rate of ammonia formation dropped significantly and reached a value of 1.0×10^{-10} mol s^{-1} cm^{-2} which probably due ammonia decomposition at high temperature [73, 75].

Unlike the LSCM-CGDC composite cathode, in the case of LSCrF-CGDC system, the ammonia production rates dropped significantly as the operating temperature increased from 375 to 425 ºC (Figure 7.9b). Furthermore, the maximum rate of ammonia formation was found to be up to 4.0×10^{-10} mol s^{-1} cm^{-2} at 375 ºC at which the generated current density and the Faradaic efficiency were 2.99 mA/cm^2 and 3.87 % respectively as listed in Table 7.1. This low efficiency indicates that there is more than one process over the cathode surface and that the competitive hydrogen evolution reaction (HER) is the dominant one [41, 70]. As described above, the decrease in the ammonia formation rate with temperature, although the electrolyte ionic conductivity increases with temperature could be due the ammonia decomposition which becomes predominant at high temperature [73].

(a)

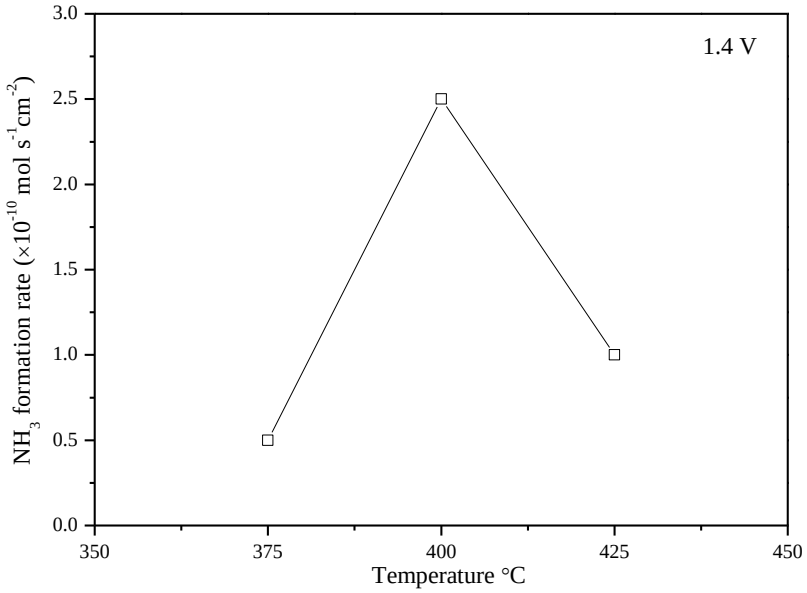

(b)

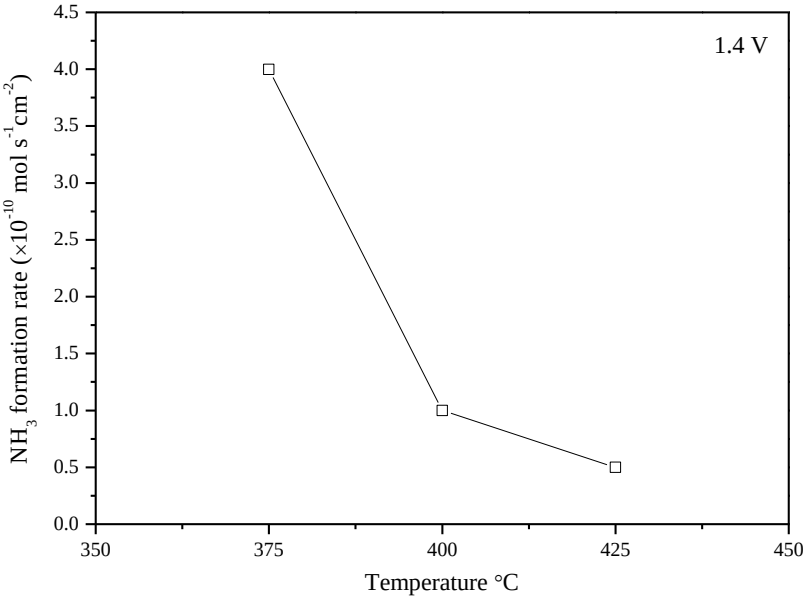

Figure 7.9 Dependence of the rate of ammonia formation on the operating temperature; (a) LSCM-CGDC composite cathode; (b) LSCrF-CGDC composite cathode

Table 7.1 Corresponding current densities and Faradaic efficiencies of ammonia formation over LSCM-CGDC and LSCrF-CGDC composite cathodes at 1.4 V

Temperature (°C)	LSCM-CGDC		LSCrF-CGDC	
	Current density (mA/cm^2)	Faradaic efficiency (%)	Current density (mA/cm^2)	Faradaic efficiency (%)
375	3.48	0.42	2.99	3.87
400	14.55	0.52	14.97	0.19
425	21.90	0.13	23.13	0.06

7.2.2.5 Ammonia synthesis at different applied voltages

Figures 7.1a and b show the performance stabilities of two electrolytic cells based on LSCM-CGDC and LSCrF-CGDC composite cathodes respectively at 400 and 375 ºC and different applied voltages (1.2-1.8 V) over a period of 30 min. As can be seen, both electrolytic cells exhibit almost constant current densities under all applied voltages indicating a stable electrochemical process. In the case of LSCM-CGDC system, the generated current density increased as the applied voltages increased from 1.2 to 1.8 V as shown in Figure 7.10a. This means that more oxygen ions (O^{2-}) are transported through the electrolyte to the anode surface. On the other hand, in the case of LSCrF-CGDC composite cathode, the generated current density (Table 7.2) decreased as the applied voltages is increased which indicates the difficulties of transporting more oxygen ions (O^{2-}) through the electrolyte to the anode surface at higher voltages (> 1.2 V). This could be attributed to the blocking effect of Li^+, Na^+, and K^+ ions. These ions may form a positively charged layer at cathode/electrolyte interface, thus partially block the transfer of the O^{2-} and resulting in low current densities [258, 259].

(a)

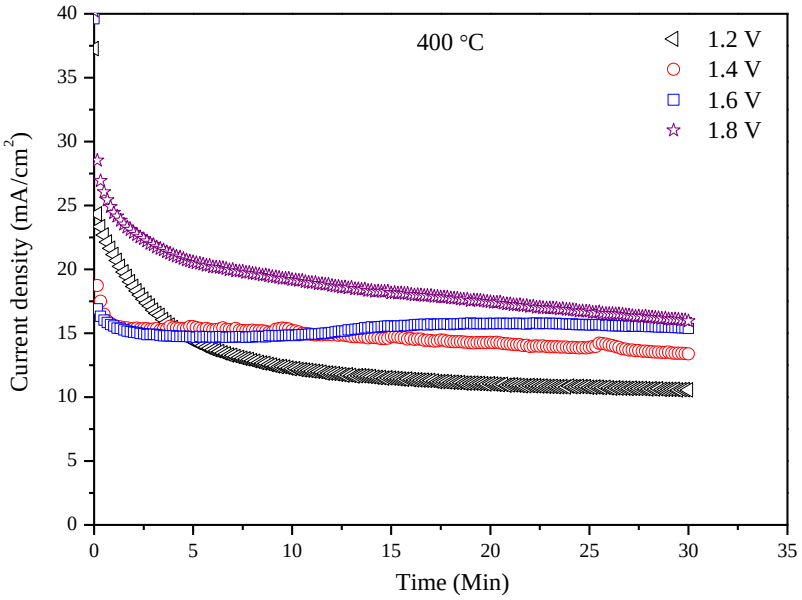

(b)

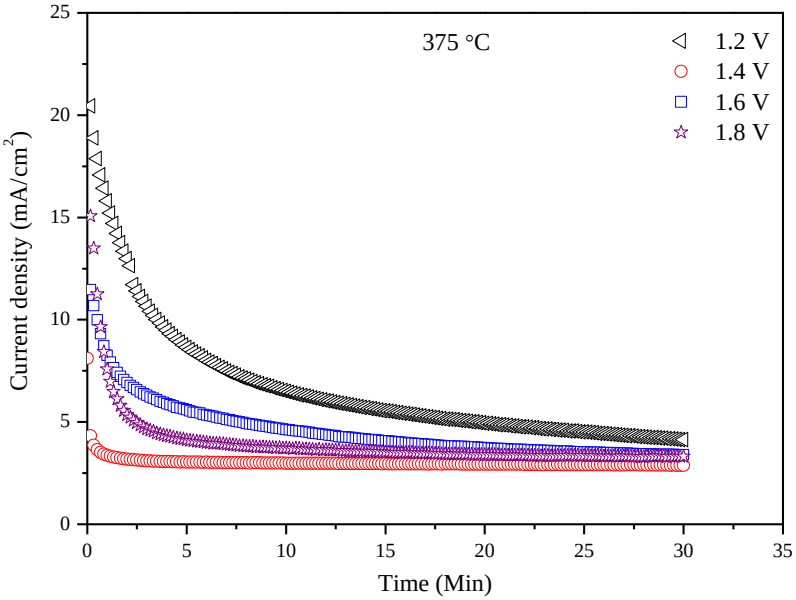

Figure 7.10 Electrolytic cell performance stability at 1.2-1.8 V. (a) LSCM-CGDC composite cathode; (b) LSCrF-CGDC composite cathode

In order to investigate the effect of the applied voltages on the rates of ammonia formation, the operating temperature of the two electrolytic cells was kept at constant value and the applied voltages varied from 1.2 to 1.8 V as shown in Figure 7.11. In the case of LSCM-CGDC composite cathode, the maximum rate was achieved when the electrolytic cell operated at 400 °C, thus the influence of the applied voltage on formation rate was studied at this temperature as presented in Figure 7.11a. On the other hand, the maximum rate of ammonia formation using LSCrF-CGDC composite cathode was obtained when the cell operated at 375 °C as shown in Figure 7.11b. It is to be noted that in both cases there was significant increase in the rate of ammonia production as the applied voltage increased from 1.2 to 1.4 V. Moreover, the maximum rates were found to be up to 2.5×10^{-10} and 4.0×10^{-10} mol s^{-1} cm^{-2} at 400 and 375 ºC for LSCM-CGDC and LSCrF-CGDC composite cathodes respectively. However, when the two electrolytic cells operated at voltages higher than 1.4 V, the rates of ammonia formation dropped significantly and reached the minimum values with an applied voltage of 1.8 V which could be due to the competitive adsorption between the N_2 and H_2 over the cathode surface [41, 70]. In addition, the low ammonia production rate with the low current efficiencies (< 4 %, Table 7.2) mean that there was more than one process occurring over the cathode surface and the hydrogen evolution is the dominant one [11, 70]. However, the obtained rates of ammonia are still higher than the reported (3.75×10^{-13} mol s^{-1} cm^{-2} at 650 °C) when ammonia was synthesised using steam and nitrogen as reactants [10]. This difference in ammonia formation could be due the different operating temperatures as described previously.

(a)

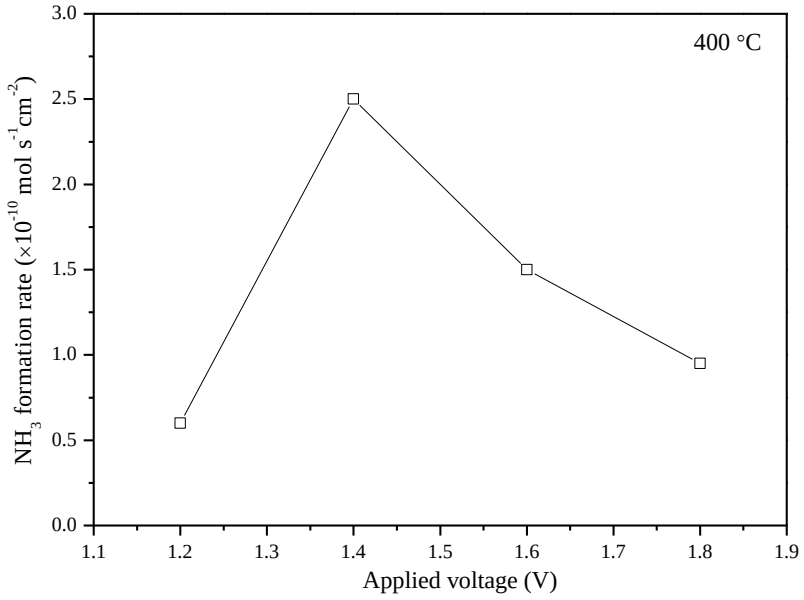

(b)

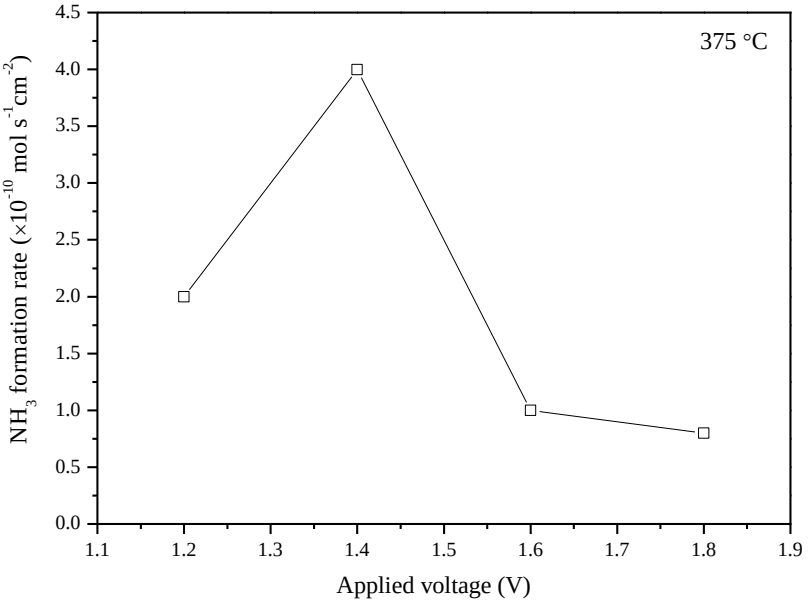

Figure 7.11 Dependence of the rate of ammonia formation on the applied voltage. (a) LSCM-CGDC composite cathode; (b) LSCrF-CGDC composite cathode

Table 7.2 The corresponding current densities Faradaic efficiencies of ammonia formation over LSCM-CGDC and LSCrF-CGDC composite cathodes at different voltages

Applied voltage (V)	LSCM-CGDC (400 °C)		LSCrF-CGDC (375 °C)	
	Current density (mA/cm^2)	Faradaic efficiency (%)	Current density (mA/cm^2)	Faradaic efficiency (%)
1.2	11.63	0.15	5.58	1.04
1.4	14.55	0.52	2.99	3.87
1.6	15.31	0.28	4.15	0.70
1.8	18.02	0.15	3.67	0.63

7.3 Preliminary investigation on ammonia synthesis directly from air and water based on LSCrF-CGDC composite cathode

In Chapters 3 and 4, it was demonstrated that ammonia was successfully synthesised from H_2 and N_2. In Chapter 5, 6 and in also in Section 7.2, it was also demonstrated that ammonia could be synthesised from water and nitrogen without the need for H_2. It is well known that air contains 78 % N_2, therefore the synthesis of ammonia directly from air is advantageous because the separation process can be eliminated [11]. Recently, Lan et al. [11, 258] reported in two separate studies the synthesis of ammonia directly from air and water without the need for N_2 separation and H_2 production. In the first study [11], Pt/C was used as electrodes (anode and cathode) and the mixed NH_4^+/H^+ Nafion 211 membrane was used as an electrolyte. The maximum rate of ammonia formation was found to 1.14×10^{-9} mol s^{-1} cm^{-2} was attained at ambient temperature and pressure with an applied voltage of 1.2 V. In the second study [258], the mixed $Li^+/H^+/NH_4^+$ Nafion 211 membrane was used as an electrolyte and Pt/C was used as electrodes. Ammonia was produced with a maximum rate of 9.37×10^{-10} mol s^{-1} cm^{-2} and Faradaic efficiency of 0.83 % at 80 °C and with an applied voltage of 1.2 V.

In Section 7.2, it was demonstrated that ammonia was synthesised from H_2O and N_2 at 375 °C with a maximum rate of 4.0×10^{-10} mol s^{-1} cm^{-2} and Faradaic efficiency of 3.87 % using LSCrF-CGDC composite as a catalyst (cathode). Building on the aforementioned information, this research investigates the possibility of synthesising ammonia from air and water in single chamber reactor using a symmetrical cell consisting of LSCrF-CGDC composite as electrodes (cathode and anode) and CGDC-carbonate composite as an electrolyte.

7.3.1 Experimental

A tri-layer symmetrical single cell was fabricated by a cost-effective one-step dry-pressing. The anode and cathode composites consist of a mixture of LSCrF, CGDC and starch (70:30:15 wt %). The composite electrolyte composite of CGDC-$(Li/Na/K)_2CO_3$ (70:30 wt %). The composite anode, composite electrolyte and composite cathode were fed into the 13 mm die, layer by layer, with the aid of a sieve to ensure uniform powder distribution, and then uniaxially pressed at pressure of 259 MPa. The green pellet was sintered in air at 700 °C for 2 h. The surface area of both electrode (cathode and the anode) was 1.21 cm^2. Silver paste was painted on each electrode surface of the cell as a current collector. Ag wires were used as output terminals for both electrodes.

The fabricated cell for ammonia synthesis was placed in a self-designed single-chamber reactor. The single chamber was fed with either 3% H_2O-Air or 3% H_2O-N_2. The water vapour (3% H_2O) was supplied to chamber by passing air or N_2 stream through a room temperature water. A constant voltage (1.2-1.7 V) was applied for a period of 1 h. The ammonia synthesised was absorbed by 20 ml of diluted HCl (0.01 M). The concentration of NH_4^+ in the absorbed solution was analysed using ion selective electrode (ISE) and the rate of ammonia formation was calculated using Equation 2.9 (Section 2.4.2).

7.3.2 Results and discussion

7.3.2.1 Synthesis of ammonia at different applied voltages

As discussed previously in Section 7.2.2.4, the optimum operating temperature was 375 °C for the electrolytic cell (two-chamber) based on LSCrF-CGDC composite cathode when ammonia was synthesised from H_2O and N_2. Therefore, this temperature was adopted in the synthesis of ammonia directly from water and air (3% H_2O-Air) using a single chamber-type reactor. For sake of comparison, ammonia was also synthesised from water and nitrogen in a single chamber reactor.

Figure 7.12 shows the generated current density as a function of time for electrolytic cell during ammonia synthesis from either H_2O and air or H_2O and N_2 at constant temperature (375 °C) and different applied voltages (1.2-1.7 V) over a period of 1 h. As can be seen, the electrolytic cell demonstrated almost a stable performance in both cases indicating a stable electrochemical process. In the case of wet air (Figure 7.12a), the generated current density decreased with an increase in the applied voltage from 1.2 to 1.7 V and reached a minimum value of 0.21 mA/cm^2 at 1.7 V, as shown in Table 7.3. When wet N_2 was fed into the single chamber (Figure 7.12b), the generated current densities increased with voltage applied. However, when the applied voltage was further increased above 1.3 V, the generated current decreased and reached a minimum value of 0.29 mA/cm^2 at 1.7 V, as shown in Table 7.3. This indicates the difficulty of transporting more oxygen-ions (O^{2-}) through the electrolyte to the anode surface at higher voltages (> 1.3 V). This may be due to the blocking effect of Li^+, Na^+, and K^+ ions. These ions will move under the electric field and accumulate at the cathode/electrolyte interface forming positively charged layer, thus partially block the transfer of the oxygen ions (O^{2-}) and resulting in low current densities [258, 259].

(a)

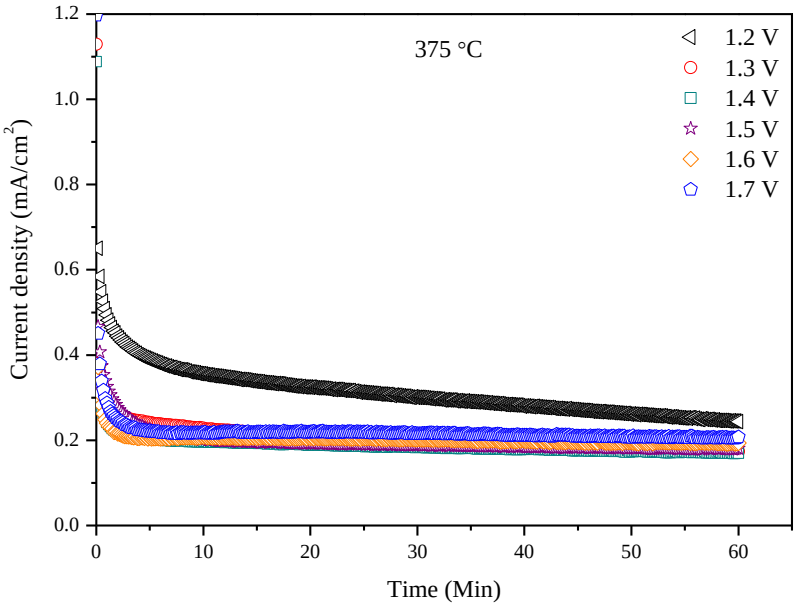

(b)

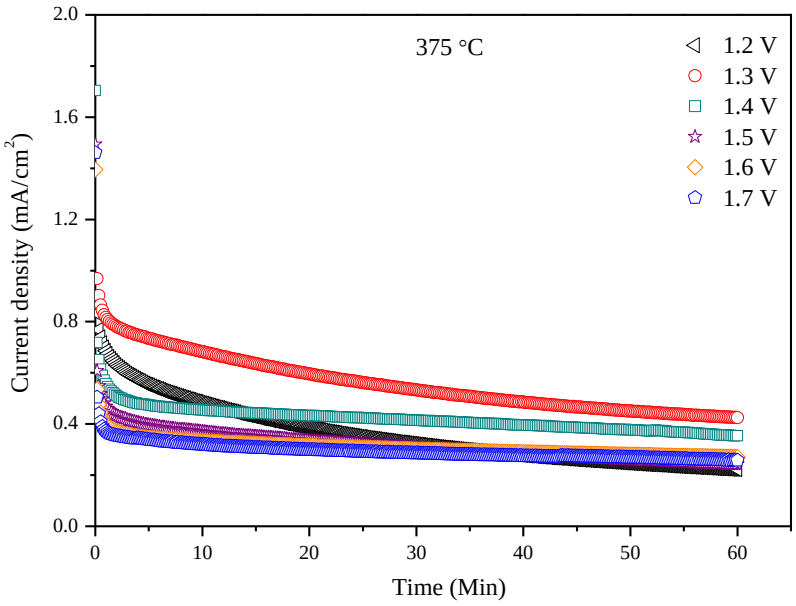

Figure 7.12 Electrolytic cell performance stability under different applied voltage at 375 °C. (a) 3% H_2O-Air; (b) 3% H_2O-N_2

Ammonia was successfully synthesised and the effect of the applied voltages (1.2-1.7 V) on the rate ammonia formation at 375 °C is shown in Figure 7.13. As can be seen, when wet air (3% H_2O-air) was supplied to the single chamber, the

ammonia formation rate decreased significantly as the applied voltage was increased from 1.2 to 1.7 V. In addition, a maximum rate of 1.94×10^{-11} mol s^{-1} cm^{-2} was attained at 1.2 V, at which the generated current density was 0.28 mA/cm^2 and the corresponding Faradaic efficiencyiy was about 2.01 % as shown in Table 7.3. In the case of using wet N_2 (3 % H_2O-N_2), there was significant increase in the rate of ammonia formation with an increase in the cell applied voltage, reaching a maximum value of 3.24×10^{-11} mol s^{-1} cm^{-2} at 1.4 V, at which the corresponding current density and Faradaic efficiency were 0.39 mA/cm^2 and 2.5 % respectively, as shown in Table 7.3. However, the rates of ammonia formation decreased significantly when the applied voltage was further increased to values higher than 1.4 V and reached the minimum values at 1.7 V. In both cases, the decrease in the ammonia formation rates at high applied voltage could be attributed to the competitive adsorption of H_2 and N_2 over the cathode surface [41, 70]. Although the rates of ammonia formation were rather lower that reported by Lan et al. [11] when ammonia synthesised from air and water over Pt catalyst (1.14×10^{-9} mol s^{-1} cm^{-2} at ~ 25 °C), these values are higher than those reported by Skodra et al. [10] (3.75×10^{-13} mol s^{-1} cm^{-2} at 650 °C), when water and nitrogen were used to produce ammonia in an electrolytic cell based on an oxide ion (O^{2-}) conducting electrolyte (YSZ) and Ru-based catalyst as cathode. This difference in ammonia formation rates could be due to the different operating temperatures which in turn play an important role in the ammonia decomposition and the ionic conductivity of the electrolyte as described previously.

It can be also seen from Figure 7.13 that, the ammonia production rates in the case of using wet N_2 was higher than those obtained from wet air. This could be due to the presence of excess amount of oxygen (i.e. oxygen from air and evolved oxygen) in the case of wet air compared to wet N_2, which in turn will play an important role in ammonia oxidation. In addition, the synthesised ammonia from wet N_2 using the single chamber was lower than obtained using the double chamber (4.0×10^{-10} mol s^{-1} cm^{-2}) at a similar operating condition (1.4 V and 375 °C). This could be attributed to the effect of ammonia oxidation, as the produced ammonia and evolved oxygen (O_2) are not separated in the single chamber.

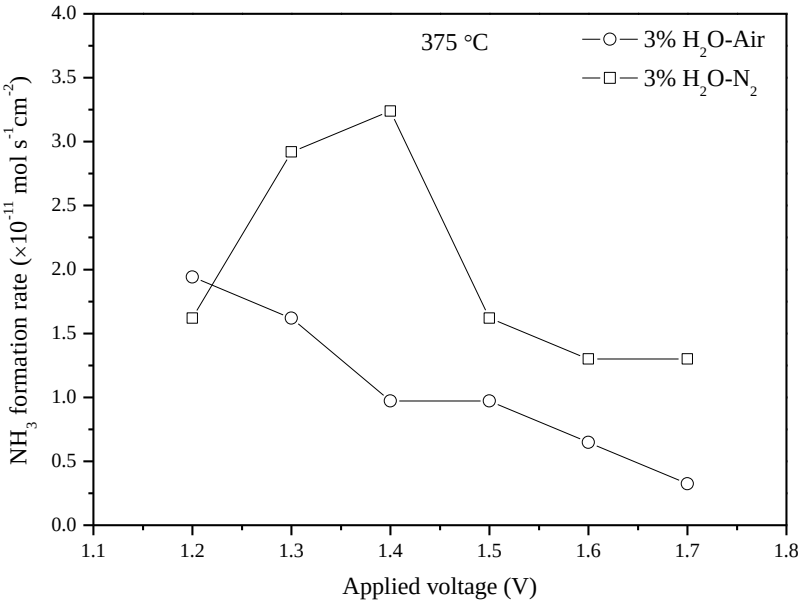

Figure 7.13 Dependence of the rate of ammonia formation on the applied voltage over LSCrF-CGDC composite cathode at 375 °C

Table 7.3 The corresponding current densities and Faradaic efficiencies of ammonia formation over LSCrF-CGDC at 1.2-17 V and 375 °C

Applied voltage (V)	3% H_2O-air		3% H_2O-N_2	
	Current density (mA/cm^2)	Faradaic efficiency (%)	Current density (mA/cm^2)	Faradaic efficiency (%)
1.2	0.28	2.01	0.27	1.74
1.3	0.20	2.34	0.44	1.92
1.4	0.18	1.56	0.39	2.5
1.5	0.19	1.55	0.31	1.51
1.6	0.20	0.94	0.30	1.25
1.7	0.21	0.46	0.29	1.3

7.3.2.2 Synthesis of ammonia at different temperatures

As mentioned in Section 7.3.2.1, the maximum rates of ammonia formation were obtained when 1.2 V and 1.4 V were applied at 375 °C in the case wet air and wet N_2 respectively. Therefore, the effect of the operating temperature on the rate of ammonia formation was studied at these values (1.2 and 1.4 V). Figure 7.14 shows

the performance stabilities of electrolytic cell during the ammonia synthesis from wet air (Figure 7.14a) and wet N_2 (Figure 7.14b) at different temperatures (375-425 °C), over a period of 1 h. As can be seen, the electrolytic cell demonstrated almost stable performance in both cases (wet air and wet N_2) at 375 °C. In addition, the generated current densities were 0.28 mA/cm^2 at 1.2 V in wet air and 0.39 mA/cm^2 at 1.4 V as shown in Table 7.4. However, when the electrolytic cell operating temperature was increased to 400 °C and 425 °C, the generated current density dropped significantly, during first 15 min, after which it started to stabilise as the experiment proceeded. It can be also seen from Figures 7.14a and b, there are significant increase in the current densities as the operating temperature are increase. These increases in the generated current densities with temperature could be attributed to the enhancement of the ionic conductivity of the electrolyte at high temperature. This indicates that that more oxygen ions (O^{2-}) were transported through the electrolyte to the anode surface.

(a)

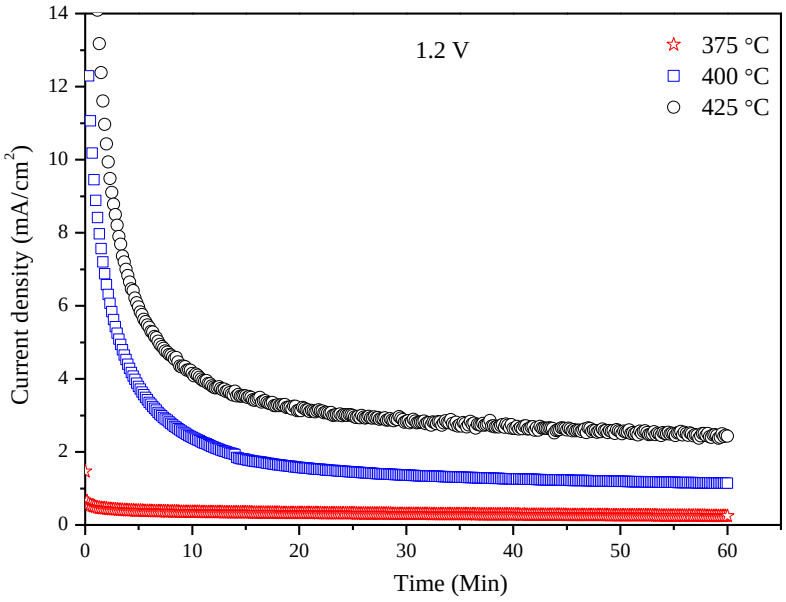

(b)

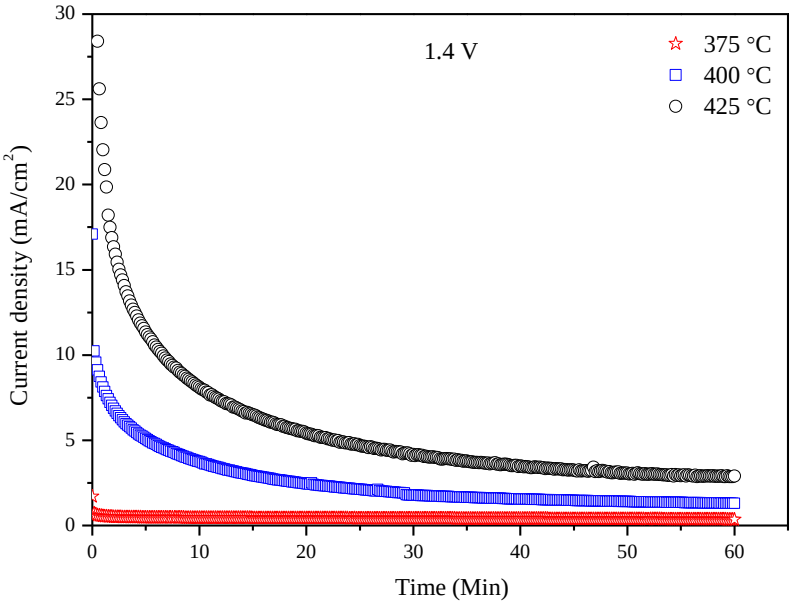

Figure 7.14 Electrolytic cell performance stability under different temperature (375-425 °C). (a) 3% H_2O-Air; (b) 3% H_2O-N_2

The effect of the operating temperature (375-425 °C) on the rates of ammonia formation was investigated under constant voltage, 1.2 V and 1.4 V when ammonia synthesised from wet air (3% H_2O-air) and wet N_2 (3% H_2O-N_2) as shown in Figure 7.15. As can be seen, the rates of ammonia formation in both cases decreased significantly as the operating temperature was decreased from 375 to 425 °C. In the case of wet air, the maximum rate of ammonia formation was found to be 1.94×10^{-11} mol s^{-1} cm^{-2} at 375 °C with an applied voltage of 1.2 V, at which the generated current density was 0.28 mA/cm^2 and the corresponding Faradaic efficiency was about 2.01 % as shown in Table 7.4. When ammonia was synthesised from wet N_2, the maximum rate of ammonia formation was found to be 3.24×10^{-11} mol s^{-1} cm^{-2} at 1.4 V, at which the corresponding current density and Faradaic efficiency were 0.39 mA/cm^2 and 2.5 % respectively, as shown Table 7.4. This decrease in the rates at high temperature might be due to ammonia decomposition or/and oxidation, although the electrolyte ionic conductivity increases with temperature [73, 75]. It can be also seen from Table 7.4 that, as the operating temperature increased from 375 to 425 °C, the Faradaic efficiencies decreased significantly and reached the minimum values of

0.07 % and 0.14 % at 425 °C in the case of wet air and wet N_2 respectively. These low Faradaic efficiencies indicates that there is more than one process occurring over the cathode surface and the hydrogen evolution is the dominant one [11, 70].

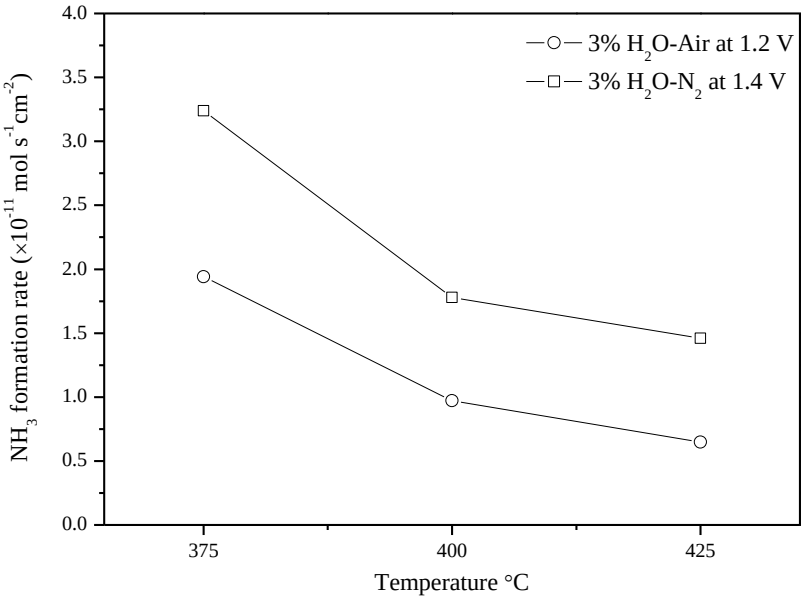

Figure 7.15 Dependence of the rate of ammonia formation on the operating temperature over LSCrF-CGDC composite cathode

Table 7.4 The corresponding current densities and Faradaic efficiencies of ammonia formation over LSCrF-CGDC at 375-425 °C

Temperature (°C)	**3% H_2O-air at 1.2 V**		**3% H_2O-N_2 at 1.4 V**	
	Current density (mA/cm^2)	**Faradaic efficiency (%)**	**Current density (mA/cm^2)**	**Faradaic efficiency (%)**
375	0.28	2.01	0.39	2.5
400	1.35	0.2	1.52	0.34
425	2.79	0.07	2.96	0.14

7.4 Conclusion

Two perovskite oxides, based on $La_{0.75}Sr_{0.25}Cr_{0.5}Mn_{0.5}O_{3-\delta}$ (LSCM) $La_{0.75}Sr_{0.25}Cr_{0.5}Fe_{0.5}O_{3-\delta}$ (LSCrF) were synthesised via a combined EDTA-citrate complexing sol-gel process. The properties of these materials, including phase composition, microstructure, and thermal behaviour were investigated. It was found that the oxides were thermally stable in N_2 atmosphere. In addition, both oxides were chemically compatible with $Ce_{0.8}Gd_{0.18}Ca_{0.02}O_{2-\delta}$ (CGDC) at the single cell sintering temperature 700 °C.

Tri-layer electrolytic cells were successfully fabricated by a cost-effective one-step dry-pressing and co-firing process. Ammonia was successfully synthesised directly from water and nitrogen (3% H_2O-N_2) in electrolytic cells (double chamber) based on LSCM-CGDC, LSCrF-CGDC as composite cathodes, CGCD-carbonate composite as an electrolyte and SSCo-CGDC composite as an anode. The maximum rates of ammonia formation were 2.5×10^{-10} mol s^{-1} cm^{-2} with a Faradaic efficiency of 0.52 % at 400 °C for LSCM-CGDC and 4.0×10^{-10} mol s^{-1} cm^{-2} with a Faradaic efficiency of 3.87 % for LSCrF-CGDC at 375 °C with an applied voltage of 1.4 V. These rates of ammonia formation using the LSCM- and LSCrF-CGDC composite cathodes were higher than those obtained for the spinel type catalysts (6.5×10^{-11} mol s^{-1} cm^{-2} for CFO-CGDC) (Chapter 5) and the perovskite type catalyst (1.5×10^{-10} mol s^{-1} cm^{-2} for LSFCo-CGDC) (Chapter 6) at similar experimental conditions.

Ammonia was also synthesised directly from air and water in a single chamber reactor using a symmetrical cell composed of LSCrF-CGDC as cathodes and CGDC-$(Li/Na/K)_2CO_3$ composite as electrolyte. The maximum rate of ammonia formation was found to be 1.94×10^{-11} mol s^{-1} cm^{-2} at 375 °C with an applied voltage of 1.2 V and the corresponding Faradaic efficiency was about 2.01 %. Ammonia was also synthesised from water and N_2 using the single chamber. The maximum rate of ammonia formation was found to be 3.24×10^{-11} mol s^{-1} cm^{-2} at 375 °C with an applied voltage of 1.4 V, at which the corresponding Faradaic efficiency was 2.5 %. This rate of ammonia formation is one order of magnitude lower than that obtained when ammonia was synthesised using the double chamber. This difference of ammonia formation could be attributed to the effect of ammonia oxidation as the

produced ammonia and the evolved oxygen are not separated in the single chamber. This indicates that the in order to reduce the ammonia oxidation effect, two chamber reactor is a better choice.

8 Conclusions and Future work

This research has investigated the electrochemical synthesis of ammonia under atmospheric pressure using different cathode and electrolyte materials. Three different types of catalysts were synthesised and characterised, including molybdenum-containing nitrides, spinel-type oxide and perovskite-type oxides. Oxide-carbonate composite electrolytes, namely $LiAlO_2$-$(Li/Na/K)_2CO_3$ and doped ceria-$(Li/Na/K)_2CO_3$ were prepared with the aim of reducing the cell operating temperature. This chapter highlights the key findings in this thesis and the suggested future work.

8.1 Conclusions

This section summarises the overall conclusions which have been drawn from each chapter:

Chapter 3 described the ammonia synthesis from H_2 and N_2 in two-chamber reactor using either nitride- (Fe_3Mo_3N and Co_3Mo_3N) or spinel- ($CoFe_2O_4$) based catalysts and oxide-carbonate composite electrolyte ($LiAlO_2$-$(Li/Na/K)_2CO_3$). As a first step, a new electrolyte consisting of $LiAlO_2$-$(Li/Na/K)_2CO_3$ (50:50 wt %) was prepared via a solid state reaction. The ionic conductivity of this composite electrolyte was measured in three different atmospheres (air, dry O_2 and wet 5% H_2-Ar) using AC impedance spectroscopy. The ionic conductivity was in the range of $0.22\text{-}10^{-5}$ S/cm in all atmospheres, within the measured temperature 600-300°C. In the second step, electrolyte supported cells were fabricated using Ag-Pd as the anode, $LiAlO_2$-$(Li/Na/K)_2CO_3$ as the electrolyte and one of the following catalysts Fe_3Mo_3N-Ag, Co_3Mo_3N-Ag, $CoFe_2O_4$-Ag as the cathode. In the case of the nitride-based cathode, the maximum rate of ammonia formation was found to be to be 1.88×10^{-10} mol s^{-1} cm^{-2} at 425 °C for Fe_3Mo_3N-Ag, 3.27×10^{-10} mol s^{-1} cm^{-2} at 450 °C for Co_3Mo_3N-Ag, with an applied voltage of 0.8 V. For the spinel based cathode ($CoFe_2O_4$-Ag), the maximum rate was found to be 2.32×10^{-10} mol s^{-1} cm^{-2} at 400 °C

with an applied voltage of 0.8 V. These results confirm the proton conduction in the $LiAlO_2$-carboante composite electrolyte.

Chapter 4 described the synthesis of ammonia from H_2 and N_2 in two-chamber reactor using a perovskite-based cathode and Sm-doped ceria-carbonate composite electrolyte. Firstly, a new perosvkite oxide with the form $La_{0.6}Sr_{0.4}Fe_{0.8}Cu_{0.2}O_{3-\delta}$ (LSFCu) was synthesised. The electrical conductivity of LSFCu was measured in air and the highest value was found to be ~ 19 S cm^{-1} at 470 °C. Secondly, a composite electrolyte consisting of SDC-$(Li/Na/K)_2CO_3$ (70:30 wt %) was prepared. The AC ionic conductivity of the composite electrolyte was found to be 0.35-4.91 × 10^{-6} in air, 0.37-4.61 × 10^{-5} in in dry O_2 and 0.24-4.14 × 10^{-4} S cm^{-1} in wet 5% H_2-Ar, within the measured temperature range of 600-300 °C. Finally, a tri-layer electrolytic cell was successfully fabricated by a cost-effective one-step dry-pressing and co-firing process. In this cell, NiO-SDC, SDC-$(Li/Na/K)_2CO_3$ and LSFCu-SDC composites were used as anode, electrolyte and cathode, respectively. Ammonia was synthesised in a two-chamber reactor when wet H_2 was supplied to the anode and dry N_2 was supplied to the cathode, with a maximum rate of 5.39×10^{-9} mol s^{-1} cm^{-2} at 450 °C and 0.8 V. This rate is one order of magnitude higher than those obtained using nitride and spinel based catalysts (Chapter 3). In addition, this formation rate (5.39×10^{-9} mol s^{-1} cm^{-2} at 450 °C) is also higher than that reported by Wang et al. [75] (4.1×10^{-9} mol s^{-1} cm^{-2} at 530 °C) using a proton conductor electrolyte ($BaCe_{0.85}Y_{0.15}O_{3-\delta}$, BCY) and perovskite-based cathode ($Ba_{0.5}Sr_{0.5}Co_{0.8}Fe_{0.2}O_{3-\delta}$, BSCF). Furthermore, the results also confirm the proton conduction in the SDC-carbonate composite electrolyte.

Chapter 5 described that ammonia was synthesised successfully from water and nitrogen in a two-chamber reactor using spinel type catalyst ($CoFe_2O_4$, CFO), an oxygen-ion conducting electrolyte (doped ceria-carbonate composite) and a perovskite-based anode $Sm_{0.5}Sr_{0.5}CoO_{3-\delta}$ (SSCo). Firstly, a new electrolyte was prepared by mixing $Ce_{0.8}Gd_{0.18}Ca_{0.02}O_{2-\delta}$ with the ternary carbonate ($(Li/Na/K)_2CO_3$, 70:30 wt %). The ionic conductivity of the composite electrolyte was measured by AC impedance under different atmospheres (Air, dry O_2 and wet 5% H_2-Ar). Additionally, the effect of sample sintering temperature on the ionic conductivities was also investigated at 600 and 700 ºC. The results showed that the sample sintered

at 700 ºC exhibited the highest values, which were found to be 0.49-3.731 × 10^{-6}, 0.50-3.34 × 10^{-5} and 0.52-1.21 × 10^{-3} S cm^{-1} in air, dry O_2 and wet 5% H_2-Ar, respectively. This could be due to the higher sintering temperature resulting in better contact at the interfacial region between the two phases, which, in turn, provides a superionic highway for ion conduction [296]. Furthermore, the ionic conductivities of CGDC-carbonate composite are higher than those of $LiAlO_2$-carbonate (Chapter 3) and SDC-carbonate (Chapter 4). Secondly, a tri-layer electrolytic cell for ammonia synthesis was fabricated by a cost effective one-step dry-pressing and co-firing process. The cell was based on CFO-CGDC composite as a cathode, CGDC-carbonate composite as an electrolyte and SSCo-CGDC composite as an anode. The maximum rate of ammonia formation was found to be up to 6.5 × 10^{-11} mol s^{-1} cm^{-2} at 400 ºC, with an applied voltage of 1.6 V.

Chapter 6 described the synthesis of ammonia from water and nitrogen in a two-chamber reactor using doped-$LaFeO_3$ based perosvkite oxide cathodes, namely $La_{0.6}Sr_{0.4}FeO_{3-\delta}$ (LSF), $La_{0.6}Sr_{0.4}Fe_{0.8}Co_{0.2}O_{3-\delta}$ (LSFCo) and $La_{0.6}Sr_{0.4}Fe_{0.8}Cu_{0.2}O_{3-\delta}$ (LSFCu). Tri-layer electrolytic cells composed of LSF-CGDC, LSFCu-CGDC and LSFCo-CGDC as composite cathodes, CGDC-carbonate composite as an electrolyte and SSCo-CGDC composite as an anode were fabricated. Ammonia was synthesised at the cathode chamber with maximum formation rates of 0.7 × 10^{-10} mol s^{-1} cm^{-2} for LSF-CGDC, 0.5 × 10^{-10} mol s^{-1} cm^{-2} for LSFCu-CGDC and 1.5 × 10^{-10} mol s^{-1} cm^{-2} for LSFCo-CGDC at 400 °C, with an applied voltage of 1.4 V. These figures indicate that the catalytic activity of LSFCo-CGDC is better than that of LSF-CGDC and LSFCu-CGDC. This could be due the polarisation resistance (Rp) of LSFCo-CGDC being lower than that of LSF-CGDC and LSFCu-CGDC composite cathodes. In addition, the formation rate using the LSFCo-CGDC composite cathode was one order of magnitude higher than that of the spinel type catalyst (CFO-CGDC), under similar experimental conditions (Chapter 5).

Chapter 7 described the synthesis of ammonia using perovskite catalysts based on doped-$LaCrO_3$) oxides, namely $La_{0.75}Sr_{0.25}Cr_{0.5}Mn_{0.5}O_{3-\delta}$ (LSCM) $La_{0.75}Sr_{0.25}Cr_{0.5}Fe_{0.5}O_{3-\delta}$ (LSCrF). In first step, ammonia was synthesised from water and nitrogen in a two-chamber reactor. In the reactor, the electrolytic cell was

composed from either LSCM-CGDC or LSCrF-CGDC as composite cathode, CGDC-carbonate as an electrolyte and SSCo-CGDC as anode. Ammonia was synthesised in the cathode chamber and its maximum formation rates were 2.5×10^{-10} mol s^{-1} cm^{-2}, with a Faradaic efficiency of 0.52 % at 400 °C for LSCM-CGDC and 4.0×10^{-10} mol s^{-1} cm^{-2} with a Faradaic efficiency of 3.87 % for LSCrF-CGDC at 375 °C, with an applied voltage of 1.4 V. These formation rates were higher than those obtained for the spinel type catalyst (CFO-CGDC) presented in Chapter 5 and the perovskite type catalyst (LSFCo-CGDC) presented in Chapter 6, under similar experimental conditions.

In the second part of Chapter 7, the possibility of the synthesis of ammonia synthesis directly from air and water was investigated in a single chamber reactor. In this case, a symmetrical cell composed of CGDC-carbonate composite was used as electrolyte and LSCrF-CGDC composite was used as cathode and anode. The maximum rate of ammonia production was found to be 1.94×10^{-11} mol s^{-1} cm^{-2} at 375 °C, with an applied voltage of 1.2 V, and the corresponding Faradaic efficiency was about 2.01 %. For the sake of comparison, ammonia was also synthesised from water and N_2 using the single chamber. A maximum rate of about 3.24×10^{-11} mol s^{-1} cm^{-2} was attained at 375 °C, with an applied voltage of 1.4 V, at which the corresponding Faradaic efficiency was 2.5 %. This rate is one order of magnitude lower than that obtained when ammonia was synthesised using the two chamber reactor. This could be attributed to the effect of ammonia oxidation, as the produced ammonia and the evolved oxygen are not separated in the single chamber. This indicates that the in order to reduce the ammonia oxidation effect, a two chamber reactor is a better choice.

In general, despite the low rates of ammonia formation, the obtained rates either using water and nitrogen or water and air are two or three orders of magnitude higher than those previously reported by Skodra et al. [10], when ammonia was synthesised from H_2O and N_2 at 650 °C, over a Ru-based catalyst.

8.2 Future work

The results indicated that perosvkite-based oxides exhibit the best catalytic activity from ammonia synthesis, under all experimental conductions. However, the rate of ammonia formation and the Faradic efficiency are low, which still need to be improved. Thus, minimising the hydrogen evolution at the cathode is of crucial importance to ensure high Faradaic efficiencies. To achieve this goal, good electrocatalysts with high catalytic activity for ammonia synthesis need to be used. This could be achieved by using electrocatalyst materials which favoring the nitrogen reduction reaction over hydrogen evolution. Recently, Skulason et al. [331] published a theoretical evaluation of possible transition metal electrocatalysts for N_2 reduction. In this study it was found out that the early transition metals such as Sc, Ti, Y and Zr bind N-adatoms more strongly than H-adatoms. Therefore, a significant ammonia production rate would be expected on those metals compared to hydrogen gas.

In addition, although the oxide-carbonate composite electrolytes enabled us to work at slightly lower operating temperatures (375-475 ºC), further reduction in the temperature (< 375 ºC) is preferred to minimise the effect of ammonia decomposition. Therefore, new electrolyte materials that exhibit high ionic conductivity below 375 ºC need to be investigated. Also the synthesis of ammonia directly from air and water needs to be investigated in a two-chamber reactor, aiming to minimise the effect of ammonia oxidation.

In addition, by using two-electrode configuration, the overall processes occurring at both anode and cathode are observed in the AC impedance spectra. Thus, three-electrode set-up would be helpful to investigate the processes occurring at the cathode side. Furthermore, by changing the cathode atmosphere and fixing the anode condition, it might be possible to differentiate between the cathode and anode polarisation by the AC impedance measurement.

References

[1] V. Smil, Nature, 400 (1999) 415-415.
[2] H.C.J. Godfray, J.R. Beddington, I.R. Crute, L. Haddad, D. Lawrence, J.F. Muir, J. Pretty, S. Robinson, S.M. Thomas, C. Toulmin, Science, 327 (2010) 812-818.
[3] D. Tilman, C. Balzer, J. Hill, B.L. Befort, Proceedings of the National Academy of Sciences, 108 (2011) 20260-20264.
[4] V. Smil, Ambio: A Journal of the Human Environment, 31 (2002) 126-131.
[5] M. Appl, Ammonia: Principles and Industrial Practice, Wiley-VCH Weinheim, Germany, 1999.
[6] I. Rafiqul, C. Weber, B. Lehmann, A. Voss, Energy, 30 (2005) 2487-2504.
[7] R. Michalsky, P.H. Pfromm, Solar Energy, 85 (2011) 2642-2654.
[8] G. Marnellos, M. Stoukides, Science, 282 (1998) 98-100.
[9] T. Murakami, T. Nohira, T. Goto, Y.H. Ogata, Y. Ito, Electrochimica Acta, 50 (2005) 5423-5426.
[10] A. Skodra, M. Stoukides, Solid State Ionics, 180 (2009) 1332-1336.
[11] R. Lan, J.T. Irvine, S.W. Tao, Scientific Reports, 3 (2013) 1145.
[12] I.A. Amar, R. Lan, C.T. Petit, S.W. Tao, Journal of Solid State Electrochemistry, 15 (2011) 1845-1860.
[13] S. Giddey, S.P.S. Badwal, A. Kulkarni, International Journal of Hydrogen Energy, 38 (2013) 14576-14594.
[14] H. Liu, Ammonia Synthesis Catalysts: Innovation and Practice, World Scientific Publishing Company, 2013.
[15] A. Slack, G. James, Ammonia. Fertilizer Science and Technology Series, Vol. 2, in, New York: Marcel Dekker, Inc, 1973.
[16] M. Appl, The Haber-Bosch heritage: The ammonia production technology, in: 50th Anniversary of the IFA Technical Conference, 1997.
[17] J.W. Erisman, M.A. Sutton, J. Galloway, Z. Klimont, W. Winiwarter, Nature Geoscience, 1 (2008) 636-639.
[18] J. Douglas, Synthesis of Ammonia, The Macmillan Press Ltd, 1971.
[19] J.M. Modak, Resonance, 7 (2002) 69-77.
[20] US, G. Survey, Mineral Commodity Summaries, Geological Survey, 2012.
[21] G.R. Maxwell, Nitrogen Products: Production and Consumption, in: Synthetic Nitrogen Products, Springer US, 2005, pp. 15-42.
[22] C. Zamfirescu, I. Dincer, Journal of Power Sources, 185 (2008) 459-465.
[23] G.C. Miller, Journal of Chemical Education, 58 (1981) 424.
[24] H.J. Bomelburg, Plant/Operations Progress, 1 (1982) 175-180.
[25] L. Green Jr, International Journal of Hydrogen Energy, 7 (1982) 355-359.
[26] R. Lan, J.T. Irvine, S.W. Tao, International Journal of Hydrogen Energy, 37 (2012) 1482-1494.
[27] A. Klerke, C.H. Christensen, J.K. Nørskov, T. Vegge, Journal of Materials Chemistry, 18 (2008) 2304-2310.
[28] R. Lan, S.W. Tao, Electrochemical and Solid-State Letters, 13 (2010) B83-B86.
[29] C. Zamfirescu, I. Dincer, Fuel Processing Technology, 90 (2009) 729-737.
[30] V. Alagharu, S. Palanki, K.N. West, Journal of Power Sources, 195 (2010) 829-833.
[31] L. Zhang, W. Yang, Journal of Power Sources, 179 (2008) 92-95.

[32] C.H. Christensen, T. Johannessen, R.Z. Sørensen, J.K. Nørskov, Catalysis Today, 111 (2006) 140-144.
[33] K. Scott, Electrochemical Processes for Clean Technology, Springer Verlag, 1995.
[34] A.D. Carbó, Microporous Materials in Electrosynthesis and Environmental Remediation, in: Electrochemistry of Porous Materials, CRC Press, 2009, pp. 265-274.
[35] A.H. Sulaymon, A.H. Abbar, Scale-Up of Electrochemical Reactors, InTech, 2012.
[36] A.J. Bard, M. Stratmann, D. McDonald, P. Schmuki, Encyclopedia of Electrochemistry, Volume 5, Electrochemical Engineering, in, Wiley-VCH Verlag GmbH&Co. KGaA, Weinheim, 2007.
[37] K. Scott, Developments in Chemical Engineering and Mineral Processing, 1 (1993) 71-117.
[38] E.E. Van Tamelen, B. Akermark, Journal of the American Chemical Society, 90 (1968) 4492-4493.
[39] A.V. Gorodyskii, V.V. Danilin, O.N. Efimov, N.E. Nechaeva, V.N. Tsarev, Reaction Kinetics and Catalysis Letters, 11 (1979) 337-342.
[40] A. Tsuneto, A. Kudo, T. Sakata, Chemistry Letters, 22 (1993) 851-854.
[41] A. Sclafani, V. Augugliaro, M. Schiavello, Journal of The Electrochemical Society, 130 (1983) 734-736.
[42] F. Köleli, D.B. Kayan, Journal of Electroanalytical Chemistry, 638 (2010) 119-122.
[43] T. Murakami, T. Nishikiori, T. Nohira, Y. Ito, Journal of the American Chemical Society, 125 (2003) 334-335.
[44] T. Murakami, T. Nishikiori, T. Nohira, Y. Ito, Journal of The Electrochemical Society, 152 (2005) D75-D78.
[45] N. Serizawa, H. Miyashiro, K. Takei, T. Ikezumi, T. Nishikiori, Y. Ito, Journal of The Electrochemical Society, 159 (2012) E87-E91.
[46] S. Klinsrisuk, Novel Electrocatalytic Membrane for Ammonia Synthesis, in: School of Chemistry, University of St. Andrews, 2010.
[47] A.R. West, Journal of Materials Chemistry, 1 (1991) 157-162.
[48] M. Stoukides, Industrial & Engineering Chemistry Research, 27 (1988) 1745-1750.
[49] C. Wagner, Advances in Catalysis, 21 (1970) 323.
[50] N. Baskaran, G. Govindaraj, A. Narayanasamy, Journal of Power Sources, 55 (1995) 153-157.
[51] H. Iwahara, H. Uchida, K. Morimoto, Journal of The Electrochemical Society, 137 (1990) 462-465.
[52] S. Zhuiykov, International Journal of Hydrogen Energy, 21 (1996) 749-759.
[53] H. Matsumoto, T. Shimura, H. Iwahara, T. Higuchi, K. Yashiro, A. Kaimai, T. Kawada, J. Mizusaki, Journal of Alloys and Compounds, 408 (2006) 456-462.
[54] I. Garagounis, V. Kyriakou, C. Anagnostou, V. Bourganis, I. Papachristou, M. Stoukides, Industrial & Engineering Chemistry Research, 50 (2010) 431-472.
[55] R.L. Cook, A.F. Sammells, Catalysis letters, 1 (1988) 345-349.
[56] G. Marnellos, C. Athanasiou, P. Tsiakaras, M. Stoukides, Ionics, 2 (1996) 412-420.

[57] E. Panagos, I. Voudouris, M. Stoukides, Chemical Engineering Science, 51 (1996) 3175-3180.
[58] C.G. Zoski, Handbook of Electrochemistry, Elsevier Science, 2007.
[59] A.J. Bard, L.R. Faulkner, Electrochemical methods: Fundamentals and Applications, Wiley New York, 2001.
[60] L. Malavasi, C.A.J. Fisher, M.S. Islam, Chemical Society Reviews, 39 (2010) 4370-4387.
[61] O. Tillement, Solid State Ionics, 68 (1994) 9-33.
[62] A.J. Jacobson, Chemistry of Materials, 22 (2009) 660-674.
[63] M. Ni, M.K. Leung, D.Y. Leung, International Journal of Hydrogen Energy, 33 (2008) 2337-2354.
[64] Z.J. Li, R.Q. Liu, Y.H. Xie, S. Feng, J.D. Wang, Solid State Ionics, 176 (2005) 1063-1066.
[65] M. Ouzounidou, A. Skodra, C. Kokkofitis, M. Stoukides, Solid State Ionics, 178 (2007) 153-159.
[66] G.C. Xu, R.Q. Liu, J. Wang, Science in China Series B: Chemistry, 52 (2009) 1171-1175.
[67] Z. Zhang, Z. Zhong, R. Liu, Journal of Rare Earths, 28 (2010) 556-559.
[68] G. Xu, R. Liu, Chinese Journal of Chemistry, 27 (2009) 677-680.
[69] P.I. Cowin, C.T. Petit, R. Lan, J.T. Irvine, S.W. Tao, Advanced Energy Materials, 1 (2011) 314-332.
[70] V. Kordali, G. Kyriacou, C. Lambrou, Chemical Communications, (2000) 1673-1674.
[71] G. Marnellos, S. Zisekas, M. Stoukides, Journal of Catalysis, 193 (2000) 80-87.
[72] Z.J. Li, R.Q. Liu, J.D. Wang, Y.H. Xie, F. Yue, Journal of Solid State Electrochemistry, 9 (2005) 201-204.
[73] C. Chen, G. Ma, Journal of Alloys and Compounds, 485 (2009) 69-72.
[74] B. Liu, Y. Zhang, Journal of University of Science and Technology Beijing, Mineral, Metallurgy, Material, 15 (2008) 84-90.
[75] W. Wang, X. Cao, W. Gao, F. Zhang, H. Wang, G. Ma, Journal of Membrane Science, 360 (2010) 397-403.
[76] R.Q. Liu, Y.H. Xie, J.D. Wang, Z.J. Li, B.H. Wang, Solid State Ionics, 177 (2006) 73-76.
[77] J.D. Wang, Y.H. Xie, Z.F. Zhang, R.Q. Liu, Z.J. Li, Materials Research Bulletin, 40 (2005) 1294-1302.
[78] B. Wang, R. Liu, J. Wang, Z. Li, Y. Xie, Chinese Journal of Inorganic Chemistry 21 (2005) 1551-1555.
[79] T. Norby, Solid State Ionics, 125 (1999) 1-11.
[80] S. Stotz, C. Wagner, Berichte der Bunsengesellschaft für Physikalische Chemie, 70 (1966) 781-788.
[81] H. Iwahara, T. Esaka, H. Uchida, N. Maeda, Solid State Ionics, 3 (1981) 359-363.
[82] R.C.T. Slade, N. Singh, Solid State Ionics, 61 (1993) 111-114.
[83] H. Iwahara, Solid State Ionics, 52 (1992) 99-104.
[84] G. Chiodelli, L. Malavasi, C. Tealdi, S. Barison, M. Battagliarin, L. Doubova, M. Fabrizio, C. Mortalò, R. Gerbasi, Journal of Alloys and Compounds, 470 (2009) 477-485.

[85] E. Gorbova, V. Maragou, D. Medvedev, A. Demin, P. Tsiakaras, Journal of Power Sources, 181 (2008) 207-213.
[86] K.D. Kreuer, Chemistry of Materials, 8 (1996) 610-641.
[87] K. Kreuer, Annual Review of Materials Research, 33 (2003) 333-359.
[88] H. Iwahara, T. Yajima, T. Hibino, H. Ushida, Journal of The Electrochemical Society, 140 (1993) 1687-1691.
[89] N. Bonanos, K. Knight, B. Ellis, Solid State Ionics, 79 (1995) 161-170.
[90] H. Matsumoto, S. Hamajima, H. Iwahara, Solid State Ionics, 145 (2001) 25-29.
[91] H. Matsumoto, S. Hamajima, T. Yajima, H. Iwahara, Journal of The Electrochemical Society, 148 (2001) D121-D124.
[92] N. Maffei, A. Kuriakose, Sensors and Actuators B: Chemical, 56 (1999) 243-246.
[93] H. Matsumoto, S. Okada, S. Hashimoto, K. Sasaki, R. Yamamoto, M. Enoki, T. Ishihara, Ionics, 13 (2007) 93-99.
[94] H. Iwahara, H. Uchida, N. Maeda, Journal of Power Sources, 7 (1982) 293-301.
[95] H. Iwahara, H. Uchida, I. Yamasaki, International Journal of Hydrogen Energy, 12 (1987) 73-77.
[96] F. Zhang, Q. Yang, B. Pan, R. Xu, H. Wang, G. Ma, Materials Letters, 61 (2007) 4144-4148.
[97] C. Yiokari, G. Pitselis, D. Polydoros, A. Katsaounis, C. Vayenas, The Journal of Physical Chemistry A, 104 (2000) 10600-10602.
[98] A. Skodra, M. Ouzounidou, M. Stoukides, Solid State Ionics, 177 (2006) 2217-2220.
[99] L. Pelletier, A. McFarlan, N. Maffei, Journal of Power Sources, 145 (2005) 262-265.
[100] K. Kreuer, Solid State Ionics, 97 (1997) 1-15.
[101] Y.H. Xie, J.D. Wang, R.Q. Liu, X.T. Su, Z.P. Sun, Z.J. Li, Solid State Ionics, 168 (2004) 117-121.
[102] X. Su, R. Liu, J. Wang, Acta Chimica Sinica, 61 (2003) 505-509.
[103] T. Hibino, K. Mizutani, T. Yajima, H. Iwahara, Solid State Ionics, 57 (1992) 303-306.
[104] Y. Guo, B. Liu, Q. Yang, C. Chen, W. Wang, G. Ma, Electrochemistry Communications, 11 (2009) 153-156.
[105] C. Cheng, W. Wenbao, M. Guilin, Acta Chimica Sinica, 67 (2009) 623-628.
[106] Y. Du, A.S. Nowick, Solid State Ionics, 91 (1996) 85-91.
[107] M. Mogensen, N.M. Sammes, G.A. Tompsett, Solid State Ionics, 129 (2000) 63-94.
[108] W.B. Wang, J.W. Liu, Y.D. Li, H.T. Wang, F. Zhang, G.L. Ma, Solid State Ionics, 181 (2010) 667-671.
[109] J. Yin, X. Wang, J. Xu, H. Wang, F. Zhang, G. Ma, Solid State Ionics, 185 (2011) 6-10.
[110] X. Wang, J. Yin, J. Xu, H. Wang, G. Ma, Chinese Journal of Chemistry, 29 (2011) 1114-1118.
[111] M. Zhang, J. Xu, G. Ma, Journal of Materials Science, 46 (2011) 4690-4694.
[112] J. Phair, S.P.S. Badwal, Ionics, 12 (2006) 103-115.
[113] R. Liu, Y. Xie, Z. Li, J. Wang, Y. Snn, Acta Physico Chimica Sinica, 21 (2005) 967.

[114] C.H. Lee, H.B. Park, Y.M. Lee, R.D. Lee, Industrial & Engineering Chemistry Research, 44 (2005) 7617-7626.
[115] Z.J. Li, R.Q. Liu, J.D. Wang, Z. Xu, Y.H. Xie, B.H. Wang, Science and Technology of Advanced Materials, 8 (2007) 566-570.
[116] C. Chen, G. Ma, Journal of Materials Science, 43 (2008) 5109-5114.
[117] J. Liu, Y. Li, W. Wang, H. Wang, F. Zhang, G. Ma, Journal of Materials Science, 45 (2010) 5860-5864.
[118] B.H. Wang, J.D. Wang, R.Q. Liu, Y.H. Xie, Z.J. Li, Journal of Solid State Electrochemistry, 11 (2007) 27-31.
[119] J. Wang, R. Liu, Acta Chim. Sinica, 66 (2008) 717-721.
[120] R. Liu, G. Xu, Chinese Journal of Chemistry, 28 (2010) 139-142.
[121] S.J. Skinner, J.A. Kilner, Materials Today, 6 (2003) 30-37.
[122] H. Iwahara, T. Mori, T. Hibino, Solid State Ionics, 79 (1995) 177-182.
[123] G. Marnellos, G. Karagiannakis, S. Zisekas, M. Stoukides, Studies in Surface Science and Catalysis, 130 (2000) 413-418.
[124] M. Tanaka, T. Ohshima, Fusion Engineering and Design, 85 (2010) 1038-1043.
[125] H. Iwahara, T. Yajima, T. Hibino, K. Ozaki, H. Suzuki, Solid State Ionics, 61 (1993) 65-69.
[126] S.V. Bhide, A.V. Virkar, Journal of The Electrochemical Society, 146 (1999) 2038-2044.
[127] S.V. Bhide, A.V. Virkar, Journal of The Electrochemical Society, 146 (1999) 4386-4392.
[128] K.H. Ryu, S.M. Haile, Solid State Ionics, 125 (1999) 355-367.
[129] K. Katahira, Y. Kohchi, T. Shimura, H. Iwahara, Solid State Ionics, 138 (2000) 91-98.
[130] J. Le, L.N. van Rij, R.C. van Landschoot, J. Schoonman, Journal of the European Ceramic Society, 19 (1999) 2589-2591.
[131] M. Zhou, A. Ahmad, Sensors and Actuators B: Chemical, 129 (2008) 285-291.
[132] M. Dudek, Materials research bulletin, 44 (2009) 1879-1888.
[133] T. Ishihara, H. Matsuda, Y. Takita, Journal of the American Chemical Society, 116 (1994) 3801-3803.
[134] E. Djurado, M. Labeau, Journal of the European Ceramic Society, 18 (1998) 1397-1404.
[135] K. Yamaji, T. Horita, M. Ishikawa, N. Sakai, H. Yokokawa, Solid State Ionics, 121 (1999) 217-224.
[136] G. Ma, F. Zhang, J. Zhu, G. Meng, Chemistry of Materials, 18 (2006) 6006-6011.
[137] F. Krug, T. Schober, Solid State Ionics, 92 (1996) 297-302.
[138] H.G. Bohn, T. Schober, T. Mono, W. Schilling, Solid State Ionics, 117 (1999) 219-228.
[139] T. Schober, H.G. Bohn, T. Mono, W. Schilling, Solid State Ionics, 118 (1999) 173-178.
[140] S. Tao, J.T.S. Irvine, Solid State Ionics, 154–155 (2002) 659-667.
[141] T. Shimura, S. Fujimoto, H. Iwahara, Solid State Ionics, 143 (2001) 117-123.
[142] P. Wilde, C. Catlow, Solid State Ionics, 112 (1998) 173-183.

[143] B.J. Wuensch, K.W. Eberman, C. Heremans, E.M. Ku, P. Onnerud, E.M.E. Yeo, S.M. Haile, J.K. Stalick, J.D. Jorgensen, Solid State Ionics, 129 (2000) 111-133.
[144] J. Isasi, M. Lopez, M. Veiga, C. Pico, Solid State Ionics, 89 (1996) 321-326.
[145] T. Shimura, M. Komori, H. Iwahara, Solid State Ionics, 86 (1996) 685-689.
[146] H. Inaba, H. Tagawa, Solid State Ionics, 83 (1996) 1-16.
[147] T. Matsui, T. Kosaka, M. Inaba, A. Mineshige, Z. Ogumi, Solid State Ionics, 176 (2005) 663-668.
[148] R. Fuentes, R. Baker, International Journal of Hydrogen Energy, 33 (2008) 3480-3484.
[149] Y. Nigara, J. Mizusaki, K. Kawamura, T. Kawada, M. Ishigame, Solid State Ionics, 113 (1998) 347-354.
[150] N. Sakai, K. Yamaji, T. Horita, H. Yokokawa, Y. Hirata, S. Sameshima, Y. Nigara, J. Mizusaki, Solid State Ionics, 125 (1999) 325-331.
[151] Y. Nigara, K. Yashiro, T. Kawada, J. Mizusaki, Solid State Ionics, 145 (2001) 365-370.
[152] A. Atkinson, Solid State Ionics, 95 (1997) 249-258.
[153] T. Schober, Electrochemical and Solid-State Letters, 8 (2005) A199-A200.
[154] B. Zhu, X. Liu, P. Zhou, Z. Zhu, W. Zhu, S. Zhou, Journal of Materials Science Letters, 20 (2001) 591-594.
[155] B. Zhu, Journal of Power Sources, 114 (2003) 1-9.
[156] J. Di, M. Chen, C. Wang, J. Zheng, L. Fan, B. Zhu, Journal of Power Sources, 195 (2010) 4695-4699.
[157] B. Zhu, X. Yang, J. Xu, Z. Zhu, S. Ji, M. Sun, J. Sun, Journal of Power Sources, 118 (2003) 47-53.
[158] G. Meng, Q. Fu, S. Zha, C. Xia, X. Liu, D. Peng, Solid State Ionics, 148 (2002) 533-537.
[159] B. Zhu, Journal of Power Sources, 93 (2001) 82-86.
[160] C. Xia, Y. Li, Y. Tian, Q. Liu, Z. Wang, L. Jia, Y. Zhao, Journal of Power Sources, 195 (2010) 3149-3154.
[161] K. Wang, R. Ran, Z. Shao, Journal of Power Sources, 170 (2007) 251-258.
[162] S. McIntosh, R.J. Gorte, Chemical Reviews-Columbus, 104 (2004) 4845-4866.
[163] Y. Takagi, B.K. Lai, K. Kerman, S. Ramanathan, Energy & Environmental Science, 4 (2011) 3473-3478.
[164] B. Zhu, X. Liu, P. Zhou, X. Yang, Z. Zhu, W. Zhu, Electrochemistry Communications, 3 (2001) 566-571.
[165] J. Huang, Z. Mao, Z. Liu, C. Wang, Electrochemistry Communications, 9 (2007) 2601-2605.
[166] X. Wang, Y. Ma, R. Raza, M. Muhammed, B. Zhu, Electrochemistry Communications, 10 (2008) 1617-1620.
[167] L. Zhang, R. Lan, X. Xu, S.W. Tao, Y. Jiang, A. Kraft, Journal of Power Sources, 194 (2009) 967-971.
[168] R. Raza, X. Wang, Y. Ma, B. Zhu, Journal of Power Sources, 195 (2010) 6491-6495.
[169] X. Wang, Y. Ma, S. Li, A.-H. Kashyout, B. Zhu, M. Muhammed, Journal of Power Sources, 196 (2011) 2754-2758.
[170] A. Bodén, J. Di, C. Lagergren, G. Lindbergh, C.Y. Wang, Journal of Power Sources, 172 (2007) 520-529.

[171] M. Benamira, A. Ringuedé, V. Albin, R.N. Vannier, L. Hildebrandt, C. Lagergren, M. Cassir, Journal of Power Sources, 196 (2011) 5546-5554.
[172] C. Xia, Y. Li, Y. Tian, Q. Liu, Y. Zhao, L. Jia, Y. Li, Journal of Power Sources, 188 (2009) 156-162.
[173] Y.P. Fu, S.H. Chen, J.J. Huang, International Journal of Hydrogen Energy, 35 (2010) 745-752.
[174] B. Zhu, International Journal of Energy Research, 30 (2006) 895-903.
[175] B. Zhu, M.D. Mat, International Journal of Electrochemical Science, 1 (2006) 383-402.
[176] B. Zhu, S. Li, B.E. Mellander, Electrochemistry Communications, 10 (2008) 302-305.
[177] S. Li, X. Wang, B. Zhu, Electrochemistry Communications, 9 (2007) 2863-2866.
[178] Y. Zhao, C. Xia, Y. Wang, Z. Xu, Y. Li, International Journal of Hydrogen Energy, 37 (2012) 8556-8561.
[179] M.A. Khan, R. Raza, R.B. Lima, M.A. Chaudhry, E. Ahmed, G. Abbas, International Journal of Hydrogen Energy, 38 (2013) 16524-16531.
[180] B. Zhu, I. Albinsson, C. Andersson, K. Borsand, M. Nilsson, B.E. Mellander, Electrochemistry Communications, 8 (2006) 495-498.
[181] Q. Liu, Y. Tian, C. Xia, L.T. Thompson, B. Liang, Y. Li, Journal of Power Sources, 185 (2008) 1022-1029.
[182] H. Li, Q. Liu, Y. Li, Electrochimica Acta, 55 (2010) 1958-1965.
[183] Y. Li, Z. Rui, C. Xia, M. Anderson, Y.S. Lin, Catalysis Today, 148 (2009) 303-309.
[184] J.L. Wade, C. Lee, A.C. West, K.S. Lackner, Journal of Membrane Science, 369 (2011) 20-29.
[185] L. Zhang, N. Xu, X. Li, S. Wang, K. Huang, W. Harris, W.K.S. Chiu, Energy & Environmental Science, 5 (2012) 8310-8317
[186] I.A. Amar, C.T.G. Petit, L. Zhang, R. Lan, P.J. Skabara, S.W. Tao, Solid State Ionics, 201 (2011) 94-100.
[187] B. Zhu, L. Fan, P. Lund, Applied Energy, 106 (2013) 163-175.
[188] L. Fan, C. Wang, M. Chen, B. Zhu, Journal of Power Sources, 234 (2013) 154-174.
[189] J.B. Goodenough, Annual Review of Materials Research, 33 (2003) 91-128.
[190] C. Ding, H. Lin, K. Sato, T. Hashida, Surface and Coatings Technology, 205 (2011) 2813-2817.
[191] J. Will, A. Mitterdorfer, C. Kleinlogel, D. Perednis, L. Gauckler, Solid State Ionics, 131 (2000) 79-96.
[192] L.E. Smart, E.A. Moore, Solid State Chemistry, CRC, 2012.
[193] Z. Shao, W. Zhou, Z. Zhu, Progress in Materials Science, 57 (2012) 804-874.
[194] J. Sunarso, S. Baumann, J. Serra, W. Meulenberg, S. Liu, Y. Lin, J. Diniz da Costa, Journal of Membrane Science, 320 (2008) 13-41.
[195] A.R. West, Solid State Chemistry and its Applications, John Wiley & Sons Ltd, 1985.
[196] K.S. Alber, J.A. Cox, Microchimica Acta, 127 (1997) 131-147.
[197] S. Liu, X. Tan, K. Li, R. Hughes, Ceramics International, 28 (2002) 327-335.
[198] K.C. Patil, S.T. Aruna, S. Ekambaram, Current Opinion in Solid State and Materials Science, 2 (1997) 158-165.

[199] K.C. Patil, S. Aruna, T. Mimani, Current Opinion in Solid State and Materials Science, 6 (2002) 507-512.
[200] A. Mukasyan, P. Dinka, International Journal of Self-Propagating High-Temperature Synthesis, 16 (2007) 23-35.
[201] S.T. Aruna, A.S. Mukasyan, Current Opinion in Solid State and Materials Science, 12 (2008) 44-50.
[202] L.A. Chick, L.R. Pederson, G.D. Maupin, J.L. Bates, L.E. Thomas, G.J. Exarhos, Materials letters, 10 (1990) 6-12.
[203] R. Purohit, B. Sharma, K. Pillai, A. Tyagi, Materials Research Bulletin, 36 (2001) 2711-2721.
[204] W.E. Lee, W.M. Rainforth, Ceramic Microstructures: Property Control by Processing, Springer, 1994.
[205] D. Richerson, Modern Ceramic Engineering: Properties, Processing, and use in Design, Marcel Dekker, New York, 1992.
[206] J.S. Reed, Principles of ceramics processing, John Wiley & Sons, Inc., 1995.
[207] R.A. Terpstra, P. Pex, A.H. de Vries, Ceramic processing, Chapman & Hall, 1995.
[208] R. Oberacker, Ceramics Science and Technology, Synthesis and Processing, 3 (2012) 3-37.
[209] W.D. Callister, Materials Science and Engineering: An Introduction, John Wiley & Sons, Inc, 1991.
[210] I.J. McColm, N. Clark, Forming, Shaping, and Working of High-Performance Ceramics, Blackie and Son Ltd.,, 1988.
[211] M. Barsoum, Fundamentals of Ceramics, IOP Publishing Ltd, 2003.
[212] Q. Yin, B. Zhu, H. Zeng, Microstructure, Property and Processing of Functional Ceramics, Springer, 2009.
[213] A. Clearfield, J.H. Reibenspies, N. Bhuvanesh, Principles and Applications of Powder Diffraction, John Wiley and Sons, 2008.
[214] P.J. Haines, Principles of Thermal Analysis and Calorimetry, Royal Society of Chemistry, 2002.
[215] S.B. Warrington, G.W. Höhne, Ullmann's Encyclopedia of Industrial Chemistry, (2012).
[216] A. Schindler, J. Blumm, K. Hodor, The new STA 449 *Jupiter*® Platform: Highest Flexibility and Performance in Simultaneous Thermal Analysis, in, Chemine Technologija, 2009.
[217] C. Schick, D. Lexa, L. Leibowitz, Characterization of Materials, (2012).
[218] P.J. Goodhew, F.J. Humphreys, R. Beanland, Electron microscopy and analysis, Taylor & Francis, 2001.
[219] W. Zhou, Z.L. Wang, Scanning Microscopy for Nanotechnology: Techniques and Applications, Springer 2006.
[220] P.W. Hawkes, J.C. Spence, Science of Microscopy, Springer, 2007.
[221] J.R. MacDonald, Impedence Spectroscopy: Emphasizing Solid Materials and Systems, 1987.
[222] E. Barsoukov, J.R. Macdonald, Impedance Spectroscopy: Theory, Experiment, and Applications, John Wiley & Sons, Inc, 2005.
[223] H.R. Allcock, Introduction to Materials Chemistry, John Wiley and Sons, 2008.

[224] R.P. O'Hayre, S.W. Cha, W. Colella, F.B. Prinz, Fuel Cell Fundamentals, John Wiley & Sons New York, 2006.
[225] J.T. Irvine, D.C. Sinclair, A.R. West, Advanced Materials, 2 (1990) 132-138.
[226] X.Z. Yuan, C. Song, H. Wang, J. Zhang, Electrochemical Impedance Spectroscopy in PEM Fuel Cells: Fundamentals and Applications, Springer, 2010.
[227] I. Gamry, Basics of Electrochemical Impedance Spectroscopy, in, Gamry Instruments, Inc., 2010.
[228] D.C. Harris, Quantitative Chemical Analysis, Macmillan, 2010.
[229] M. Radojevic, V.N. Baskin, Practical Environmental Analysis, Royal Society of Chemistry, 2006.
[230] D. Skoog, D. West, F. Holler, S. Crouch, Analytical Chemistry. An Introduction. Saunders, Thomson Learning, Inc, 2000.
[231] J.P. Sibilia, A Guide to Materials Characterization and Chemical Analysis, VCH Publishers, Inc, 1996.
[232] N. Uvarov, Journal of Solid State Electrochemistry, 15 (2011) 367-389.
[233] X. Li, N. Xu, L. Zhang, K. Huang, Electrochemistry Communications, 13 (2011) 694-697.
[234] F. Xie, C. Wang, Z. Mao, Z. Zhan, International Journal of Hydrogen Energy, 38 (2013) 11085-11089.
[235] G.J. Janz, M.R. Lorenz, Journal of Chemical and Engineering Data, 6 (1961) 321-323.
[236] E. Antolini, Ceramics International, 39 (2013) 3463-3478.
[237] J.Y. Cho, S.H. Hyun, S.A. Hong, Journal of the American Ceramic Society, 84 (2001) 937-940.
[238] L. Roux, J. Hanus, J. Francois, M. Sigrist, Solar Energy Materials, 7 (1982) 299-312.
[239] W.R. Lambrecht, M. Miao, P. Lukashev, Journal of Applied Physics, 97 (2005) 10D306-310D306-303.
[240] P. Hones, R. Consiglio, N. Randall, F. Leacutevy, Surface and Coatings Technology, 125 (2000) 179-184.
[241] W. Setthapun, S.K. Bej, L.T. Thompson, Topics in Catalysis, 49 (2008) 73-80.
[242] K.i. Aika, A. Ozaki, Journal of Catalysis, 14 (1969) 311-321.
[243] J.G. Choi, J.R. Brenner, C.W. Colling, B.G. Demczyk, J.L. Dunning, L.T. Thompson, Catalysis Today, 15 (1992) 201-222.
[244] H. Zhong, X. Chen, H. Zhang, M. Wang, S.S. Mao, Applied Physics Letters, 91 (2007) 163103-163103-163103.
[245] H. Zhong, H. Zhang, G. Liu, Y. Liang, J. Hu, B. Yi, Electrochemistry Communications, 8 (2006) 707-712.
[246] D.S. Bem, C.P. Gibson, H.C. zur Loye, Chemistry of Materials, 5 (1993) 397-399.
[247] R. Kojima, K.i. Aika, Applied Catalysis A: General, 215 (2001) 149-160.
[248] L. Volpe, M. Boudart, The Journal of Physical Chemistry, 90 (1986) 4874-4877.
[249] R. Kojima, K.i. Aika, Applied Catalysis A: General, 219 (2001) 141-147.
[250] R. Kojima, K.I. Aika, Chemistry Letters, 29 (2000) 514-515.
[251] C.J. Jacobsen, Chemical Communications, (2000) 1057-1058.
[252] D. McKay, J.S.J. Hargreaves, J.L. Rico, J.L. Rivera, X.L. Sun, Journal of Solid State Chemistry, 181 (2008) 325-333.

[253] R. Chockalingam, S. Basu, International Journal of Hydrogen Energy, 36 (2011) 14977-14983.
[254] B. Nettelblad, B. Zhu, B.E. Mellander, Physical Review B, 55 (1997) 6232-6237.
[255] S. Li, Z. Lü, N. Ai, K. Chen, W. Su, Journal of Power Sources, 165 (2007) 97-101.
[256] C.H. Li, S.H. Hu, K.W. Tay, Y.P. Fu, Ceramics International, 38 (2012) 1557-1562.
[257] E. Perman, G. Atkinson, Proceedings of the Royal Society of London, 74 (1904) 110-117.
[258] R. Lan, S.W. Tao, RSC Advances, 3 (2013) 18016-18021.
[259] L. Fan, G. Zhang, M. Chen, C. Wang, J. Di, B. Zhu, International Journal of Electrochemical Science, 7 (2012) 8420-8435.
[260] N.E. Rajeevan, R. Kumar, D.K. Shukla, P.P. Pradyumnan, S.K. Arora, I.V. Shvets, Materials Science and Engineering: B, 163 (2009) 48-56.
[261] N. Russo, D. Fino, G. Saracco, V. Specchia, Catalysis Today, 119 (2007) 228-232.
[262] C.N.R. Rao, J. Gopalakrishnan, New Directions in Solid State Chemistry, Cambridge University Press, 1997.
[263] N. Sivakumar, A. Narayanasamy, K. Shinoda, C. Chinnasamy, B. Jeyadevan, J.-M. Greneche, Journal of applied physics, 102 (2007) 013916-013916-013918.
[264] R. Rai, S. Wilser, M. Guminiak, B. Cai, M. Nakarmi, Applied Physics A, 106 (2012) 207-211.
[265] N. Rezlescu, N. Iftimie, E. Rezlescu, C. Doroftei, P. Popa, Sensors and Actuators B: Chemical, 114 (2006) 427-432.
[266] D. Fino, N. Russo, G. Saracco, V. Specchia, Journal of Catalysis, 242 (2006) 38-47.
[267] M.I. Godinho, M.A. Catarino, M. da Silva Pereira, M. Mendonça, F. Costa, Electrochimica Acta, 47 (2002) 4307-4314.
[268] J.G.D. Haenen, W. Visscher, E. Barendrecht, Journal of applied electrochemistry, 15 (1985) 29-38.
[269] R.N. Singh, J.F. Koenig, G. Poillerat, P. Chartier, Journal of Electroanalytical Chemistry and Interfacial Electrochemistry, 314 (1991) 241-257.
[270] M.U. Anu Prathap, R. Srivastava, Nano Energy, 2 (2013) 1046-1053.
[271] J. Tong, L. Bo, Z. Li, Z. Lei, C. Xia, Journal of Molecular Catalysis A: Chemical, 307 (2009) 58-63.
[272] A.B. Bodade, A.B. Bodade, H. Wankhade, G. Chaudhari, D. Kothari, Talanta, 89 (2012) 183-188.
[273] W.X. Wang, H.Q. Zhao, B.S. Du, J.M. Wen, F. Li, D.M. Wang, Applied Catalysis A: General, 122 (1995) 5-20.
[274] R.R. Rajaram, P.A. Sermon, Journal of The Chemical Society, Faraday Transactions 1, 81 (1985) 2577-2591.
[275] R.R. Rajaram, P.A. Sermon, Journal of The Chemical Society, Faraday Transactions 1, 81 (1985) 2593-2603.
[276] V.L.E. Simonsen, M. Lilliedal, R. Petersen, K. Kammer, Topics in Catalysis, 45 (2007) 143-148.
[277] I.A. Amar, R. Lan, C.T.G. Petit, V. Arrighi, S.W. Tao, Solid State Ionics, 182 (2011) 133-138.

[278] R. Voorhoeve, D. Johnson, J. Remeika, P. Gallagher, Science, 195 (1977) 827-833.
[279] T. Screen, Platinum Metals Review, 51 (2007) 87-92.
[280] H. Tanaka, M. Misono, Current Opinion in Solid State and Materials Science, 5 (2001) 381-387.
[281] G. Pecchi, M. Jiliberto, E. Delgado, L. Cadús, J. Fierro, Journal of Chemical Technology and Biotechnology, 86 (2011) 1067-1073.
[282] Z. Zhong, K. Chen, Y. Ji, Q. Yan, Applied Catalysis A: General, 156 (1997) 29-41.
[283] J. Irvine, Perovskite Oxide Anodes for SOFCs, in: Perovskite Oxide for Solid Oxide Fuel Cells, Springer, 2009, pp. 167-182.
[284] R. Voorhoeve, J.P. Remeika, D. Johnson, Science, 180 (1973) 62-64.
[285] C. Xia, W. Rauch, F. Chen, M. Liu, Solid State Ionics, 149 (2002) 11-19.
[286] Z. Shao, S.M. Haile, Nature, 431 (2004) 170-173.
[287] X. Yue, J.T.S. Irvine, Solid State Ionics, 225 (2012) 131-135.
[288] Y. Gan, J. Zhang, Y. Li, S. Li, K. Xie, J.T. Irvine, Journal of The Electrochemical Society, 159 (2012) F763-F767.
[289] S.P. Jiang, Journal of materials science, 43 (2008) 6799-6833.
[290] N. Oishi, A. Atkinson, N. Brandon, J. Kilner, B. Steele, Journal of the American Ceramic Society, 88 (2005) 1394-1396.
[291] Y. Ling, J. Yu, B. lin, X. Zhang, L. Zhao, X. Liu, Journal of Power Sources, 196 (2011) 2631-2634.
[292] G. Coffey, J. Hardy, O. Marina, L. Pederson, P. Rieke, E. Thomsen, Solid State Ionics, 175 (2004) 73-78.
[293] J. Maier, Progress in Solid State Chemistry, 23 (1995) 171-263.
[294] H. Ding, X. Xue, X. Liu, G. Meng, Journal of Power Sources, 194 (2009) 815-817.
[295] L. Zhang, R. Lan, C.T. Petit, S.W. Tao, International Journal of Hydrogen Energy, 35 (2010) 6934-6940.
[296] Y. Xia, Y. Bai, X. Wu, D. Zhou, X. Liu, J. Meng, International Journal of Hydrogen Energy, 36 (2011) 6840-6850.
[297] Y. Zhao, C. Xia, Z. Xu, Y. Li, International Journal of Hydrogen Energy, 37 (2012) 11378-11382.
[298] I. Kaus, H.U. Anderson, Solid State Ionics, 129 (2000) 189-200.
[299] B. Wei, Z. Lü, X. Huang, M. Liu, N. Li, W. Su, Journal of Power Sources, 176 (2008) 1-8.
[300] J. Wackerl, T. Koppitz, D.H. Peck, S.K. Woo, T. Markus, Journal of Applied Electrochemistry, 39 (2009) 1243-1249.
[301] I.M. Hung, C.Y. Liang, C.J. Ciou, R.Z. Song, Z.Y. Lai, Journal of Materials Science, 45 (2010) 3824-3832.
[302] Y. Tanabe, Y. Nishibayashi, Coordination Chemistry Reviews, 257 (2013) 2551-2564.
[303] B.C.H. Steele, Solid State Ionics, 129 (2000) 95-110.
[304] F.Y. Wang, S. Chen, S. Cheng, Electrochemistry Communications, 6 (2004) 743-746.
[305] X. Guan, H. Zhou, Z. Liu, Y. Wang, J. Zhang, Materials Research Bulletin, 43 (2008) 1046-1054.

[306] S. Banerjee, P.S. Devi, D. Topwal, S. Mandal, K. Menon, Advanced Functional Materials, 17 (2007) 2847-2854.
[307] P.S. Cho, S.B. Lee, D.S. Kim, J.H. Lee, D.Y. Kim, H.M. Park, Electrochemical and Solid-State Letters, 9 (2006) A399-A402.
[308] P.S. Cho, S.B. Lee, Y.H. Cho, D.Y. Kim, H.M. Park, J.H. Lee, Journal of Power Sources, 183 (2008) 518-523.
[309] A. Moure, J. Tartaj, C. Moure, Journal of the European Ceramic Society, 29 (2009) 2559-2565.
[310] W. Liu, Y. Liu, B. Li, T.D. Sparks, X. Wei, W. Pan, Composites Science and Technology, 70 (2010) 181-185.
[311] T. Sakai, S. Matsushita, H. Matsumoto, S. Okada, S. Hashimoto, T. Ishihara, International Journal of Hydrogen Energy, 34 (2009) 56-63.
[312] R. Shannon, Acta Crystallographica Section A: Crystal Physics, Diffraction, Theoretical and General Crystallography, 32 (1976) 751-767.
[313] A. Mai, V.A. Haanappel, S. Uhlenbruck, F. Tietz, D. Stöver, Solid State Ionics, 176 (2005) 1341-1350.
[314] P. Plonczak, M. Gazda, B. Kusz, P. Jasinski, Journal of power sources, 181 (2008) 1-7.
[315] A. Esquirol, N. Brandon, J. Kilner, M. Mogensen, Journal of The Electrochemical Society, 151 (2004) A1847-A1855.
[316] Y. Teraoka, H.M. Zhang, K. Okamoto, N. Yamazoe, Materials research bulletin, 23 (1988) 51-58.
[317] N.F. Szabo, P.K. Dutta, Solid State Ionics, 171 (2004) 183-190.
[318] R. Spinicci, A. Tofanari, A. Delmastro, D. Mazza, S. Ronchetti, Materials Chemistry and Physics, 76 (2002) 20-25.
[319] B. Wang, B. Zydorczak, Z.-T. Wu, K. Li, Journal of Membrane Science, 344 (2009) 101-106.
[320] O.A. Marina, L.R. Pederson, M.C. Williams, G.W. Coffey, K.D. Meinhardt, C.D. Nguyen, E.C. Thomsen, Journal of The Electrochemical Society, 154 (2007) B452-B459.
[321] J. Kong, Y. Zhang, C. Deng, J. Xu, Journal of power sources, 186 (2009) 485-489.
[322] N.Q. Minh, Journal of the American Ceramic Society, 76 (1993) 563-588.
[323] H. Yokokawa, N. Sakai, T. Kawada, M. Dokiya, Solid State Ionics, 52 (1992) 43-56.
[324] S.W. Tao, J.T. Irvine, Chemistry of Materials, 16 (2004) 4116-4121.
[325] S.W. Tao, J.T. Irvine, Solid Oxide Fuel cells VIII, 8 (2003) 793-798.
[326] S.W. Tao, J.T.S. Irvine, Nature Materials, 2 (2003) 320-323.
[327] S.W. Tao, J.T.S. Irvine, Journal of The Electrochemical Society, 151 (2004) A252-A259.
[328] D.M. Bastidas, S. Tao, J.T.S. Irvine, Journal of Materials Chemistry, 16 (2006) 1603-1605.
[329] X. Yang, J.T.S. Irvine, Journal of Materials Chemistry, 18 (2008) 2349-2354.
[330] I. Jung, D. Lee, S.O. Lee, D. Kim, J. Kim, S.H. Hyun, J. Moon, Ceramics International, 39 (2013) 9753-9758.
[331] E. Skulason, T. Bligaard, S. Gudmundsdóttir, F. Studt, J. Rossmeisl, F. Abild-Pedersen, T. Vegge, H. Jónsson, J.K. Nørskov, Physical Chemistry Chemical Physics, 14 (2012) 1235-1245.